Volume II, Final Report

GE Astro Space

Final Study Report
Phase I
Contract No. NAS8-37589
26 March 1990

Definition and Preliminary Design of the LAWS Laser Atmospheric Wind Sounder

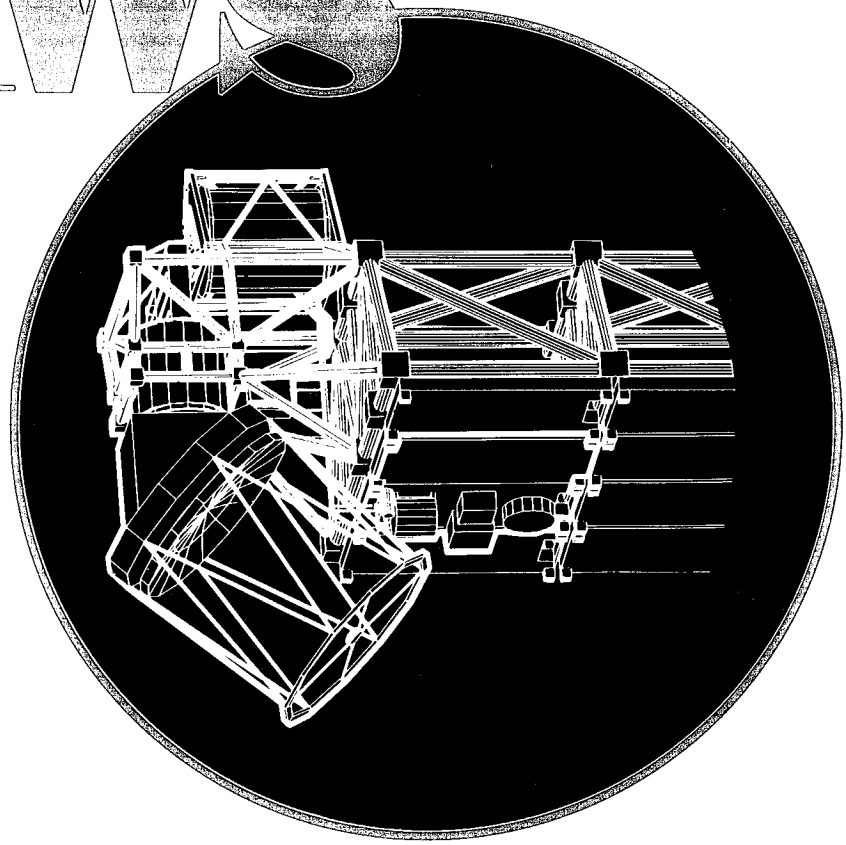

Marshall Space Flight Center

GE Astro Space
Hughes Danbury
Spectra Technology

GE Astro Space Division
PO Box 8555
Philadelphia, PA 19101

Definition and Preliminary Design of the

LAWS

Laser Atmospheric
Wind Sounder

PHASE I
FINAL REPORT VOLUME II

Date: 3/26/90
(Final Submission: 5/15/90)

Contract Number: NAS8-37589

GE Astro Space
Hughes Danbury
Spectra Technology

TABLE OF CONTENTS

LIST OF FIGURES

LIST OF TABLES

1.0 INTRODUCTION

The Laser Atmospheric Wind Sounder (LAWS) Study (Phase I) was conducted by GE Astro-Space Division, with the support of Hughes Danbury Optical Systems (formerly Perkin-Elmer, optical subsystem) and Spectra Technology (laser subsystem). Lassen Research (receiver support) and Simpson Weather Associates (mission support) also participated, in a secondary supporting role. The contract was managed by the NASA Marshall Space Flight Center and performed over a 12-month period from March 27 1989 to March 26, 1990.

This document is Volume II of the Phase I Final Study Report. It records the steps and engineering trades and analyses used in establishing the initial requirements and in developing a concept and configuration for the LAWS instrument. It also contains a summary of the performance anticipated from the baseline configuration, and a bibliography. Volume I contains an Executive Summary and Volume III details of the cost and schedule for the Phase C/D procurement.

LAWS, which is a facility instrument of the Earth observing system (Eos), is the culmination of over 20 years of effort in the field of laser Doppler wind sensing and will be the first instrument to fly in space capable of providing global-scale tropospheric wind profiles at high spatial resolutions. Global-scale wind profiles are necessary for:

- More accurate diagnostics of large-scale circulation and climate dynamics;
- Improved numerical weather prediction;
- Improved understanding of mesoscale systems;
- Improved understanding of global biogeochemical and hydrologic cycles.

The objective of phase I of the LAWS study was to define and perform a preliminary design for the LAWS instrument. The definition phase consisted of identifying realistic concepts for LAWS and analyzing them in sufficient detail to be able to choose the most promising one for the LAWS application. System and subsystem configurations were then developed for the chosen concept. The concept and subsequent configuration were to be compatible with two prospective platforms- the Japanese Polar Orbiting Platform (JPOP) and as an attached payload on the Space Station Freedom.

After a thorough and objective concept selection process, we chose a heterodyne detection Doppler lidar using a CO_2 laser transmitter operating at 9.1 μm over a 2.1 μm solid state system. The choice of CO_2 over solid-state reflects the advanced state of development of CO_2 lasers and the eased subsystem requirements associated with the longer wavelength.

The CO_2 lidar concept was then analyzed in detail to arrive at a configuration for the instrument and its major subsystems. Our approach throughout the configuration design was to take a systems perspective and trade requirements between subsystems, wherever possible, to arrive at configurations which made maximum use of existing, proven technology or relatively straightforward extensions to existing technology to reduce risk and cost. At the conclusion of Phase I we arrived at a configuration for LAWS which meets the performance requirements, yet which is less complex than previous designs of space-based wind sensors (e.g. Windsat), employs lightweight technologies to meet its weight goal (<800 kg) and sufficiently flexible to offer various operational scenarios with power requirements from about 2 kW to 3 kW. Highlights of the design are:

- A unitary construction, compact, lightweight, efficient laser with substantial heritage including the proven NOAA Windvan design. The laser uses the oxygen-18 isotope of CO_2 to increase atmospheric transmission; a combination of funded and in-house measurement programs have shown that the use of this

gas is a straightforward extension of techniques developed with the normal oxygen-16 isotope. The laser operates asynchronously at up to 20 Hz maximum repetition rate and therefore offers a variety of measurement scenarios.;

- A new optical subsystem design which is simpler than the previous Windsat design and overcomes known Windsat design deficiencies. The optical subsystem fully supports asynchronous operation by eliminating the mechanisms for lag angle compensation and Transmit/Receive (T/R) switching.
- A receiver system which uses a circularly symmetric array detector to increase the SNR of the received signal, enable a closed loop alignment and control system by measuring the phase of the returned signal, and offers redundancy. The receiver design benefits from significant in-house development of mercury cadmium telluride (MCT) detectors and arrays aimed at increasing the quantum efficiencies at the high bandwidths necessary for LAWS.
- Extensive use of existing technology for the support subsystems including: a graphite-epoxy truss support structure based on the GE technology developed for UARS and the Space Station Polar Platforms Work Package 3 (WP-3); a thermal subsystem based on heat pipe and capillary-pumped-loop technology developed under WP-3; a momentum compensation approach from an in-house communications satellite program (GSTAR) and system controller technology from Space Station.

The layout of Volume II largely follows the chronological flow of the tasks performed during the Phase I study. For this reason it should be read with the understanding that the work documented in the earlier sections of the report was performed at an earlier time than that documented in the later sections. The whole report therefore reflects the maturing of our understanding and thinking regarding LAWS which accrued as the Study progressed.

2.0 BACKGROUND LITERATURE REVIEW

This section details the results of LAWS study task 5.1.1- Background Literature Review. Emphasis has been placed on reviewing those previous studies relating specifically to space based operation of a Doppler lidar. A bibliography is provided as section 7.0 of this document.

The invention of the laser in 1960 gave rise to a rapid growth in the field of remote velocity measurements in the atmosphere. Initial efforts were divided into two different techniques.

One approach used the variations in refractive index present in the atmosphere to track the movement of so-called turbulent eddies through an illuminated volume. Instruments were built which used a single beam illuminating a detector at a distance to measure the path averaged scintillation. Double beam instruments were also constructed which allowed a degree of range resolution by crossing two beams at a given range and examining the cross-correlation statistics of the received intensities. A knowledge of the scintillation statistics allows the mass field motion over the path, or through the illuminated volume, to be deduced. A variation of the cross-beam technique, whereby two coherent beams interfere at the volume under investigation producing fringes, was also succesfully used to make wind measurements. In this technique particles passing through the illuminated volume scatter light in the direction of a receiver. The amplitude of the scattered light varies as the particle passes throught the fringes allowing time of flight calculations to be made providing the fringe spacing is known. A knowledge of the time of flight allows the particle velocity to be calculated. Such techniques are limited in range and the size of the volume being probed, but have found applications in such diverse fields as blood flow analysis and wind tunnel diagnostics, and have given rise to an active subfield known as Laser Doppler Velocimetry (LDV).

An alternative, and more direct, approach to the problem of atmospheric wind field measurement uses the Doppler frequency shift imposed on the laser beam by the motion of scattering particles suspended in the atmosphere. The efficiency with which particles scatter electromagnetic radiation is determined, according to Mie theory, by the relationship between the circumference of the particle and the illuminating wavelength, the ratio being known as the size parameter. For Doppler radar, Mie theory implies and experience shows that scattering particles in the atmosphere are mostly hydrometeors, hail or rain drops, which possess significant inertias and do not necessarily reflect the behaviour of the surrounding wind field. Most lasers of interest, however, have wavelengths at least a thousand times shorter than radar which means that the particles which most strongly scatter the beam are smaller, generally from 0.5 μm to 10 μm in size. The particles are typically, dust, pollen or water droplets. It is obviously a reasonable assumption to make, and the central tenet of Doppler lidar, that such small, buoyant particles move with the velocity of the wind.

The Doppler technique quickly became the approach of choice for wind sensing after various succesful demonstrations in the atmosphere in the late 1960's and early 1970's. The demonstrations used both direct detection, in which high resolution interferometers are used, and coherent detection, where the signal is mixed with a frequency stable local oscillator, to recover the small (about 100 kHz per knot for a wavelength of 10 μm) Doppler shifts imposed on the return signal. Subsequently, in 1976, the idea of using pulsed coherent lidar for satellite based wind measurements was suggested (Huffaker, R.M. et al, 1976) with the first detailed study of the feasibility of making global wind measurements from an Earth orbiting platform conducted by NOAA in 1978 (Huffaker, R.M. ed., 1978). This study and a follow-up in 1980 (Huffaker, R.M. et al, 1980) established the feasibility and identified the issues for an Earth orbiting system based on using carbon dioxide lasers emitting near a wavelength of 10 μm with coherent detection. The direct detection community performed a similar study

in 1979 (Abreu, 1979), which showed the feasibility of a technique based on a Nd:YAG laser at a wavelength of 0.5 μm.

The issues raised and the recommendations made by the NOAA study remain pertinent today, in particular:

- They realized that in order to avoid attenuation by the naturally occurring atmospheric CO_2, a laser which used a rare isotope of CO_2 (either based on carbon-13 at 11.16 μm or oxygen-18 at 9.11 μm) should be used.
- The necessity of making Doppler measurements from at least two different directions to recover the horizontal wind vector. They identified the conical scan or step-scan as the simplest way of achieving the different pointing directions.
- The realization that the data generated would be large and the conclusion that for the platforms envisaged at the time the data rate would require on board Doppler processing to make the down-link feasible.
- The realization that the instrument would be large and that platform accommodation requirements such as weight, power and pointing accuracy and stability would constrain the design.
- The horizontal, vertical and velocity resolutions thought to be attainable by the instrument from orbit were established by an integrated system model. A horizontal grid size of 300 km x 300 km was assumed with a vertical resolution of 1 km. A velocity accuracy of <2 m/s was thought to be attainable from 800 km, throughout the troposphere.
- The lack of sufficient global aerosol data was identified as the principal unknown in the analysis.

During this time the global wind measuring satellite concept became known as WINDSAT. Both of the NOAA studies advanced the understanding of the principles involved in global wind sensing to the extent that real space platforms could be considered for the WINDSAT instrument.

An earlier study (Global Wind Measuring Satellite System, 1981) considered flying a Doppler lidar instrument, based on a CO_2 lidar, on a Shuttle mission. The study was able to specify a large lidar system, with few restrictions on volume, weight, or power. It was recognized, however, that such a system, if flown, would have served merely as a proof of concept demonstration due to the short duration of the average Shuttle flight and the non-polar orbit.

An attempt to advance the Doppler lidar concept toward an operational instrument was made by a later study (Feasibility Study of a WINDSAT Free-Flyer, 1983), which considered the accommodation of the instrument on an existing class of free flying meteorological satellite, known as TIROS. Since TIROS satellites fly over the poles, taking ~90 minutes for one orbit, a lidar flown on a TIROS allows global coverage. Due to the limited amount of room on the spacecraft, and propulsion system and launch constraints, however, it was necessary to reduce the payload weight significantly from the figure used in the Shuttle study. This reduction was accomplished by the use of a lightweight telescope and new packaging concepts for the laser and associated optics. A more serious problem was posed by the limited amount of power available on the spacecraft. Even after adding two more solar array panels (increasing power 25%) and limiting the range of sun angles over which the spacecraft operated, the laser repetition rate still had to be reduced from the 8 Hz, assumed in the Shuttle study, to 2 Hz. This low repetition rate has a direct and significant impact on the accuracy of the horizontal wind vector measurement, since fewer pulses can be averaged in any given volume of interest. Because of this limitation interest in a Doppler lidar on TIROS waned.

The advent of Space Station and the accompanying large polar platforms (with much greater resources than TIROS) renewed interest in the possibility of deploying a space-based Doppler lidar. The Doppler lidar was designated as a facility instrument of the Earth observing system (Eos) and the name changed from WINDSAT to LAWS. The name change reflected the fact that the larger platforms now coming into existence would no longer have to be dedicated totally to the lidar sensor, which would simply become one payload among many.

An early experiment, again from the Shuttle, was planned (SCALE, 1985) to confirm the performance of a coherent lidar from orbit, establish the existence of sufficient backscatter and answer questions regarding laser transmitter engineering issues. This would have been a low-cost precursor to an actual Eos flight, which, using largely existing technology (e.g. the laser design was an upgrade of an existing ground-based NOAA facility, scanning was performed by yawing the Shuttle about nadir) would have shown the utility of wind measurements from orbit, particularly in the Tropics where wind data is scarce. The Challenger accident, however, terminated plans for SCALE.

As the concepts for the Space Station polar platforms became better defined it was possible to understand how the new polar platform philosophy and the increased resources available impacted the LAWS design. A small study was conducted (Feasibility Study of a Carbon Dioxide Doppler Lidar on an Earth Orbiting Platform, 1987, and Petheram, J.C. et al, 1989) which was in many ways a compromise between the earlier Shuttle study and the TIROS study, with various assumptions regarding the Doppler payload being drawn from both. For example, the laser was assumed to operate at a repetition rate of 8 Hz, similar to the Shuttle laser, but the telescope was assumed to be the lightweighted 1.25-m aperture specified in the TIROS design. Unlike the two previous studies, however, the platform then existed only in a conceptual form and so the accommodation study was much less detailed. Results of the study showed that a LAWS-type payload could be accommodated on a Space Station polar platform as the concept was then understood. The power, weight and thermal issues appeared to be resolvable. A potential issue was the fact that with the payload mounted to the Earth facing panel, the sun-shade of the 1.25-m telescope just touched the Shuttle cargo-bay wall. By trimming the sunshade slightly it could be made to fit, but a larger telescope would require special accommodation.

In 1987, the report of the LAWS facility instrument panel was published (LAWS, 1987). This document succesfully encapsulated and summarized the previous work in the field of atmospheric wind sensing and clarified ideas in light of the new platform opportunities. LAWS was subsequently proposed as an attached payload on the Space Station manned base (LAWS as a Space Station Attached Payload, 1988), where it could provide detailed wind fields in the Tropics, as well as on one of the polar platforms.

The LAWS instrument has continued to evolve over time as the importance of making wind measurements from space has become better understood. Electro-optic and laser technology has continued to progress. For example, solid state systems have now advanced to the stage where ground based coherent Doppler lidar instruments have been demonstrated at 1 μm as well as the more ubiquitous 10.6 μm (Henderson, S. et al, CLEO 1989). A ground based incoherent detection Doppler lidar has been demonstrated at a wavelength of 0.5 μm (Sroga, J. et al, 1987). A continuing question for space based systems, however, remains the strength of the atmospheric backscatter and its variation with wavelength. The GLOBE program, due to make measurements of atmospheric backscatter in the Pacific in Fall, 1989 and Spring, 1990 will further clarify the properties of the atmosphere at a range of wavelengths from 0.5 μm to 10.6 μm.

All of this recent activity and the wealth of knowledge gained from previous studies were carefully assimilated and used in the LAWS study, to define the mission requirements and to select the concept and subsequent configuration for the LAWS instrument.

3.0 REQUIREMENTS DEFINITION

The primary scientific objective of the LAWS mission is to improve our understanding of atmospheric circulation, climate dynamics, and global biogeochemical and hydrologic cycles, as well as improving numerical weather prediction, by making measurements of wind profiles through the lower and upper troposphere.

An understanding of this scientific objective allows a set of mission requirements to be defined, which then serve as one constraint on the choice of instrument concept and ultimately on the more detailed design. There are other constraints on the instrument design process, however, namely the properties of the atmosphere, and the accommodations and services available on the space vehicle chosen for the mission. The way these three constraints influence the concept selection process are discussed in more detail in section 4.0.

The mission requirements and strawman accommodation allocations which were initially used to choose between candidate concepts for LAWS are given below:

- Global scale wind measurements commensurate with coverage available from the designated space platform.
- Horizontal resolution of 100 km x 100 km.
- Vertical resolution of 1 km throughout the troposphere.
- Horizontal wind vector accuracy of $\pm$ 1 m/s in the lower troposphere and $\pm$ 5 m/s in the upper troposphere.
- Operational lifetime of 10^9 shots.
- Continuous operations.
- Serviceability
- Weight < 800 kg
- Average power < 3 kW

Once realistic concepts for LAWS were identified, the missions requirements were extended to aid in making the final concept selection (section 4.3.1).

4.0 CONCEPT IDENTIFICATION, ANALYSIS AND SELECTION

The objective of this section is to identify realistic concepts for meeting the LAWS mission requirements and to specify, by virtue of trades and analyses, their properties in sufficient detail to collect a data base of information typifying each concept. The data base collected then enables a choice to be made between competing concepts. Some concepts can be rejected early in the decision making process, based on some relatively top-level considerations. Others, however, are more difficult to evaluate using simple criteria and require a more structured approach in order to assure an objective assessment. Thus, one of the early contractual requirements was to develop an Evaluation and Selection Criteria Plan which would be used to choose between concepts with apparently similar credentials. This Plan (designated as DR-18) which was submitted in final form at the Orientation Meeting (April 13th, 1989) is briefly described in the next section.

4.1 Evaluation and Selection Criteria Plan

The evaluation and selection criteria plan provides an objective and methodical framework to select the best overall design for LAWS in terms of performance, cost and safety. The plan consists of a set of criteria against which to evaluate those concepts which appear to have the potential to meet the LAWS mission requirements. The criteria used are given in Figure 4-1. Concepts are broken down into component subsystems which are then scored against the criteria shown. Each criterion is assigned a weight reflecting its relative importance and weighted scores added for each concept. The meanings of the various criteria are given in detail in DR-18.

The risk criterion uses a risk assessment methodology which attempts to quantify the total risk to the program by considering technology, cost and schedule risk. We define technology risk for a particular subsystem or component as the product of the part's criticality with its technical maturity. Cost and schedule risk is then defined as the product of technology risk with development risk. Figure 4-2 shows the risk assessment methodology.

Competing concepts are scored on an Evaluation and Selection Criteria score chart shown in Figure 4-3.

4.2 Decision Tree Approach to Concept Selection

The path we follow to arrive at concepts for evaluation is illustrated in the form of a decision tree in Figure 4-4. The shaded circles show the route taken through the tree; the open circles end in dialogue boxes which give a brief synopsis of the reasons for terminating that particular branch of the tree. The following paragraphs discuss those reasons in more detail. We have concluded that the most viable candidates for LAWS at the present time are concepts based on the Tm:Ho:YAG laser at 2.1 μm and the rare isotope $^{12}C^{18}O_2$ laser at 9.1 μm, the decision tree shows the path taken to arrive at this conclusion. The following paragraphs refer to branches in the decision tree.

Although there have been a number of ways proposed for making wind measurements from space which could potentially satisfy the LAWS requirements, they generally fall into one of two categories which we call Doppler techniques or other techniques.

4.2.1 *Other Techniques*

In the category of techniques other than Doppler for making wind measurements, we first evaluate aerosol pattern correlation and laser based stereoscopy.

Criteria	Score	Weight
Mission Requirements and System Performance	1 - 5	4
System Safety	0 or 1	N/A
Technology	1 - 5	4
Design Simplicity	1 - 5	3
Reliability	1 - 5	3
Accommodations	1 - 5	2
Serviceability	1 - 5	2
System Operations	1 - 5	2
Verification	1 - 5	3
Risk	1 - 5	5
Survivability	1 - 5	2
Cost	1 - 5	4

Figure 4-1. Criteria Used in Evaluation and Selection Criteria Plan (DR-18)

Criticality Dategory	Score	Technology Maturity Category	Score	Development Risk Category	Score	Total	Evaluation and Selection Criteria Score
Marginal Impact	4	Flight Qualified	5	Built One Before	4	1-8	1
Moderate Impact	3	Component Tested	4	Built Similar Item	3	9-13	2
Significant Impact	2	Component Development	2	Capability Under Development	2	19-30	3
Loss of Mission	2	SOA Improve-ments to Basic Physics	2	No Capability	1	31-47	4
		Basic Physics Only	1			48-80	5

Technology Risk = Criticality x Technical Maturity

Cost and Schedule Risk = Technology Risk x Development Risk

Figure 4-2. Risk Assessment Methodology for Evaluation and Selection Criteria Plan

SUBSYSTEMS/COMPONENTS	SELECTION CRITERIA												
	PERFORMANCE	TECHNOLOGY	DESIGN SIMPLICITY	RELIABILITY	ACCOMMODATIONS	SERVICEABILITY	SYSTEM OPERATIONS	VERIFICATION	RISK	SURVIVABILITY	COST	SAFETY	TOTAL SCORE
WEIGHTING FACTOR	4	4	3	3	3	2	2	3	5	2	4	N/A	
2.1 μm CONCEPT													
LASER SUBSYSTEM													
OPTICAL SUBSYSTEM													
RECEIVER SUBSYSTEM													
9.1 μm CONCEPT													
LASER SUBSYSTEM													
OPTICAL SUBSYSTEM													
RECEIVER SUBSYSTEM													

Figure 4-3. Evaluation and Selection Criteria Plan Score Chart

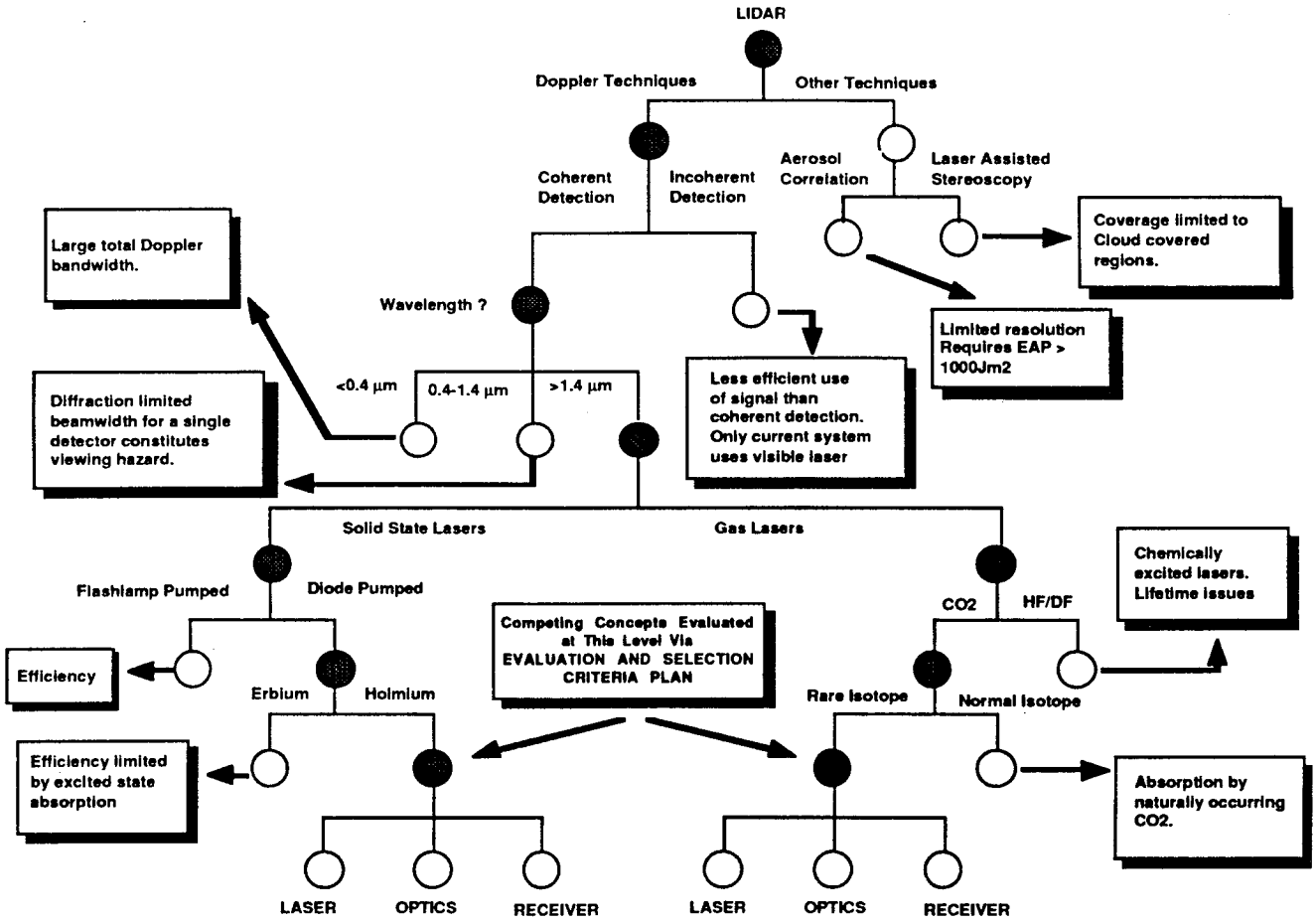

Figure 4-4. Decision Tree Illustrating the Route Taken to Arrive at Realistic Concepts

4.2.1.1 *Aerosol Pattern Correlation*

Since naturally occurring atmospheric aerosols are used as passive tracers of the atmospheric flow field, one technique to derive the wind vector using a lidar system is to measure the displacement of the aerosol inhomogeneity patterns in time in an analogous method to cloud tracked winds. The method may be described as follows.

A series of two dimensional aerosol spatial distributions is obtained by scanning the lidar system through the same atmospheric volume at closely spaced time intervals. An atmospheric wind vector is determined by measuring the displacement vector of the aerosol inhomogeneity patterns between successive lidar scans of the same volume using a two dimensional lag correlation technique or a computationally more efficient fast Fourier transform. Velocity vectors measured by this technique require that 1) sufficient spatial structures exist in the signal which exceeds the noise level, 2) the coherent lifetime of the aerosol inhomogeneities is longer than the time interval between successive scans, 3) the aerosol inhomogeneities must be passive tracers which drift with the wind and are not due to origraphic effects or wave motions. This technique has been used by a number of researchers to measure wind profiles in the convective planetary boundary layer (PBL) with ground based lidar systems (Eloranta et al., 1975, Kunkel et al., 1980, Sroga et al.,1980, Sansano et al, 1982, Hooper and Eloranta 1986, Kolev et al., 1988). Measurement accuracies $\leq$1m/s and $\leq$ 10 degrees have been demonstrated using this technique. Atlas and Korb (1981) have proposed an extension of this technique to measure winds from a spaceborne platform. A review of the technique and an analysis of the potential spaceborne application has been given by Eloranta (1985).

To analyse the aerosol correlation technique and to assess its potential for LAWS we have assumed measurements are obtained from a 25 x 25 grid sample, 3 km on each side with two scans required to derive a vector wind measurement. Each 25 x 25 grid would require approximately 28 seconds to acquire. The receiver aperture is assumed to be 1 meter in diameter and the energy requirements listed in Atlas and Korb (1981) and Eloranta (1985) have been scaled to a satellite operational altitude of 800 km. Figure 4-5 lists the results of the initial Energy-Aperture Product (EAP) and power estimates for a spaceborne aerosol correlation lidar to measure winds. Calculations indicate that an EAP of between approximately 3 and 4 kJm^2 is required to measure horizontal winds in the PBL, using the aerosol correlation technique. Extension of this technique to aerosol structures in the free troposphere or stable atmospheric conditions requires a higher EAP and has not been demonstrated.

The following conclusions can be inferred from our first order analysis of the aerosol pattern correlation technique: 1) vector wind measurements from a spaceborne aerosol pattern correlation lidar system would be acquired from convective planetary boundary layers (maximum altitudes 1-2 km) and from cloud regions where sufficient structure in the cloud particle concentration exists and multiple scatter contributions can be ignored; 2) initial estimates of the EAP for this vector wind measurement technique are large, primarily driven by the high laser repetition rate (>20Hz) and pulse energies required to measure $\geq$10% fluctuation levels accurately.

4.2.1.2 *Laser Assisted Stereoscopy*

This approach to measuring winds from orbit uses a cloud top lidar in conjunction with a fore/aft looking imager. The imager has an ambiguity in apparent cloud height because of cloud motions occurring between observations. By measuring the cloud height directly using a simple, low energy lidar, the ambiguity is removed and wind fields can be deduced from the images. Advantages of such a system are: 1) the simultaneous determination of cloud heights and motions, 2) it uses a simple low energy lidar which could use available laser diode pumped solid state lasers, 3) low power

	Atlas and Korb	Eloranta
Aperture	1 m diam.	1 m diam.
Energy	2.9 J/pulse	4 J/pulse
Rep. Rate	22 Hz	22 Hz
Grid	25 x 25	25 x 25
EAP*	2815 J-m^2	3977 J-m^2
Power	2.6 kW	3.6 kW

**Energy-Aperture Product (EAP) scaled to 800 km.*

Figure 4-5. Aerosol Pattern Correlation EAP and Power Estimates

requirements probably <200 W and 4) a large swath width (estimated at ~2000 km from an orbit of 800 km). Disadvantages and unknowns are 1) the magnitude of the errors due to non-advective cloud field changes, 2) cloud top sampling requirements, 3) resolution and spectral band limitations (reflective/thermal etc.), 4) pointing requirements (stability, co-registration etc.), and 5) processing algorithms impact (stereo processing requirements can be large).

The technique has recently been proposed by CNES for the French Tropical System Energy Budget (BEST) platform as an adjunct to a CO_2 Doppler lidar.

Our principal conclusion regarding the two above mentioned techniques is that they are limited in coverage; aerosol correlation to the planetary boundary layer and clouds, laser stereoscopy to dense cloud tops, and therefore that neither meets the LAWS mission requirements given in section 3.1. We turn now to consideration of Doppler techniques.

4.2.2 *Doppler Techniques*

In a backscatter Doppler lidar, the wind speed may be deduced by recovering the Doppler shift imposed on the backscattered laser signal by the motion of the suspended aerosol particles. Systems which use both direct and heterodyne detection techniques have been demonstrated on the ground.

4.2.2.1 *Direct Detection Doppler Lidar*

An incoherent or direct detection technique to measure the Doppler shift incorporates a single frequency laser as the transmitter source with a high resolution interference technique to measure the spectrum of the light backscattered from the atmosphere.

There have been a number of direct detection Doppler lidar systems investigated (see e.g. Benedetti-Michelangli et al., 1972 and Congeduti et al., 1981). Abreu, 1979, has proposed a spaceborne incoherent Doppler lidar utilizing a narrow band laser transmitter and a Fabry-Perot Interferometer (FPI) with a multiple ring Image Plane Detector (IPD), to simultaneously measure the backscattered spectrum. A passive sensor utilizing the FPI-IPD combination was flown on the Dynamics Explorer satellite (Hays et al., 1981) to measure temperature, wind and density in the thermosphere.

Analyses of similar lidar systems have been given by Hays, et al., 1984, McDermid et al., 1985 and Menzies, 1986. Sroga and Rosenberg, 1987, have constructed a ground-based, direct-detection, 532-nm, Doppler lidar using an FPI-IPD receiver and a single frequency, pulsed Nd:YAG laser transmitter.

Our analysis of direct detection Doppler lidar techniques for spaceborne wind sensing is based on the technology demonstrated at GE by Sroga and Rosenberg. A block diagram of the GE Direct Detection Doppler Lidar is shown in Figure 4-6 and some recent results shown in Figure 4-7. The Atlantic City RAOB referred to in the latter Figure is the nearest rawinsonde station to GE Astro, East Windsor, NJ where the lidar is located.

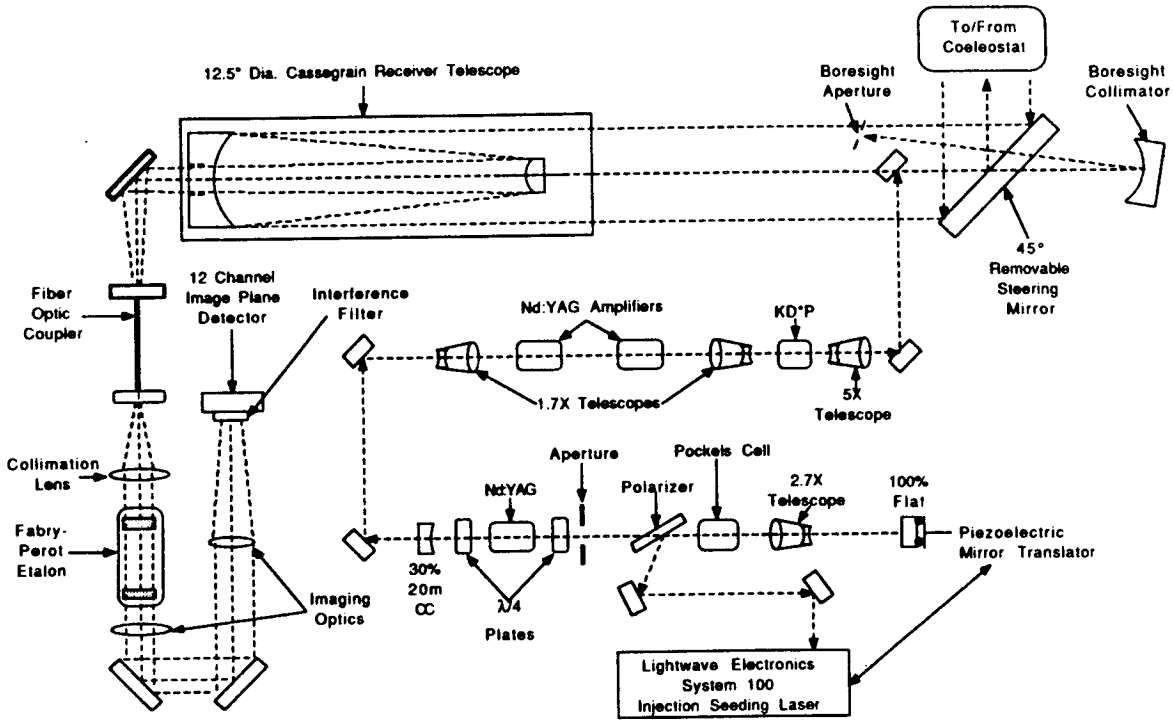

Figure 4-6. GE Direct Detection Doppler Lidar Block Diagram

In a direct detection Doppler lidar the signal intensity measured in each channel of the FPI-IPD receiver depends upon the spectral distribution of the input source (laser or atmospheric backscatter) and the instrument transmission function for that particular channel. The spectral distribution of the atmospheric backscatter consists of a narrow aerosol backscatter spike, which represents the signal, superimposed upon the thermal, Doppler-broadened, molecular-backscatter contributions, which represents noise. Killeen and Hays, 1984, have developed an instrument model of the FPI-IPD combination which we fit to the data using a regression analysis. The instrument model and the regression analysis can be used to simulate the performance of a spaceborne Doppler lidar system utilizing this technique. We have simulated the signal intensity

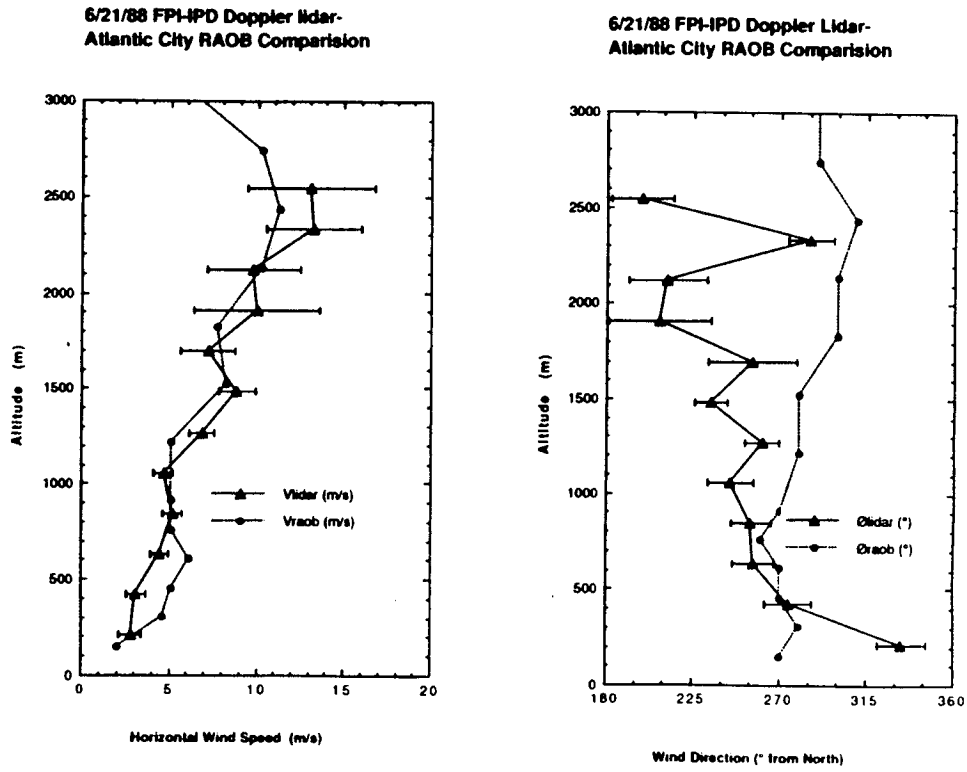

Figure 4-7. Direct Detection Doppler Lidar - Recent Results

measured by a FPI-IPD detector system under various atmospheric scattering conditions and signal intensities. For our initial analysis of the performance capabilities of a direct detection Doppler lidar system, we have calculated the rms errors in the line of sight (LOS) Doppler velocity estimate based upon the statistical uncertainty in the simulated FPI-IPD signal.

Figure 4-8 illustrates the required EAP for a direct detection Doppler lidar to achieve a given LOS velocity error as a function of the aerosol backscatter cross section at 5 km altitude, with a 1 km vertical resolution. An 800 km satellite altitude and a 45° conical scan were assumed in these calculations. Two different detection efficiencies were simulated, the solid line representing an overall efficiency of 10% (50% optical throughput efficiency, 20% quantum efficiency) and the dashed line an overall efficiency of 25% (optical efficiency 50%, quantum efficiency 50%). The justification for the latter figure is some recent work by Paul Hays at the University of Michigan, who has suggested replacing the conventional microchannel plate photomultiplier by a charge coupled device (CCD) detector, which has a higher quantum efficiency.

In contrast to coherent or heterodyne detection which can approach shot noise limited detection, direct detection is limited by the magnitude of the return from molecular backscattering. Since the aerosol backscatter cross section, at a wavelength of 0.5μm (the wavelength of operation), in the free troposphere (>5km) is less than the molecular backscatter cross section (~10^{-6} $m^{-1}sr^{-1}$ at 5km), a large EAP (>100 Jm^2) is required to make accurate (~1-2 m/s) Doppler LOS velocity measurements at >5 km altitude.

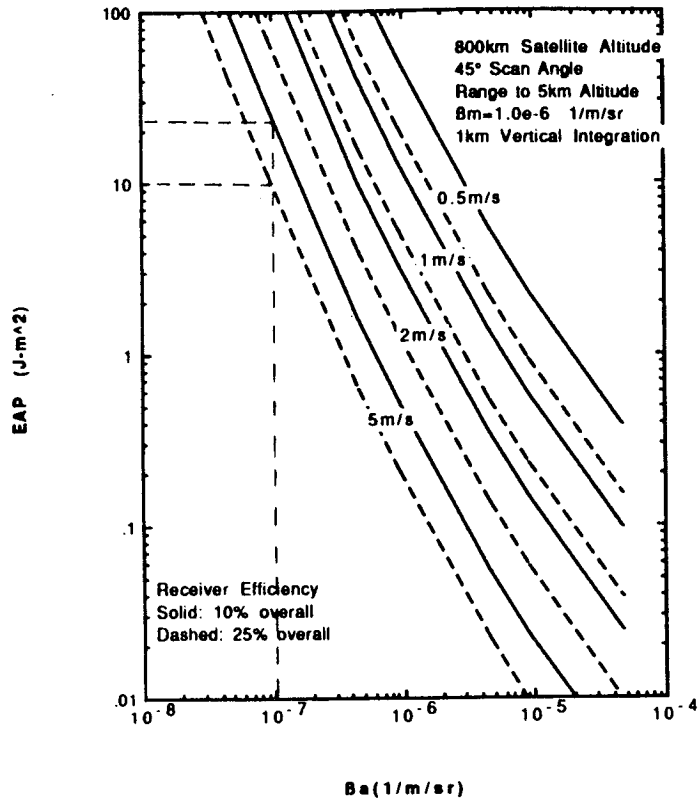

Figure 4-8. EAP Required for Direct Detection Doppler Lidar

To summarize direct detection systems the advantages are: 1) a ground based system has been demonstrated, 2) it uses a solid state laser which could be diode pumped for space applications, 3) it uses a space proven receiver similar to one which has flown on Dynamics Explorer and will shortly fly on UARS and 4) the beam may be made eyesafe because, in contrast to a heterodyne detection system, the beam may be expanded beyond the diffraction limit. It may also be made eyesafe by transmitting low energy pulses at high repetition rate and averaging a large number of return pulses to extract the Doppler information. The disadvantages are: 1) the system uses the return energy much less efficiently than heterodyne detection (for a comparison of the sensitivities see the next section), 2) for measurements in the free troposphere in excess of 4 kW of prime power would be required, 3) the current system employs a laser which would be visible to observers on the ground (even though it could be eyesafe) and 4) averaging large numbers of pulses may degrade the spatial resolution. Changing the wavelength to a non-visible one would require the use of new detection technology.

4.2.2.2 *Heterodyne Detection Doppler Lidar*

Heterodyne detection (also known as coherent detection) Doppler lidars also operate by measuring the Doppler shift imposed on the return signal. They differ from direct detection lidars in that the return signal is mixed with a single-frequency, local-oscillator laser prior to the optical detector. The detector acts as a photomixer and

transforms the signals to the RF regime, where standard RF techniques can be used for amplification, filtering and frequency analysis. Many Doppler lidars using coherent detection have been built (for a comprehensive bibliography see LAWS, 1987) most using the CO_2 laser as the transmitter. An EAP analysis of a coherent Doppler lidar, operating at the same altitude and scan angle, as the direct detection lidar is shown in Figure 4-9. In an effort to compare like parameters, we have performed the heterodyne calculation for a Nyquist velocity of 130 m/s, which is the maximum velocity which can be accommodated by one free spectral range of the GE direct detection FPI. We have also equated one channel of the direct detection IPD with the heterodyne detection electronic bandwidth. The IPD has 12 channels, therefore each channel is equivalent to a velocity range of ~10 m/s; a 10 m/s Doppler velocity at a wavelength of 9 μm corresponds to an electronic bandwidth of 2 MHz. Note that Figure 4-9 was generated using a pulse-pair autocovariance algorithm and does not represent our current assessment of the performance of LAWS. Improved signal processing algorithms have subsequently been developed which substantially improve the heterodyne performance at low values of SNR.

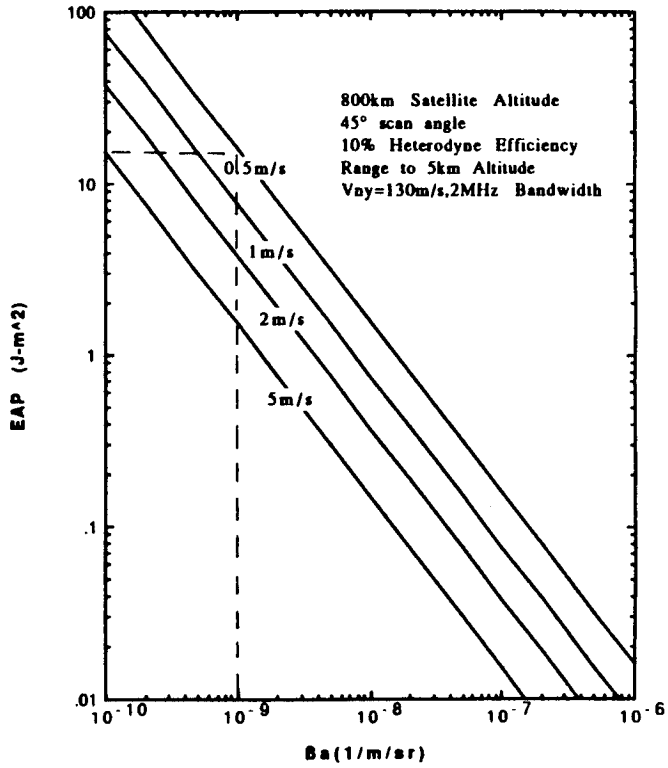

Figure 4-9. EAP Required for Coherent Detection Doppler Lidar

To compare Figures 4-8 and 4-9, we assume that, at 5 km, the respective backscatter coefficients at 9 μm and 0.5 μm are 10^{-9} $m^{-1}sr^{-1}$ and 10^{-7} $m^{-1}sr^{-1}$. This represents a wavelength dependence of the backscatter coefficient of about $1/\lambda^{1.5}$, which, as we see later, is a reasonable assumption. Under this assumption, for an EAP of ~30 Jm^2, we might expect a velocity accuracy of ~5 m/s for the direct detection system and 0.5 m/s for the heterodyne detection system. This order of magnitude increase in efficiency of heterodyne receivers over direct detection receivers has been noted before

(see e.g. Menzies, 1986) and leads us to abandon direct detection concepts from consideration for LAWS and concentrate on heterodyne detection Doppler lidar concepts.

Following on down the decision tree we see that having chosen the heterodyne detection path the next immediate question concerns the choice of wavelength. In order to structure the heterodyne detection wavelength selection we assume throughout the discussion a strawman system consisting of a 5-20 Joule laser and a 1.5 m aperture telescope scanning at 45° about nadir.

When choosing a wavelength at which to operate a space based lidar the single most overriding factor which must be taken into consideration is the risk of eye damage to potential observers on the ground. This is particularly so for the case of heterodyne lidar since the transmitter beam is necessarily narrow, implying large energy densities at the ground. Generally this consideration (known as eye safety) leads us to exclude any wavelength which can be transmitted by the cornea and lens and brought to a focus on the retina. The excluded wavelengths lie in the range 0.4 μm - 1.4 μm. Thus we are left with wavelengths shorter than 0.4 μm or longer than 1.4 μm. (But note later discussion in section 4.4 which shows that high energy 2.1 μm lasers may not be eyesafe for observers using binoculars or telescopes.)

When we consider a heterodyne lidar system using a wavelength shorter than 0.4 μm, we find that although, in principle, the question of eye safety is not an issue, there are a number of system issues which make it difficult to recommend. Chief among these are the large total Doppler bandwidth and the stringent pointing requirement.

The satellite orbital speed of 7.4 km/s induces a Doppler shift on the return signal which is inversely proportional to wavelength. For a system operating at 0.35 μm (e.g. tripled Nd:YAG) the shift amounts to a maximum of 42 GHz, sinusoidally varying as the telescope scans about nadir. This large bandwidth is outside the range of operation of practical heterodyne receivers and would require a frequency swept local oscillator, synchronized to the scanner, to recover the signal. The signal bandwidth is also large amounting to 1.15 GHz at the LAWS maximum requirement of ±100 m/s wind speed. Since this has to be digitized at the Nyquist rate a digitizer operating at 2.3 Gsamples/sec with a data rate 26 times larger (per detector) than for a 9 μm system would be required. This is currently beyond the state of the art.

The beamwidth in a UV heterodyne lidar would give rise to a pointing requirement for the optical subsystem that would be beyond the state of the art for scanning systems. If we assume an aperture of 1.5 m (although this may be larger than refractive turbulence considerations will allow), the diffraction limited beamwidth is 0.57 μrad for a wavelength of 0.35 μm. Later we show that the round trip pointing requirement needs to be ~20% of the beamwidth, about 100 nrad in this case. If we error budget this number, in a similar fashion to the procedure we show later for the 2.1 μm and 9.1 μm concepts, we find that most of the derived requirements for the optics and scan mechanisms are beyond the state of the art.

We therefore concentrate on systems with operating wavelengths greater than 1.4 μm and come down one more level in the decision tree, to consider the question of whether we should pick a solid state laser or a gas laser for LAWS.

4.2.2.2.1 Solid State Lasers

In the past a solid state laser could not have been considered for an application such as LAWS which requires a 100 W average power device, simply on the grounds of efficiency. Solid state lasers are traditionally pumped by flashlamps and operate typically with efficiencies in the range of 0.1-1%. Recently, however, there has been a renaissance in the solid state laser field driven by the availability of high power, large area semiconductor lasers which can replace flashlamps as the pump source for certain materials and offer lasers of much higher efficiencies. For example, with diode-pumped neodymium an overall electrical to optical conversion efficiency of around 10% may be

expected. Unfortunately for LAWS, however, almost all of the diode pumped laser work (and certainly all of the higher energy devices built) have concentrated on neodymium, which lases most efficiently at wavelengths shorter than 1.4 μm. The next decision point in the tree is therefore whether we should consider techniques based on frequency shifting the neodymium laser to longer wavelengths, or find materials capable of being pumped by diodes, which lase directly at wavelengths >1.4 μm.

Frequency shifting techniques which may be applicable for LAWS are: Raman, optical parametric oscillators (OPO) or neodymium pumped erbium.

Erbium, which occurs in the same part of the periodic table as neodymium, has the advantage of a lasing wavelength around 1.6 μm, and is therefore eyesafe. It has limitations (discussed later) which preclude it from consideration as a direct, diode pumped source, however, it can be pumped rather efficiently by a neodymium glass laser operating at 1055 nm. Some recent Russian results show that by heavily doping erbium glass with ytterbium which absorbs from 900-1060 nm, the upper laser level in erbium can be populated by resonant energy transfer from the ytterbium. When pumped with a long pulse, neodymium glass laser at 1055 nm, they were able to achieve an energy conversion efficiency $E_{1.54}/E_{1.055}$ of 35% and an energy output at 1.54 μm of 90 J. Diode pumped Nd:glass lasers (which operate at 1055 nm) have been demonstrated and projected efficiencies of 5-10% would seem reasonable. A Nd pumped erbium laser might therefore exhibit efficiencies in the range 1-4%. As we show later this is a moderate efficiency projection when compared with a diode pumped holmium laser and is therefore not considered further.

Optical parametric oscillation (OPO) is an optical technique for frequency shifting similar in many ways to harmonic conversion. However, in OPO a pump photon of frequency ω_p is converted to two photons, known as the signal and the idler whose energies add up to that of the pump, $\omega_p = \omega_s + \omega_i$. Whereas harmonic conversion is not tunable, OPO is, within the constraints that the crystal used is transparent at all three wavelengths and that the crystalline indices of refraction allow phase matching. In order to achieve reasonable efficiencies the crystal is placed in a cavity which is resonant (due to reflective or partially reflective mirrors) at either one or both of the signal and idler frequencies. One of the most commonly used crystals is $LiNbO_3$ due to its transparency out to about 5 μm. Unfortunately, it has a relatively low damage threshold which would limit its usefulness for an application such as LAWS which requires high energies. Other limitations of OPO's which preclude them from further consideration are: 1) presumably only one of the frequencies produced is of use which limits the efficiency of conversion to 10-15% at best, and 2) since both angle and temperature are used to tune the crystal they must be both maintained very accurately (e.g. ammonium dihydrogen phosphate (ADP) tunes ~6 nm/°C, about 1 MHz/10^{-6}°C at 1500 nm). In a heterodyne detection system where we must retain a fixed relationship between the transmitter wavelength and the local oscillator, this latter consideration alone implies temperature stabilities <10^{-6}°C would be required for m/s level velocity resolution and precludes OPO's from further consideration.

The last frequency shifting technique discussed here is known as stimulated Raman scattering. In the Raman effect if a high power laser is incident on some Raman active medium, energy may be given up to the medium causing a downshift in the frequency of the output radiation. Raman media may be solid, liquid or gas, but most practical Raman lasers use gases because of their ability to handle high power without damage. The two most common Raman lasers use hydrogen, which has a Raman shift of 4155 cm^{-1} and methane which has a shift of 2914 cm^{-1} (illustrated in Figure 4-10). These shifts mean that a Nd:YAG/hydrogen Raman laser operates at 1.88 μm and a Nd:YAG/methane Raman laser 1.54 μm. The stimulated Raman effect can be very efficient and quantum efficiencies as high as 90% have been reported (energy efficiencies are, of course, lower as they are a function of the wavelength shift).

Disadvantages of the technique which allow us to remove it from further consideration are: 1) it is a non-linear effect and as such requires short pulse lengths, Doppler velocity resolution, however, requires relatively long pulse lengths; 2) in a coherent detection lidar we must be able to provide a reference local oscillator which is locked in frequency to the transmitted pulse, this is difficult in a Raman laser since the input laser frequency is shifted by a fixed, large amount; 3) frequency stability from pulse to pulse is difficult to achieve since the linewidths of the transitions in the gas are very broad due to the need to operate at high pressures (typically 1500 psi in CH_4 for example, with a linewidth of >100 GHz); 4) the large linewidth also makes maintaining a transform limited pulse width a difficult proposition; and 5) there are other competing processes such as stimulated Brillouin scattering and the backward Raman effect, which limit the conversion efficiency, particularly when narrow line pump lasers are used.

Having dismissed frequency shifted neodymium lasers we return now to the branch of the tree related to *direct laser techniques*, and consider whether there are suitable solid state laser materials which lase at a wavelength >1.4 μm and can be diode pumped.

If we look at the Periodic Table of the elements we find that lasing species are concentrated in the transition metals and the lanthanides. Although the first laser to be demonstrated used an ion from the transition metal series (chromium), the strongest absorption bands of the transition metals lie in the visible where high power diode lasers do not, as yet, operate. We therefore concentrate on the lanthanides(sometimes called the rare earths) which contain neodymium, the most succesful solid state laser to date.

Currently, all of the lanthanides with the exception of number 71, lutetium, have exhibited laser action, in a variety of host crystals and glasses. These ions are: Cerium (Ce), Praseodymium (Pr), Neodymium (Nd), Promethium (Pm), Samarium (Sm), Europium (Eu), Gadolinium (Gd), Terbium (Tb), Dysprosium (Dy), Holmium (Ho), Erbium (Er), Thulium (Tm), and Ytterbium (Yb). They differ from one another only in the number of electrons in the inner 4f electron shell, and operate almost exclusively (and most usefully) on trivalent transitions between 4f energy levels.

The energy level diagrams for the 4f electron shell of the lanthanides are shown in Figure 4-11. The dotted lines at 13,300cm^{-1} (750nm) and 11,600cm^{-1} (860nm) bracket the energy levels accessible to diode pumping, using AlGaAs diodes. Since the emission wavelength must always be longer (i.e a lower energy) than the pump wavelength (barring multiphoton excitation), only laser transitions between energy levels lower than the dotted lines are considered further.

We see immediately that Ce, Sm, Eu, Gd, and Tb have upper laser levels far above those accessible to diode pumping and are not considered further.

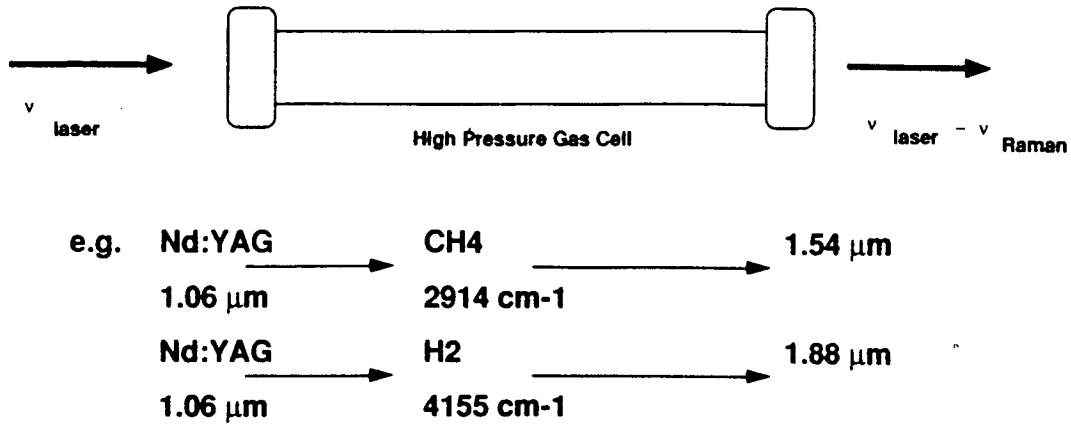

Figure 4-10. Raman Lasers - Issues

Neither Pr nor Yb have absorption levels directly accessible to diode pumping, but both have lasing transitions at a lower energy than diode pumps. Thus, in principle, if a donor ion could be found, capable of itself being diode pumped and then decaying to an energy level close to resonant with the upper laser level of Pr or Yb, energy transfer could take place. By this method both ions could then be pumped by diodes. This practice of using donor or sensitizer ions is common among the lanthanides, both in flashlamp pumped systems and diode pumped systems, but has not been demonstrated in either Pr or Yb. The most likely reason for the disinterest is that the laser transitions in Pr and Yb are 3-level (and therefore inefficient) and at almost the same wavelength as the 1.06 μm transition in Nd, which is 4-level, and by far the most important laser in the lanthanide series.

Thus, we are left with Dy, Ho, Er, Tm, Nd and Pm. Of these six, Dy has attracted very little attention and, in its trivalent configuration (there are divalent transitions among the lanthanides which are, in general, higher threshold and of less interest), warrants only one reference in the "Laser Handbook" (CRC Press, 1986). This reference describes emission on the $^6H_{13/2}$ to $^6H_{15/2}$ transition at 3.02 μm. This transition has an impractically high threshold (around 500J in the reference), and requires cooling to 77K. Dy is not considered further. Nd and Pm which operate at wavelengths shorter than 1.4 μm are also not considered further. The remaining three ions, Er, Tm and Ho are discussed below.

The laser transitions in *Erbium* which can be directly pumped by diodes are $^4I_{11/2}$ to $^4I_{13/2}$ at 2.8 μm and $^4I_{13/2}$ to $^4I_{15/2}$ at 1.6μm. The 4-level transition (2.8 μm) has a long lived lower level (~5 msec) which effectively terminates laser oscillation. The transition which has become the most studied, therefore, is the 3-level transition at 1.6 μm.

In many respects the 1.6 μm wavelength would be the ideal one for a space-based, wind sensor. The wavelength is eyesafe and the performance of InGaAs detectors near optimum. In addition, fiber-optic absorption is a minimum near 1.6 μm, a fact which has led the fiber-optics, communication community to develop local oscillator technology, based on narrow-linewidth, semiconductor diode lasers. Such semiconductor lasers could also be used to injection lock the Erbium laser, in a way analogous to single-frequency Nd:YAG lasers. Furthermore, all of the transfer optics, beam splitters etc. could be replaced by fibers, thereby considerably reducing the alignment tolerances (fiber optics can also be used at the Holmium wavelength of 2.1 μm provided they are fabricated with low OH^- concentrations).

Erbium can be directly pumped by diodes into the $^4I_{9/2}$ level, but is normally sensitized with Yb, Tm, Ho, or Nd. Unfortunately, there does not appear to be a cross relaxation scheme in Er similar to that, discussed later, between Tm and Ho, and so the maximum slope efficiency is 0.8/1.6=50%. Also, the fact that the upper laser level at $^4I_{13/2}$ is almost midway between the $^4I_{9/2}$ level and the ground state at $^4I_{15/2}$, means that under conditions of high inversion an upconversion process, whereby ions can make the transition from $^4I_{13/2}$ to $^4I_{9/2}$, can occur and deplete the gain.

Two laser transitions have been demonstrated in *Thulium.* The 2.35 μm transition, $^3F_4$-$^3H_5$, can be directly pumped by diodes, but the gain is very low. The 1.95 μm, $^3H_4$-$^3H_6$, transition can also be diode pumped and has an internal quantum efficiency of 2, for the same reasons as discussed for Ho in the next few paragraphs. The gain is low, however, because the lower laser level is close to the ground state and resonant reabsorption can occur. Tm is best used as a sensitizer ion in Ho laser crystals.

As shown in Figure 4-11, the *Holmium* ion has operated on many transitions in the 4f energy shell. Those accessible to direct diode pumping include wavelengths at 3.9 μm ($^5I_5$ to $^5I_6$, the longest solid-state laser wavelength to date), 1.6 μm ($^5I_5$ to $^5I_7$), 2.9 μm ($^5I_6$ to $^5I_7$) and 2.1 μm ($^5I_7$ to $^5I_8$). The first three transitions operate as 4-level lasers, but have the disadvantage that the terminal level is, in each case, metastable (long-lived). The laser action is thus self terminating (the population inversion, which gives rise to the gain, disappears as the lower level fills up). As a consequence, the 3-level, 2.1 μm, $^5I_7$ to $^5I_8$ emission has become the most studied.

Interest in the $^5I_7$ to $^5I_8$ transition is not new. The first laser operation was demonstrated in Ho doped Calcium Tungstate ($CaWO_4$) in 1962, with the crystal cooled to liquid nitrogen temperatures. Room-temperature, flashlamp-pumped, pulsed operation of Ho:YAG and Ho doped Yttrium Lithium Fluoride (YLF) was first reported in 1970, using laser rods sensitized with Er and Tm.

As mentioned previously, the use of sensitizer ions is common among the lanthanides, and an understanding of the spectroscopy of the internal conversion mechanism between Tm and Ho, together with the emergence of high power 780nm laser diodes, were key reasons for the resurgence of interest, recently, in the Ho ion. The interest centers around YAG co-doped with Ho and Tm, pumped at room temperature by laser diodes emitting at 780nm.

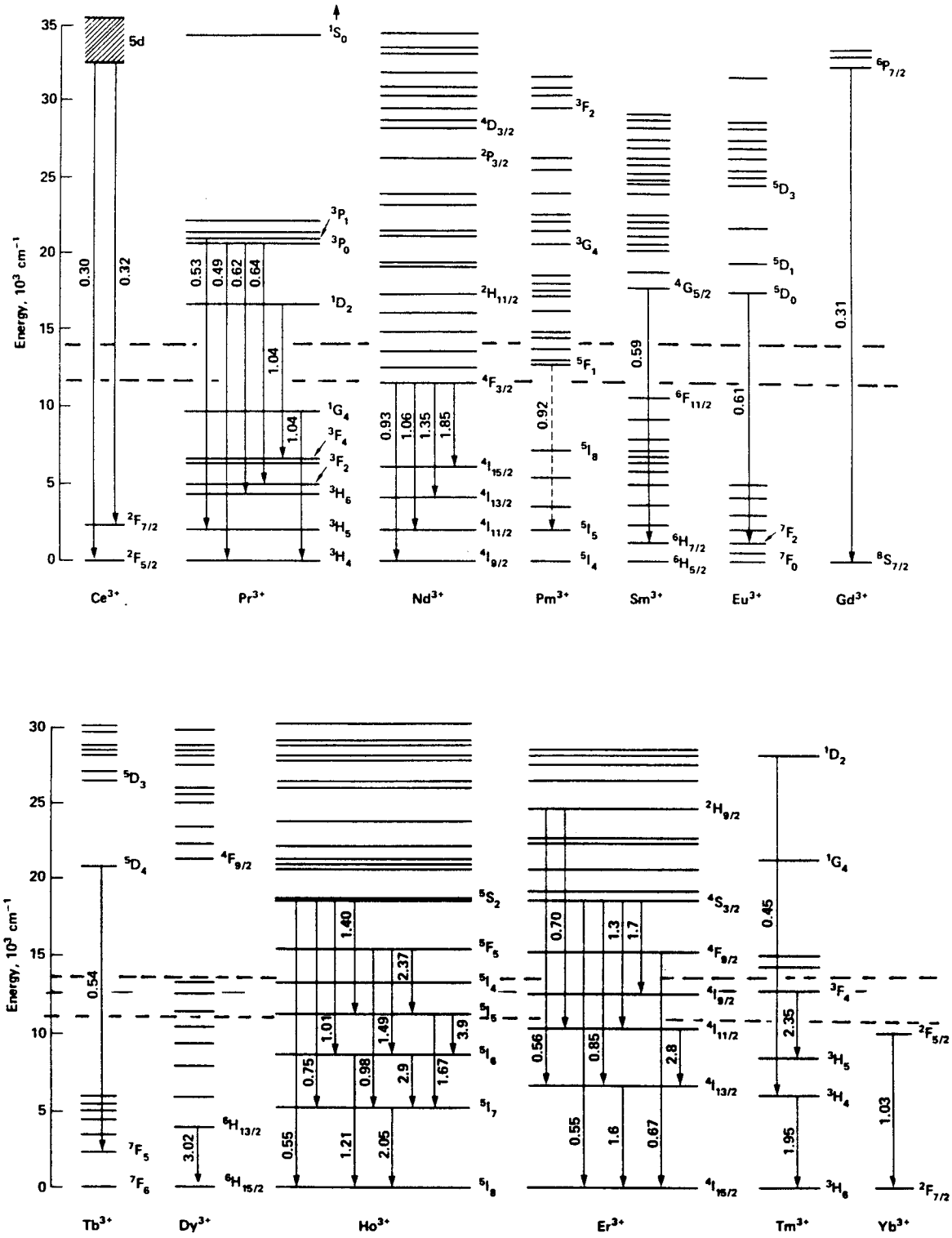

Figure 4-11. Energy Level Diagrams for 4f Electron Shell of the Lanthanides

Ordinarily, a laser which operated by absorbing pump light at 780nm and reemitted light at 2.1μm could operate, at best, with a slope efficiency of 0.78/2.1 i.e. 37%. Given all of the other factors which have to be included in the efficiency calculation, this so-called quantum defect efficiency, is a large penalty to pay if an efficient laser is the desired outcome. However, by adding Tm to the crystal a fortuitous coincidence between the 4f energy level structures of Ho and Tm can be exploited to effectively increase the internal quantum efficiency of the material to 2. An internal quantum efficiency of 2 means that for every photon absorbed at 780 nm, two excited Ho ions are produced. This is an extremely beneficial effect and together with the recent developments in high power AlGaAs laser diodes, explains the upsurge of interest in this crystal system.

We therefore selected Tm:Ho:YAG as a concept for LAWS worthy of further consideration and in section 4.3 develop data at this wavelength to aid in the selection process.

Having selected one concept from the solid state side of the decision tree we return to the gas laser side for our second concept selection.

4.2.2.2.2 Gas Lasers

There are literally hundreds of transitions which have been observed in gases at wavelengths >1.4 μm but by far the most important in terms of efficiency belong to the diatomic HF/DF species lasing at 2.8 μm (HF) and 3.8 μm (DF), and the triatomic CO_2 molecule lasing in the 9-11 μm region.

Although they are available commercially as electrically excited devices, HF and DF lasers are most efficient when operated as chemical lasers. The fuel is fluorine and either hydrogen or deuterium gas, a chemical reaction causing the formation of the vibrationally excited HF or DF molecules. The main drawback is the need to continuously replenish the fuel.

CO_2 lasers are some of the most efficient known. They can perform at 30% efficiency for multiline, multikilowatt, cw operation. In pulsed mode, lasers can be bought commercially which have hundreds of Joules of output in <1μs pulses, and pulses in excess of thousands of Joules have been demonstrated. The efficiency of typical commercial lasers is 5-10%.

Virtually all CO_2 lasers use $^{12}C^{16}O_2$ as the active species. Depending on the gas pressure and cavity design they can be operated on discrete vibrational lines near 9.4μm and 10.6 μm, or can be continuously tuned between lines, if the laser is operated at high pressure (~10 Atm). Single frequency, TEM_{00} operation, necessary for measuring winds with heterodyne detection, has been demonstrated. These lasers have reached an advanced stage of development and diffraction limited output is possible with normal quality optics (due to the long wavelength).

CO_2 lasers have been used in ground based and airborne Doppler wind sensors. However, wind sensors operating from orbit could not use the normal isotope, because of absorption by naturally occurring CO_2 in the atmosphere. They need to be operated using $^{12}C^{18}O_2$ at 9.1 μm, or $^{13}C^{16}O_2$ at 11.1 μm. Data on the operational characteristics of lasers using these isotopes is just now becoming available, particularly in pulsed TEA lasers. Research continues, and encouraging results have been obtained, particularly recently with the oxygen-18 isotope at 9.1 μm (Hamilton et al, 1989).

Given this rich heritage in the wind sensing community and the potential efficiency of CO_2 lasers based on rare isotopes we selected $^{12}C^{18}O_2$ as a concept to study further.

4.3 Evaluation of 2.1 μm and 9.1 μm Concepts

The previous section has shown by use of a decision tree how we have arrived at two competing concepts for LAWS. They are both heterodyne detection concepts, one founded on the use of the solid state laser material Tm:Ho:YAG operating at 2.1 μm, and the other based on the gas laser $^{12}C^{18}O_2$ operating at 9.1 μm. The approach we take to choose between them is to first consider the systems aspects of using a heterodyne lidar to measure winds and then to generate data regarding the likely performance, problems and issues in the main LAWS subsystems, i.e. the laser, the optics and the receiver. The data generated is then assimilated and run through the Evaluation and Selection Criteria Plan, DR-18, producing a leading concept.

To discuss the systems aspects of the concept selection for LAWS we begin by deriving requirements from the top-level mission requirements under the assumption that LAWS uses a high energy pulsed laser, a large-aperture telescope scanning about nadir, and heterodyne detection. We then discuss the properties of the atmosphere as they influence the choice of one wavelength over another.

Finally, in sections 4.3.3-4.3.5 we discuss laser, optical and receiver subsystem concepts for 2.1 μm and 9.1 μm systems. The data generated is used to choose the LAWS concept in section 4.4

4.3.1 *Derived Requirements Definition*

The design constraints for LAWS are illustrated in Figure 4-12. Around the periphery of the diagram are three constraints, mission requirements, atmospheric properties and spacecraft requirements. Emerging from the bottom of the diagram is the instrument specification. The three shaded areas in the diagram bound the design process as the study progresses, allowing, first, the design concept selection to take place and, later, the configuration selection. While two of the three shaded areas-mission requirements and spacecraft requirements, are dynamic, the spacecraft requirements are essentially a given being determined by the type of space vehicle chosen. The mission requirements, however, which play the major role in determining the properties of the instrument are selectable and must be carefully chosen at the outset to allow realistic instrument concepts and configurations to be determined. The next few paragraphs discuss mission requirements and illustrate by means of summary matrices (Figure 4-13), derived from Figure 4-12, the effect that particular requirements have on aspects of the LAWS system.

A secondary scientific objective for LAWS, which has been suggested recently, is to enhance our understanding of the distribution of the atmospheric aerosol and the role it plays in determining, for example, the Earth's radiation budget, by making measurements of the atmospheric backscatter from space. To measure backscatter with the LAWS instrument relies on being able to measure the intensity of the signal returned from the atmosphere (to measure the wind velocity we need only determine the frequency of the returned signal) which is a product obtained automatically from the Doppler processor. The statistics of the scattering process, however, are such that many shots need to be averaged to obtain a measurement with an acceptable standard deviation. The ramifications this has on the design of the instrument are given in the matrices, although it is understood that a backscatter measurement requirement shall not be a system driver.

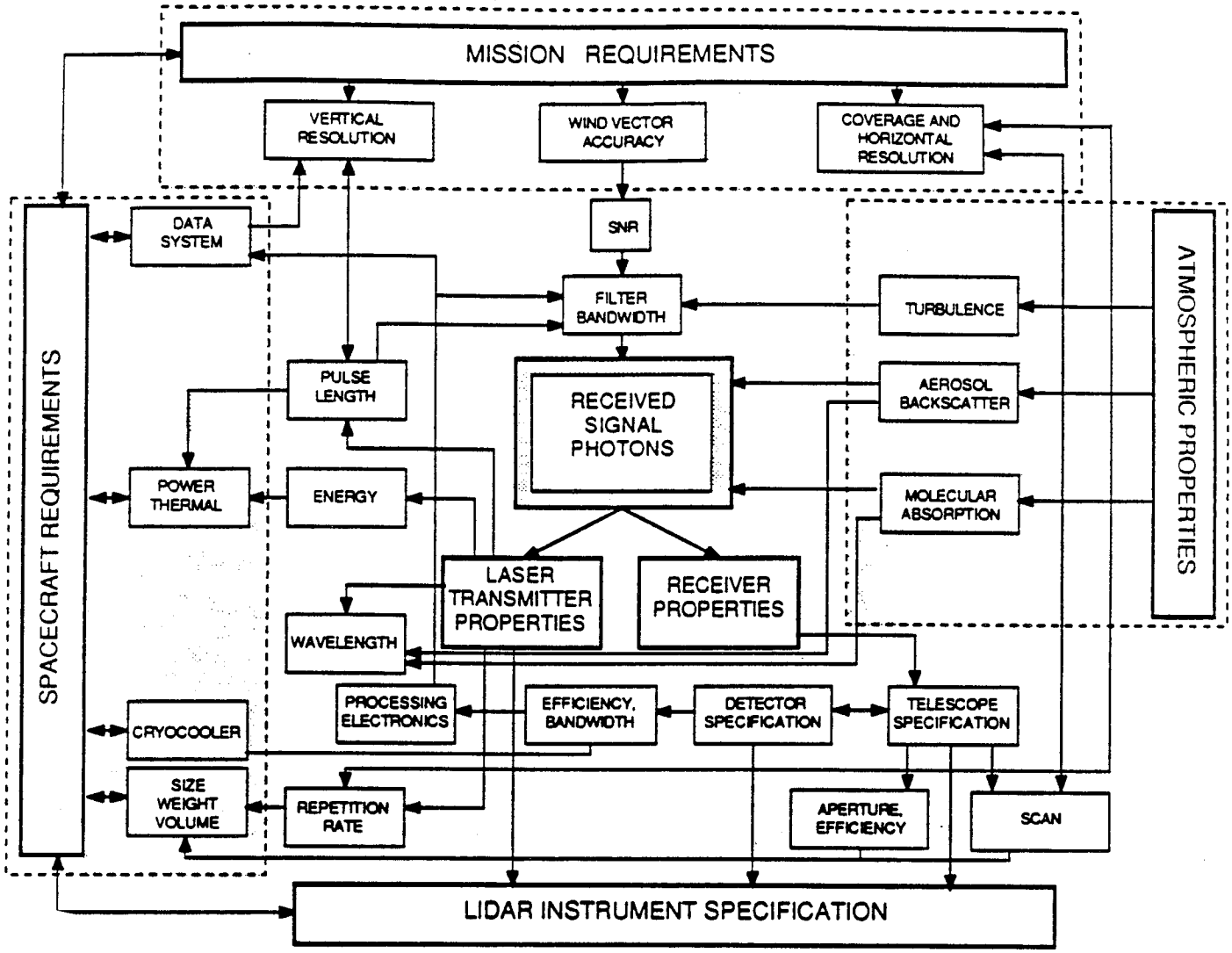

Figure 4-12. LAWS Requirements Development Methodology

MISSION / FACTOR	LASER (Transmitter + LO)	TELESCOPE Transmit/ Receive	RECEIVER/ PROCESSOR	INTEGRATED INSTRUMENT/ PLATFORM	SOFTWARE	FLIGHT OPER. SERVICING	GROUND OPS. CSE
WIND SENSING							
Adequate sensitivity for ±5 m/s velocity accuracy at tropopause and ± 1 m/s at ground	Pulse Energy 10-20 J Pulse Rep. Rate 10 pps average	Telescope Diam. 1.5 m Telescope LOS Stability 3 μR (9 μm) 0.6 μR (2 μm) Tel. Tolerance Strehl=0.9	Detector Quant. Efficiency Processor BW Narrowing 2 MHz (9 μm) 10 MHz (2 μm)	Instrument Accommodation Constrained by Fairing	Adaptive SW to obtain data product		
Adequate pointing knowledge for orbital velocity component removal	IF Removal Freq. swept LO one approach stability to 0.1 m/s req'd. (25 KHz 9μm, 250 KHz 2μm)	Position of Tel. req'd. to 50μR	IF Removal Frequency swept LO vs. Electronic Freq. Synth. ~0.1 m/s rms stability. Adequate dynam. range to use ground return?	Inertial Ref. and navigation. Star sensor and GPS colocated-TBD with sensor to update gyros	IF Removal Azimuth depend. control of LO laser or digital freq. synthesizer to ± 0.1 m/s rms. Examine ground return to check accuracy of freq. removal	Gyro Updates via colocated star sensor	

Figure 4-13. Derived LAWS Instrument Technical Requirements Matrix

MISSION / FACTOR	LASER (Transmitter + LO)	TELESCOPE Transmit/ Receive	RECEIVER/ PROCESSOR	INTEGRATED INSTRUMENT/ PLATFORM	SOFTWARE	FLIGHT OPER. SERVICING	GROUND OPS. GSE
WIND SENSING							
Earth Coverage							
Polar & above 30°				Polar Platform			
Tropics				Polar Platform or Space Station (SS better)			
Shot Distribution Optimization	Pulse Rep Rate Variable 0-15 pps (sin2az. angle variation for 10 pps avge.)	Lag Angle Comp. Asynchronous operation req.	Data Processor needs to accom. highest rep rate	Power & Therm. need to accom. variable loads	Prf Control Synchronize w. scan azimuth		

Figure 4-13. Derived LAWS Instrument Technical Requirements Matrix(Cont'd)

Figure 4-13. Derived LAWS Instrument Technical Requirements Matrix(Cont'd)

MISSION / FACTOR	LASER (Transmitter + LO)	TELESCOPE Transmit/ Receive	RECEIVER/ PROCESSOR	INTEGRATED INSTRUMENT/ PLATFORM	SOFTWARE	FLIGHT OPER. SERVICING	GROUND OPS. GSE
WIND SENSING							
Variable Vertical Resolution 1 km nomin.	Pulse length = 6.6μs/cos (scan) per km vert. resolution max. Also limited by vert. shear and transform limit.		Data Rate is a function of range gate length. Digitize at highest rate.		Adaptive to add successive range gates to obtain a data product		
Horizontal Resolution of 100 x 100 km	Pulse Rep. rate 10 pps nominal	Conical Scan Period 10 sec nominal					
Scan Coverage		Scan Mode Conical with nadir 30°-60° 45° nominal Scan rate 6 rpm nom. Lag angle Comp. Accommodate various return times due to varying nadir angles		Momentum Compensation required			

MISSION / FACTOR	LASER (Transmitter + LO)	TELESCOPE Transmit/ Receive	RECEIVER/ PROCESSOR	INTEGRATED INSTRUMENT/ PLATFORM	SOFTWARE	FLIGHT OPER. SERVICING	GROUND OPS. GSE
BACKSCATTER							
Intensity Measurement Req.	Measure outgoing pulse energy	Meas./Calib. Transmission	Dynamic Range 75 dB if ground used for calib.		Integrate N shots and define spatial resolution 300 x 300 km nominal		
Local/Regional Scan Capability	Pulse Rep Rate 1 minute burst mode at 20 pps	Conical Scan 100 sec per revolution Lag Angle Comp. Needs to accomm. burst	Data Processor Needs to accom. burst mode	Power/Thermal Need to accom. burst mode	Scan Control Advance Synchr. of scan azimuth for specific earth coord.		
BOTH							
Electrical Power NTE 3 kW	Lasers NTE 2 kW Efficiency >5% (wallplug)						
Mass NTE 800 kg	Laser NTE 180kg	Optical SS NTE 250 kg	Receiver SS NTE 20 kg	Support Struct. NTE 150 kg			

Figure 4-13. Derived LAWS Instrument Technical Requirements Matrix(Cont'd)

The mission requirements given in section 3.0 are now expanded to facilitate trades between the 2.1 μm and 9.1 μm concepts.

Horizontal Velocity Accuracy- LAWS is required to measure horizontal wind speed to ±1 m/s in the lower troposphere and ±5 m/s in the upper troposphere. The LAWS instrument measures the radial or line-of-sight (LOS) component of the horizontal wind field and a critical design driver is to decide on a requirement for the LOS accuracy, which will be adequate to reach the desired horizontal accuracies. As shown in Figure 4-12 the choice of wind vector accuracy, where we understand now that this refers to the LOS, immediately fixes the Signal-to-Noise-Ratio (SNR) and, for a given filter bandwidth, the required magnitude of the received signal. The smaller the LOS accuracy, the larger the SNR required and the larger the returned signal. Since the strength of the returned signal is primarily determined by the transmitted laser energy and the area of the receiver we must be careful not to choose a LOS accuracy which is too low, in the belief that this will result in a significant improvement in the recovered horizontal wind vectors, because of the risk of specifying an unmanageably large laser and telescope.

The factors which go into determining the horizontal wind vector accuracy are: LOS accuracy, the number of laser shots in the grid square of interest, the positioning of the shots in the region of interest and the structure of the wind field. As shown in Figure 4-14 doubling the LOS accuracy from 1m/s to 0.5 m/s has relatively little effect (about 0.2 m/s to 0.3 m/s) on the horizontal wind speed accuracy, providing greater than 4 shots land in a 100 km x 100 km grid. We therefore used as baseline for concept selection LOS accuracies of ±1 m/s and ±5 m/s, the lower number applying in regions of strong backscatter and the higher number applying in regions of low backscatter.

BASELINE: *± 1 m/s LOS from STRONG Backscatter*
± 5 m/s LOS from WEAK Backscatter

We believe from preliminary calculations that these numbers are consistent with a 10-20 J laser and a 1.5 m aperture receiver (Figure 4-13). The appropriate values for the derived requirements for the subsystems and the meanings of the terms strong and weak backscatter were determined during the concept selection phase. Note, however, that on each shot a range of backscatter values will be encountered which means that the data product (i.e. the velocity accuracy and vertical resolution (see later discussion)) will vary as a function of altitude.

Vertical Resolution- LAWS is required to produce wind profiles with a 1 km vertical resolution. To achieve such a resolution implies a pulsed laser system with a pulse length and a range gate length of at maximum ~6.7 μsec/cos(nadir angle). The backscatter coefficient, however, can vary over 4 orders of magnitude from the boundary layer to the tropopause and a vertical resolution of 1 km may not be possible or even desirable over the whole range. For example, in the boundary layer and lower troposphere, where the backscatter coefficient is large, a resolution of 0.5 km may be possible. Conversely, in the middle and upper troposphere, where the backscatter is weak, it may be necessary to combine several successive range gates to achieve a data product.

This flexible approach to vertical resolution has an impact on the design of the signal processor in that the length of the range gate could be as short as the pulse length itself. Such a processor would operate at the minimum accuracy of which the system was capable per range gate, with as stated, range gate combining being used to achieve the desired velocity accuracy. We therefore baseline a variable vertical resolution

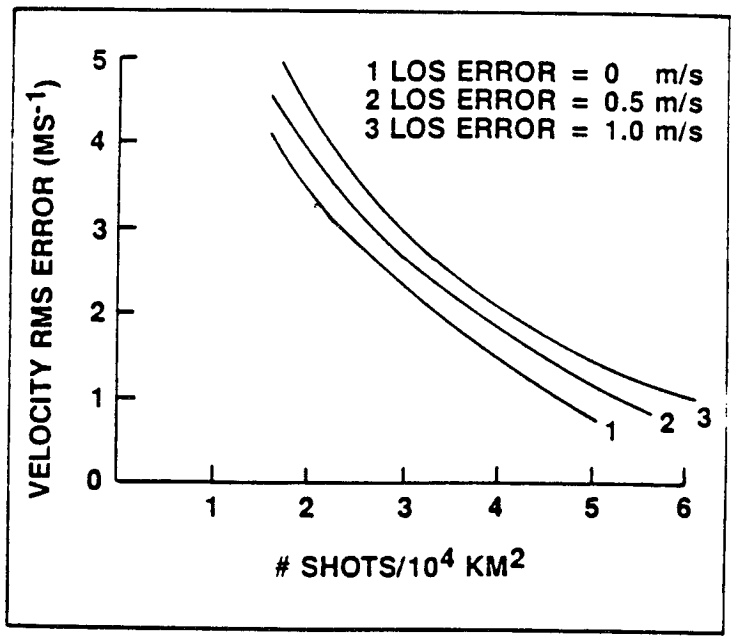

Figure 4-14. The RMS Error in the Horizontal Wind Estimate is a Function of Sampling Density and LOS Measurement

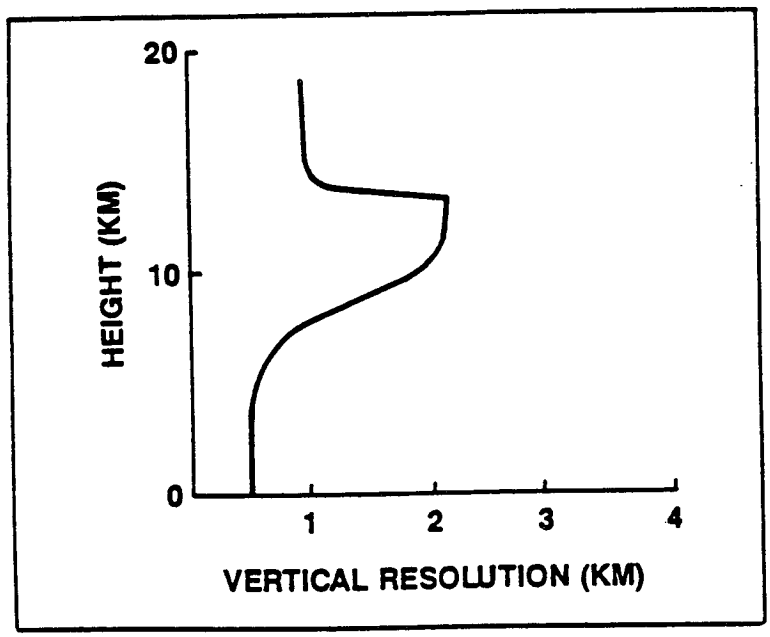

Figure 4-15. Possible Variation of Vertical Resolution in the LAWS Wind Profiles Resulting from a Minimum Accuracy Driven Signal Processor

processor for LAWS with a digitization rate equivalent to a minimum vertical resolution of 0.5 km.

BASELINE: Variable Vertical Resolution to Achieve a Data Product Over the Region of Interest with a Minimum Resolution of 0.5 km.

A schematic representation of the possible variation in the vertical resolution of LAWS is shown in Figure 4-15.

Horizontal Resolution- The LAWS horizontal resolution requirement is one horizontal wind vector per 100 km x 100 km grid square. The size of the grid square chosen impacts the system in a number of ways. As shown in the matrix (Figure 4-13) it has a direct influence on the laser repetition rate and the conical scan period because of the need to place a minimum number of shots in each grid. The number of shots, and their relative direction and location, directly influences the accuracy of the horizontal wind vector. As previously discussed for the vertical resolution, this is another area where we would envisage a flexible approach. In this instance when signals are weak or the shot density, for whatever reason, is lower than normal in a particular grid square, we anticipate the ability to enlarge the grid to 300 km x 300 km to achieve a data product.

BASELINE: Nominally 100 km x 100 km Horizontal Resolution but Can Be 300 km x 300 km to Achieve a Data Product.

A grid square of 100 km x 100 km is consistent with a laser pulse repetition rate of about 10 Hz and a scan period of about 10 sec at 45°.

Vertical coverage- The LAWS vertical sampling domain will be bounded below by the Earth's surface and opaque clouds and above by the lack of adequate backscatter. The tropopause is likely to delineate the region at which the LAWS sensitivity is reached and often occurs at heights less than 20 km. Although reducing the vertical coverage requirement to less than 20 km would reduce the data rate, the savings would be minimal. We therefore baseline a vertical coverage of 0-20 km.

BASELINE: 0 - 20 km Vertical Coverage

Global Scale Coverage- The amount of the Earth's surface covered by the LAWS instrument is a function of the type of scan employed, the laser repetition rate, and the orbit. Assuming a conical scan, increasing the scan angle increases the swath width and hence the percentage of the globe covered. The length of the atmospheric path increases with increasing scan angle, however, and the SNR decreases. The choice of scan angle is therefore a trade between percentage of the globe covered and SNR. This is illustrated graphically in Figure 4-16, where we see that for an 824 km sun synchronous orbit and a 45° scan angle (a scan period of 10 sec has been assumed throughout) approximately 78% of the Earth's surface is viewed (in a 12 hour period), for a SNR of 20dB at the surface.

The latitudes covered by the instrument for two sun synchronous polar orbits are shown in Figure 4-17(a), where we see the good coverage above 40° but with some gaps at the Tropics. A similar plot for two Space Station manned base orbits is shown in Figure 4-17(b) illustrating the complementary nature of the polar platform and the Space Station. The Space Station which gives a total global coverage of about 50% (in 24 hours) gives excellent coverage in the Tropics and has the advantage of operating with a SNR about 8 dB higher than the polar orbiter.

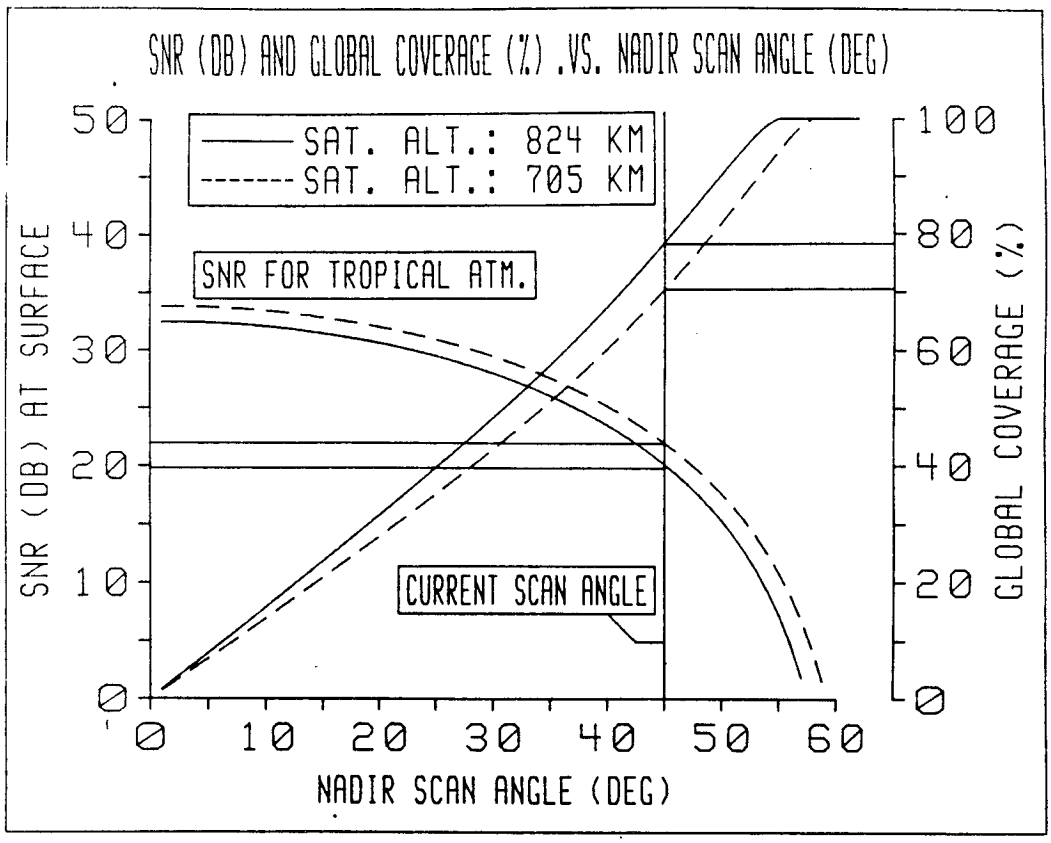

Figure 4-16. SNR and Global Coverage (%) vs. Nadir Scan Angle

Choosing a baseline mission requirement for global coverage is clearly not possible without picking the platform. At this time, however, we choose a scan pattern and scan angle which we believe is a good compromise whatever the final platform.

BASELINE: Conical Scan, 45° Scan Angle, 10 sec period (later changed to a 5 sec period)

Operational Lifetime- An instrument lifetime of 10^9 shots is quoted as a minimum system requirement. If we assume an average laser repetition rate of 10 Hz this number of shots is equivalent to about 3 years continuous operation. However, if we assume the baseline scan with a 10 Hz laser transmitter we find that there is oversampling at the extremes of the ground swath. By inhibiting the laser firing where overlap occurs we can extend the life of the laser. Figure 4-18 shows how this simple scheme can extend the life by about 20% for the 824 km orbit. Other shot management techniques are discussed later.

BASELINE: Shot Management to Extend Instrument Life Beyond 3 Years

Continuous Operations- Whether or not the instrument is idle for any extended periods of time or operates continuously has an impact on various of the subsystems. For example, in the thermal system and the power system, where the amount of back-up power required, and the system warm-up time impacts the system design. Conversely, an instrument which operates non-continuously will generally require less power on the average than one operating all the time. Whether or not LAWS is duty-cycled will depend on the power available from the platform and the power required by the instrument. At this stage our preliminary estimates show that LAWS will be able to operate within the anticipated power budget (< 3 kW) and therefore we assume that it will operate continuously.

BASELINE: Continuous Operations

Serviceability- One of the major original requirements of the Space Station polar platform design was that they be serviceable. The scenario chosen was that every 2-3 years the platform descends to shuttle altitude for servicing by either astronaut EVA, the remote manipulator system or the orbital maneuvering vehicle (OMV). Complete payloads, mounted to the platform by standard interface connectors, could be exchanged, smaller subsystems known as orbital replacement units (ORU's) could be exchanged or even larger pieces of the spacecraft, known as core/carrier sections. At the completion of servicing the propulsion module would be replaced and the platform return to operational orbit. However, with the demise of the OMV and the uncertain future for the Western Test Range, the exact servicing scenario is yet to be decided. As a minimum, however, we assume serviceability to mean that the instrument will be capable of being removed and replaced as a whole on orbit. At the same time it must be realized that the most likely candidate for replacement each time the platform is serviced will be the laser subsystem. Accordingly we will consider a modular approach in the configuration design phase, which would allow the laser head to be replaced as a unit. Issues of maintaining coalignment between the transmitter and the receiver and the increased complexity such a modular approach might bring to the system design, will be addressed.

BASELINE: As a minimum LAWS will be replaceable on orbit. Subsystem modularity will be studied.

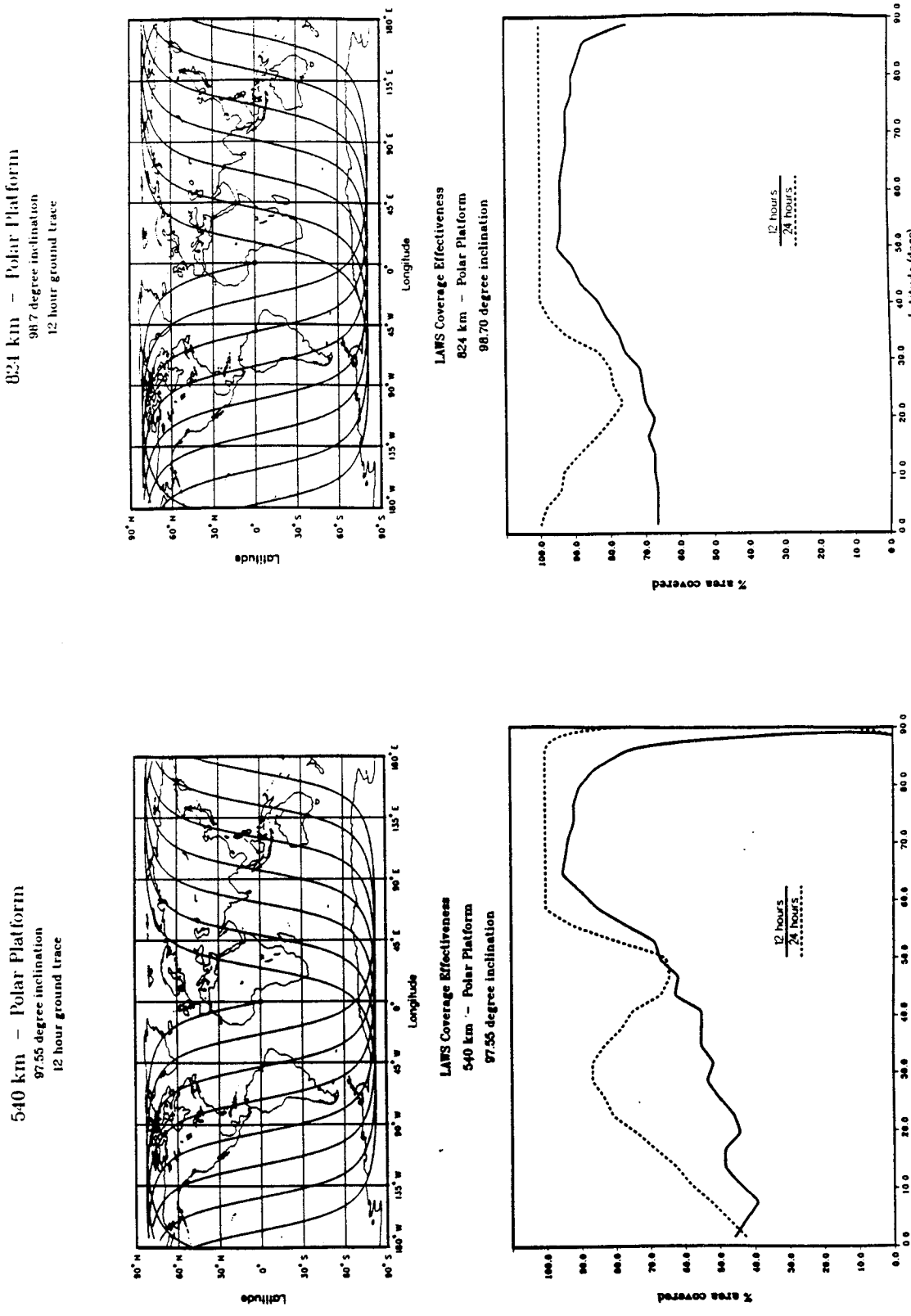

Figure 4-17a. Orbit Tracks and Coverage for 540 km and 824 km Polar Platform

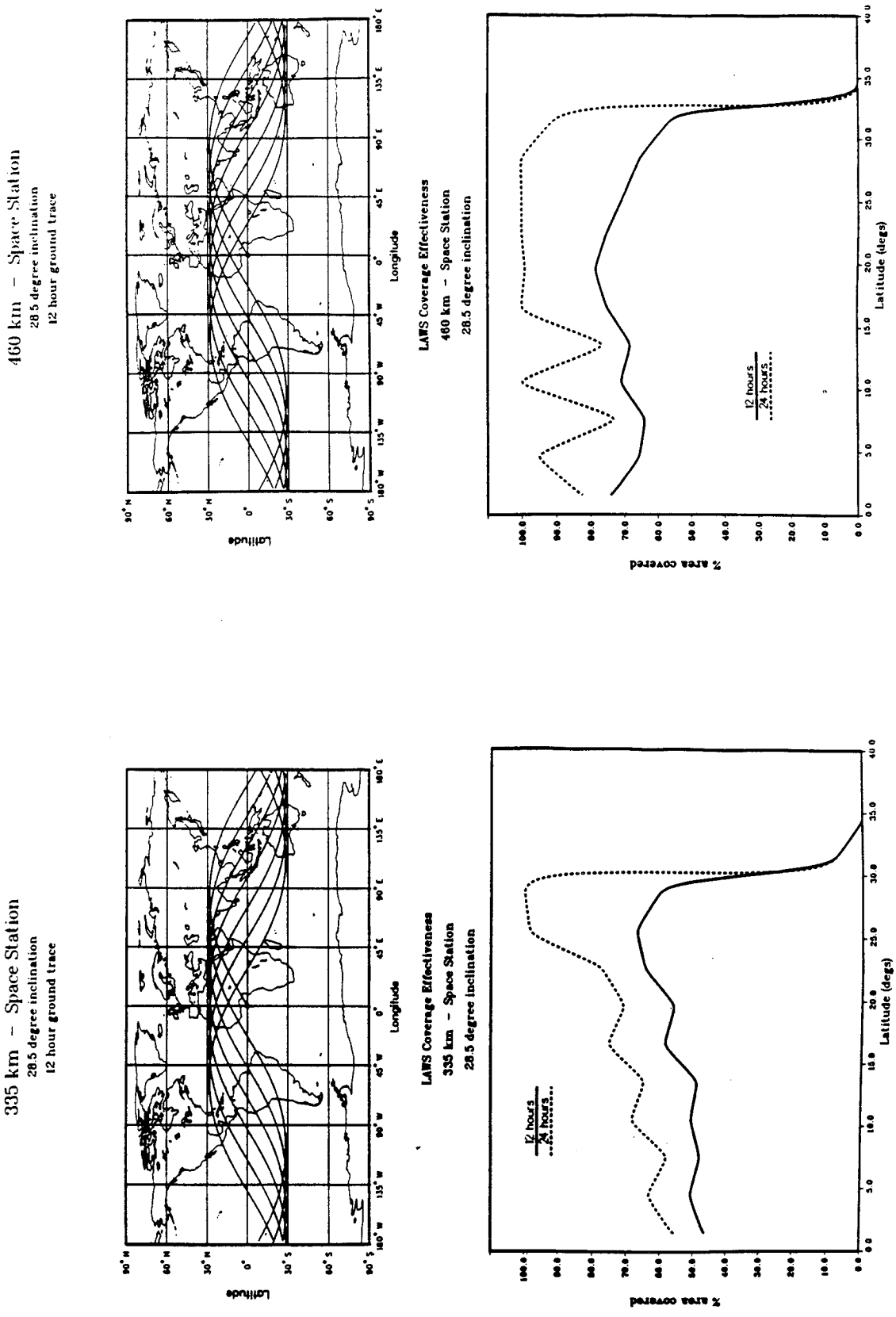

Figure 4-17b. Orbit Tracks and Coverage for 335km and 460 km Space Station

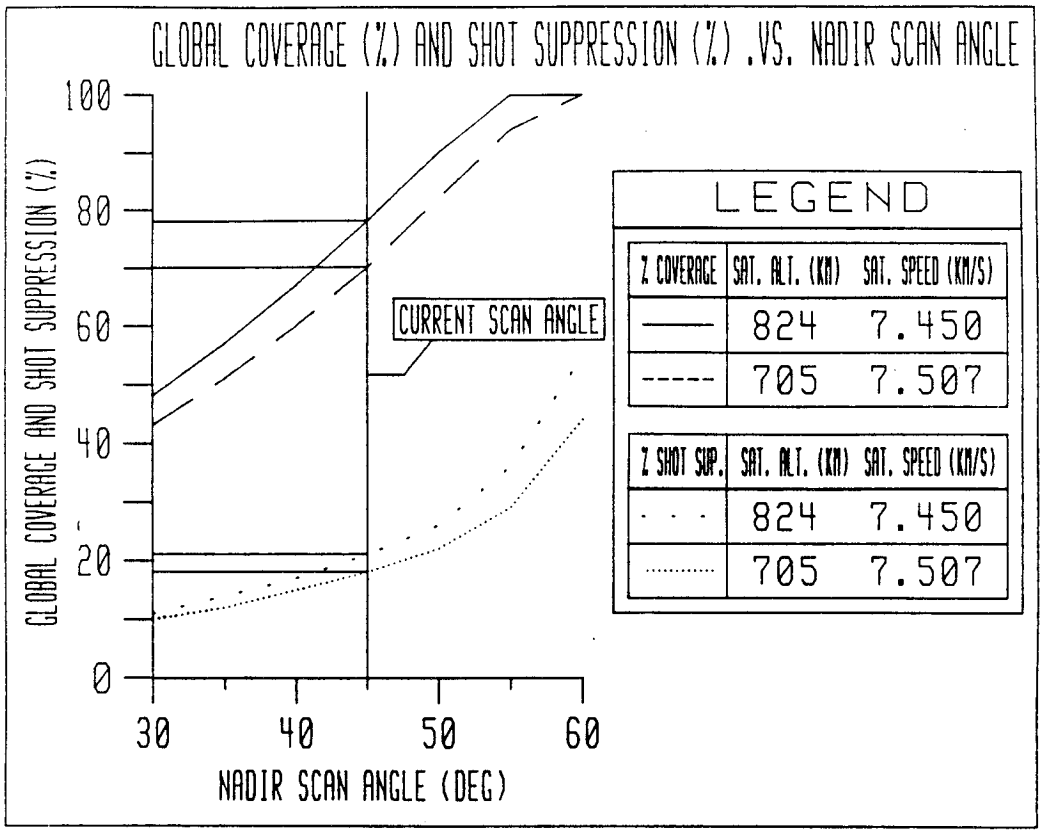

Figure 4-18. Global Coverage (%) and Shot Suppression (%) vs. Nadir Scan Angle

4.3.2 Atmospheric Considerations for Concept Selection

This section discusses the properties of the atmosphere which can influence the choice of one wavelength over another for the Doppler lidar design. Given a choice unencumbered by the constraints of technology we would naturally choose a wavelength which best matched those properties of the atmosphere which have a bearing on the design process. If we examine the simplest form of the lidar equation,

$$E_r = E_t T_o T_a \beta \Delta R (A/R^2) \eta$$

where, E_r is the energy received, E_t is the energy transmitted, T_o is the optical transmission, T_a is the two way atmospheric transmission, β is the volume backscattering coefficient of the atmosphere, ΔR is the range gate length, A is the area of the receiver, R is the range and η is the efficiency of detection; we see that those properties are manifested as transmission, T_a and backscatter coefficient, β.

There is a third property of the atmosphere, refractive turbulence, which must be considered in the design of coherent detection lidars. Turbulence ultimately determines the maximum size of the receiver aperture since it determines the far field irradiance distribution. Any radiation which falls outside of a diffraction limited spot in the far field is not collected by the detector in the focal plane of the telescope (for a single detector).

Calculations have shown (Figure 4-19) that the coherence diameter at 9.1 μm is almost always above the strawman aperture diameter of 1.5m. Turbulence should therefore have little impact on system performance at 9.1 μm. At 2.1 μm, however, the coherence diameter is below 1m for a large portion of the lower atmosphere. (Note while the calculations are model dependent, the atmospheric model used (NOAA-ERL-251-WPL-22) is considered conservative. Indeed, the effect on coherence diameter will always be about 6 times greater ($\lambda^{6/5}$ dependence) at 2.1 μm than at 9.1 μm, whatever the atmospheric model).

The atmospheric transmission spectrum is well known and can be accurately modeled by such codes as FASCODE2, the AFGL high resolution atmospheric propagation program. Choosing a wavelength which is well transmitted by the atmosphere is generally a matter of avoiding well defined absorption lines associated with species normally present such as water vapor, carbon dioxide and ozone. For space based CO_2 lidars, for example, this consideration requires that the laser operate using an isotope of CO_2, either based on oxygen-18 or carbon-13, because isotopic CO_2 is extremely rare in the normal atmosphere.

A minor consideration, which also must be remembered when choosing the wavelength of operation, is that as a conically scanned lidar revolves the transmitted frequency sweeps back and forth due to the Doppler shift imposed by the spacecraft velocity. The excursions for lidars operating with a 45° scan angle are typically ±1.2 GHz for a 9-μm CO_2 lidar and ±7 GHz for a 2-μm lidar. Such excursions in the case of a short wavelength system can cover many atmospheric absorption lines (in the lower troposphere linewidths of ~0.1 cm^{-1} or 3 GHz are typical), and could result in a modulated return signal as the telescope revolved, unless care was taken to place the transmitter wavelength many halfwidths away from the absorption features.

By comparison with understanding atmospheric transmission, quantifying the atmospheric volume backscattering coefficient as a function of wavelength is more difficult. To understand the key role the wavelength dependence of β plays in heterodyne lidar we begin with a discussion of SNR.

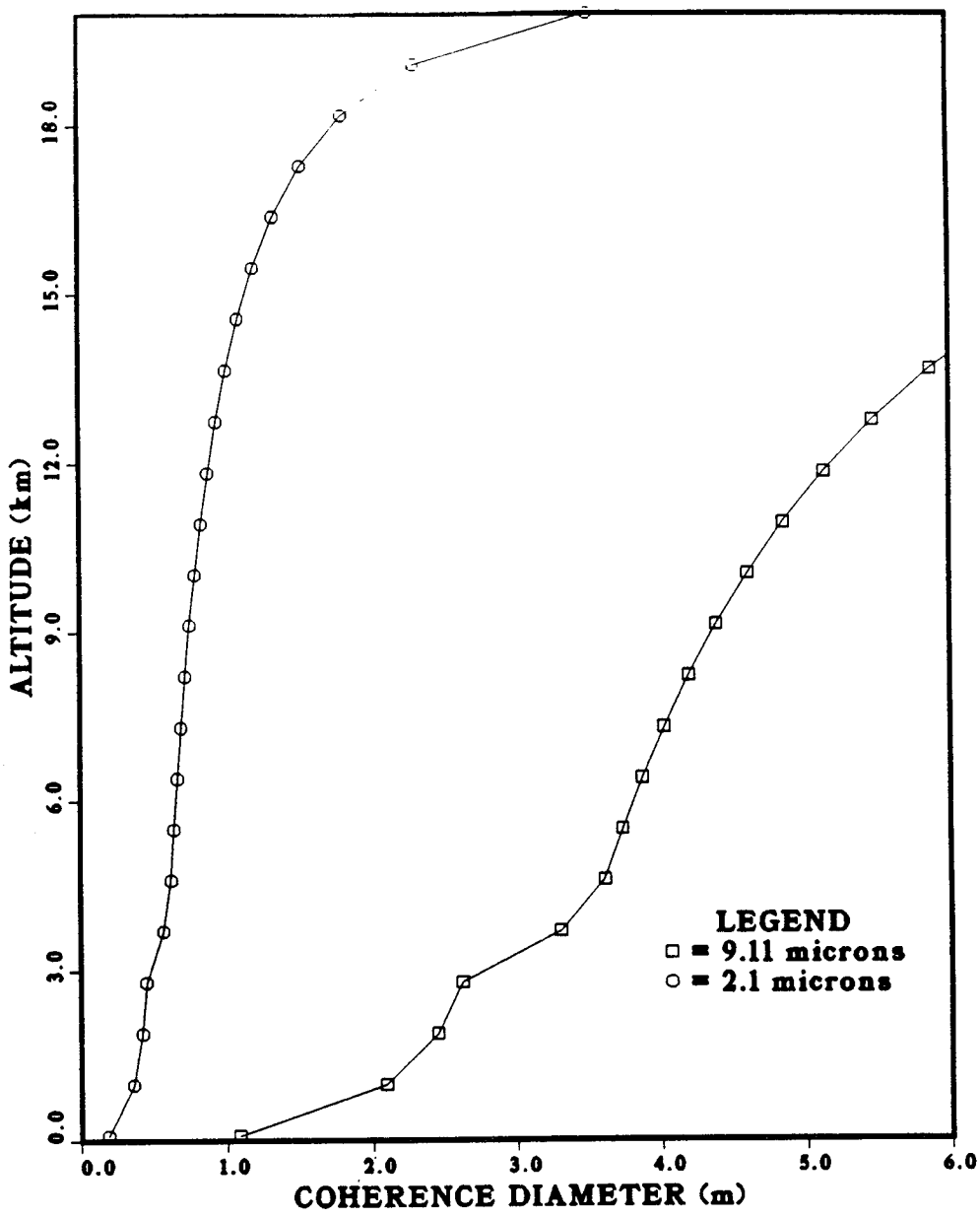

Figure 4-19. Atmospheric Coherence Diameter Using NOAA Cn^2 Model

The sensitivity of a coherent detection Doppler lidar is expressed by the SNR, which, for a space-based system may be written:

$$SNR = \pi\eta E\beta c D^2 \exp(-2kR)/(8h\nu BR^2)$$

where:

η is the overall system efficiency including the heterodyne quantum efficiency,
E is the transmitted pulse energy,
β is the atmospheric backscattering coefficent,
c is the speed of light,
k is the atmospheric extinction coefficient,
R is the range,
D is the diameter of the transmitter/receiver telescope,
$h\nu$ is the photon energy,
B is the electronic bandwidth.

In order to determine the best wavelength at which to operate a Doppler lidar, we must examine the wavelength dependencies of the parameters in this equation. The required electronic bandwidth, B, depends on the Doppler shift ($2V/\lambda$) to be measured; thus for a particular value of velocity, V, a shorter wavelength system requires a larger B, i.e. $B \propto 1/\lambda$. The presence of the optical frequency, ν, in the denominator also indicates an inverse λ dependence. Therefore, neglecting for the moment the wavelength dependent atmospheric transmission, we see,

$$SNR \propto \lambda^2 \beta(\lambda)$$

The wavelength dependence of the backscattering coefficient, β, is unknown, in general, being a complex function of particle size, particle shape, refractive index and distribution function. In the small particle, or Rayleigh limit, $\beta \propto \lambda^{-4}$; in the limit of very large particles, there is no wavelength dependence. The actual value of the exponent, for a real atmosphere, is likely to be between -1 and -4. Designating the exponent as α, we may therefore write,

$$SNR \propto \lambda^{2-\alpha}$$

Of course, the quantity of interest in a Doppler lidar is not SNR, but rather the velocity accuracy, σ_V. The velocity accuracy may be related to the SNR, by the following expression (for a pulse pair autocorrelation algorithm),

$$\sigma_V = (l/4\pi)(f/(2NLt))^{0.5}(2\pi^{1.5}W + 16\pi^2 W^2/SNR + SNR^{-2})^{0.5}$$

where,

$f = 2Vmax/\lambda$, is the sampling frequency,
N, is the number of pulses averaged,
L, is the ratio of a range gate sampling period to the pulse length, t
W, is the frequency spread of the return signal.

When considering the question of the optimum wavelength at which to operate a Doppler lidar, we are interested in conditions when the SNR is low. From the above equation, we see that for low values of the SNR the final term is dominant and,

$$\sigma_V = \lambda(f/(2NLt))^{0.5})/(4\pi SNR)$$
$$= \lambda Vmax/(\lambda NLt)^{0.5}/(4\pi SNR)$$

The number of samples in a range gate, L is inversely proportional to t, the pulse duration, which is in turn proportional to λ. The wavelength dependencies of these two terms therefore cancel, and we have,

$$\sigma_V \propto \lambda^{0.5}/\lambda^{2-\alpha}$$
$$\sigma_V \propto \lambda^{\alpha-1.5}$$

Thus, unless it can be shown that the aerosol backscattering coefficient varies other than as $1/\lambda^{1.5}$, the performance of a coherent detection Doppler lidar is independent of wavelength. (Note, with other Doppler estimators e.g., FFT or adaptive poly-pulse pair, the wavelength dependence of σ_V may well be different). The pulse-pair case is illustrated in Figure 4-20 which is a plot of the Energy-Aperture-Product (EAP) required to make a 1m/s line-of-sight wind measurement at a wavelength λ, relative to the EAP required at 9.1 μm, for various values of α. The EAP is simply the laser pulse energy multiplied by the area of the receiver and is a useful way of comparing lidar systems without the need to specify particular values for laser energy and receiver size. EAP provides an envelope within which trades can be made between the two major subsystems, the transmitter and the receiver, to arrive at an optimum solution.

In Figure 4-20 we see that for an α of 1.5 the EAP required is indeed independent of wavelength (the calculation was performed for a 1 m/s velocity accuracy). We see also that if we can justify an inverse-square wavelength dependence for the backscattering coefficient, whether theoretically or by measurement, then the EAP required for a wavelength of 2.1 μm is a factor of 2 lower than that required for 9.1 μm. How β varies with λ in actuality, is unknown and would require global measurements, using lidars at each wavelength of interest.

Actual measurements of the aerosol backscatter coefficient, made using colocated lidars at different wavelengths, are very few. Such measurements are difficult to make, requiring precise calibration at both wavelengths. Also, making backscatter measurements at two arbitrary wavelengths, at a single geographic location is of debatable usefulness, when what is desired is global data. Extrapolation of the results to other wavelengths is not straightforward, particularly from 10.6 μm to 9.1 μm, where there is an apparent enhancement in the backscatter coefficient due to structure in the refractive index near 9 μm (Ancellet et al, 1988). The Global Backscatter Experiment (GLOBE), addresses the perceived uncertainties in backscatter-coefficient models in the 10-μm region by four methods 1) direct measurements of backscatter, 2) measurement of other aerosol physical and optical properties, 3) modeling of aerosol backscatter properties and their global distribution, and 4) validation of measurements and models.

Some measurements of backscatter which were made using colocated lidars, were reported in Lawrence, 1985. Backscatter data were collected at Boulder, Colorado, for the 10.6 μm wavelength, using the NOAA CO_2 lidar, and at 0.69 μm using a ruby lidar. The results of those measurements are shown in Figure 4-21, plotted as a histogram of the wavelength dependence coefficient, α, with the data divided into the free troposphere and the stratosphere. We see that for the two wavelengths used, there is an approximate $\lambda^{-1.5}$ dependence for $\beta(\lambda)$ in the free troposphere. In the stratosphere, where there are fewer large particles, the wavelength dependence tends to higher values of α.

Theoretical calculations, made using Mie theory assuming spherical particles, for measured aerosol size distributions (Deepak, 1982), show a more pronounced λ dependence for the free troposphere and the stratosphere. Figure 4-22 is a plot of data from the Deepak reference replotted for comparison with Figure 4-21. We see that the peak for the stratosphere falls at an α value of 2, which is higher than the measured NOAA values, while the peak for the free troposphere shows values clustered around α=1.0-1.18, lower than the observed NOAA values.

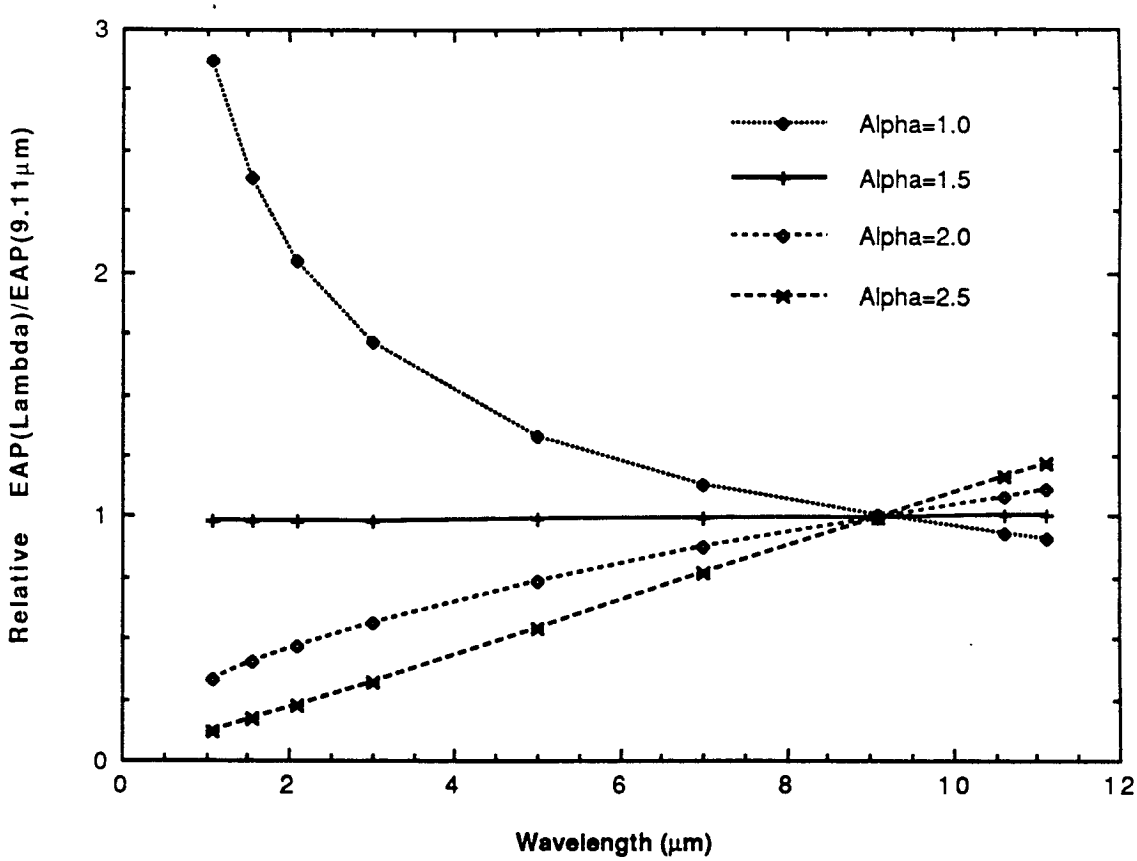

Figure 4-20. Heterodyne Relative EAP for 1 m/s LOS Error

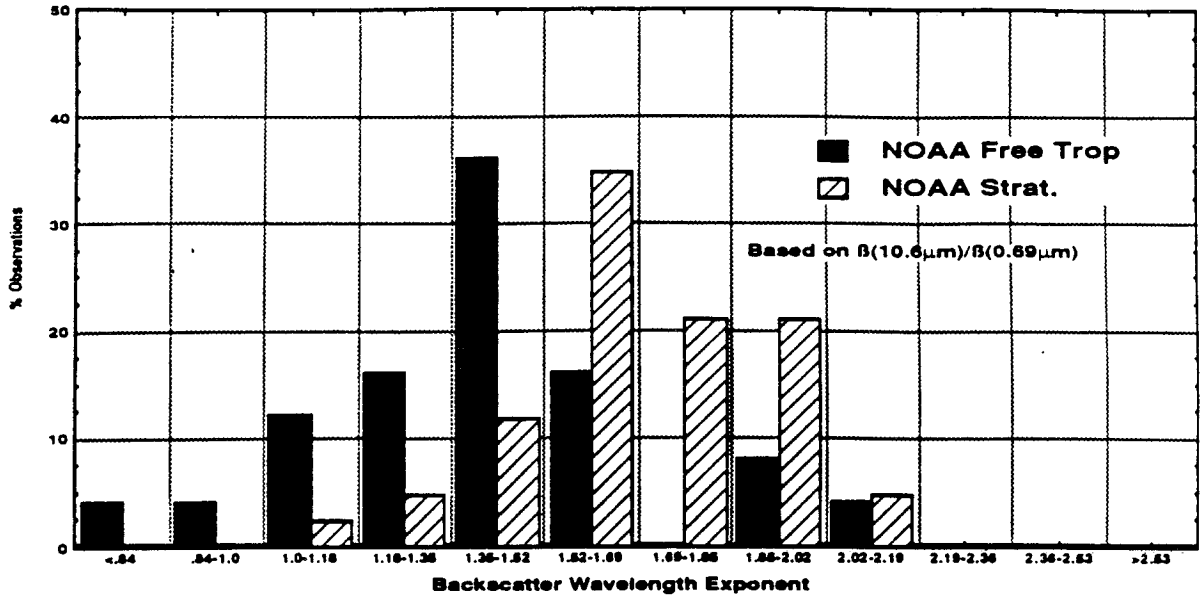

Figure 4-21. NOAA Simultaneous and Colocated Backscatter Measurements

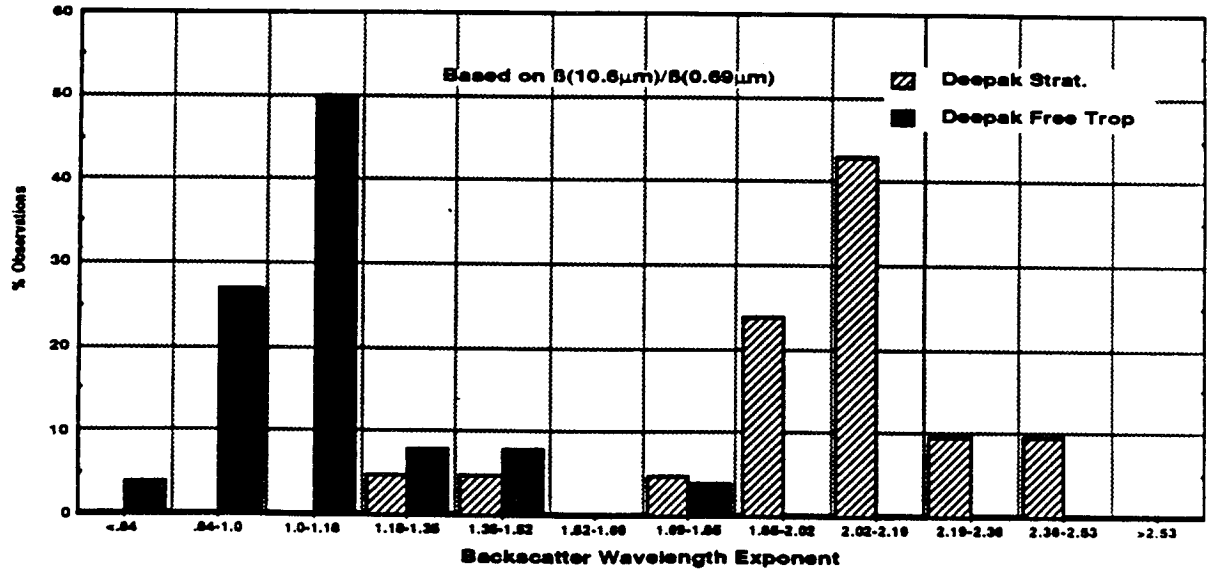

Figure 4-22. Deepak (1982) Modeled Aerosol Backscatter Wavelength Dependence

It should be stressed that the foregoing measurements and Mie calculations concern wavelengths which are inappropriate for LAWS. There appears to be no published results regarding either measurements or calculations at the two LAWS candidate wavelengths 2.1 μm and 9.1 μm. Accordingly we have performed Mie calculations at a range of wavelengths including wavelengths close to 2.1 and 9.1 μm for which we had refractive index data.

Refractive index data were taken from McClatchey and Selby (1974) and the values are reproduced in Table 4-1 over the 0.2 to 40 μm wavelength interval. Values are quoted for two types of particles, 'water soluble' and 'dust-like' respectively. We use for our analysis the particle size distribution recommended in McClatchey and Selby, which is the well known Deirmendjian Haze C model (shown in Figure 4-23, normalized to 1 particle /cc). Backscatter cross section and extinction coefficients were calculated using Mie theory for this size distribution for several wavelengths using the refractive indices for the particular wavelength from Table 3-1. The results are shown in Figures 4-24 and 4-25 for backscatter coefficent and extinction coefficient respectively. The values given are also normalized to 1 particle/cc.

Significantly we find that over the wavelength range 2 to 10 μm the wavelength dependence is weak, approximately the inverse square root of the wavelength, which indicates that for this size distribution and these refractive indices, the longer wavelength has an advantage that is linear with wavelength. This advantage has probably been underestimated since an exact value of the refractive index at 9.1 μm (the supposed peak of the refractive index resonance) was not available.

Since the argument can be made that at higher altitudes the relative population of the larger particles is less, the calculations were repeated for a size distribution that is 'Rayleigh', by ignoring particles with radius larger than 0.1 μm in Figure 4-23. The data are shown in Figure 4-26, and it is now evident that, over the 2 to 10 μm interval the backscatter cross section varies as approximately the inverse 2 to 2.5 power of the wavelength, which would yield a net advantage to the shorter wavelength (n.b. the refractive index variation has modified the inverse fourth power dependence that we would expect for small particles). As expected the wavelength dependence of the backscatter cross section is a strong function of both the size distribution and the refractive index and it is thus important to establish experimentally the size distributions and refractive indices that are applicable.

Thus, for the three wavelength dependent terms in the lidar equation the conclusions are:

1) The atmospheric transmission is about the same at 2.1 μm and 9.1 μm.
2) There is not enough data on β to favor one wavelength over another, and
3) Refractive turbulence considerations would seem to favor 9.1 μm.

We now turn to a technology assessment of the LAWS major subsystems.

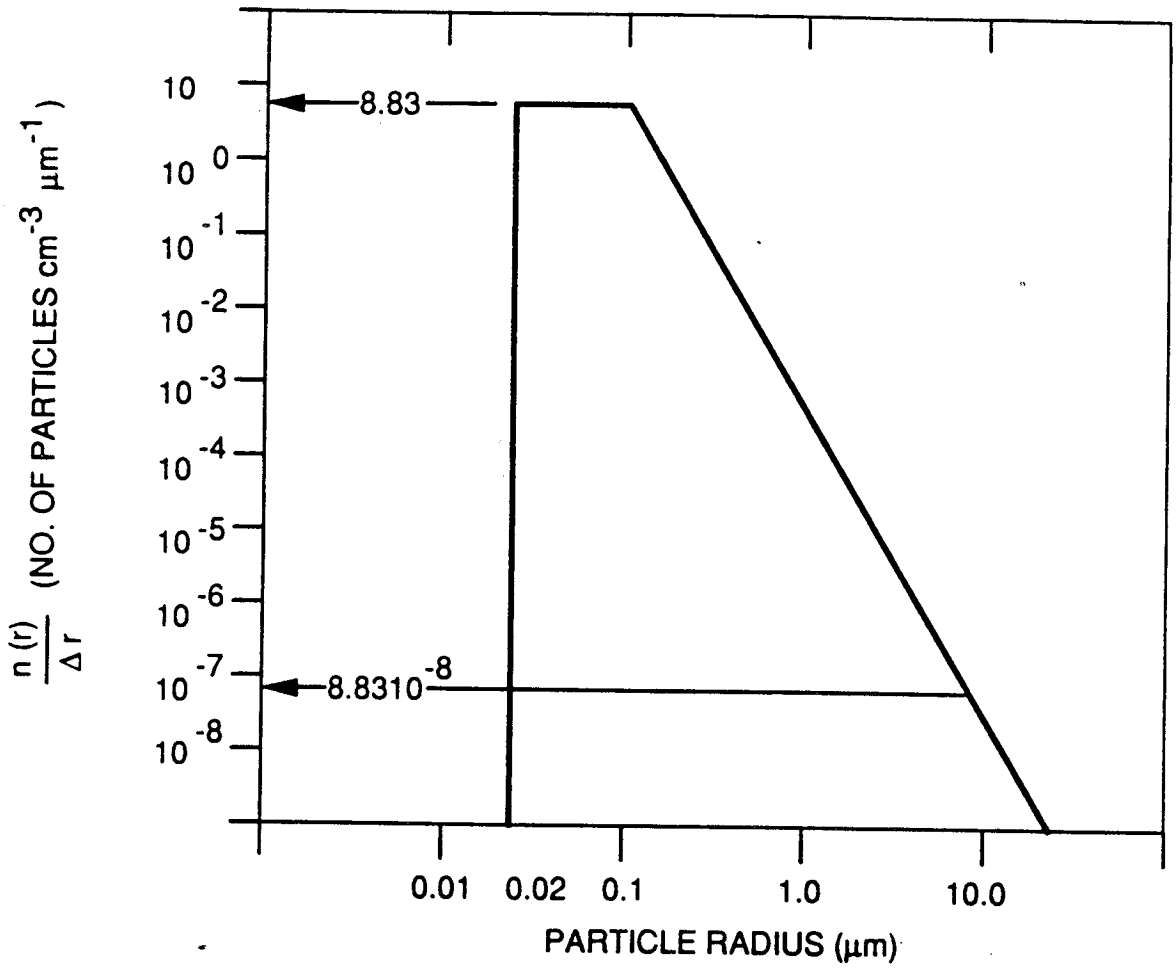

Figure 4-23. Aerosol Size Distribution used in Mie Theory Modeling

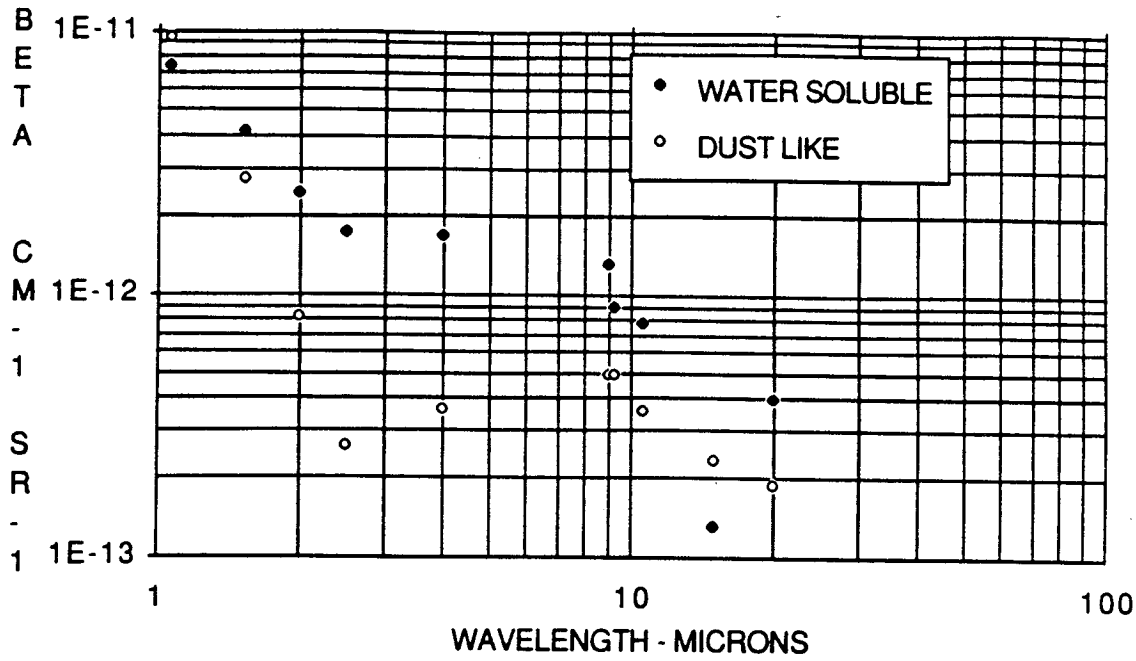

Figure 4-24. Backscatter Coefficient vs. Wavelength for Haze C Model

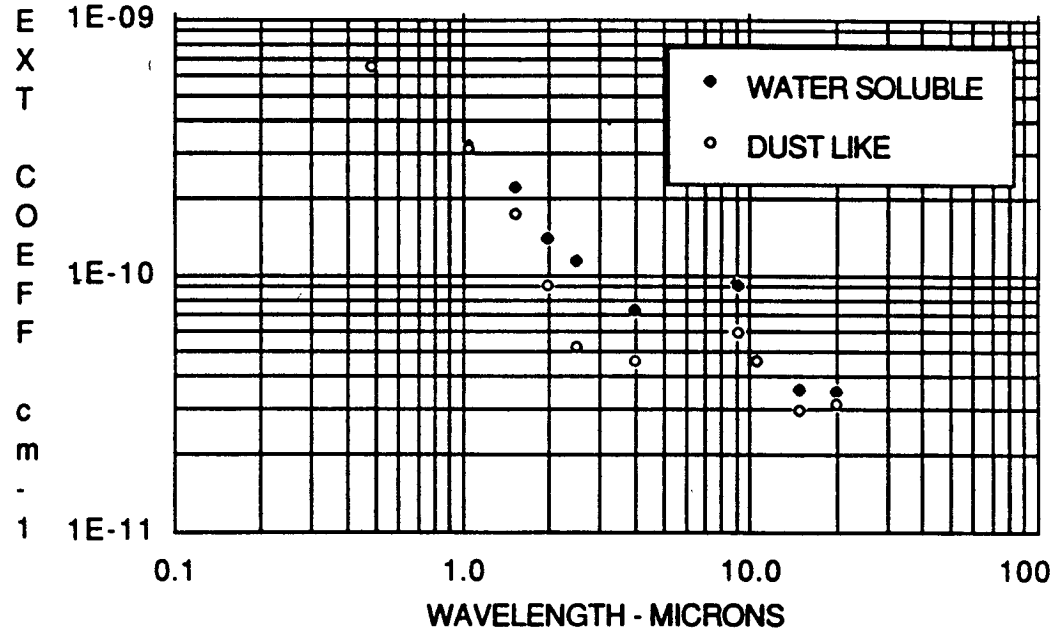

Figure 4-25. Extinction Coefficient vs. Wavelength for Haze C Model

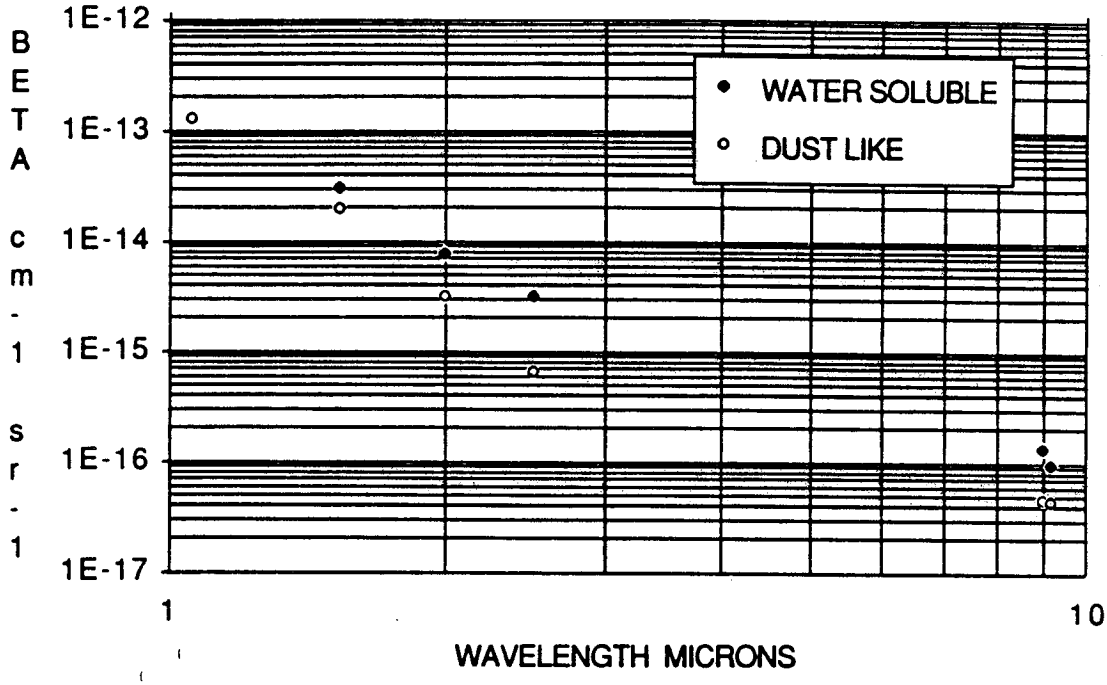

Figure 4-26. Backscatter Coefficient vs. Wavelength for 'Rayleigh' Model

Wavelength	Water Soluble Refractive Index	Dust-Like Refractive Index
.20000	1.530 -.070*I	1.530 -.070*I
.25000	1.530 -.030*I	1.530 -.030*I
.30000	1.530 -.008*I	1.530 -.008*I
.33710	1.530 -.005*I	1.530 -.008*I
.48800	1.530 -.005*I	1.530 -.008*I
.51450	1.530 -.005*I	1.530 -.008*I
.63280	1.530 -.006*I	1.530 -.008*I
.69430	1.530 -.007*I	1.530 -.008*I
.86000	1.520 -.012*I	1.520 -.008*I
1.06000	1.520 -.017*I	1.520 -.008*I
1.53600	1.510 -.023*I	1.400 -.008*I
2.00000	1.420 -.008*I	1.260 -.008*I
2.50000	1.420 -.012*I	1.180 -.009*I
2.70000	1.400 -.055*I	1.180 -.013*I
3.00000	1.420 -.022*I	1.160 -.012*I
3.20000	1.430 -.008*I	1.220 -.010*I
3.39230	1.430 -.007*I	1.260 -.013*I
3.50000	1.450 -.005*I	1.280 -.011*I
3.75000	1.452 -.004*I	1.270 -.011*I
4.00000	1.455 -.005*I	1.260 -.012*I
4.50000	1.460 -.013*I	1.260 -.014*I
5.50000	1.440 -.018*I	1.220 -.021*I
6.00000	1.410 -.023*I	1.150 -.037*I
6.50000	1.460 -.033*I	1.130 -.042*I
7.20000	1.400 -.070*I	1.400 -.055*I
7.90000	1.200 -.065*I	1.150 -.040*I
8.20000	1.010 -.100*I	1.130 -.074*I
8.50000	1.300 -.215*I	1.300 -.090*I
8.70000	2.400 -.290*I	1.400 -.100*I
9.00000	2.560 -.370*I	1.700 -.140*I
9.20000	2.200 -.420*I	1.720 -.150*I
9.50000	1.950 -.160*I	1.730 -.162*I
10.00000	1.820 -.030*I	1.750 -.162*I
10.59100	1.760 -.070*I	1.620 -.120*I
11.00000	1.720 -.050*I	1.620 -.105*I
13.00000	1.620 -.055*I	1.470 -.100*I
14.80000	1.400 -.100*I	1.570 -.100*I
15.00000	1.420 -.200*I	1.570 -.100*I
17.20000	2.080 -.240*I	1.630 0.100*I
18.50000	1.850 -.170*I	1.648 -.120*I
20.00000	2.120 -.220*I	1.680 -.220*I
25.00000	1.880 -.280*I	1.970 -.248*I
27.90000	1.840 -.290*I	1.890 -.320*I
30.00000	1.820 -.300*I	1.800 -.420*I
35.00000	1.920 -.400*I	1.900 -.500*I
40.00000	1.860 -.500*I	2.100 -.600*I

Table 4-1. Aerosol Complex Index of Refraction (after McClatchey and Selby)

4.3.3 *Laser Subsystems at 2.1 μm and 9.1 μm*

Concepts for 2.1 μm and 9.1 μm laser subsystems are now generated. The assumed nominal requirements for the laser subsystem are given in Table 4-2.

Table 4-2. Nominal Requirements for Laser Subsystem

Requirement	*Concept Wavelength*		*Motivation*
	9.1 μm	2.1 μm	
Energy per Pulse	10 J	10J	SNR
Pulse Length	3 μsec	600 nsec	Range/Vel. Resolution
Repetition Rate	10 pps	10 pps	Coverage
Chirp	200 kHz	1 MHz	Vel. Resolution
Bandwidth	Single Frequency	Single Frequency	Vel. Resolution
Beam Quality	Near D.L.	Near D.L.	System Efficiency
Efficiency	5%	5%	Prime Power
Lifetime	10^9 shots	10^9 shots	Mission Duration
Mass	<150 kg	<150 kg	Platform Accommod.
Other		Single Beam Line	Spatial Coherence

4.3.3.1 *2.1 μm Laser Subsystem*

The spectroscopic scheme for a diode-pumped Tm:Ho:YAG laser is shown in Figure 4-27. The $^3F_4$ manifold of the trivalent Tm ion is directly pumped by a diode laser operating near 785 nm. For high Tm concentrations (>2%), this is followed mainly by the cross-relaxation process $Tm(^3F_4\text{-}^3H_4)$ - $Tm(^3H_6\text{-}^3H_4)$ among adjacent Tm ions. This process is very efficient at high Tm concentrations and, as discussed earlier, can lead to an overall pump quantum efficiency of 2. There is fast energy migration among the Tm ions followed by energy transfer from the $^3H_4$ manifold of Tm to the $^5I_7$ manifold of Ho. Laser action occurs on the Ho $^5I_7\text{-}^5I_8$ transition at 2.1 μm.

The Ho fluorescence lifetime has been measured to be about 8 msec (Fan et al, 1987, Kintz et al, 1989). The energy transfer time between Tm and Ho is estimated to be between 5 to 20 μsec depending on dopant concentrations (Fan et al, 1987). Short pulse extraction (<1 μsec) from Tm:Ho:YAG, which is required to meet LAWS requirements, will leave energy behind in the $^3H_4$ manifold of Tm. Dopant densities, pump rates, and the time delay between the pump pulse and extraction pulse must be varied to maximize the energy stored in the $^5I_7$ Ho manifold. Even so, the energy left behind in Tm limits the efficiency of short pulse amplification in this laser system.

Tm:Ho:YAG lasers operating at 2.1 μm are inherently three level in nature. The lower laser level is in the ground-state $^5I_8$ Ho manifold. The degeneracies of the energy manifolds of both Ho and Tm are lifted by the crystal field splitting. The upper laser level is at the bottom of the $^5I_7$ manifold and the lower level at 464 cm-1 above ground for the dominant 2.097 μm line (Ashurov et al, 1979). The relative populations of the levels in the lower manifold are given by a Boltzmann distribution. At room temperature, about 2% of the population in the lower manifold are in the lower laser level. Cooling reduces the lower level population, and at very low temperatures, the system becomes four level in nature.

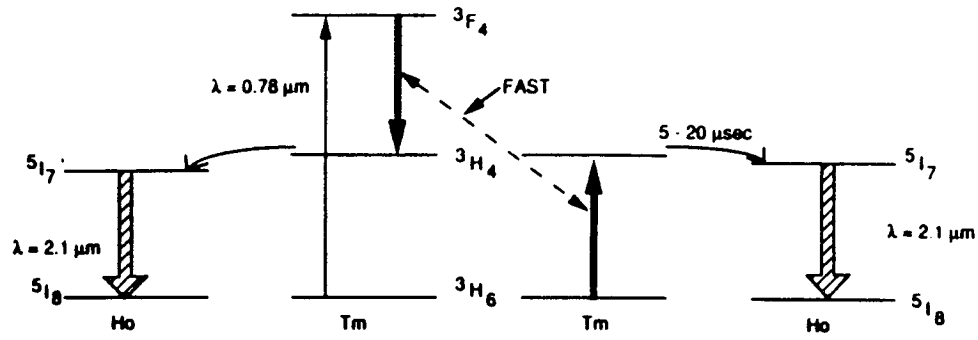

Figure 4-27. Spectroscopy of Tm:Ho:YAG Pumped at 785 nm

The stimulated emission cross section for the 2.097 μm line has been measured to be 9 x 10^{-20} cm^2 (Fan et al, 1987). This is about 7 times smaller than the value for Nd:YAG. The saturation fluence, an important parameter in pulsed amplifier design, varies as a function of temperature. The product of the small signal gain times the saturation fluence gives the energy which can be extracted from the amplifying medium. For efficient operation, an amplifier must be operated above the saturation fluence. The saturation fluence for Tm:Ho:YAG varies from about 5 J/cm^2 at 100 K to 8.5 J/cm^2 at 300 K (see Figure 4-28). The temperature dependence is due to the dependence of the relative populations of the upper and lower laser levels. These values for the saturation fluence were obtained under the assumption that the relaxation between the levels in the upper and lower laser manifolds is rapid compared to the laser pulse duration so that the relative populations of the upper and lower laser levels can be given by a Boltzmann distribution.

A Tm:Ho:YAG kinetics model has been developed and incorporated into Spectra Technology's multi-stage amplifier computer code. The kinetics model consists of a set of rate equations for the ground and first excited manifolds of both Tm and Ho. The energy transfer processes included in the model are the Tm-Ho transfer and upconversion. The pumping process is characterized by a pump quantum efficiency (~2) for pumping the $^3H_4$ Tm manifold. The $^3H_4$ Tm, $^5I_8$ Ho, $^3H_6$ Tm, $^5I_7$ Ho rate constant used in all the calculations is consistent with an initial transfer time of 10 μsec. The rate constant for the reverse process is computed from the equilibrium constant at the crystal temperature.

Upconversion is a loss mechanism which depopulates the upper $^5I_7$ Ho manifold. The process has been postulated as follows (Fan et al, 1987). The $^5I_7$ manifold of holmium interacts with a thulium ion in the $^3H_4$ manifold. The Tm ion decays to the ground state while the Ho ion is excited to a higher manifold. The upconverted Ho ion relaxes rapidly by the emission of phonons and decays to the ground state while exciting

a Tm ion to a higher manifold. The excited Tm ion then relaxes rapidly to the excited $^3H_4$ manifold. The total relaxation process of the upconverted Ho ion to an excited $^3H_4$ Tm ion occurs with a quantum efficiency of near unity. The net result of this process is a loss mechanism by which a Ho ion in the upper $^5I_7$ manifold decays to the ground state. The rates of this process at room temperature for four doping densities have been measured by G. Kintz et al, at NRL.

It is assumed in the present model that the laser pulse duration is much longer than the relaxation time between the energy levels in a given manifold. Thus, the relative populations of the energy levels in the lower and upper Tm and Ho manifolds can be described by a Boltzmann distribution even during the extraction process.

The kinetics model developed for a diode-pumped Tm, Ho:YAG system was coupled to an oscillator extraction model for comparison with the pulsed experiments performed at NRL. The computed slope efficiency was 65.2% which compares very well with the measured value of 65.8% (Kintz, et al, 1987).

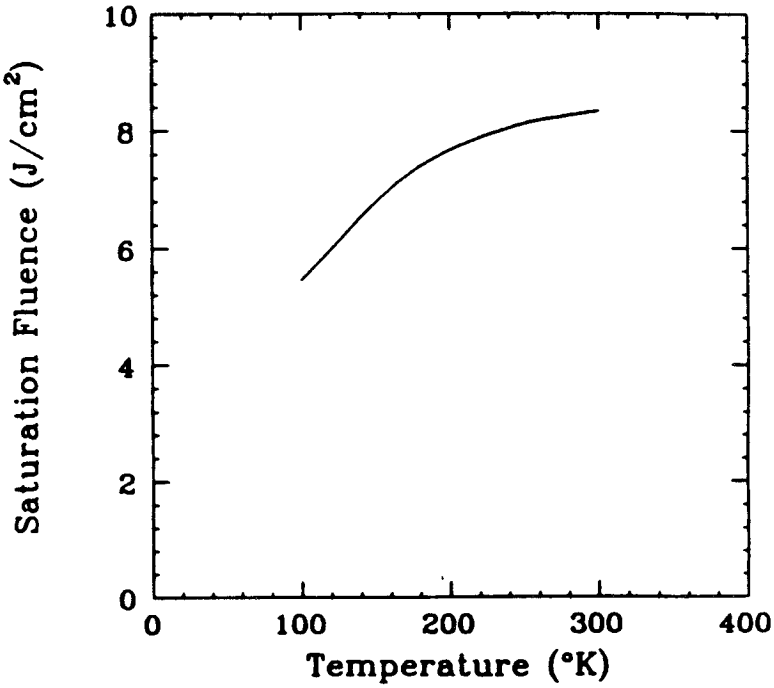

Figure 4-28. Saturation Fluence as a Function of Temperature

For efficient short pulse extraction, the fraction of the pump energy which ends up in the upper $^5I_7$ Ho manifold must be maximized since the energy in the upper Tm manifold is left behind. This fraction is heavily concentration dependent. The concentration of Tm must be high enough for efficient cross-relaxation. During and after the pumping process, the Tm and Ho manifolds begin to equilibrate. The optimum Ho concentration for a given Tm concentration is that for which the largest fraction of the pump energy ends up in the Ho $^5I_7$ manifold. This will, in general, be temperature dependent. The doping densities must be kept low enough, however, to minimize upconversion losses. The upconversion rate constant is concentration dependent, and measured values of this rate are available at room temperature for four doping densities.

It was found that the conventional 5.7% Tm, 0.37% Ho densities maximized the fraction of the pump energy in the $^5I_7$ Ho level compared to the other concentrations studied by the NRL group. Since upconversion rates are not available for other concentrations, this concentration was used in the subsequent calculations. This doping density is standard and has been used by many research groups performing Tm: Ho:YAG laser experiments.

The fraction of the absorbed pump energy which ends up in the $^5I_7$ Ho manifold is shown as a function of the absorbed energy at both 235 K and 300 K in Figure 4-29. Also shown is the computed peak small-signal gain. In these calculations, the sample was pumped for 10 μsec. The small-signal gain peaked after the pump pulse terminated at a time which depended on the pump energy absorbed. For low pumping, this time was near 10 μsec after the pumping was terminated. For higher pumping rates, this time was much longer since the Tm-Ho transfer time decreases as the ground state Ho manifold becomes depleted. At both temperatures, the fraction of the absorbed energy which ends up in the $^5I_7$ manifold of Ho is nearly constant up to 10 J/cc of absorbed energy. The slight decrease in this fraction as the absorbed energy increases is due to the increasing upconversion rate as the upper Tm and Ho manifold population increases. When the absorbed energy is greater than 10 J/cc, upconversion becomes large and the ground-state manifold of Ho becomes depleted. The small-signal gain rises linearly with the absorbed energy and levels off as the ground-state Ho manifold is depleted. The optimum pump energy at both temperatures is around 10 J/cc, since this pump energy gives a high fraction in the upper Ho manifold and a reasonably high small-signal gain.

The fraction of the absorbed energy in the upper Ho manifold is higher at 235 K than at 300 K because the $^5I_7$ Ho manifold is lower in energy than the $^3H_4$ Tm manifold. Thus the reverse rate $^5I_7$ Ho-$^3H_4$ Tm decreases with decreasing temperature. The small-signal gain also increases as the temperature decreases because the relative population in the lower laser level decreases.

The kinetics model was used in a multi-stage amplifier code to determine a MOPA configuration for LAWS using diode-pumped Tm:Ho:YAG amplifiers. The amplifier staging was configured for maximum efficiency. It is assumed that the master oscillator output is 0.1 Watt cw. A pulse of about 1 μsec in duration is chopped from the cw beam. The energy gain to obtain a 10 J pulse is about 10^8. The maximum small- signal gain-length product was set to 4 for each amplifier for ASE suppression, and each amplifier is optically isolated. The beam area is tailored to minimize the number of amplifier stages, and the maximum design fluence was set to 40 J/cm^2 for optical coating damage. All stages are single passed with a 5% interstage transmission loss. Nonsaturable losses were neglected. The extraction pulse is spatially top-hat, and the initial temporal pulse shape is supergaussian.

Since the fluorescence lifetime of the Ho and Tm upper manifolds is much longer than the extraction pulse width, the amplification process is based on the energy stored in the upper Ho manifold prior to the arrival of the extraction pulse. In the calculations, the extraction pulse arrives about 60 μsec after the pump pulse is terminated. This is the time it takes for the small-signal gain to reach its maximum value.

As mentioned above, nonsaturable losses were neglected in the calculations. Further, no consideration was given to the laser diode pumping geometry. A uniform deposition of the pump intensity was assumed throughout the crystal, and the mode-matching of the pump pulse with the extracted pulse is neglected. These idealizations mean that the calculated efficiencies are to be taken as upper bounds on the efficiencies which can be realistically achieved in practice.

A 10 J per pulse MOPA Tm:Ho:YAG laser system at 300 K is shown schematically in Figure 4-30. It consists of four smaller preamps and two larger power amplifiers.

The four small preamps are run at small- signal, i.e., the input signal is much smaller than the saturation fluence and the energy gain is roughly exp(goL). The first power amplifier has an energy gain of 10, and the final power amplifier has an energy gain of 4. Since the pump energy into the power amplifiers is much larger than in the preamps, the power amplifiers determine the efficiency of the total amplifier chain. The preamps are used to achieve much of the needed energy gain so that the power amplifiers can be operated in saturation and the stored energy extracted efficiently. The intrinsic efficiency of the amplifier chain, defined as the optical energy out divided by the total energy absorbed by the crystal is 21% at 300 K.

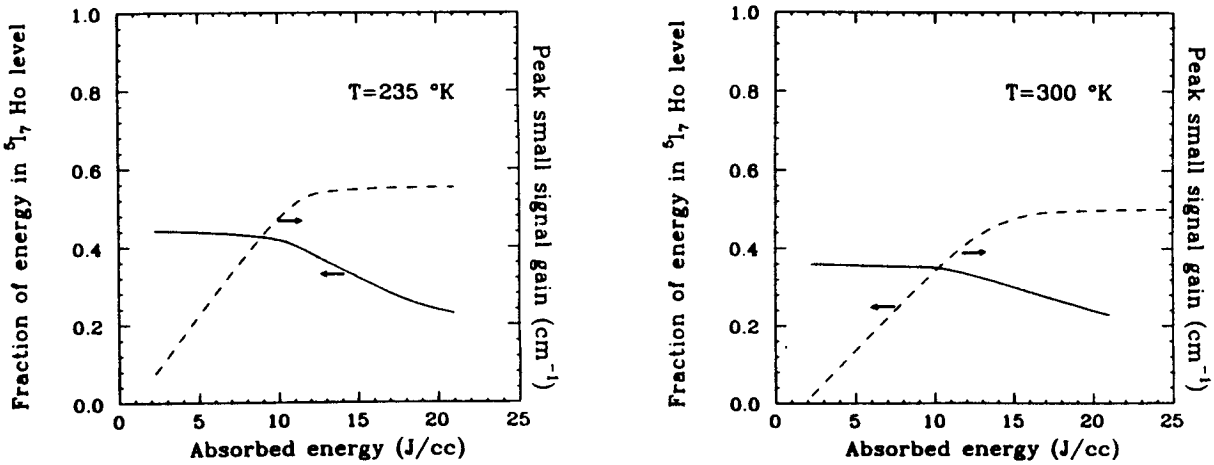

Figure 4-29. Fraction of Absorbed Pump Energy Reaching Upper Laser Level

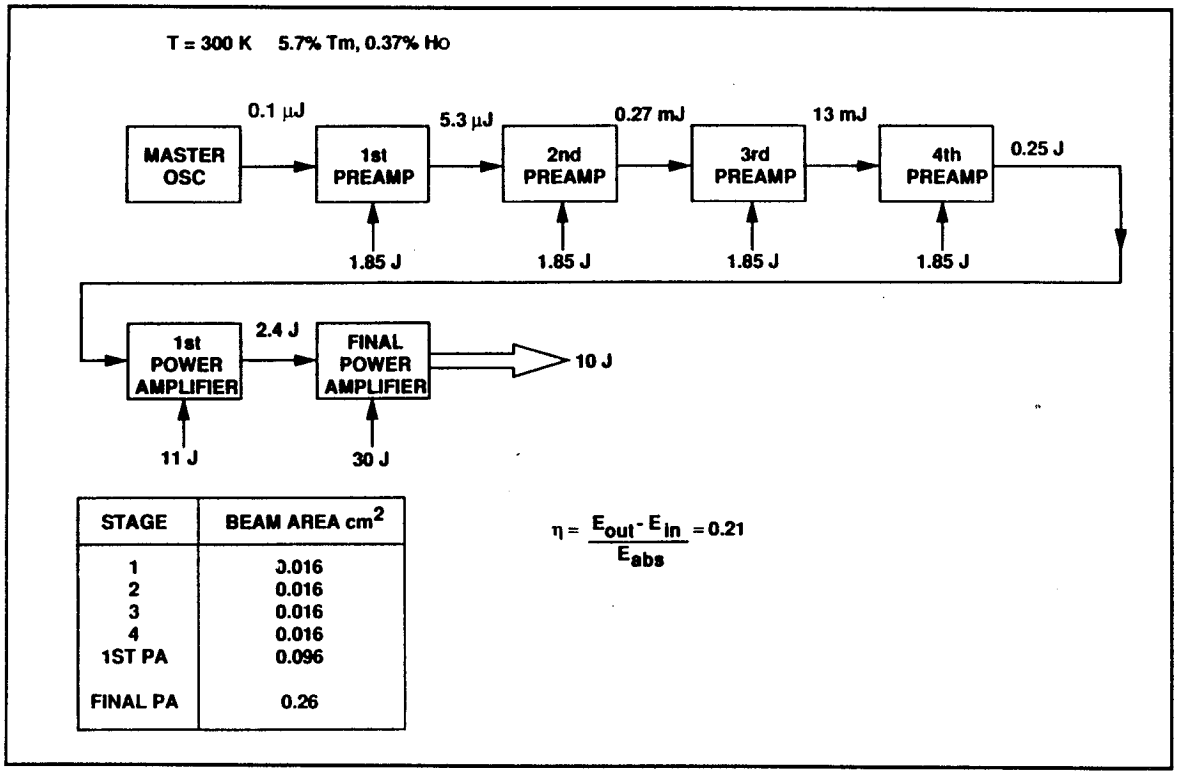

Figure 4-30. Tm:Ho:YAG Laser-Conceptual Design

The predicted output temporal pulse shape is shown in Figure 4-31. Also shown is the input pulse shape. The large amplifier gain sharpens the leading edge of the pulse considerably. This is simply because the leading pulse edge sees a larger gain than does the trailing edge, and for these short extraction pulses, the upper Ho manifold is not replenished from the upper Tm manifold.

Cooling the samples increases the intrinsic efficiency of the amplifier chain as shown in Figure 4-32. This increase in efficiency is mainly due to the increase in the fraction of the pump energy which ends up in the upper $^5I_7$ Ho manifold as the temperature is reduced.

A rough (and optimistic) estimate of the wall-plug efficiency of the Tm:Ho:YAG laser subsystem can be made by making the following assumptions: a) the electrical to diode optical power conversion is 40% efficient, and b) the pumping geometry can be arranged so that 70% of the diode output is absorbed by the medium. Using the model results for an intrinsic efficiency of 21% at 300 K gives a laser wall-plug efficiency of 5.9%.

4.3.3.2 *9.1 μm Laser Subsystem*

The carbon dioxide laser has been the transmitter of choice in all operational wind-sensing lidars to date. Until recently it has been the only laser source capable of providing the copious supply of single line output power at an eye-safe wavelength needed for the application. Starting around 1965 with efforts at NASA/Marshall Space Flight Center, it has been used with considerable success in systems built by various organizations world-wide, e.g. NASA/Marshall, NOAA, JPL and others in the USA, and RSRE, DFVLR, the University of Hull and others in Europe. Ranges of operation out to

30km have been obtained in the troposphere even when using the abundant isotope. In the concept being presented, use of a rare isotope is proposed since this circumvents extinction by the atmospheric carbon dioxide which would add considerably to the laser pulse energy required for a space-based abundant isotope laser. Extinction of an abundant isotope beam can exceed 20 dB for the nadir angles of interest. The choice of the $^{12}C^{18}O_2$ isotope has been made on the basis of the increased backscattering at its 9.1 μm line due to the refractive index resonances of the aerosol constituents. Evidence of an enhancement of a factor of about 3 has been obtained experimentally at JPL using 9.25 μm and 10.6 μm lasers (Ancellet et al, 1988). The lasing performance of the $^{12}C^{18}O_2$ isotope has been found to be very efficient during experiments at Spectra Technology funded jointly by the USAF and NASA/MSFC.

The transmitter approach we have selected is the external injection of a transversely excited transverse flow laser incorporating an unstable resonator cavity. The external injection selection is based on the heritage of this approach for long-range wind-sensing and in its high power potential since the high gain possible allows an unstable mode to be generated. This results in efficient utilization of the gain medium. The hybrid transmitter approach was rejected because of the requirement to incorporate a CW gain cell within the cavity which forces the cavity to be a stable one because of the low cavity losses necessary for CW operation. This reduces the mode fill factor within the cavity and has an adverse effect on efficiency in the pulsed mode. This scheme also exposes more components to high power radiation and is thus limited to low pulse energies. The master oscillator power amplifier (MOPA) approach was determined to be unsuitable for the LAWS laser for reasons of low efficiency and complexity. The low efficiency derives from the fill factor mismatch that occurs between the modes and gain medium due to the requirement to physically separate the various passes through the amplifier for high beam quality. Since the waveform modulation potential of a MOPA is not useful for the LAWS laser, this architecture is also considered too complex. Efficient MOPA systems generally require an additional preamplier to efficiently extract energy

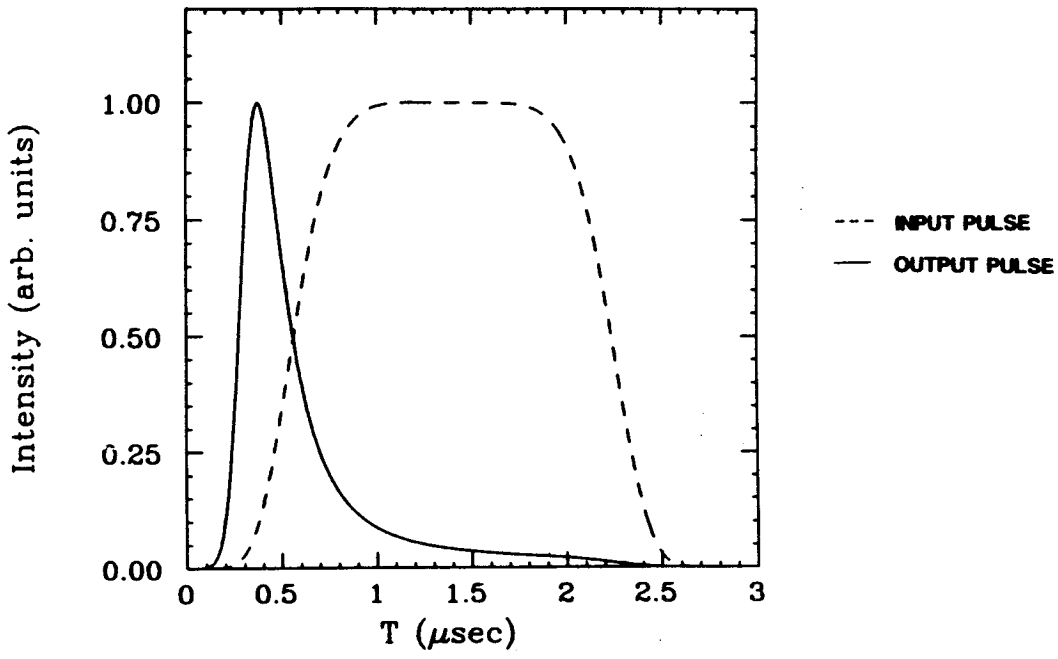

Figure 4-31 Tm:Ho:YAG Laser-Output Pulse Shape

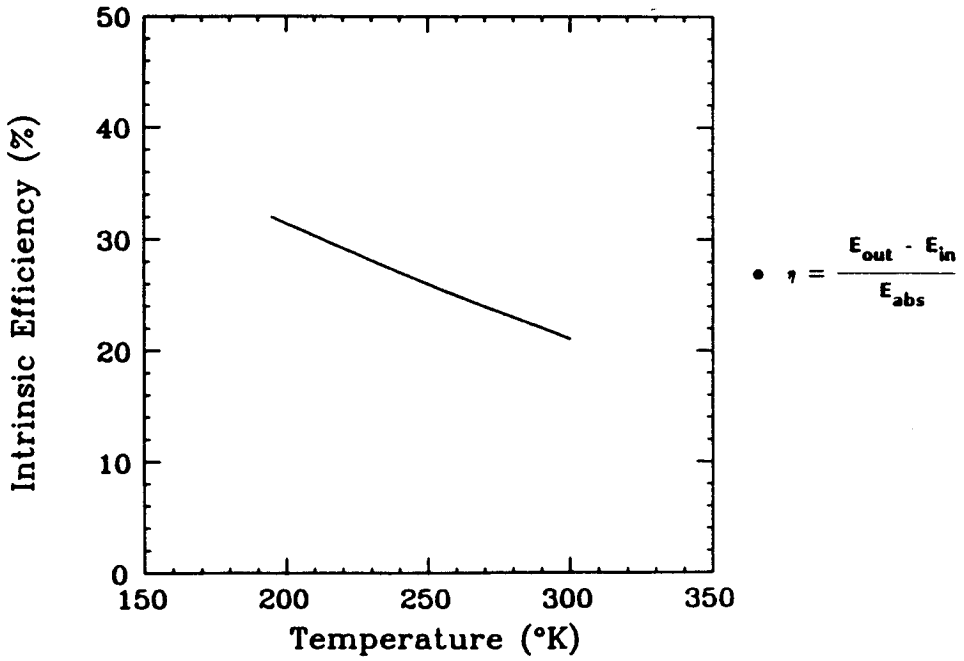

Figure 4-32. Tm:Ho:YAG Laser-Temperature Dependent Efficiency

from the power amplifier, and at the 9 micron wavelength requires imaging of the mode between stages to minimize the effects of diffraction as well as Faraday isolators to isolate successive stages to minimize parasitics.

An optical schematic of the proposed concept is shown in Figure 4-33. Radiation from a low power CW waveguide laser is line center locked and its output provided to the receiver as the local oscillator beam and also injected into the transmitter laser through the zeroth order of a Littrow grating. The CW beam that exits the transmitter cavity via this path is used to tune the transmitter laser cavity to the injection frequency via an active control circuit, while the pulsed output is processed to provide a correction for the offset between the transmitted and injection frequencies which is provided to the signal processor. Accommodation is made for a redundant CW laser. In the event that the injection geometry provides insufficient isolation between the TE laser and the IO/LO lasers we will investigate the inclusion of a Bragg cell or other isolation method in phase II.

The cavity incorporates a graded reflectivity feedback/output coupler which we have chosen because of its superior mode properties, in particular its mode separation margin and excellent far field pattern properties. The gain section incorporates the TE laser head, flow-loop, gas regenerator and pulsed power. Prime power is derived from the spacecraft and thermal control is achieved by a coolant loop connected to the spacecraft thermal control system. Command and control information is derived from the lidar master control computer. The gain section is mechanically isolated from the lidar optical bench. A preliminary laser subsystem concept isometric is shown in Figure 4-34, which includes all of the detail depicted in Figure 4-33.

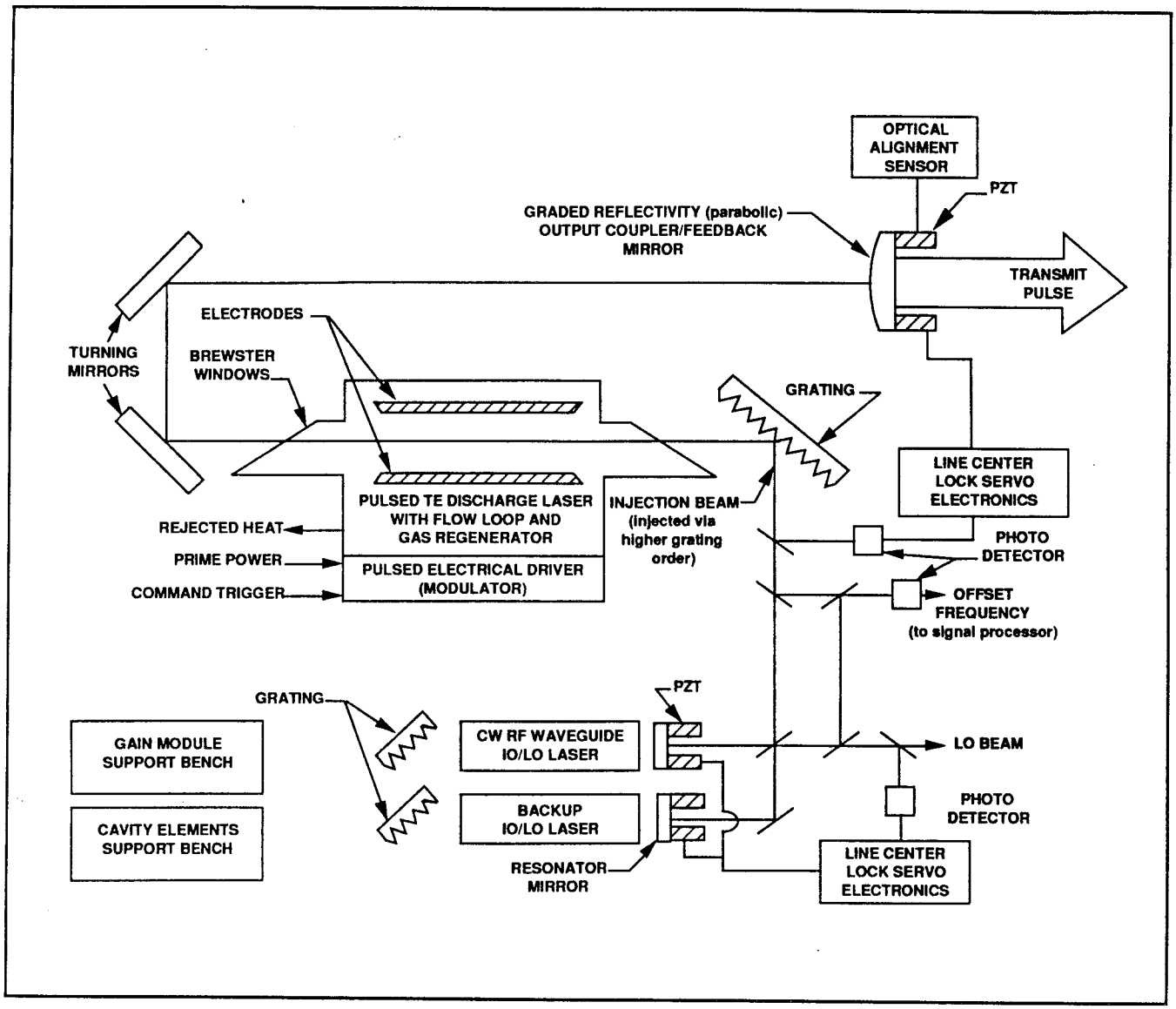

Figure 4-33. CO_2 Laser-Schematic Diagram

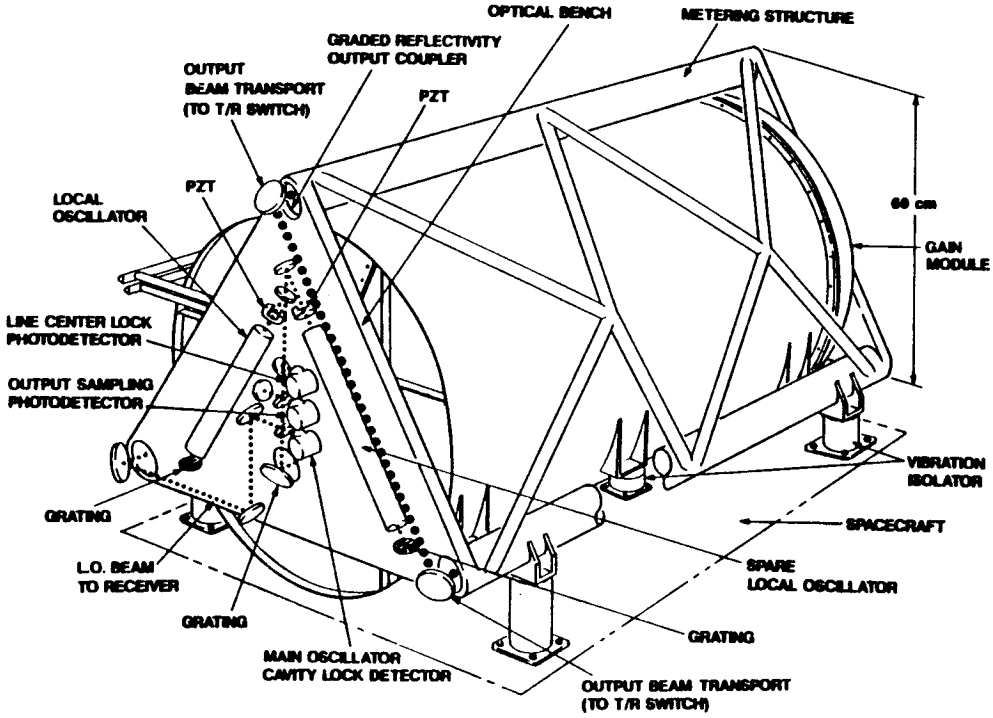

Figure 4-34. CO_2 Laser-Isometric

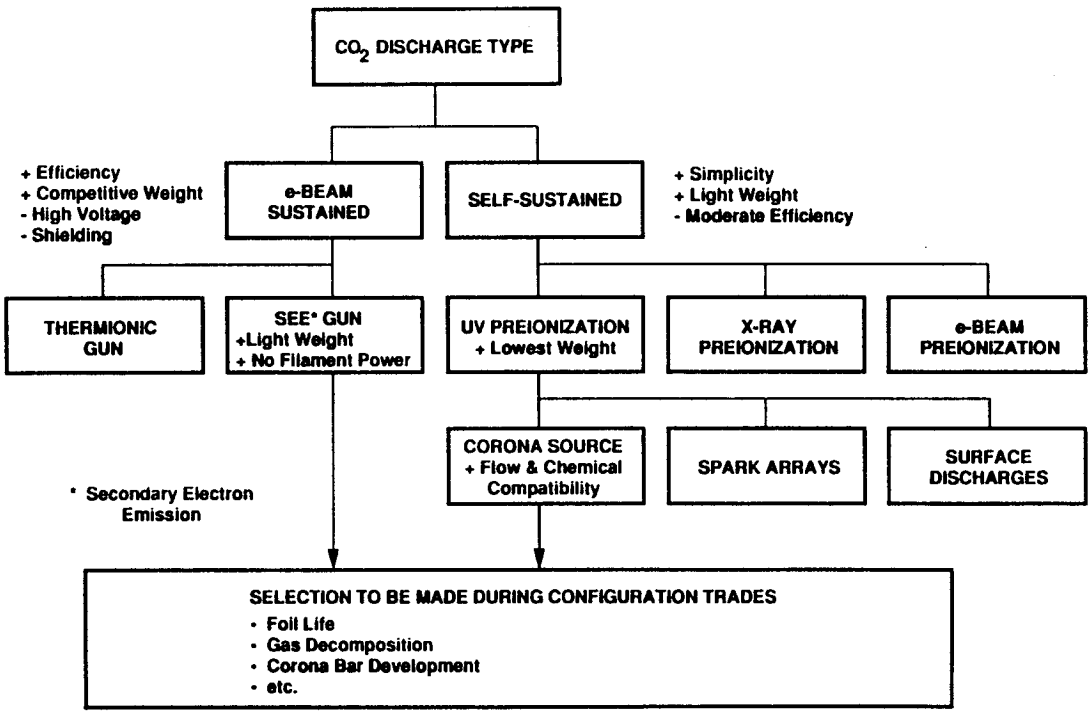

Figure 4-35. Technology Options for CO_2 Laser

A major LAWS laser trade is the choice of discharge type. Two options considered were the use of either a self-sustained or an electron beam sustained discharge with the final choice being self-sustained. The trades conducted are summarized in Figure 4-35 The advantages of the self-sustained approach are simplicity and low weight. These are countered by moderate excitation efficiency. An e-beam sustained discharge has an efficiency advantage which is countered by the need for a high e-gun voltage (in excess of 100 KV) and lead shielding for protection against the X-rays that are generated. For the self-sustained approach we have selected an ultra-violet light source to preionize the gas over an x-ray or electron-beam approach primarily for the reasons of weight minimization and simplicity. It is also the technique most popular in current lidar systems. A corona discharge was selected as the source of the UV light because this method provides a smooth aerodynamic profile to the cavity flow and causes minimal gas degradation. For the e-beam sustained approach, considered in the trade-offs, a thermionic e-gun was rejected in favor of a Secondary Electron Emission Gun, (SEE Gun) for reasons of weight and efficiency.

The SEE Gun is a recent significant development that makes possible consideration of space-basing an e-beam sustained system. In a SEE Gun, a locally generated plasma of He ions are accelerated to strike the cathode which generates 10 - 20 electrons/ion which are accelerated through the foil window. The helium pressure is low enough to avoid Paschen breakdown in the high-voltage gap and high enough such that a uniform cold-cathode discharge can be formed easily. Its principle and construction is summarized in Figure 4-36.

Significantly, no filament power is required to heat the cathode, which leads to a higher efficiency and a high quality vacuum is not required. These and other favorable characteristics relative to a thermionic gun are summarized in Figure 4-37.

To choose between self sustained and e-beam sustained approaches we developed point designs for each, which allowed us to estimate weights and efficiencies, considered the relative rates of gas degradation from in-house data on both e-beam and self sustained devices, and assessed the reliability of components from data available from the CORA program (e-beam) and NOAA WINDVAN (self sustained). The self sustained approach chosen is discussed in further detail in section 5.0.

Another major technology option was whether to incorporate a fixed frequency or a frequency-agile local-oscillator laser. The former has the advantage of simplicity and is within the current state-of-the-art, but requires a wide-bandwidth receiver up to 1.5 GHz. A frequency agile local oscillator laser deriving input from the scan azimuth encoder (via. the master computer), to compensate for the orbital/earth spin motion, relaxes the receiver bandwidth requirement. A CW laser capable of being slewed in frequency over 1.5 GHz is however a developmental item. This is discussed further in section 5.0.

The choice of cavity design is influenced by many factors which include efficiency, mode quality (including the far-field beam profile) and the single mode oscillation margin. Efficiency considerations dictate the selection of a positive-branch unstable resonator approach because of the better cavity fill factor possible. The graded reflectivity feedback/output coupler approach has shown considerable promise in the areas of single-mode control and maximizing the energy within the diffraction limited field of view of the lidar.

The performance of CO_2 lasers is well understood as exemplified by the plots shown in Figure 4-38 of the pulse energy profiles obtained experimentally and by simulation (which uses the measured discharge I,V curves as input). Very good agreement exists between measurement and theory for both the temporal profiles and the extracted energy, which is testimony to the level of understanding of CO_2 lasers. This result was obtained using the $^{12}C^{18}O_2$ isotope by Spectra Technology during a measurement program to study the kinetics and extraction characeristics of $^{12}C^{18}O_2$

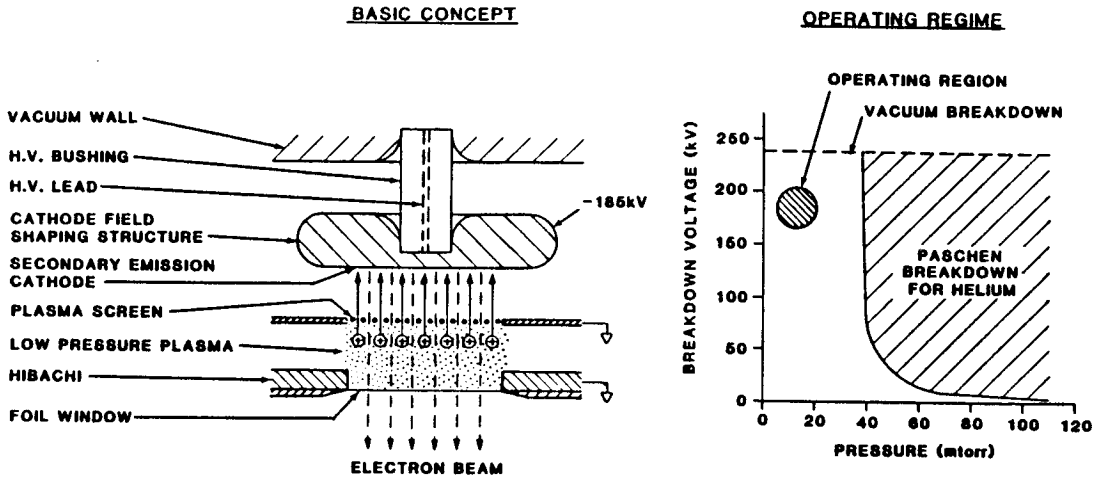

- HELIUM IONS STRIKE CATHODE AND GENERATE 10-20 ELECTRONS/ION WHICH ARE ACCELERATED THROUGH THE FOIL WINDOW
- THE PRESSURE IS LOW ENOUGH TO AVOID PASCHEN BREAKDOWN IN THE H.V. GAP
- THE PRESSURE IS HIGH ENOUGH THAT A UNIFORM COLD CATHODE DISCHARGE CAN BE FORMED EASILY

Figure 4-36. SEE Gun Concept

- Simple Design, Small, Light Weight, Reliable, Long Life
- The SEE-Gun is Gas Filled With Helium at 5-20 mtorr
  - Better HV stand-off properties
  - Faster and more stable conditioning
  - High quality vacuum not required
  - Simple vacuum system: exhaust to space
- Reduced Thermal Loading Since No Hot Filaments
  - Plasma generat or operates at an average power ~ 100 W
- No Delicate Parts
- Simple DC HV Power Supply With Filter Capacitor (~1 kJ) To Meet Peak Current Requirements
- Current Waveform Controlled By A Low Voltage (~3 kV) Low Energy (~ 5 J/pulse) Pulser At Ground Potential
- No Warm-Up Required, Start-Up is Instantaneous
- No Significant Design Or Reliability Issues

Figure 4-37. SEE Gun Summary

SELF-SUSTAINED LUCY DATA

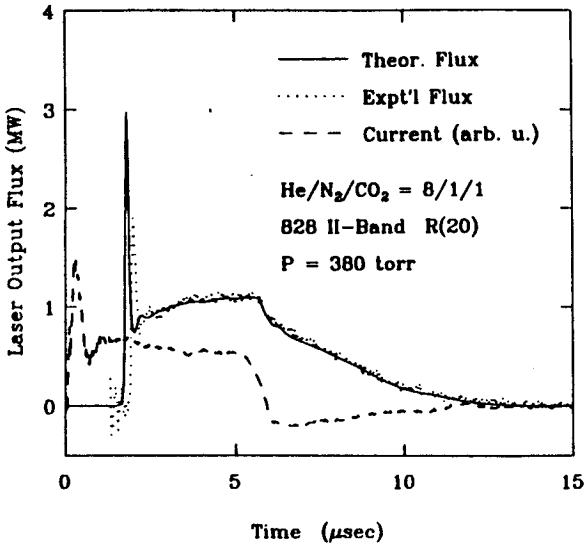

PARAMETER COMPARISON

	LUCY	LAWS PRELIM.
P	0.5 atm	0.5 atm
E	6.7 J	10 J
Aperture	4 x 4 cm^2	7 x 7 cm^2
Length	90 cm	50 cm
Energy Density	10 J/ℓ-atm	8 J/ℓ-atm
Pulse Duration	5 μsec	3 μsec
Mixture	8/1/1	7/2/1

Higher energies have been achieved in LUCY. This is a point comparison.

Figure 4-38. Modelled and Experimental Performance of CO_2 Lasers

- 828 CO_2 R(20) at 9.1 μm
- Lucy X-ray Preionized Self-Sustained - 4 x 4 x 90 cm

  $He/N_2/CO_2$=45/10/15 p = 380 torr E_{laser} = 12 J n^* = 16%
  $He/N_2/CO_2$=45/10/15 p = 760 torr E_{laser} = 25 J n^* = 15%

- Delilah E-beam Sustained - 4 x 4 x 90 cm

  $He/N_2/CO_2$=45/40/15 p = 380 torr E_{laser} = 15 J n^* = 12%
  $He/N_2/CO_2$=45/40/15 p = 760 torr E_{laser} = 26 J n^* = 10%

- Similar Results for 626 CO_2

*Intrinsic Efficiency

Figure 4-39. Extraction data for Oxygen-18 CO_2 Laser

lasers which was funded jointly by USAF/AFGL and NASA/MSFC. Highlights of the extraction data obtained during this study are presented in Figure 4-39. This is presented as evidence that a laser transmitter based on the $^{12}C^{18}O_2$ laser is fully capable of providing the pulse energies at high efficiency required for LAWS.

4.3.3.3 *Laser Subsystem Concept Summary*

The relative merits of the two laser concepts presented are summarized in Figure 4-40, by category, representing each of the critical laser requirements. It is evident that the CO_2 laser proves superior in each of the categories.

4.3.4 *Optical Subsystems at 2.1 μm and 9.1 μm*

Our approach in the concept selection task was to develop the requirements and data base for conceptual optical subsystems for 2.1 μm and 9.1μm operational wavelengths. In the concept evaluation and selection section (section 4.4) this data base was weighted, evaluated and used to select our concept recommendation.

To facilitate comparisons between these two large optical systems, we have adopted as a baseline the requirements listed in Figure 4-41; basically, a diffraction-limited 1.5 m aperture diameter beam expander/ telescope. The heterodyne field of view (FOV) is approximately the same size as the Airy pattern, which is given by 2.44 times the wavelength (λ) divided by the aperture diameter. The FOV for the two wavelengths and the key pointing or boresight requirements are included in the Figure and are discussed below in section 4.3.4.1. Additional optical subsystem requirements including an optical quality or wavefront error budget are discussed in section 4.3.4.2.

4.3.4.1 *Boresight Error Budget*

The error budgets are based upon a previous optical design developed during the Windsat studies for a CO_2 laser concept as shown in Figure 4-42. We have constructed preliminary boresight error budgets based on this design for 9.1 μm and 2.1 μm operational wavelengths, as shown in Figures 4-43 and -44. We traded error budget allocations with design and manufacturing capabilities to achieve the best mix of performance and program cost.

The boresight requirement is proportional to the design wavelength, because the heterodyne field of view (FOV) is proportional to wavelength. During the concept selection phase of the study we allocated ~20% of the FOV to pointing errors. All entries in an error budget for a 2 μm wavelength concept are divided by a factor of ~4.5, the ratio of 9.1 μm to 2 μm.

We converted the boresight error budget into a tolerance table, using our computed sensitivities of the WINDSAT optical prescription. These tolerances are shown in Figure 4-45 for both the 2 μm and 9.1 μm wavelength concepts, along with a comparison to the current State of the Art in precision optics represented by the Hubble Space Telescope.

Figure 4-45 shows that three of the tolerances are critical for the 2 μm wavelength concept, and one is critical for both concepts. These are: primary mirror tilt, secondary mirror decenter, and the telescope rigid body tilt error caused by the scan bearings. The most important of these tolerances is the rigid-body tilt error caused by imperfections in the bearings of the conical scan mechanism. The best available ball or roller bearings have a random run-out in the vicinity of 0.5 micrometers. However, we have prior experience with configurations that are able to meet the line of sight stability requirements for the 9.1 μm concept. In addition, recent developments in magnetic suspension bearings provide an additional option as we refine the optical subsystem design. We are confident that for the 9.1 μm concept, careful

Item	*CO_2*	*Tm:Ho:YAG*
Pulse Energy (10J) Prime Energy	Demonstrated All Solid-State Pulse-Power in Existence	Not Demonstrated Large Diode Array Not Available, in Particular at 785 nm
Pulse Repetition Frequency (10 Hz)	Demonstrated	Not Demonstrated, Particularly with Coherence
Wall Plug Efficiency(>5%)	>5%	Optimistic Assumptions of Model Indicate <10%
Lifetime (10^9 shots)	>10^8 Routine Commercially	Potentially >10^9 shots but not Demonstrated
Frequency Stability (~100 kHz)	Demonstrated	Not Demonstrated
Eye Safety	Eye safe	May not be Eye Safe for Aided Viewing (see 4.4)

Figure 4-40. Tm:Ho:YAG and CO_2 Laser Concepts-Summary

REQUIREMENTS

- Aperture Diameter: ~1.5 m
- Diffraction-limited optical system
- Heterodyne Field of View: 14.8 μrad. @ 9.1 μ, 3.25 μm @ 2 μm
- Boresight Stability
  - During shot transit time (~ 5 msec.): 3 μrad. (1σ) @ 9.1 μm
    0.64 μrad. (1σ) @ 2 μm
- Accessible pupil for Lag Angle Compensation
- Beam Expansion ratio appropriate for laser output beam

ASSUMPTIONS

- Scaled "WINDSAT" optical design
- Scan rate = 6 RPM
- Scan Angle = 45°

Figure 4-41. Optical Subsystem Requirements and Assumptions

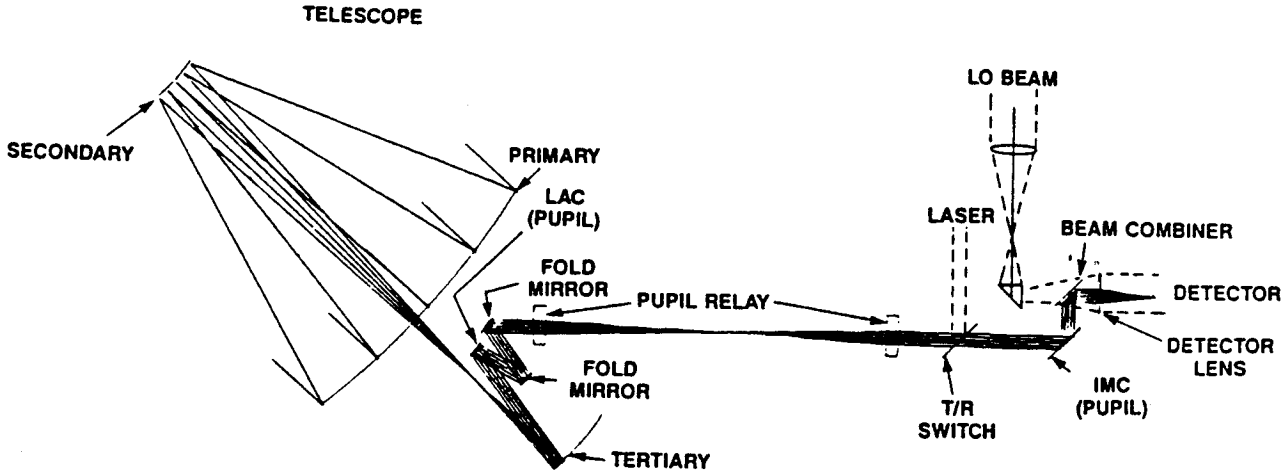

Figure 4-42. WINDSAT Optical Design

LAWS ERROR BUDGET FOR POINTING - 9.1 μm CONCEPT

SINGLE DETECTOR

SYSTEM FOCAL RATIO = 4.36
SYSTEM MAGNIFICATION = 33

BUDGET = 3.0 μRad. (object space)

BORESIGHT ERROR=	2.93	μRadian, RSS

ALL UNITS are μradians or μmeters

OPTICS	2.11
PRIMARY	1.65
Tilt (μRad.)	0.58
Decenter (μm)	2.42
SECONDARY	0.73
Tilt (μRad.)	1.65
Decenter (μm)	1.27
TERTIARY	0.46
Tilt (μRad.)	3.75
Decenter (μm)	4.52
TEL. RIGID BODY	0.95
RELAY OPTICS	0.2
FOCAL PLANE	0.18
Decenter(μ)	1.2

MECHANISMS	2.04	
SCAN MECH.	0.25	
LAG ANGLE COMP	1.36	
		22.5
IMC (rel to inertial space)	1.36	22.5
T/R SWITCH	0.61	
		10

Figure 4-43. 9.1 μm Boresight Error Budget

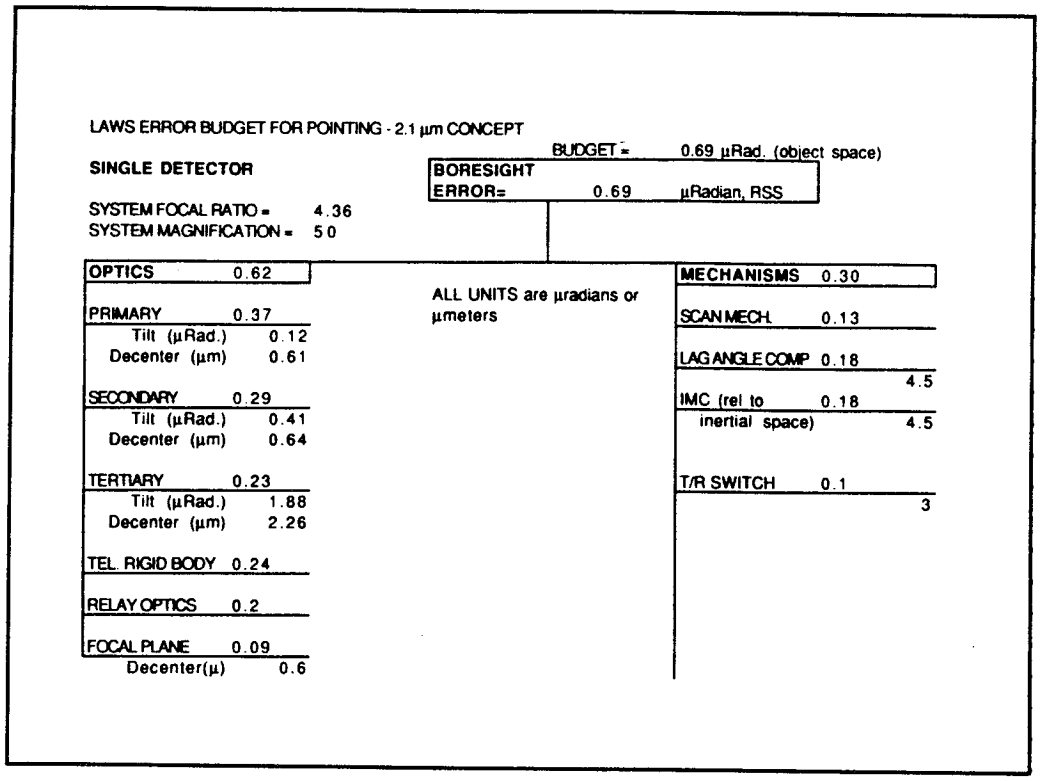

Figure 4-44. 2.1 µm Boresight Error Budget

Mirror Tilt and Decenter Tolerances (based on shot transit time)	**Concept Wavelength** 9.1 µm	2.1 µm	**State of the art**
Primary Mirror Tilt	**0.58µrad**	**0.12µrad**	Exceeded for 2.1µm
Primary Mirror Decenter	**2.42µm**	**0.61µm**	Within
Secondary Mirror Tilt	**1.65µrad**	**0.41µrad**	Within
Secondary Mirror Decenter	**1.27µm**	**0.64µm**	SOA=2µm long term
Tertiary Mirror Tilt	**3.75µrad**	**1.88µrad**	Within
Tertiary Mirror Decenter	**4.52mm**	**2.26µm**	Within
Mechanisms (TiltTolerances)			
Scan Mechanism	**0.25µrad**	**0.13µrad**	Exceeded for 2.1µm
T/R Switch	**10µrad**	**3µrad**	Within
Image Motion Compensation	**16µrad**	**3.2µrad**	Within
• **Magnification = 30 x @ 9.1µm, 50x @ 2.1 µm**		• **Based on single detector**	

Figure 4-45. Tolerances and Comparisons to SOA for 2.1 µm and 9.1 µm Concepts

design control of the stiffness and compliances of the telescope structure and mount will alleviate the bearing-induced boresight errors.

On the other hand, the 2 μm wavelength system would probably require active control devices or developmental scan bearings for a concept with a single detector matched to the diffraction spot size at f/4.4 (i.e. detector 1/4.5 as large as the 9.1μm detector). Several of the tolerances would be relaxed if the effective focal length of the optical system could be increased, say to f/20. An f/20 design (efl = 30 m) would require a detector the same size as the 9.1 μm detector, but capable of the increased bandwidth needed for operation at 2.1 μm.

4.3.4.2 *Wavefront Error Budget*

In a similar manner, we have constructed a spreadsheet that computes the RSS errors in the image-forming wavefront that result from a variety of design, fabrication and alignment errors. The spreadsheet is based on an optical sensitivity table, and the component tolerances and their effects are displayed on the error trees shown in Figure 4-46 and -47.

We used a diffraction-limited performance requirement (defined as an rms wavefront error of λ/13 at the operational wavelength) as the top of the error tree. The tolerances are shown in units of common shop tolerances (figure errors measured at 6328Å and alignment tolerances in μmeters or degrees). Again, tolerances were selected with regard to current shop practice.

For the 9.1 μm concept, almost none of the figure or alignment tolerances press the state of the art. The primary mirror figure requirement is only λ/15 and larger mirrors have been fabricated with tolerances four times more stringent.

Note that the "design residual" is one of the larger error contributors. The design residual is the aberration inherent in the design at the nominal lag angle, and consists mainly of coma. The system design could be improved to reduce the coma, but hardly seems worth while in view of the mild tolerances that meet the diffraction limit at 9.1 μm.

Maintenance of alignment as required for image quality will be proportionately more difficult in the 2.1 μm wavelength concept. The effect of reducing the operational wavelength to 2.1 μm is to increase the sensitivity of all of the tolerances by ~4.5x, including the design residual. The first conclusion reached is that the optical design must be improved commensurately, since the design residual alone contributes more than λ/5 to the error budget. Clearly, the WINDSAT optical design cannot be applied directly to the 2.1μm concept.

There are certainly optical designs that perform very well at wavelengths much shorter than 2.1 μm, and we believe there are designs that will satisfy all of the LAWS requirements for a 2.1 μm concept. However, these designs may tend to limit the trade space for configuring the system. In addition, requirements on the quality of the optics and alignment tolerances would be closer to the state of the optics art and a more expensive optical system would be required.

Some of the possible optical subsystem options for a 2.1 μm are listed in Figure 4-48.

4.3.4.3 *System Weight Considerations*

A further issue where wavelength plays an important role is in overall optical subsystem weight. A weight allocation was made for the optical subsystem, based on a LAWS weight allocation of 800 Kg. In the preliminary weight budget 250 Kg was allocated for the Optical Subsystem (this allocation later changed as part of the Configuration trades) with 85 Kg as our tentative allocation for the primary mirror assembly. Meeting this weight allocation is close to the state of the art for diffraction-

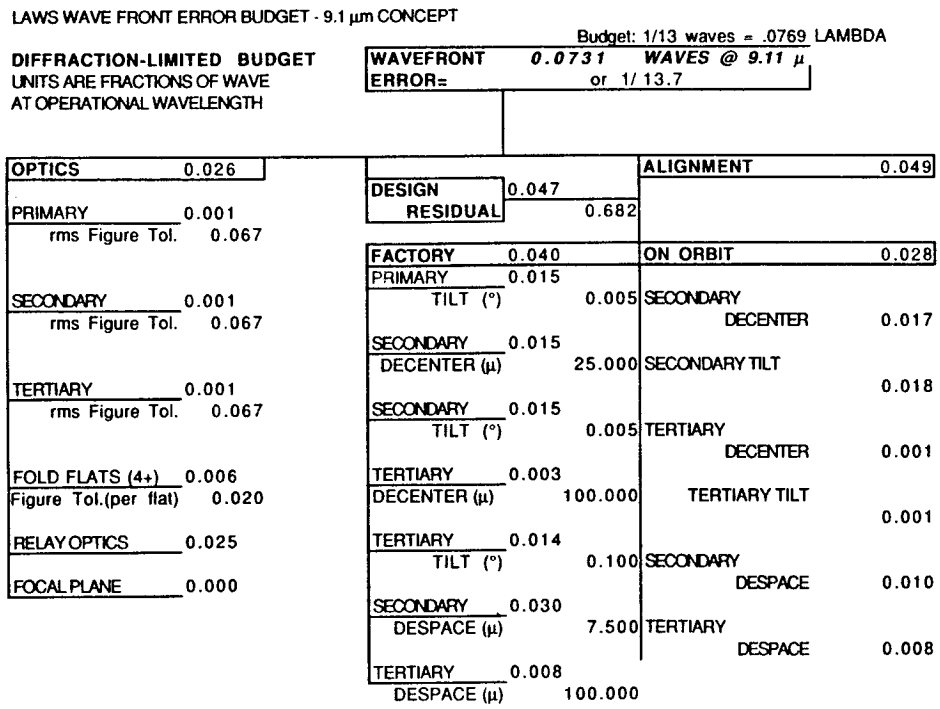

Figure 4-46. 9.1 μm Wavefront Error Budget

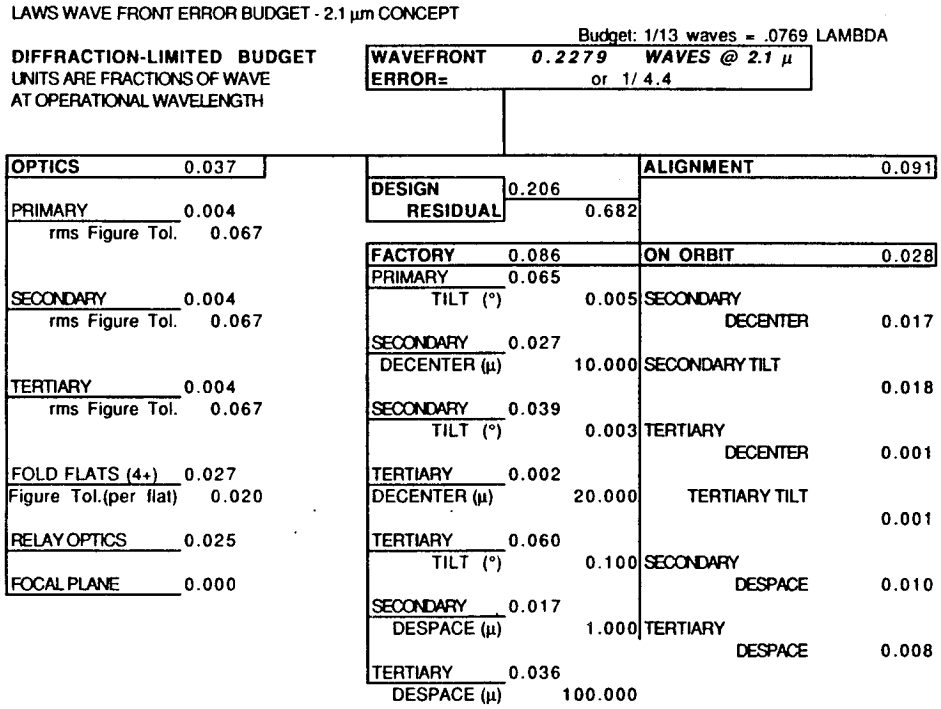

Figure 4-47. 2.1 μm Wavefront Error Budget

limited frit-bonded glass and beryllium mirrors at 9.1 μm, but would require development for a 2 μm concept. Weight is a severe cost and technology driver, as shown by the earlier RCA/Perkin-Elmer Windsat, 1983 study.

4.3.2.4 *Optical Subsystem Concept Summary*

Keeping in mind the necessity of minimizing the risk and cost of LAWS, we recommend the 9.1 μm CO_2 laser concept, since the optical system would be entirely within the optical state of the art.

4.3.3 *Receiver Subsystems at 2.1 μm and 9.1 μm*

Coherent receiver technology can be developed for either 9.1 μm or 2.1 μm to satisfactorily meet the requirements of the LAWS system. Heterodyne detectors have been produced in the past at (or near) 9.1 μm using HgCdTe. No such experience base exists for InGaAs detectors although they are touted as an emerging technology with great promise. The most important figures of merit regarding receiver performance for LAWS are quantum efficiency and bandwidth. A goal of 35% quantum efficiency is set for a receiver at 9.1 μm. This is seen as an attainable enhancement of the state of the art based on experimental data. A goal for the 2.1 μm receiver is not stated as there is no data on heterodyne detectors at this wavelength. A quantum efficiency of 20% is considered the minimum that either system design can tolerate. Greater values of quantum efficiency will place less demand on other system parameters. Large Doppler frequencies due to the relative motion of the spacecraft and the atmosphere place wide bandwidth requirements on the receiver. Lower detector bandwidths and corresponding higher quantum efficiencies can be realized if a tunable local oscillator is used. This is a system level trade that was addressed later in the study.

The most promising detectors for 9.1 μm and 2.1 μm are HgCdTe and InGaAs, respectively. HgCdTe detectors have been tested in heterodyne receivers with the characteristics shown in Figure 4-49. Laboratory measurements indicate that HgCdTe detectors have the potential of up to 120 K operation. Approximately 1 mW local oscillator power is necessary to overcome Johnson Noise in the detector and preamplifier. InGaAs detectors (also see Figure 4-49) have only recently been fabricated for 2.1 μm applications. This technology seems promising and prototype devices are becoming commercially available; however, InGaAs detectors have not yet been used in a heterodyne receiver. These devices do not require cryogenic cooling but the requirement of higher Doppler frequencies at 2.1μm dictates a higher bandwidth preamplifier. Higher bandwidth preamplifiers for the 2.1 μm system exhibit greater noise figures than those for 9.1 μm thus necessitating more LO power (≈20 mW) to operate in the shot-noise-limited regime.

Preamplifiers for the 9.1 μm and 2.1 μm receivers are selected based on the system requirements. The data quoted in Figure 4-50 for the 9.1 μm receiver are specifications given for a commercially available amplifier. The 2.1 μm receiver design requires a specialized high bandwidth amplifier. The data quoted in Figure 4-50 for the 2.1 μm receiver preamplifier is taken from a HEMT device model made at GE's E-lab. This model does not predict performance of the HEMT amplifier when cooled but reduction of noise figure is expected.

A generic schematic of the receiver electronics is shown in Figure 4-51. The RF mixing frequencies introduced will be a function of the optical wavelength chosen, as will the numerical values of the component specifications. A higher IF will be required for a receiver at 2.1 μm because of the larger Doppler frequencies involved. The higher bandwidth requirements make impedance matching difficult in the receiver electronics. Faster A/Ds will also be required. Although the functional block diagram remains the same for the 2.1 μm system, the receiver is more difficult to build because of the extremely wide Doppler IF frequencies encountered.

WINDSAT design will not meet optical quality requirements @ 2.1 μm

- Alternative designs exist
  - Ring field systems
  - Coma compensation telescope
  - Offner three-mirror telescope
  - and maybe others
- Each has limitations that may restrict trade space, e.g.
  - Lag angle (& scan rate) restricted to two values
  - Lag angle compensation by tilting secondary mirror
  - Limited lag angle compensation (& scan rate)

Figure 4-48. Alternative Designs for a 2.1 μm Optical System

Parameter	HgCdTe	InGaAs
Wavelength	9.1 μm	2.1 μm
Bandwidth	>2 GHZ	7 GHz*
DC Quantum Efficiency	85%	80%
Effective Heterodyne Quantum Efficiency	35%	> 20% not measured
Operating Temperature	77-87 K (120 K potential)	200-300 K
LO Power Required	~1 mW	~20 mW (amp. dependent)

** Ramon Martinelli, David Sarnoff Labs. Private Communication, 1989*

Figure 4-49. Comparison of Receivers at 2.1 μm and 9.1 μm

9.1 μm	
Type	GaAs FET*
Gain	35 dB
Noise Figure	< 1 dB
Band	40 MHz-1.8 GHz
1 dB Comp.	10 dBm
Gain Flat	+/- 1 dB
Operating Temp.	100 K
$VSWR_{input}$	2:1
$VSWR_{output}$	2:1
Impedance	50 Ω
Built in bias tee	

* Operating at GE

2.1 μm	
Type	HEMT*
Gain	30 dB
Noise Figure	< 7 dB
Band	200 MHz-7 GHz
Operating Temp.	300 K
Impedance	200 Ω

* Design based on GE State of the art Technology

Figure 4-50. Preamplifiers for 2.1 μm and 9.1 μm Concepts

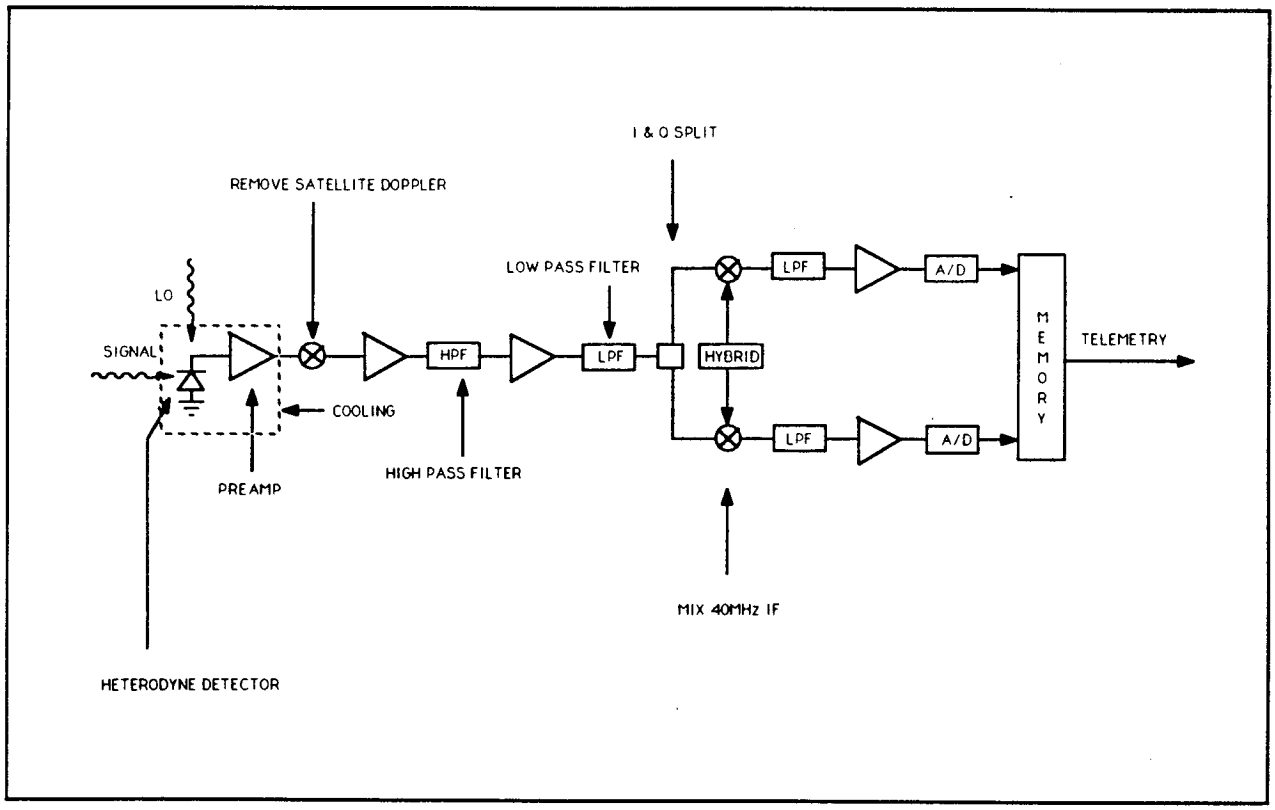

Figure 4-51. Receiver Electronics-Generic Block Diagram

In conclusion, receiver technology for either 9.1 μm or 2.1 μm can be developed to meet the requirements of the LAWS system. There is greater confidence in the 9.1 μm detector technology at this time, however. The existing amplifier technology for the receiver design at 9.1 μm is also preferable to the still to be developed amplifier technology for the 2.1 μm system. Although InGaAs detectors will require less cooling than HgCdTe, substantial development may have to take place before a useful receiver can be made.

4.4 Concept Selection

The concept for LAWS was selected using the information generated by trades and analysis at the major subsystem level and documented in the previous three sections.

The scores for the 2.1 μm and 9.1 μm concepts are shown in Figure 4-52.. There we see that both concepts have been given the score of 1 in the "eye safety" category. Further analysis, however, has shown that, as the ANSI Standards are currently formulated, the 2.1 μm concept may not be eyesafe for observers using binoculars and telescopes. This is illustrated in Figure 4-53 where we have plotted the minimum divergence required of a space-based laser in order that the ANSI maximum permitted exposure (MPE) not be exceeded for observers using both the unaided eye (an assumed 7-mm aperture at night) and sight aids. We see that both the 2.1 μm and 9.1 μm concept are safe for the unaided eye at both the orbits plotted. The 2.1 μm concept is borderline for binocular aided viewing from 800 km and exceeds the MPE for larger apertures. The 2.1 μm concept is unsafe for all apertures (other than the unaided eye) from 500 km. Note that although 9.1 μm is borderline for a 250-mm aperture (ten inch telescope) from 500 km, most telescope eyepieces will not transmit 9.1 μm radiation (they will transmit 2.1 μm). Thus, it would seem that we would be justified in rejecting the 2.1 μm concept on eye safety grounds alone. We must remember, however, that the ANSI standards are very conservative and, in general, are not the result of experimental measurements. If measurements were to be made at 2.1 μm the MPE for this wavelength might be expected to increase, in a similar fashion to the situation at 1.54 μm which has a much higher MPE than nearby wavelengths, due to a measurement program at 1.54 μm. With this caveat in mind we now proceed to the rest of the scores.

In the area of overall technical risk the 2.1 μm concept scores lower than the 9.1 μm concept for all the subsystems. The scores in the risk category are arrived at by multiplying together scores for criticality, technology maturity and development risk, which are then adjusted to fall in the range 1-5. The scores for the two concepts in these three categories are shown in Figure 4-54. The scores in the criticality column reflect the likelihood of being able to include redundancy in the design, such that failure of a component would not mean loss of the mission.

The telescope, for example, is a single point failure and any failure in the scan bearing or lag angle compensator, would mean loss of the mission. The optical subsystem scores 1 in this category for both concepts.

The receiver, however, is small and could easily be made 100% redundant, hence the score of 3 for both concepts.

Both laser concepts also receive the same score, 2, indicating that any failure will have a significant impact on the mission. Originally, in the proposal, where we chose the 2.1 μm and 9.1 μm concepts to illustrate our methodology for concept selection, we had scored the Tm:Ho:YAG concept higher than the CO_2. This was based on the belief that the solid state laser would be modular and small, and that redundancy could be easily built in. Having performed a point design for the 2.1 μm concept, however, we find that it is more complex than we thought, requiring six amplifiers and almost 70 Joules of diode array energy. This is not a trivial amount of energy to extract from diodes and would require a substantial thermal management system to dissipate the

SUBSYSTEMS/COMPONENTS	SELECTION CRITERIA												
	PERFORMANCE	TECHNOLOGY	DESIGN SIMPLICITY	RELIABILITY	ACCOMMODATIONS	SERVICEABILITY	SYSTEM OPERATIONS	VERIFICATION	RISK	SURVIVABILITY	COST	SAFETY	TOTAL SCORE
WEIGHTING FACTOR	4	4	3	3	3	2	2	3	5	2	4	N/A	
2.1 μm CONCEPT													
LASER SUBSYSTEM	2/8	2/8	2/6	2/6	4/12	3/6	4/8	2/6	1/5	2/4	2/8	1	77
OPTICAL SUBSYSTEM	2/8	3/12	3/9	3/12	4/12	1/2	4/8	3/9	1/5	5/10	2/8	1	95
RECEIVER SUBSYSTEM	4/16	3/12	4/12	3/9	5/15	5/10	5/10	3/9	2/10	3/6	3/12	1	121
9.1 μm CONCEPT													
LASER SUBSYSTEM	4/16	5/20	4/12	3/9	4/12	3/6	4/8	3/9	3/15	4/8	3/12	1	127
OPTICAL SUBSYSTEM	4/16	4/16	4/12	4/12	4/12	1/2	4/8	3/9	2/10	5/10	3/12	1	119
RECEIVER SUBSYSTEM	5/20	5/20	5/15	4/12	5/15	5/10	5/10	4/12	4/20	3/6	4/16	1	156

Figure 4-52. Evaluation and Selection Criteria Plan Scores for Both Concepts

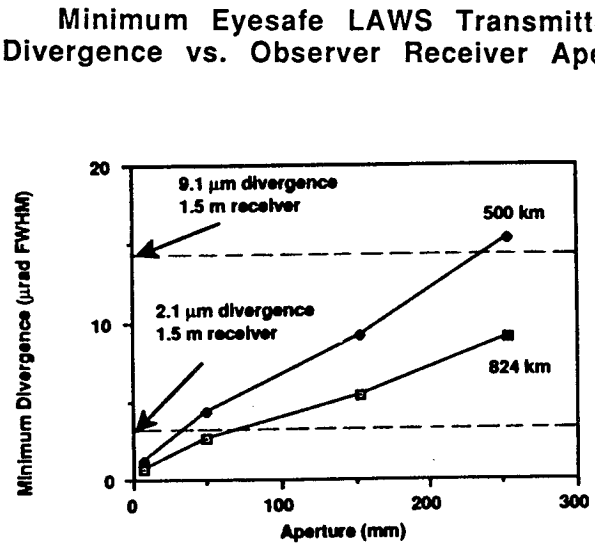

Figure 4-53. Eye Safety Considerations

	Criticality	Technology Maturity	Development Risk	Total
2 μm				
Laser	2	2	2	8
Optics	1	3	2	6
Receiver	3	3	2	18
9.1 μm				
Laser	2	4	3	24
Optics	1	4	3	12
Receiver	3	4	3	36

Figure 4-54. Risk Assessment Scores for Both Concepts

400 W of waste heat produced, and keep the pump wavelengths stable. The size of such a laser is not likely to be any smaller than the CO_2 laser when all the peripheral systems are taken into account. We therefore feel justified in giving both lasers the same score in the criticality column.

The scores for both concepts in the technology maturity and development risk columns are self explanatory and emphasize the much more advanced stage of development of the CO_2 laser concept.

The scoring reflects both the state of development of lasers, optical subsystems and receivers for operation at 2.1 μm, as well as issues associated with the shorter wavelength. These include: the difficulty and cost of fabricating large diffraction limited optical telescopes, the increased pointing requirements because of the 4.5x smaller FOV, the 4.5x larger Doppler bandwidth (~8 GHz), the 4.5x larger measurement bandwidth (~200 MHz) which leads to a large increase in the data rate for the shorter wavelength concept, and the issue of turbulence discussed earlier. The overall scores show that the 9.1 μm concept is the clear choice for LAWS at the present time.

We therefore selected a 9.1 μm $^{12}C^{18}O_2$ laser with a HgCdTe heterodyne receiver as the concept for the LAWS instrument.

5.0 CONFIGURATION IDENTIFICATION, ANALYSIS AND SELECTION

In the previous section we have evaluated the alternate concepts proposed for LAWS and selected one for configuration development. The concept selected is based on the use of a 9.1 μm CO_2 lidar operating in the heterodyne mode with a HgCdTe detector in the focal plane of a large, conically scanning telescope. This section considers alternate configurations for the selected concept, with the selection being detailed in section 5.3. Section 5.4 then takes the selected configuration and shows accommodation concepts for both the polar orbiting platform and the Space Station. Section 6.0 gives a summary of the anticipated performance of the selected baseline instrument configuration.

The approach for configuration selection is slightly different to that used for the concept selection. A set of requirements is still generated at the system level and handed down to the subsystems, but more of the trades and issues are resolved at the subsystem level and firm recommendations made as to preferred configurations within each subsystem. Any outstanding subsystem trades, such as between alternate optical configurations, are then made at the system level, and a final instrument configuration chosen. Accordingly, section 5.1 discusses the methodology used to select the system and subsystem requirements, and section 5.2 the alternate subsystem configurations.

5.1 System Requirements Definition

The LAWS mission requirements initially discussed in section 3.1 are given below:

- Global scale wind measurements commensurate with coverage available from the designated space platform.
- Horizontal resolution of 100 km x 100 km.
- Vertical resolution of 1 km throughout the troposphere.
- Horizontal wind vector accuracy of ± 1 m/s in the lower troposphere and ± 5 m/s in the upper troposphere.
- Operational lifetime of 10^9 shots.
- Continuous operations.
- Serviceability.

In order to choose between candidate concepts which would seem to be capable of meeting the above mission requirements we used the following strawman instrument requirements:

- Laser energy 10 Joules
- Telescope aperture 1.5 m
- Laser pulse length 3 μsec (9.1 μm)
- Nadir angle 45°
- Laser repetition rate 10 Hz
- Telescope scan rate 6 rpm

It is the purpose of this section to reevaluate the strawman requirements, now the concept selection has been made, and to come up with a definitive set of requirements from which to proceed with subsystem configuration definition.

5.1.1 *Baseline Specification Definition*

The above six LAWS parameters impact the instrument performance and accommodation as shown in Figure 5-1. Four of the six parameters, energy, aperture,

pulse length and nadir angle, affect the accuracy of the LOS velocity; while three, nadir angle, laser repetition rate and scan rate, affect the fidelity of the horizontal inversion. The laser energy and repetition rate determine the overall power requirements for the system, while the weight of the system is largely determined by the laser energy and the telescope aperture. The envelope required by the instrument is principally determined by the telescope aperture.

Choosing the requirements for an instrument such as LAWS will always be a trade-off between desired performance and ease of accommodation, with power and weight being of foremost concern. When considering the range of possible values for the LAWS instrument parameters, and how that range is bounded by the need to be accommodated on the spacecraft, we have used as an underlying philosophy the fact that power can be duty cycled (i.e. reduced by turning off the instrument or reducing the laser repetition rate), whereas weight cannot.

Given that philosophy we now turn to a discussion of possible values for the six LAWS parameters. Since the nadir angle affects both LOS accuracy and horizontal inversion it has to be chosen first.

Parameter	Performance	Accommodation
Energy	LOS Velocity Accuracy	Power, Weight
Aperture	LOS Velocity Accuracy	Weight, Envelope
Pulse Length	LOS Velocity Accuracy	
Nadir Angle	LOS Velocity Accuracy Horizontal Inversion	Weight (if Variable)
Repetition Rate	Horizontal Inversion	Power
Scan Rate	Horizontal Inversion	

Figure 5-1. LAWS Parametric Trade Drivers

5.1.1.1 *Nadir Angle Considerations*

The first choice to be made regarding the nadir angle is whether it should be fixed or variable. A variable angle would allow an extra degree of freedom in placing shots in the atmosphere. It would also allow the LOS SNR to be chosen depending on atmospheric conditions, e.g. if at some future time the atmospheric backscatter coefficient were to increase, say due to volcanic activity, the nadir angle could be increased to enhance global coverage. A danger in selecting a variable angle is, however, that it may preclude certain optical subsystem configurations and also add cost and complexity to the optical subsystem. We have therefore selected a fixed nadir angle as a baseline choice. We next need to decide on a value for that fixed nadir angle.

The nadir angle affects both the global coverage and the LOS SNR (see Figure 3.5). Larger nadir angles cover more of the globe (at ~57° the ground tracks just touch for a 824 km orbit) but reduce the LOS SNR since a larger path length of atmosphere has to be traversed by the beam. Clearly, the exact value for the nadir angle will ultimately depend on the choice of platform altitude and is not seen as a system driver for configuration selection purposes. We therefore see no reason to depart from the strawman value of 45°.

5.1.1.2 *Energy and Aperture Considerations*

The laser pulse energy and the telescope aperture are the most important of the six parameters in determining the performance of the system as well as the accommodation requirements. They are considered together because, via the energy-aperture product (EAP), they determine the performance of the system.

Figure 5-2 shows various combinations of the laser energy and telescope aperture and their performance relative to the strawman 10 J, 1.5 m system. Also shown are relative values for the weight, power and cost.

The weights for the various combinations of energy and aperture were arrived at from a knowledge of the parametric relationship between laser energy and laser subsystem weight, and telescope aperture and optical subsystem weight. The receiver and support subsystems were estimated at 125 kg and, further, we assumed that the structure to support the instrument and interface it with the spacecraft was 20% of the instrument weight.

The power requirements are driven by the laser. As will be discussed later we anticipate a laser efficiency of 6% with a goal of 7.5%. For the purposes of EAP intercomparison we assumed that the strawman 10J, laser required 2kW. This is equivalent to a repetition rate of 15 Hz at 7.5% efficiency or 12Hz at 6%, for example. Power requirements for the other energies in the table were simply scaled from the baseline. We assumed 1000 Watts for the balance of the instrument.

The relative cost was arrived at from cost parametric curves relating energy and aperture to cost (Figure 5-3), with the assumption that together the laser and optics represent 70% of the cost of the instrument.

The bar charts on the right side of Figure 5-2 show the instrument performance quantified as single-pulse, LOS SNR in three bins: SNR>-10 dB, SNR>-5 dB and SNR>0 dB. The two charts represent two different atmospheric models (provided by NASA), one with clouds and one without, which are discussed, together with details of the system model used, in section 6.0. Section 6.0, shows that in order to meet the velocity requirement of 5 m/s, in the cleanest parts of the atmosphere, a LOS SNR close to -5 dB is needed. As shown in the bar charts the strawman 10 J, 1.5 m system is the smallest (i.e. lowest value of EAP) system to give full coverage to 15 km, approach the desired minimum SNR of -5 dB and be capable of meeting the weight and power budget. We therefore selected 10 J, 1.5 m as the laser energy and telescope aperture respectively, from which to proceed to configuration definition.

5.1.1.3 *Pulse Length Considerations*

The laser pulse length affects the LOS velocity accuracy, via the spectral width of the return signal (see Figure 5-4). The broader the width of the return signal the more difficult it becomes to estimate the centroid of the distribution and hence the velocity. The width is a function of three terms: the Fourier transform of the transmitted pulse, the chirp of the transmitted pulse and an atmospheric term associated with the turbulence and shear along the LOS.

It would seem that a long pulse would be more desirable than a short pulse since a long pulse has a narrower spectral width. The maximum length we can use, however, is constrained to ~6.7 μsec/cos(nadir angle) by the desired vertical resolution of 1 km. Shorter pulses, although spectrally broader, do, however, have certain advantages. They allow for multiple estimates of the velocity within the desired vertical resolution. They chirp less than long pulses, and the atmospheric contribution may be less, so clearly a detailed trade must be made. The trade must take into account how the laser efficiency and weight scales with pulse length as well as performance considerations. Such a trade was conducted using NOAA profiler data to provide statistics for wind shear as a function of pulse length, and Spectra Technology laser codes to quantify laser performance as a

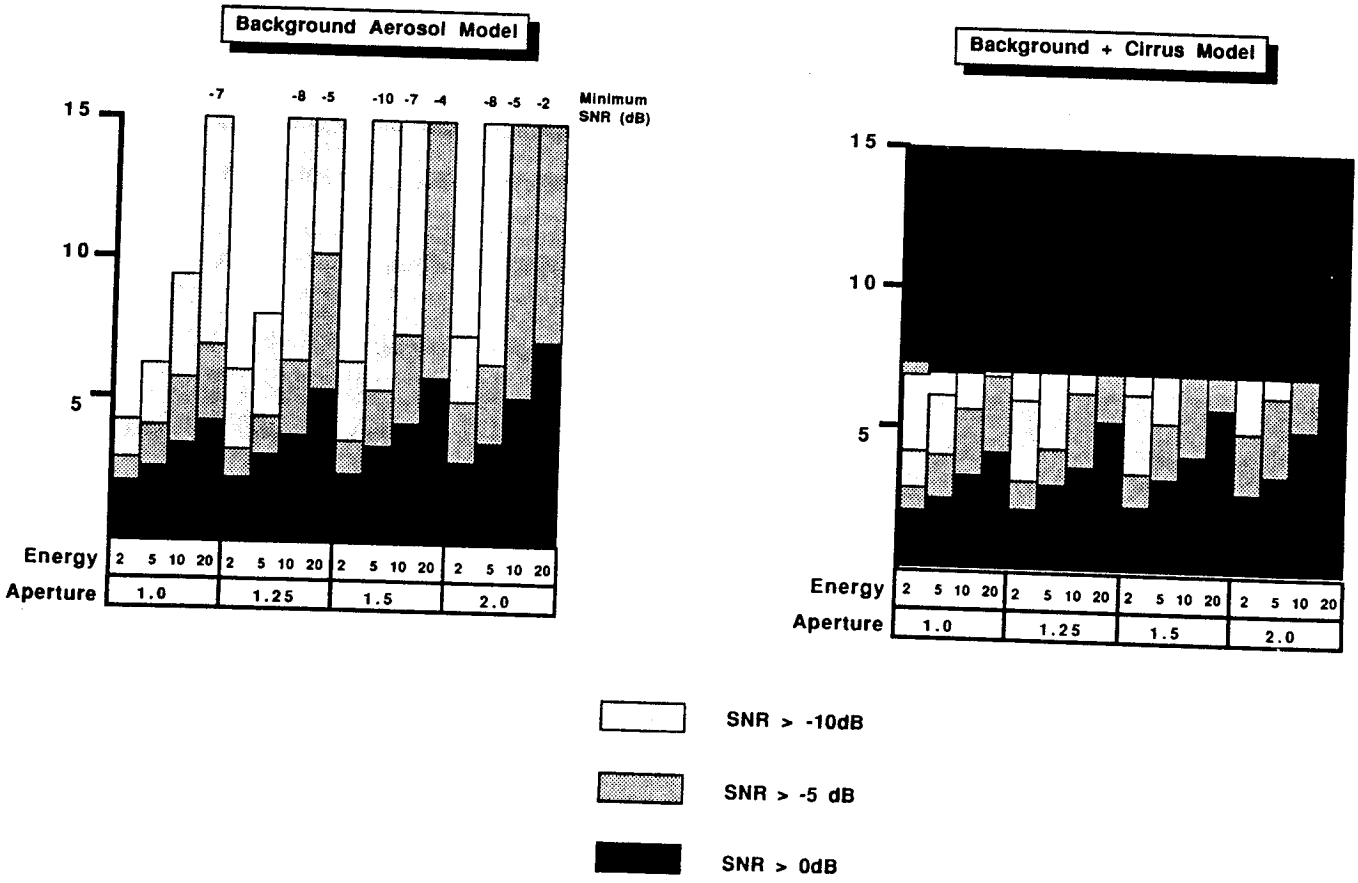

Energy (J)	Aperture (m)	EAP(J-m2)	Relative to Baseline 10 J, 1.5 m Weight	Power	Cost
2	1.00	1.57	0.52	0.47	0.74
5	1.00	3.93	0.57	0.67	0.75
10	1.00	7.85	0.65	1.00	0.76
20	1.00	15.71	0.88	1.67	0.79
2	1.25	2.45	0.70	0.47	0.86
5	1.25	6.14	0.74	0.67	0.87
10	1.25	12.27	0.83	1.00	0.88
20	1.25	24.54	1.05	1.67	0.91
2	1.50	3.53	0.87	0.47	0.98
5	1.50	8.84	0.92	0.67	0.99
10	1.50	17.67	1.00	1.00	1.00
20	1.50	35.34	1.22	1.67	1.03
2	2.00	6.28	1.40	0.47	1.26
5	2.00	15.71	1.45	0.67	1.27
10	2.00	31.42	1.53	1.00	1.28
20	2.00	62.83	1.75	1.67	1.31

Figure 5-2. Comparison of Various Energy-Aperture Products Including Weight, Power and Cost

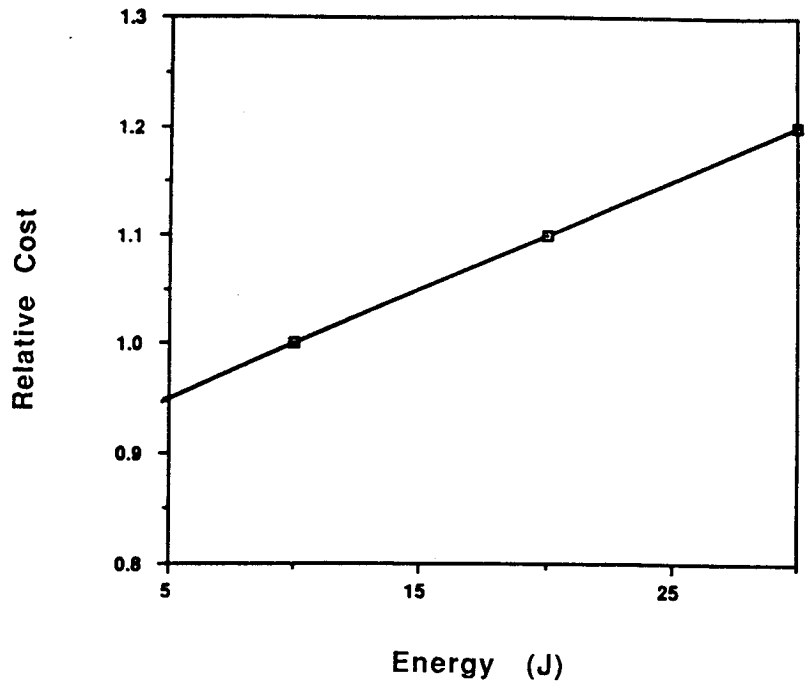

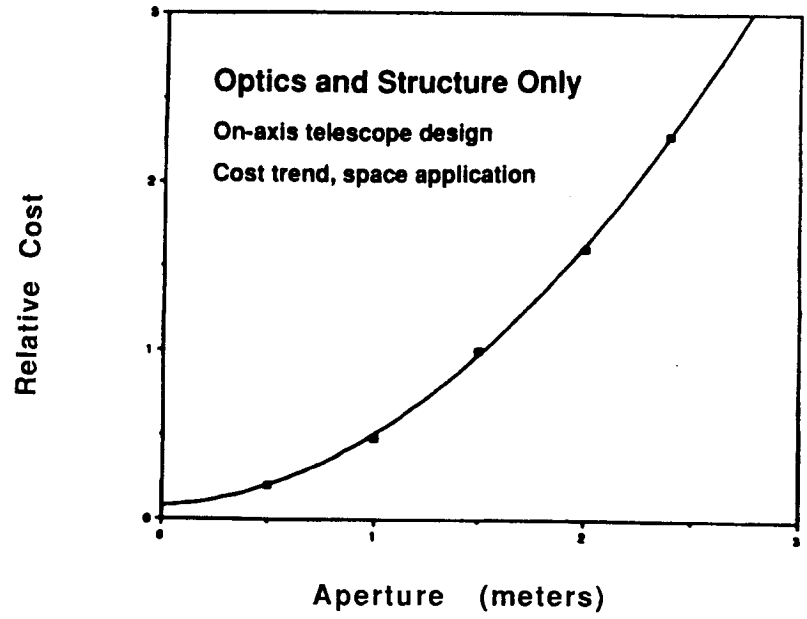

Figure 5-3. Cost Parametric Trades

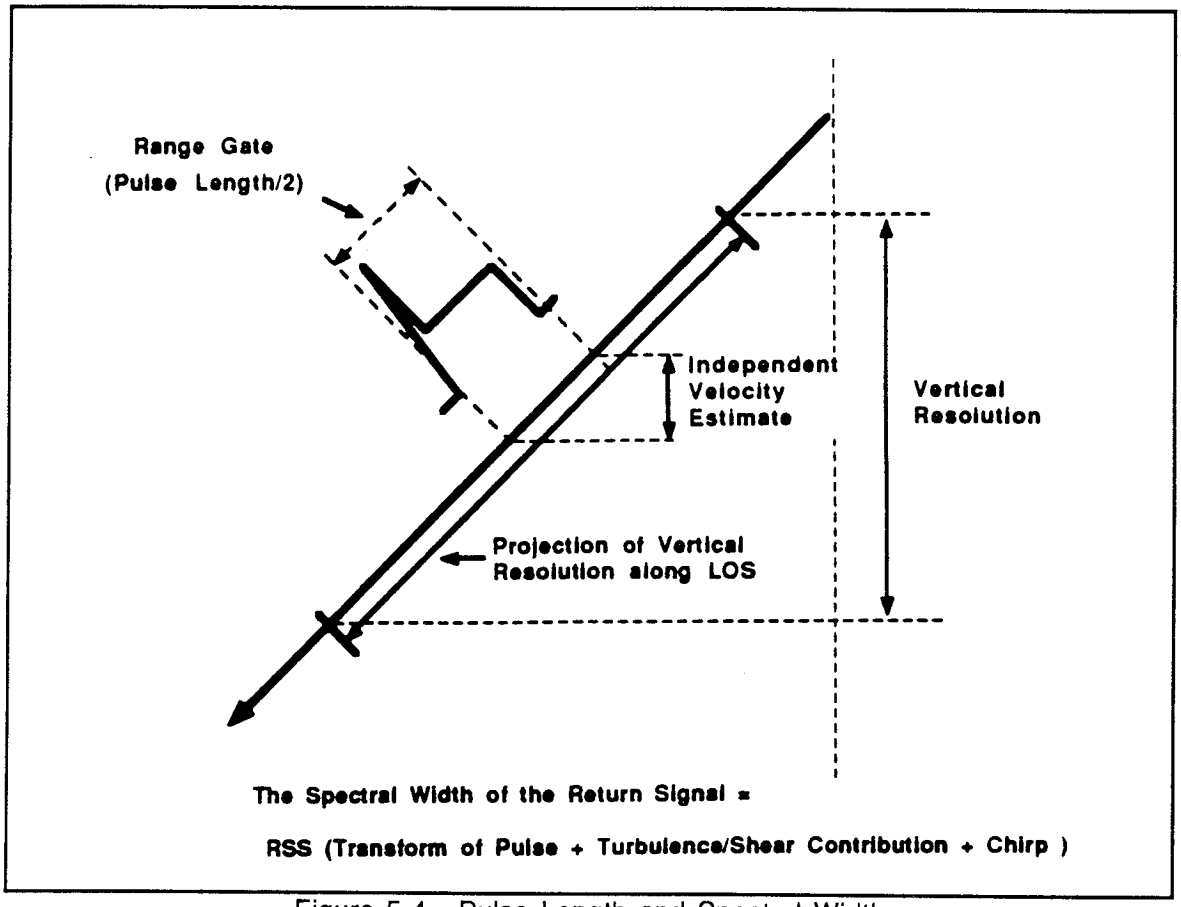

Figure 5-4. Pulse Length and Spectral Width

function of pulse length (see laser section 5.2.1). All indications point to 3 μsec being near optimum, and 3 μsec was selected as baseline for configuration design. The laser pulse length will be investigated further in Phase II.

5.1.1.4 *Repetition Rate Considerations*

The laser repetition rate influences the horizontal wind velocity accuracy via the number of shots used with the horizontal inversion algorithm. With a fixed laser repetition rate the number of shots which occur in any particular grid square is a function of the position of the grid square relative to the scan. Figure 5-5 shows the shot pattern resulting from a constant repetition rate of 20 Hz and illustrates the crowding together of shots which results perpendicular to the ground track. Shots which land in the farthest grid square have a limited range of look angles and do not produce the best horizontal inversion accuracy. There is therefore a case for reducing the number of shots which occur out towards the limb of the scan, either redistributing them in areas of the scan where they can be of most value, or simply saving power and shots by inhibiting laser operation. At minimum, therefore we would like a laser whose operation can be inhibited on command.

A truly asynchronous repetition rate is, however, much more desirable. Figure 5-6 shows the shot pattern resulting from a 20 Hz asynchronous laser (i.e. a laser fireable on command, but with a 20 Hz maximum rate) fired according to a simple 1/cosine algorithm. By this simple algorithm we have placed about the same number of shots in each grid square and reduced the total number of shots in one scan by about

30%. The inversion accuracy does not suffer, but power and laser shots are conserved. Furthermore, if we examine the variation in the Doppler shift as a function of azimuth angle we see that during certain parts of the scan the return signal will fall below the lower end cut-off of the preamplifier (assumed as 100 MHz) (Figure 5-7). If we inhibit firing at those angles we also save shots and power. Together a 1/cosine algorithm and inhibiting firing at scan angles where the Doppler is undetectable saves about 35% of the shots (and power). A 20 Hz asynchronous laser therefore offers the capability of a 20 Hz burst mode, an approximately 13 Hz scan average rate and, assuming we turn off the laser during selected parts of some orbits (say over the Poles), a 10 Hz mission average rate. We therefore selected as baseline a 20 Hz laser with the capability of firing on command.

5.1.1.5 *Scan Rate Considerations*

The first question with regard to telescope scan rate is whether it should be fixed or variable (either in a stepwise fashion or continuously). A variable rate would be useful since, like a variable repetition rate laser, it offers some flexibility in placing laser shots in the atmosphere. It also could be used to cancel out the spacecraft motion to place a large number of shots in a geographically small area (this would require a very slow scan ~1000 sec per revolution). A variable rate requirement is likely, however, to preclude some optical configurations and therefore, we baselined a fixed rate.

The value that fixed rate should take is a function of the laser repetition rate and the desired spatial resolution. A 12 rpm rate with a 20 Hz maximum rate laser gives about 9-10 shots per 100 km x 100 km grid square (see Figure 5-6), and so as baseline we chose a fixed 12 rpm scan rate for the optical subsystem.

5.1.1.6 *Baseline Specification Summary*

In summary, the specification chosen as baseline from which to proceed to configuration definition was:

Energy per pulse	10 Joules
Pulse repetition rate	Asynchronous, 20 Hz max.
Pulse length	3 μsec
Telescope aperture	1.5 m
Nadir angle	45°
Telescope rotation rate	12 rpm

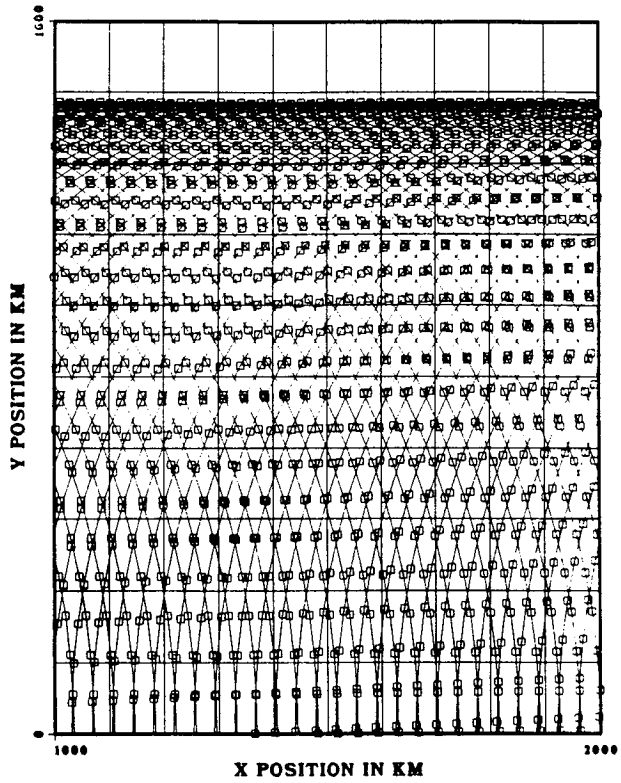

Figure 5-5. Constant 20 Hz Repetition Rate Shot Pattern

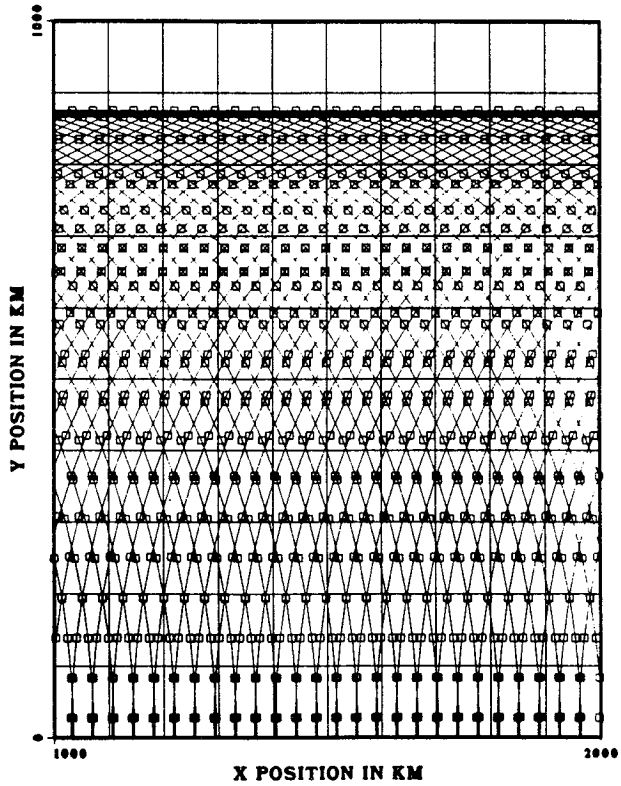

Figure 5-6. Shot Pattern for 20 Hz Asychronous Repetition Rate

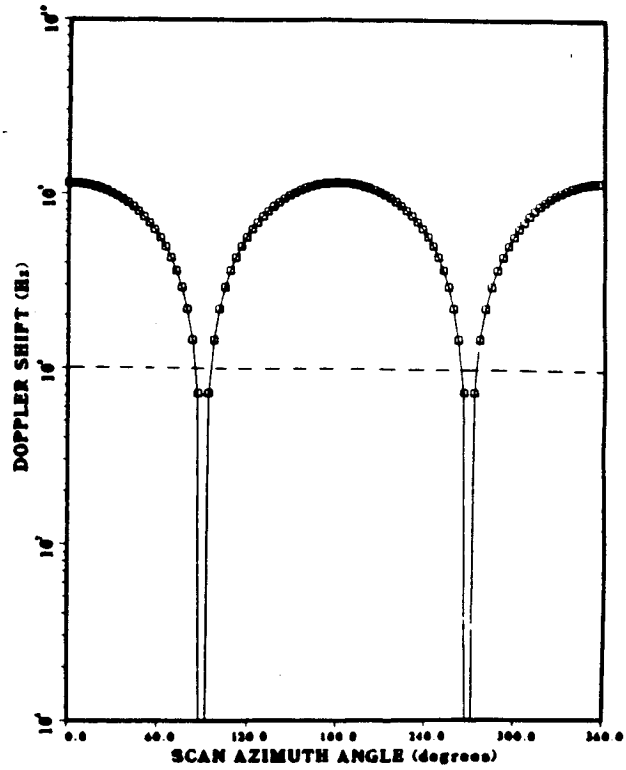

Figure 5-7. Spacecraft Induced Doppler Shift

5.1.2 *Accommodation Requirements and Constraints*

The values chosen for the six parameters given above have implicitly taken into account the constraints imposed on the instrument by the spacecraft. This section further develops the accommodation requirements and provides budgets to the subsystems where possible. The major accommodation requirements and constraints as currently understood are given in Figure 5-8.

The weight budget for the instrument is 800 kg. Of this 800 kg we have allocated 120 kg for the laser, 350 kg for the optical subsystem (with a goal of reducing this to nearer 300 kg), 40 kg for the receiver and 250 kg for the structure and support subsystems. Note that this is a revision of the preliminary allocation used for concept selection.

Weight	< 800 kg
Laser	< 120 kg
Optics	< 350 kg (goal 300 kg)
Receiver	< 40 kg
Structure, etc.	< 240 kg (goal 200 kg)
Power	< 3 kW
Laser	< 2 kW
Envelope	4.6 m Fairing Diameter (JPOP)
Pointing Knowledge	~ 100 μrad (1-sigma)
Thermal	~ 2kW to Platform Thermal System

Figure 5-8. Accommodation Requirements and Constraints

Power is to be less than 3 kW (average) with 2 kW (average) allocated for the laser. We assume that 2 kW is dumped to the platform thermal control system.

The instrument envelope is constrained by the need for the POP version of LAWS to fit within the Japanese H-II launch vehicle fairing.

The pointing knowledge of ~100 μrad is a 1-sigma requirement for removing the platform imposed Doppler shift.

A further constraint on the instrument subsystems which plays a major role in determining the performance of LAWS is the boresight error. The term boresight error is here used to quantify the ability of the optical system to view the volume of the earth's atmosphere illuminated by the laser pulse, and to return an Airy pattern centrally located on the signal detector. This is made difficult by the fact that the instrument is on a moving platform, the heterodyne FOV is small (~15 μrad) and the telescope is moving during the round trip time of the laser pulse. To decide how much misalignment the system can tolerate we need to understand the way the SNR degrades on the average as the return spot jitters around the optimum, aligned position.

Figure 5-9 is a plot of the average performance of the system for various 1-sigma values of boresight error. The detector is here assumed to be an optimum circular, single detector (i.e. ~70% of the Airy disk size) illuminated by a plane wave LO. We see that for a 1-sigma value of 3 μrad an average loss of 1.5 dB results. We have chosen this as a not-to-exceed baseline value for the boresight error, with the aim of reducing it later to closer to 1.5 μrad.

In order to meet this requirement for boresight error we have determined that a system will be required which can compensate for image motion in the focal plane. As shown in Figure 5-10, the motion is caused by a number of factors. Note in the Figure, WINDSAT refers to the WINDSAT optical design, confocal parabola to an optical design we have recently evaluated.

Image motion may be compensated for by a number of approaches (see Figure 5-11). With just a single detector in the focal plane we need a very high speed steering mirror to take out the motion. The mirror would be driven by a high bandwidth servo which would have inputs from as many sources of motion as could be identified. While the system would perform with the optimum mixing efficiency and cooling requirements would be low, we would be unable to use the signal detector to determine misalignment.

A large array detector, on the other hand, would allow the return spot to wander or jitter anywhere over its surface and use coherent combining of the IF from the individual pixels to recover the signal information. In many respects this is an ideal solution: no mechanisms are required and no knowledge of where the return spot is located is needed. However, cooling requirements are higher and there will inevitably be some signal loss in the dead streets between array elements.

Neither of these approaches are ideal and so we have chosen a hybrid approach, wherein we have a small circularly symmetric array and a two degree-of-freedom mirror. The mirror could potentially operate with a lower bandwidth servomechanism. The outside elements of the array offer an enhancement in the SNR and with the 1-sigma jitter value of 3 μrad improve the average loss figure from -1.5 dB to -1 dB. The circular array also allows the amplitude and phase of the returned signal to be measured and can therefore be used to sense misalignment in the position of the return image.

The hybrid approach was selected after carefully evaluating each concept for image motion compensation using the evaluation and selection criteria plan. The scores are shown in Figure 5-12.

5.1.2.1 *Functional Block Diagram*

To further define the instrument and to arrive at a set of subsystem requirements we have developed the functional block diagram shown in Figure 5-13.

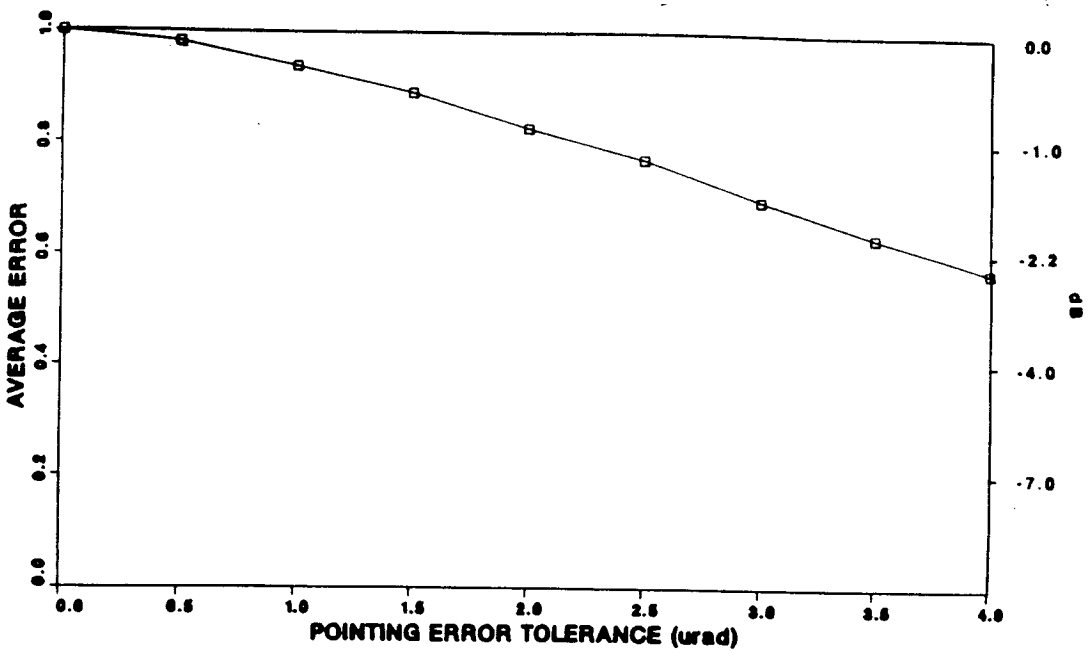

Figure 5-9. Average Signal Loss Versus Pointing Error Tolerance

To Meet the Boresight Error Budget We Need Image Motion Compensation

- After compensation for the lag angle by either a precision mechanism (WINDSAT design) or a fixed offset (confocal parabola design) there will still be residual motion of the image in the focal plane
- The motion is caused by some or all of the following:
  - Lag angle compensator residuals (WINDSAT) (fast)
  - Telescope rotation during data taking (confocal parabola) (slow)
  - The pitch of the spacecraft during the round trip time (slow)
  - Spacecraft altitude variations (e.g. 3% for a polar orbit (LANDSAT), 300-500 km for Space Station) (slow)
  - Bearing jitter (fast)
  - Laser shot-to-shot pointing stability (~25 μrad)
  - Platform jitter (TBD) (5.2 μrad/sec peak-peak for Eos-A)

Figure 5-10. Image Motion Compensation Considerations

Approach	Advantages	Disadvantages
Single detector/2 DOF fast steering mirror	Optimum mixing efficiency Low cooling requirements	High precision, high bandwidth. No end-to-end alignment sensing
Array detector, no precision IMC	No complex mechanisms	Some SNR loss in dead streets, high cooling requirements
Hybrid - single detector + surrounding elements, 2 DOF mirror	Optimum mixing efficiency, potential for simpler mechanism, SNR gain from surrounding elements. Ability to sense amplitude and phase for on-orbit alignment	Slightly higher cooling requirements

Figure 5-11. Image Motion Compensation Approaches

SUBSYSTEMS/COMPONENTS	SELECTION CRITERIA												
	PERFORMANCE	TECHNOLOGY	DESIGN SIMPLICITY	RELIABILITY	ACCOMMODATIONS	SERVICEABILITY	SYSTEM OPERATIONS	VERIFICATION	RISK	SURVIVABILITY	COST	SAFETY	TOTAL SCORE
WEIGHTING FACTOR	4	4	3	3	3	2	2	3	5	2	4	N/A	
Single Detector													
OPTICAL SUBSYSTEM	2	2	2	3	4	1	4	3	2	5	2		99
RECEIVER SUBSYSTEM	5	5	5	4	4	5	5	4	4	3	4		183
Array													
OPTICAL SUBSYSTEM	3	5	5	4	5	1	4	4	2	5	4		132
RECEIVER SUBSYSTEM	3	4	3	4	2	5	5	4	3	3	4		124
Hybrid													
OPTICAL SUBSYSTEM	3	4	4	4	5	1	4	4	2	5	4		125
RECEIVER SUBSYSTEM	5	5	4	4	3	5	5	4	3	3	4		142

Figure 5-12. Evaluation and Selection Criteria Scores for Various Image Motion Compensation Approaches

The functional block diagram identifies the major subsystems, i.e the transmitter, the optics and receiver, and the supporting subsystems (identified with an "S"). The diagram is used to identify the interfaces between the subsystems. The system controller is the instrument interface with the spacecraft accepting clock and command signals from the spacecraft bus and providing data to the spacecraft local area network for transmission to the ground. Each of the major subsystems contains a controller/monitor which is the subsystem interface with the system controller. The controller/monitors operate autonomously but may be inhibited by the system controller. The power conditioner serves as the power interface with the spacecraft, providing power to all the subsystems, with the exception of the laser. The laser power conditioner is internal to the laser

Our assumptions with regard to the support subsystems are given in Figure 5-14. Further details of the interfaces and support subsystems are given in section 5.4, Integrated System Description.

5.1.3 *Derived Subsystem Requirements*

The requirements which were handed down to the subsystems for configuration trades are shown in Figure 5-15. The requirement on laser feedback for the optical subsystem is a not-to-exceed number provided by Spectra Technology and includes both specular reflections and scattered light.

The laser transmitter is extremely sensitive to retroreflected light. Scattering or reflection of laser light back into the optical cavity causes the laser frequency and amplitude to become unstable. The total reflection of downstream optical components should therefore not exceed 0.01%.

The laser emits a pulse of 10 J in approximately 3 μs, an optical peak power of over 3 MW. The beam size is approximately 4 cm in diameter and therefore the energy and power densities will be a minimum of 1 J/cm^2 and 300 kW/cm^2 respectively (minimum because the beam will have a Gaussian intensity profile rather than uniform). The average optical power will be 100-200 W. Any optical configurations which use absorptive coatings, attenuating dots, soft apertures etc. to minimize retroreflection must be stable under this level of energy and power density.

The requirement for no internal focal points arises out of a desire to simplify the ground testing of the instrument. High energy laser beams when brought to a focus cause air breakdown by multiphoton ionization. The plasma formed at the focus then grows by electron impact ionization or inverse bremsstrahlung, absorbs laser light from the beam and distorts the phase front. Focal points in the system would therefore make system verification impossible, unless the whole instrument were tested in vacuo.

The rest of the requirements in the Figure are self explanatory.

5.2 Configuration Evaluation

With the above subsystem requirements we now consider alternate configurations for the major instrument subsystems.

5.2.1 *Laser Subsystem Configuration Analysis*

The laser subsystem consists of all the components required for the generation and frequency control of two CO_2 laser beams, the transmitter and reference beams, respectively. The transmitter laser generates a continuous train of single-frequency pulses (10-J energy, 3-μs duration) at an average PRF of 10-15 Hz (20-Hz peak), that is delivered to the optical subsystem for transmission to earth. The frequency of the transmitter laser is controlled by injecting it with a sample of a 5-W highly-stable cw laser beam. Another sample is delivered to the receiver subsystem to function as the

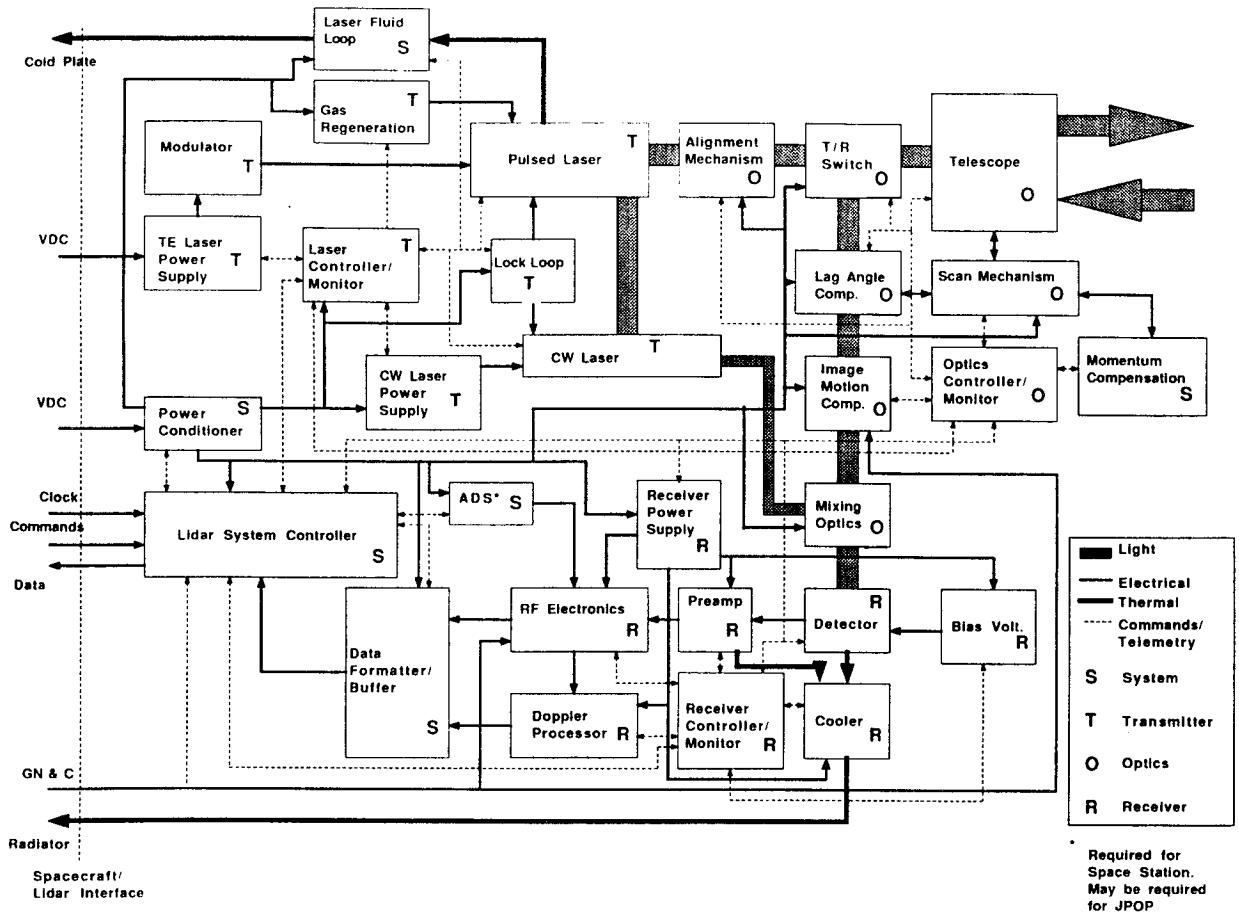

Figure 5-13. LAWS System Functional Block Diagram

• *Structure*	Graphite Epoxy Optical Bench and Truss with Titanium Fittings (UARS Heritage)
• *Thermal*	Baseline assumes Laser Heat (~2 kW) Rejected by the Platform Thermal Subsystem. Remainder of Heat Rejected Locally by Heat Pipes and Radiators as Needed. Have Studied Implications of LAWS Carrying Laser Heat Rejection Subsystem.
• *ADS*	Baseline does not include Star Trackers for JPOP. Strategy for Meeting Requirements of ~100 μrad pointing knowledge includes: - Understanding Systematic and Random Parts of Platform ADS Error Budget (~150 μrad 1-sigma) - Fitting Curve of Doppler vs. Azimuth from Ground Returns (Over Many Shots) to Take Out Systematic Biases
• *Momentum Comp.*	Standard Off-the-Shelf Wheel from GSTAR Program with Control Electronics from DMSP S-15

Figure 5-14. Support Subsystems Assumptions

Laser Subsystem	
Wavelength	9.11 μm
Energy Per Pulse	10 Joules
Pulse Length	3 μsec
Repetition Rate	Asynchronous 20 Hz max.
Chirp	< 200 kHz
Weight	120 kg
Power	< 2kW Average
Lifetime	10^9 Shots
Beam Quality	Near Diffraction Limited
Beam Profile	Near Gaussian

Optical Subsystem	
Telescope Aperture	1.5 m
Nadir Angle	Fixed at 45°
Rotation Rate	Fixed at 12 rpm
Weight	< 350 kg (goal 300 kg)
Polarization	Linear to Detector Signal and LO
T/R Switch and Lag Angle Comp.	Support Asynchronous Laser prf
Laser Feedback (Narcissus)	<0.01%
Boresight Stability During Round Trip	3 μrad (Goal 1.5 μrad)
Other	No Internal Focal Points
Power	< 250 W

Receiver Subsystem	
Detector	Optimized Single Detector With Alignment Elements
Heterodyne Quantum Efficiency	> 35% at 1.2 GHz (>40% Goal)
Doppler Processing	On-Board to Support Shot Management
Weight	< 40 kg
Data	Raw Data Downlinked
Data Rate	1.5 - 6 Mbps
Power	< 300 W

Figure 5-15. Subsystem Requirements for Configuration Trades

local-oscillator beam. The laser subsystem receives input power from the spacecraft and delivers waste heat to a cold plate. It receives control information from the system controller.

5.2.1.1 *Laser Subsystem Requirements*

The top-level requirements for the laser subsystem have been given in section 5.1.3 and are discussed in detail below.

5.2.1.1.1 Pulse Length

The pulse length is determined to first order by the range resolution requirement for the lidar. It was stated in the RFP to be 1-km vertically, which for the 45° nadir angle translates to approximately 1.4-km radially. This requirement can be met by pulse durations of up to 10 μs. Because of speckle, however, it is desirable to obtain several independent estimates within a resolution element to effect smoothing of the Doppler estimate. Since a new speckle estimate is obtained in a time period equal to half the pulse duration, a pulse length shorter than 10 μs is required. Speckle statistics (Battan (1973) indicates that averaging 3 to 5 independent speckle estimates is close to optimum. Based on this consideration we baselined a pulse duration of 3 μs and retained the option to shorten it further subject to the results of additional Doppler estimation studies to be conducted during Phase II. The shorter pulse duration also keeps open the option of enhanced range resolution for atmospheric research investigations.

5.2.1.1.2 Pulse Energy

The pulse energy requirement of 10 J derives from the need for adequate lidar photodetector output signal-to-noise-ratio (SNR). The SNR is also a function of other system parameters (primarily telescope size and system losses), atmospheric parameters (primarily the aerosol backscatter coefficient) and the measurement range. The results of computer simulations of the lidar velocity measurement process (see section 6.0) indicates that a 10-J pulse energy/1.5-m optical diameter combination is optimum for the mission measurement scenario and assumed atmospheric parameters.

5.2.1.1.3 Pulse Repetition Rate

A single lidar pulse yields an estimate of the radial velocity within each range resolution element along its path. To ascertain the total horizontal vector within a localized region on the earth's surface, the region must also be interrogated from other directions. This requirement and, of course, the need for interrogating diverse areas, dictates that the laser be pulsed repetitively while the line of sight is being scanned. The scanning is accomplished by conically scanning the telescope line-of-sight, since this approach is the only one compatible with low acceleration loads on the platform. Consideration of the scan pattern, formed for various scan rotation and pulse repetition rates, have indicated the need for a pulse repetition rate of at least 10 Hz, with 20 Hz desirable. We assumed a 10-15 Hz average repetition rate system (depending on the value of laser efficiency), with a burst mode capability of 20-Hz. Another requirement is that the pulsing be asynchronous to allow adjustment of the sampling rate to adjust for natural oversampling at high latitudes, and at scan azimuths where velocity vector measurements are not possible, (i.e., near the polar and latitudinal planes).

5.2.1.1.4 Wavelength

The laser wavelength selection was based on two factors. Minimization of extinction by atmospheric CO_2 requires that the active laser CO_2 molecule be a rare isotope. Since enhanced aerosol backscattering is expected (and has been reported) in a

narrow wavelength band in the vicinity of 9.11 μm, the $^{12}C^{18}O_2$ isotope was selected. There is also a reduction in the water continuum absorption for the 9.1 μm line of $^{12}C^{18}O_2$ as opposed to the 11.1 μm line of $^{13}C^{16}O_2$. The R(20) line of Band II of the $^{12}C^{18}O_2$ isotope oscillates at 1097.1506 cm^{-1}, a wavelength of 9.1145 μm. Spectra Technology recently completed a program, funded by the Air Force Geophysical Laboratory and the NASA/Marshall Space Flight Center, to measure the detailed lasing characteristics of this molecule. Considerable experience with lasers utilizing the $^{13}C^{16}O_2$ isotope also exists within Spectra Technology, principally as a result of the MIT/Lincoln Laboratory CORA Program.

5.2.1.1.5 Temporal Coherence

Temporal coherence refers to frequency variations as a function of time during the laser pulse, or frequency chirp, and is caused by refractive index variations in the gas within the laser cavity during pulse formation. Excessive chirp increases the pulse bandwidth and degrades the Doppler resolution. Ideally, the chirp is kept small, relative to the transform limited pulse bandwidth (given approximately by the inverse of the pulse duration). For a 3-μs pulse duration, the transform limited bandwidth can be as much as 330 kHz and, thus, for minimal impact on pulse bandwidth, the chirp should be less than 200 kHz.

Temporal coherence requirements for the reference laser are dictated by the need to limit frequency excursions over the pulse round-trip time. Maintaining a 50-kHz stability over a 10-ms round-trip time is equivalent to a frequency stability of 1 part in 10^9 over 10 ms. The 50-kHz allowable value translates to a velocity error of 0.25 m/s.

5.2.1.1.6 Spatial Coherence

Spatial coherence refers to phase distortions across the transmitter laser wavefront, which causes it to be propagated as a non-diffraction-limited beam and, consequently, spill radiation outside the diffraction-limited field of view of the lidar receiver, contributing to a signal loss. The rms optical path difference (OPD_{rms}) across the laser beam is related to two popular measures of phase distortion: the beam quality (B.Q.) and Strehl ratio, by the following relations:

$$B.Q. = \exp\left(\frac{1}{2}\left(\frac{2\pi}{\lambda}\right) OPD_{rms}\right)^2)$$

$$\text{Strehl Ratio} = \exp\left(-\left(\frac{2\pi}{\lambda} OPD_{rms}\right)^2\right)$$

The Strehl ratio is a useful measure since it is the ratio of the signal that can be expected relative to that possible for an undistorted beam.

The baseline specification for the laser transmitter is to be as near diffraction limited as possible. We interpret this requirement as a B.Q. = 1.1, which corresponds to a Strehl ratio of 0.826 and an rms OPD = 0.0695 waves. A Strehl ratio of 0.826 represents an SNR loss of 0.83 dB. In practice, the 0.0695 wave rms OPD is apportioned among all the potential contributors within the laser, e.g., the cavity optics, optical truss, flow-loop, etc., and these components are designed to meet the specifications.

5.2.1.1.7 Beam Jitter

Beam jitter refers to the directional variation in the propagation direction of successive laser pulses. The baseline specification used was 25-μr rms at the laser exit, which is approximately one third of that available to the total instrument. Note that this translates to less than 1 μr at the telescope output, since it is decreased by the telescope magnification. Excessive beam jitter, if uncompensated, would place the interaction region of the transmit beam on earth outside of the field of view of the lidar receiver.

5.2.1.1.8 Weight

The target weight of the laser subsystem exclusive of the external fluid loop is 120 kg, to facilitate accommodation on the polar platform.

5.2.1.1.9 Wall-Plug Efficiency

The overall efficiency of the laser shall exceed 6% with a goal of 7.5%.

5.2.1.1.10 Lifetime

The instrument shall have a lifetime in excess of three years, which translates to approximately 10^9 shots.

5.2.1.2 *Elements of the Laser Subsystem*

A functional block diagram of the laser subsystem is shown in Figure 5.16. It consists of four major modules, the transmitter gain, optical, control and diagnostics, and auxiliary modules, respectively. The transmitter gain module is attached to the instrument platform using vibrational isolation mounts to protect the instrument from vibrational perturbations. The optical module is the host for all the optical components and is vibrationally decoupled from both the gain module and the instrument platform such that it experiences a very quiescent vibrational environment. The controls and diagnostics module accomplishes sequencing of laser operation and conducts system health checks. The auxiliary module provides for all ground support functions during ground testing through on-orbit operation.

5.2.1.2.1 Transmitter Gain Module Assemblies

The transmitter gain module has been subdivided into major assemblies, as follows:

1. Discharge Region
2. Flow Loop
3. Pulsed Power
4. Mechanical
5. Thermal Control and Power Interfaces

The major functions and components of each of these assemblies are:

Discharge Region

The discharge assembly includes that hardware which directly interacts with the laser discharge. Major components include:

1) Discharge Cathode
2) Discharge Anode

3) Preionizer
4) Dielectric Insulator
5) Ground Return Vanes
6) Supporting 'Bed Plate' for Electrodes.

Flow Loop

The flow loop includes all the components necessary to support flow, homogenization, thermal and chemical control of the gas which is delivered to the discharge assembly. Major components include:

1. Flow Liner (ducting)
2. Heat Exchanger
3. Catalytic Converter
4. Fan and Drive Components
5. Acoustic Damper

Pulsed Power

The pulsed power conditions dc power from the spacecraft electrical subsystem into short, high-voltage electrical pulses appropriate for driving the CO_2 laser discharge. Major components include:

1. Power Conditioner.
2. Power Source Isolator.
3. Pulse Forming Network.

Mechanical

The mechanical assembly includes those components which carry major mechanical loads, or which are identified with critical static or dynamic mechanical tolerances. Major components are:

1. Shell
2. Attachment Struts
3. Window Mounts (except windows)
4. Wave Shield Tubes

Thermal Control and Power Interface

The thermal control and power interface assemblies provide for the interfacing of the heat exchangers within the laser (flow-loop and pulse power assemblies) with the spacecraft cold-plate, and of the various laser power circuits to the prime power source. These functions are also provided for the optical, controls and diagnostics and ancillaries modules, respectively.

5.2.1.2.2 Optical Module Assemblies

The optical module includes all active and passive optical components necessary to generate the required optical beams. Major optical components are:

1. Truss
2. Transmitter Gain Module Windows
3. Power Oscillator Resonator Mirrors and Mounts
4. Injection/Reference Oscillator Laser(s)
5. Alignment Sensor Optics.
6. Turning Mirrors and Mounts
7. Beam Sampling Optics.

8. Beam Sensing photodetectors
9. Transmit and Local Oscillator Beam Interfaces.

With the exception of the gain module windows, all optical components are mounted on a high rigidity optical bench.

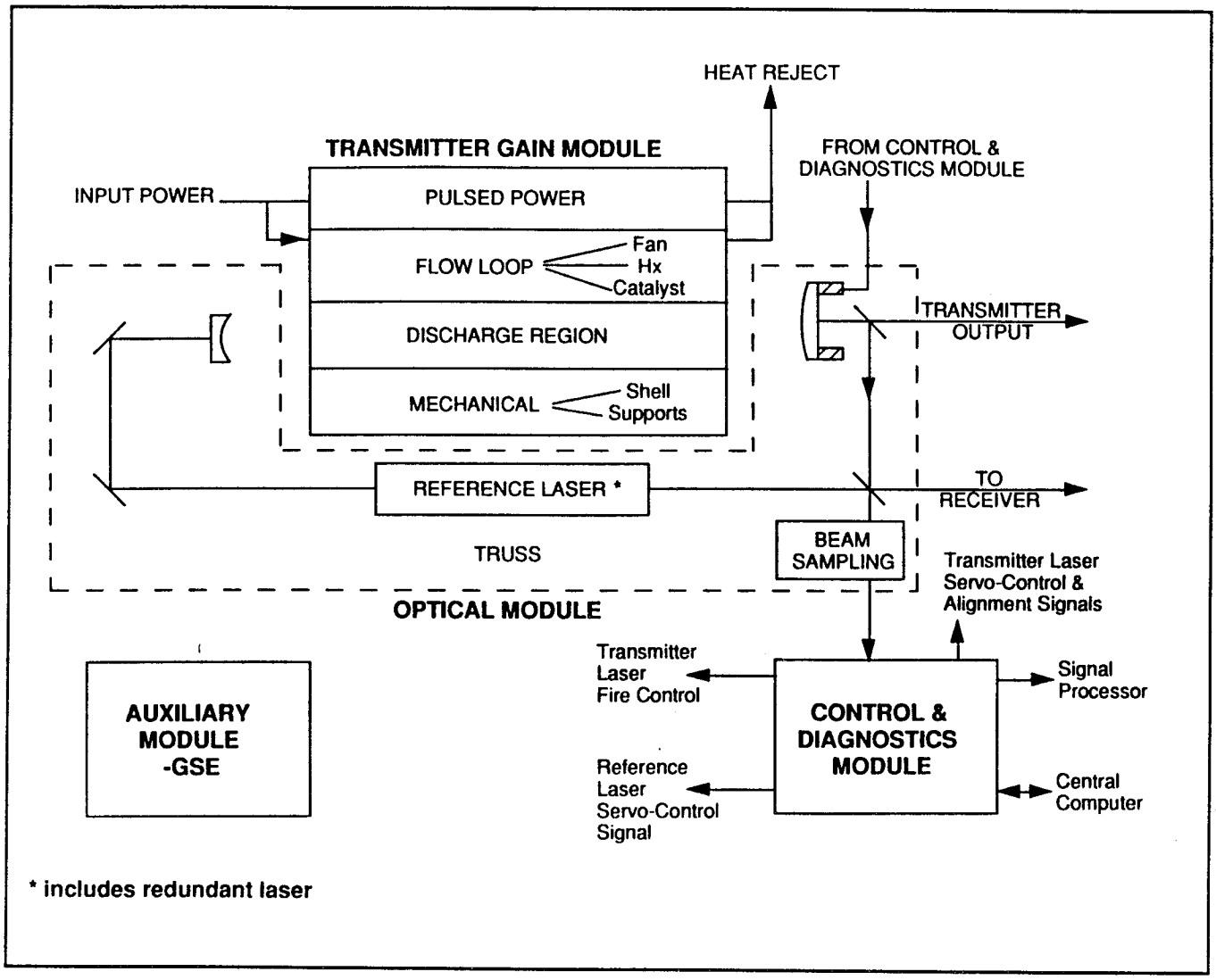

Figure 5-16. Elements of the Laser System

5.2.1.2.3 Control and Diagnostics Module Assemblies

The controls and diagnostics module provides for sequencing of all transmitter functions during warm-up, alignment, normal operation and shutdown. It also provides for gathering of health and status data, for subsequent reporting to the instrument system controller. Major components include:

1. Reference/Local Oscillator Servo loop.
2. Power Oscillator Servo Loop.
3. Alignment Sensor Servo Loop.
4. Command Trigger Interface.
5. Offset Frequency Interface.
6. Laser CPU and/or Interface with Instrument CPU.

5.2.1.2.4 Auxiliary Module

There is a variety of functions that are handled outside the transmitter proper during ground operations, or on the ground during flight operations. Therefore hardware, which must be supplied by the transmitter supplier, but are not part of the actual flight transmitter hardware, are lumped into the ancillaries assembly. Ancillary hardware includes:

1. Vacuum/Gas Fill Station for ground operations
2. Ground Test Console
3. Protective Cover and shrouds for ground operations

5.2.1.3 *Major Laser Technology Options*

This section details the trades which were performed and the choices made for the various parts of the laser transmitter subsystem.

5.2.1.3.1 Laser Architecture

The transmitter architecture approach we baselined is the external injection of a transversely-excited, transverse-flow laser incorporating an unstable resonator cavity. The external injection selection is based on the heritage of this approach for long-range wind sensing and in its high power potential, since the high gain possible allows an unstable mode to be generated. This results in efficient utilization of the gain medium.

The hybrid transmitter approach was rejected because it requires a cw gain cell within the cavity for frequency control, which forces the cavity to have a stable configuration because of the low cavity losses necessary for cw operation. This reduces the mode fill factor of the cavity, which has an adverse effect on efficiency in the pulsed mode. Recovery of the cw tube occurs in about 200 - 300 μs, which is unacceptable because of the 10-ms laser pulse round-trip times and would cause interference during pulse reception. The alternative is to clamp the tube to off during the round-trip time using an intra-cavity electro-optic modulator. Introduction of a high-power intra-cavity modulator presents the potential for optical damage and increases system complexity. However certain T/R switch designs, e.g., a spinning disc with a hole in the surface for transmission, could ameliorate this interference. In summary, the hybrid scheme exposes more components (e.g., hybrid cw cell windows) to high power radiation and is limited to low pulse energies because of the stable cavity configuration.

The master oscillator power amplifier (MOPA) approach was determined to be unsuitable for the LAWS laser for reasons of low efficiency and complexity. The low efficiency derives from the fill factor mismatch that occurs between the modes and gain

medium due to the requirement to physically separate the various passes through the amplifier for high beam quality. Since the waveform modulation potential of a MOPA is not useful for the LAWS laser, this architecture is also considered too complex. Efficient MOPA systems generally require an additional preamplier to efficiently extract energy from the power amplifier, and at the 9-μm wavelength requires imaging of the mode between stages to minimize the effects of diffraction as well as Faraday isolators to isolate successive stages and/or passes to minimize parasitics.

5.2.1.3.2 Discharge Type

A major LAWS laser trade is the choice of discharge type. Two options were considered: the self-sustained and e-beam sustained discharge, respectively.

We have selected the self-sustained approach over the e-beam sustained approach based on several factors:

- It is a significantly simpler approach to implement.
- Good intrinsic efficiencies were obtained using the self-sustained approach in extraction measurements on a $^{12}C^{18}O_2$ laser. The values obtained actually exceeded those achieved using e-beam sustained excitation. The measured self-sustained values approach the values predicted by theory for e-beam sustained excitation. Highlights of the results obtained during the USAF/AFGL- and NASA/MSFC-funded study of extraction measurements on e-beam sustained and self-sustained $^{12}C^{18}O_2$ lasers are presented in Figure 5-17. These results are presented as evidence that good intrinsic efficiencies are possible for self-sustained excitation and that a laser transmitter based on the $^{12}C^{18}O_2$ laser is fully capable of providing the pulse energies at the high efficiency required for LAWS.
- More rugged components are potentially available for the self-sustained approach (no lifelimiting foils).

The final choice between the self-sustained and e-beam sustained approaches was based on the positive results of two research efforts at Spectra Technology to evaluate the impact of the self-sustained approach on:

a) Gas life - The rate of gas degradation may depend on the method of excitation and, thus, affect catalyst requirements for long-life operation. We have conducted an IR&D program to compare gas degradation data available within Spectra Technology for e-beam sustained systems using both abundant and rare ($^{13}C^{16}O_2$) isotopes with gas degradation data obtained in a self-sustained device.

b) Component Reliability - Spectra Technology have active efforts in both e-beam sustained (the CORA high pulse energy imaging CO_2 radar power amplifier at MIT/Lincoln Laboratory) and self-sustained devices (the CO_2LT test-bed with similar characteristics to the NOAA lidar transmitter). The reliability of components in these devices is continuously monitored and assessed. Component reliability studies will also be a key part of the NASA laser breadboard program.

- 828 CO_2 R (20) at 9.1 μm
- Lucy X-ray Preionized Self-Sustained - 4 x 4 x 90 cm

  $He/N_2/CO_2$=45/10/15 p = 380 torr E_{laser} = 12 J n*=16%

  $He/N_2/CO_2$=45/40/15 p = 760 torr E_{laser} = 25 J n* =15%
- Delilah E-beam Sustained - 4 x 4 x 90 cm

  $He/N_2/CO_2$=45/10/15 p = 380 torr E_{laser} = 15 J n*=12%

  $He/N_2/CO_2$=45/40/15 p = 760 torr E_{laser} = 26 J n* =10%
- Similar Results for 626 CO_2

* Instrinsic Efficiency

Figure 5-17. High Efficiency $C^{18}O_2$ Achieved with Self-Sustained Discharges

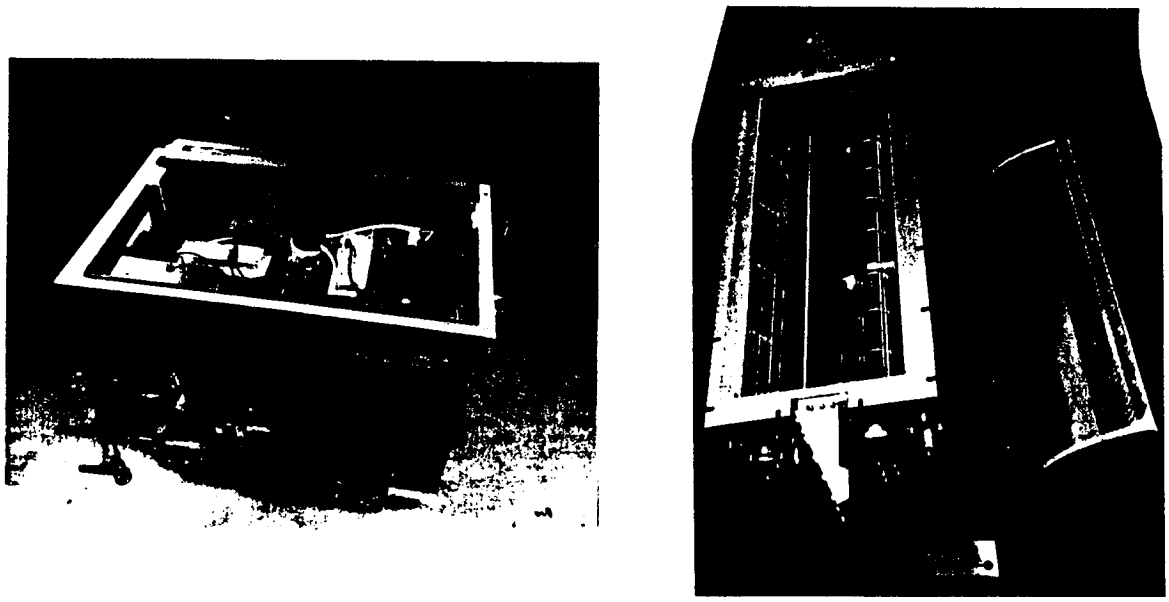

Figure 5-18. CO_2 Laser Testbed

The CO_2LT (CO_2 Laser Testbed) is a laser gain section recently completed at Spectra Technology that is being used for component evaluation and life-testing, gas life investigations and various design verification tests. It is nominally a replica of the NOAA/WINDVAN laser gain section. It will be used to support LAWS laser design verification tests during Phase II. Figure 5-18 is a photograph of the CO_2LT.

For the self-sustained approach, we selected an ultra-violet light source to preionize the gas over an x-ray or electron-beam approach primarily for the reasons of weight minimization and simplicity. It is also the technique most popular in current lidar systems. A corona discharge was selected as the source of the UV light because this method provides a smooth aerodynamic profile to the cavity flow and causes minimal gas degradation.

5.2.1.3.3 Local Oscillator

Another major technology option is whether to incorporate a fixed-frequency or a frequency-agile local-oscillator laser.

The fixed-frequency option has the advantage of simplicity and is within the current state-of-the-art, but requires a wide-bandwidth receiver (1.5 GHz). We chose this approach to avoid the complexity associated with the frequency agile option.

An agile frequency local oscillator beam can be used to compensate for the relative velocity due to platform motion and earth spin and it becomes possible to use a narrow-band detector in the receiver. The magnitude of the Doppler shift introduced by the relative motion is scan azimuth dependent (for a given nadir angle) and amounts to a maximum of ±1.2 - 1.3 GHz for an orbital altitude range of 400 - 800 km for a look directly north/south and for a nadir angle of 45°. A more realistic bandwidth limit is 1.5 GHz, since larger nadir angles may be of interest.

If a cw laser capable of being swept over ± x MHz were available, then one can conceive of a scheme where the injection and local oscillator lasers were swept in frequency between these limits cyclically (but out of phase with each other) and synchronously with the scan azimuth. The resulting detector bandwidth requirement is given by (1500. - 2*x) MHz and for various values of x MHz are listed in Figure 5-19 below.

Figure 5-19. Required Frequency Tunability vs. Detector Bandwidth

Frequency Tunability , ± x MHz	Detector Bandwidth Requirement, MHz
200.	1100.
300.	900.
400.	700.
500.	500.
600.	300.
700.	100.

Note that this concept requires separate tunable Injection and LO lasers and another low-pressure fixed-frequency reference laser. The power oscillator is tuned off line center by the shifted amount (ignoring any pressure frequency shift), which is undesirable because of the loss of gain and the varying amount of frequency pulling (anomalous dispersion) that would occur. The latter could probably be accommodated, however, since it primarily represents a frequency bias, which would be monitored and provided to the receiver. From the table, it appears that a tunability of ±500 MHz would be needed to significantly relax the bandwidth requirement for the receiver.

The technology of choice for a widely tunable source is the high-pressure waveguide laser. Enough pressure is necessary to provide adequate pressure broadened gain at the desired frequency. As the pressure is increased, the gain is diluted over a larger spectral region and the gain spectral density at the frequency of interest begins to decline. There is an optimum pressure around 230 torr. Laser length is limited by the single-mode requirement to <10cm. A space-qualified laser capable of ±300 MHz has been built by Goddard SFC and work at Hughes and Honeywell claim to have achieved 800-1000 MHz. There is consensus that achieving 600 to 700-MHz shift is relatively easy, but that the combination of wide tunability and frequency stability (even at the 50-kHz level) is a major challenge. Achieving constant excitation in a high pressure, small bore waveguide presents major problems.

It thus appears that the ±500-MHz tunability desired is at the limit of what can be considered demonstrated technology to satisfy the LAWS requirement. Its incorporation, however, would require an exceedingly complex front end and would elevate this laser subsystem to a major developmental and high risk item. It would also require several 500-MHz bandwidth detectors within the laser subsystem for control purposes and would have a major cost impact on the laser subsystem. We therefore chose the fixed frequency option.

5.2.1.3.4 Resonator Type

The choice of cavity design is influenced by many factors which include the efficiency (including far-field beam profile considerations), single mode control and alignment sensitivity.

Efficiency

Efficiency considerations dictate the selection of a positive-branch unstable resonator approach because of the better cavity fill factor possible. Thus, negative-branch unstable and stable configurations were eliminated from consideration because of the divergence between mode volumes and the cavity gain volume. The negative-branch unstable approach was also rejected because of inadequate laser feedback potential. Another aspect of the efficiency is maximizing the energy contained within the diffraction-limited field of view of the lidar. In this respect, the graded reflectivity resonator has properties far superior to other designs e.g., conventional scraper configurations. Figure 5-20 shows numerical results for a gain saturated (loaded) LAWS-like cavity design utilizing a super-parabolic graded reflectivity resonator. The curve on the left shows the radial intensity distribution at the output of the laser and the curve on the right the encircled energy after propagation to the far-field. Significantly, encircled energies in excess of 80%, are possible within the diffraction limit field-of-view. These results have been experimentally verified. Figure 5-21 shows the fraction of the energy within the first disk, due to an uniformly illuminated annular aperture as a function of the magnification of that aperture (ratio of outer to inner diameter of the annulus). This closely simulates the far-field propagation of a hard-aperture or scraper outcoupling of an unstable resonator. Since resonator magnifications of 1.5 to 1.7 are required for laser feedback purposes, it is evident that only approximately 40% of the laser energy is conveyed within the diffraction limit of the transmitted beam. This is obviously unacceptable.

Single-mode Oscillation Margin

It has been evident for some time that hard-edged resonators are unacceptable for coherent laser transmitters , because of transverse mode hopping. While not currently fully understood, graded-reflectivity resonators are superior in this regard probably due to there being no hard edges to diffract radiation to nurture the higher order transverse modes.

Alignment Sensitivity

The low-magnification (M) graded-reflectivity resonators are, in theory, more sensitive to misalignments and cavity density fluctuations than the more conventional hard aperture mirrors, since this sensitivity varies as $1/(1-M^2)$. However, in practice, this does not appear to be a limitation as evidenced by operating experience with the NOAA WINDVAN lidar. Our design approach will be to take into full account this increased sensitivity and specify laser parameters that will meet the performance requirements. Accommodation of the appropriate alignment sensitivities is implicit in our cavity simulation methods.

Thus, it is evident that the graded-reflectivity resonator is the clear choice for the LAWS transmitter and has been chosen as the baseline concept.

5.2.1.4 *Laser Parameter Selection*

The impact of laser parameter selection on major laser accommodations has been investigated using Spectra Technology scaling codes. These codes are used to generate coarse estimates for subsystem weight, power efficiency and volume for specific laser parameter sets. These codes yield numerical predictions that are in excellent agreement with measured pulse profiles, as shown in Figure 5-22. Use of the codes involves a two-step process. In the first step, detailed CO_2 laser kinetics codes are used to generate laser parameter sets that are consistent with the pulse energy and duration requirements. In the second, a collection of analytical and empirical relationships based on design and manufacturing experience are used to relate the laser parameter set to accommodations requirements. Sensitivity to variation of one or more of the parameters can be investigated. The estimates generated from these codes are only used as aids in the decision process for establishing the laser configuration. Once the configuration is established, the physical and electrical characteristics of the configuration are used as the basis for more accurate estimates.

The codes were used to select a baseline configuration for the LAWS laser. Detailed design then yielded estimates for the laser subsystem efficiency and weight. The baseline configuration uses a gas mix of 3 parts He, 2 parts N_2 and 1 part CO_2 (3/2/1), which was shown to operate efficiently with $C^{18}O_2$ in the MSFC/AFGL Study. Most of the figures in section 5.2.1.4, however, illustrate functional dependencies between various laser parameters for an alternate approach based on a low or zero He gas mix. This gas mix has the potential to offer a lower weight and higher efficiency laser subsystem than our baseline. Low He gas mixes will be investigated further during Phase II. The functional dependencies of the various laser parameters shown in the figures in this section do not change significantly when using the 3/2/1 mix.

5.2.1.4.1 Laser Weight Dependence on Gas Mix

We explore the dependence of laser subsystem weight for laser gas mixtures containing various percentages of He as a function of the N_2/CO_2 ratio. The data are shown in Figure 5-23. It is evident that a lighter laser results as the helium percentage is reduced. For the zero He case, a 5% concentration of H_2 is added to relax the CO_2 vibrational bending mode. One impact of reducing the helium is a higher discharge voltage. These are shown in Figure 5-24 along with the associated beam diameters and discharge gaps.

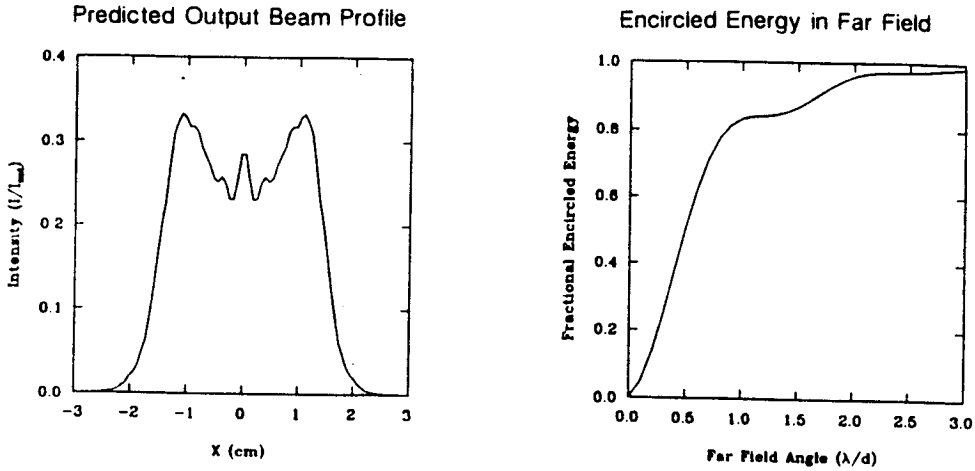

Figure 5-20. Graded Reflectivity Unstable Resonator Puts More Energy in Central Lobe

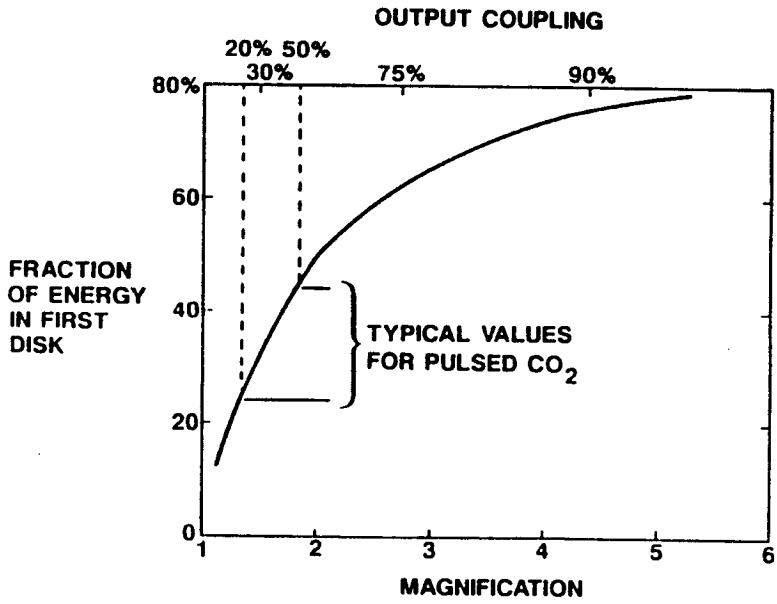

Figure 5-21. Hard Aperture Unstable Resonators Far Field Intensity Distribution

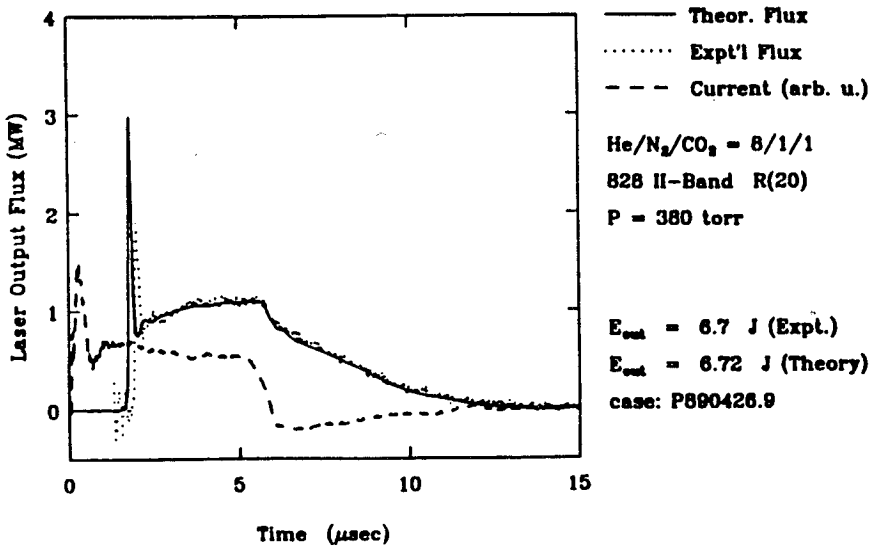

Figure 5-22. Comparison of Measured and Calculated Pulse Profiles Using STI Laser Codes

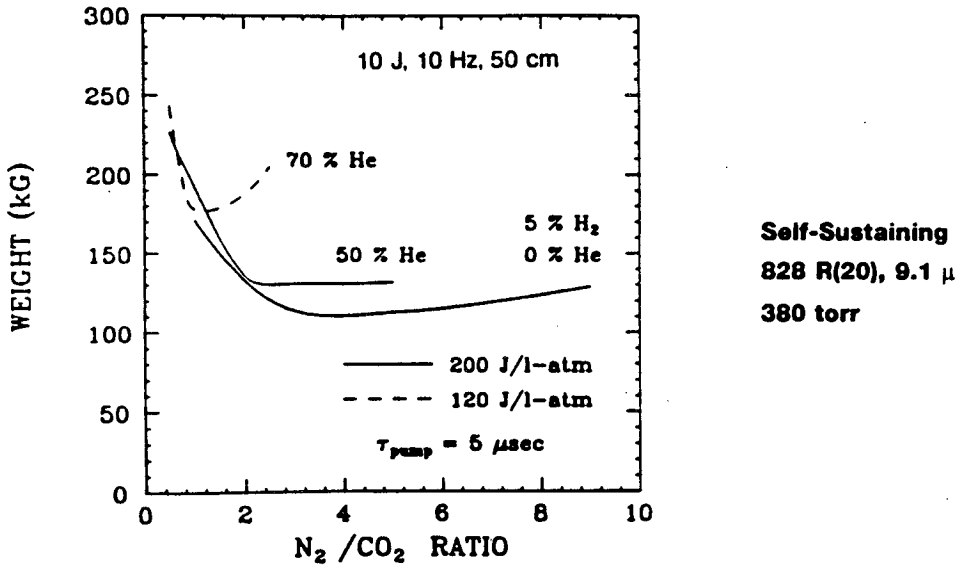

Figure 5-23. Laser Subsystem Weight vs. Gas Mix Trades

Baseline Laser Conditions:

Pulse Energy		10 J
Gain Section Length		50 cm
Laser Isotope/Line		828 R(20) 9.11μm
Discharge Loading		Optimum
Cavity Pressure		380 torr

$He/N_2/CO_2$	DISCHARGE VOLTAGE (kV)	DISCHARGE GAP (cm)	BEAM DIAMETER (cm)
7/2/1	29.6	6.9	6.3
3/2/1	31.1	5.1	4.6
$H_2/N_2/CO_2$			
5/74/21	46.0	4.7	4.37

Figure 5-24. Self-Sustaining Voltage Dependence on Laser Gas Mixture

These data were generated for a 10-J output, a gain length of 50 cm, a discharge pumping time of 5 μs, a cavity pressure of 0.5 atm and self-sustained excitation. Operation on the R(20) line of the 828 isotope at a wavelength of 9.11μm is assumed. Weight is seen to optimize at different N_2/CO_2 ratios for the various He concentrations and reflects different laser efficiencies. A gain module weight of ~110 kg is predicted for the zero He case. Our baseline laser weight is ~ 140 kg.

5.2.1.4.2 Laser Efficiency Dependence on Gas Mix

The data shown in Figure 5-25 indicate that the laser efficiency is also affected favorably by reducing the helium content of the laser gas. Efficiencies in excess of 6% are predicted for the zero He condition (Specific calculations for a zero He configuration now indicate efficiencies in excess of 7.5% are achievable and this figure is our stated goal). Our baseline laser with the conventional gas mix has an assumed efficiency of 6%. These data were generated for a 10-J output, a gain length of 50 cm, a discharge pumping time of 5 μs, a cavity pressure of 0.5 atm and self-sustained excitation. Operation on the R(20) line of the 828 isotope at a wavelength of 9.11 μm is assumed. Efficiency is seen to optimize at different N_2/CO_2 ratios for the various He concentrations and reflects differences in laser kinetics efficiencies.

Eliminating He from the discharge has a beneficial effect that is implicit in the above data. Since the sound speed of a lower He content mix is lower, it takes longer for discharge-induced shock waves to encroach on the flow and, thus, the quality of the flow-field in the laser cavity is increased, or, conversely the discharge region guard-band allotment can be decreased.

5.2.1.4.3 Laser Weight Dependence on the Pump Pulse Duration

The impact on accommodations of varying the pump (discharge) pulse duration was undertaken to evaluate the effect of shortening the optical pulse duration. There may be an advantage from the signal processing viewpoint, since more independent speckle

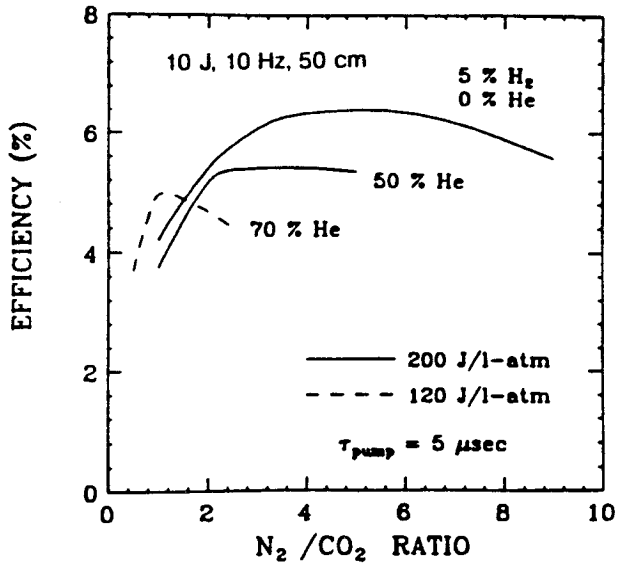

Self-Sustaining, 828 R(20) 9.1 μ, 380 torr

Figure 5-25. Laser Subsystem Efficiency vs. Gas Mix Trades

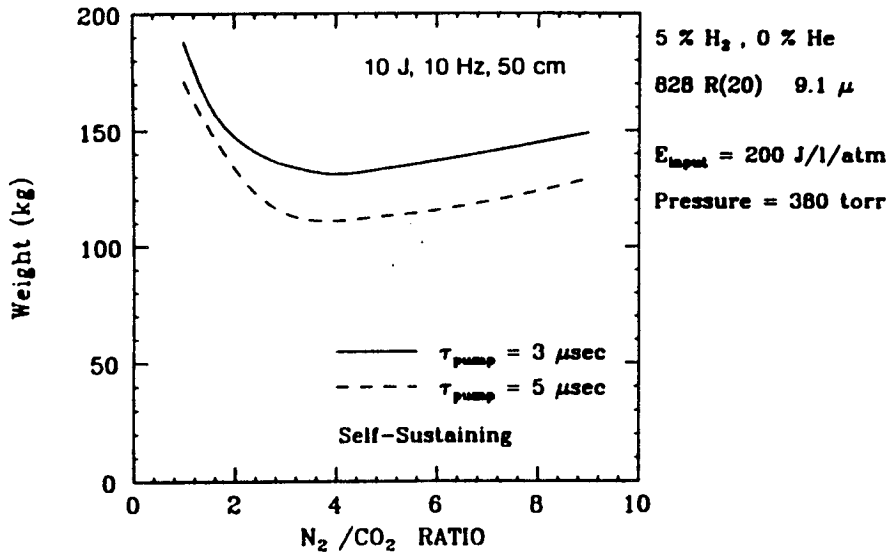

Figure 5-26. Weight Impact of Varying Pump Pulse Duration (Alternate Approach)

samples can be generated within a range resolution interval, which would lead to smoother spectral estimates. In our trade studies, we investigated the impact on accommodations of varying the laser pulse duration by varying the discharge pump pulse duration. Discharge pump pulses of 5 and 3 μs, respectively, yield optical pulses of 3 and 2 μs. Figure 5-26 shows weight estimates as a function of N_2/CO_2 ratio for the two discharge pump pulse durations. The results indicate a weight advantage for the longer pulse case. Laser parameters are indicated in the legends.

Figure 5-27 shows optical pulse profiles for several of the gas mixes considered during the study (assuming a pump pulse of 5μs). Pumping throughout the pulse is seen to yield 'squarer' temporal pulse profiles with the ratio of the energy in the gain switch spike small relative to the energy of the pulse. This leads to the minimum spectral broadening (transform limit) due to pulse shape. We note that in the NOAA WINDVAN laser the excitation pulse was arranged to be short so that the electron density contribution to the frequency chirp would be small during the optical pulse. Our simulations show however that there are minimal electron density changes during an extended pump pulse, and decreasing the pumping rate during the late pulse can be used to offset some (or all) of the frequency chirp due to gas heating. For short pump pulses, the characteristic pulse shape is a pronounced gain switch spike followed by an exponential decay, which is not as desirable from the signal processing viewpoint. There is also a significant weight penalty in generating (<0.5 μs) short pump pulses.

5.2.1.4.4 Laser Efficiency Dependence on the Duration of the Pump Pulse

Figure 5-28 shows the impact on wall-plug efficiency of varying the discharge pump pulse duration. We show enhanced efficiency estimates for the longer pulse duration.

5.2.1.4.5 Laser Weight Dependence on the Cavity Pressure

Increasing the pressure in the cavity increases the laser gain and, thus, reduces the gain volume required for a given pulse energy. This translates to a reduced laser weight as shown in Figure 5-29 where a weight reduction of 20 kg is predicted, as the cavity pressure is increased from 0.5 atm to 1-atm. We chose a 0.5-atm cavity pressure laser, however, because of significantly reduced chirp.

5.2.1.4.6 Laser Efficiency Dependence on the Cavity Pressure

Figure 5-30 indicates that a 1-atm cavity pressure laser is somewhat less efficient than a 0.5-atm. laser. This is due to the fact that the discharge guard-band allotment is independent of the pressure (cf. the sound-speed is essentially pressure independent) and is, thus, less of a fraction of the cavity cross-section at 0.5 atm, since the cavity cross-section is larger.

5.2.1.4.7 Laser Efficiency Dependence on the Cavity Loading (J/l-atm)

We have assigned an optimum discharge loading value in the data presented. These optimum values were determined as a result of the trade results shown in Figure 5-31, which shows how the loading value optimizes for various gas mixtures. The increased loading potential of the low helium mixes is a contributor to the increased efficiency of these mixes which will be investigated during Phase II. Figure 5-32 shows the efficiency variation with discharge loading at 0.5 and 1 atm, respectively.

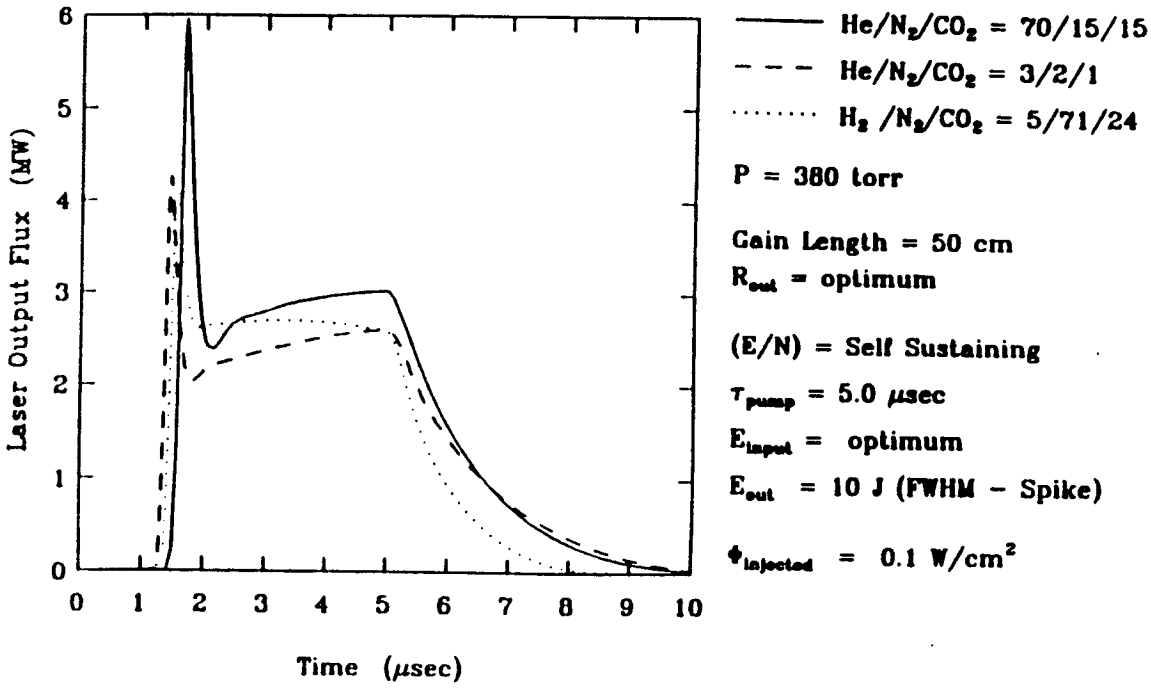

Figure 5-27. Simulated Laser Pulse Profiles for Several Gas Mixtures

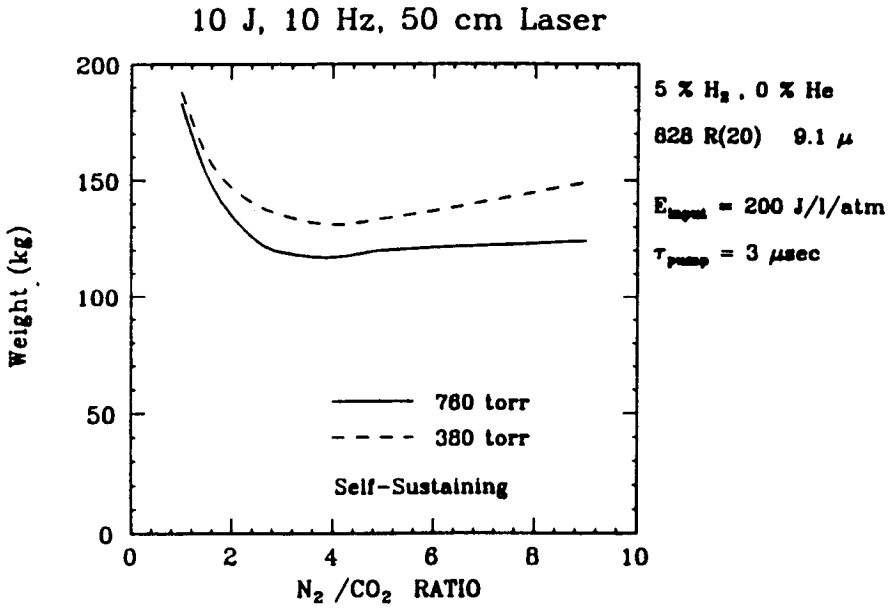

Figure 5-28. Efficiency Impact of Varying Pump Pulse Duration (Alternate Approach)

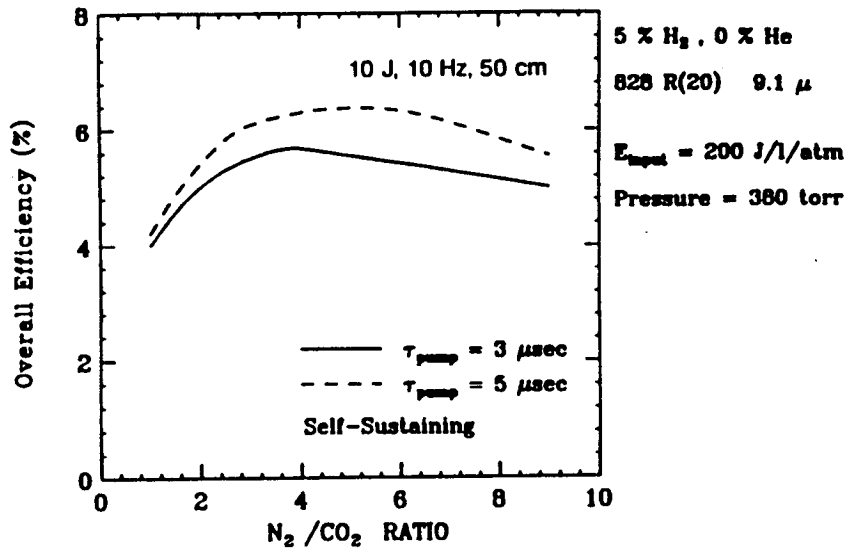

Figure 5-29. Laser Subsystem Weight Impact of Varying Cavity Pressure (Alternate Approach)

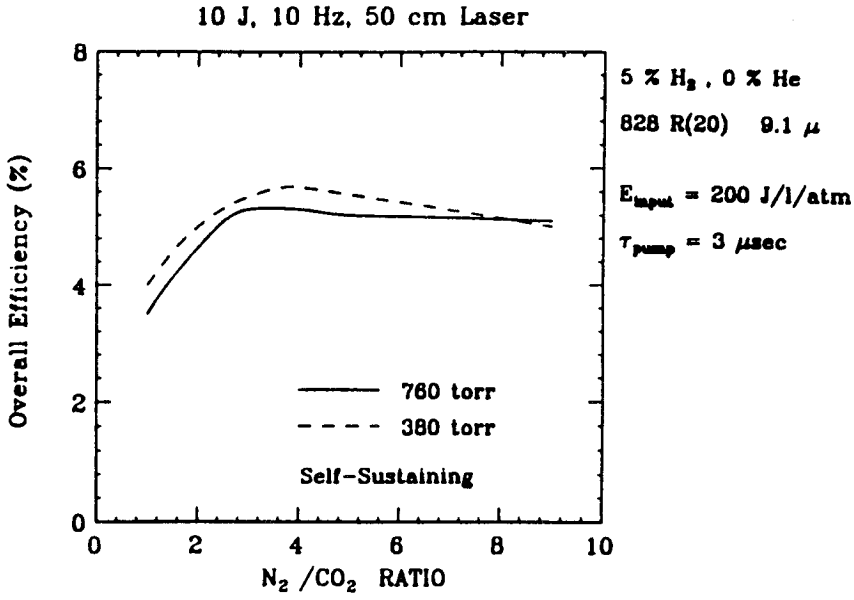

Figure 5-30. Laser Subsystem Efficiency Impact of Varying Cavity Pressure (Alternate Approach)

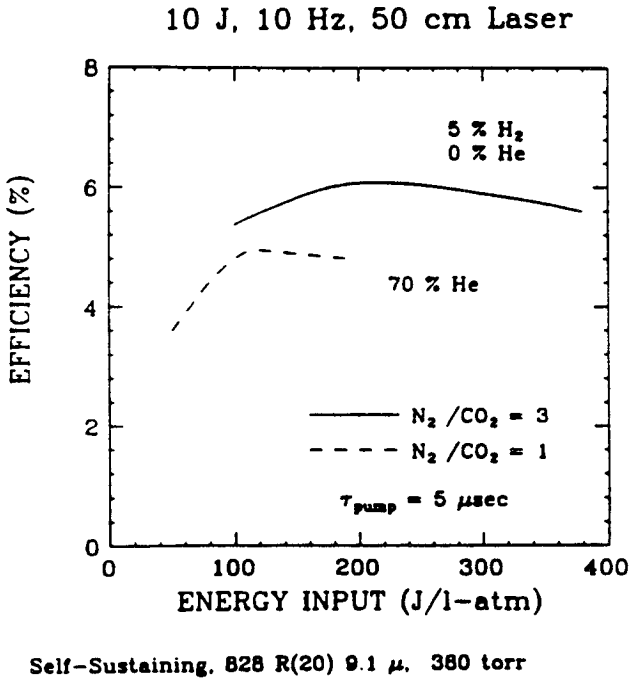

Figure 5-31. Impact of Gas Mix Selection on Discharge Loading Potential (Alternate Approach)

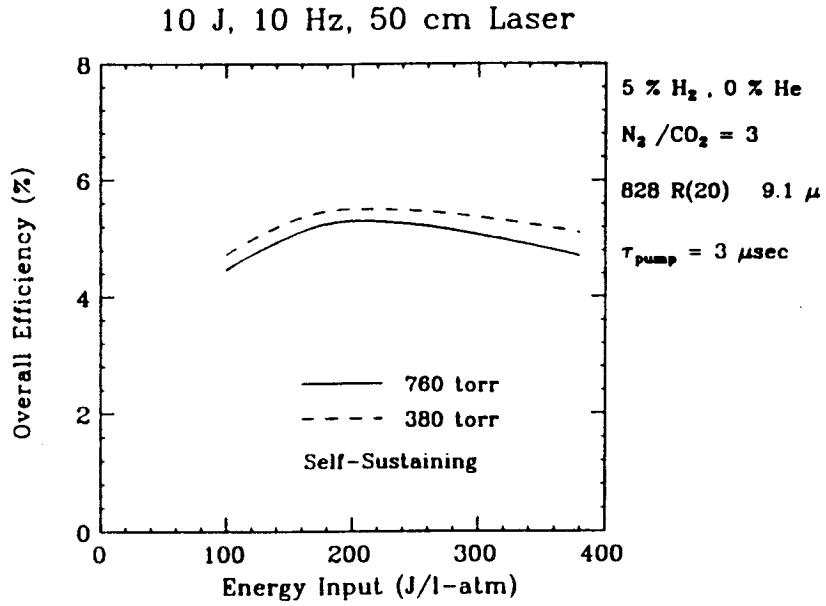

Figure 5-32. Impact of Cavity Pressure on Discharge Loading Potential for the Zero He Gas Mixture (Alternate Approach)

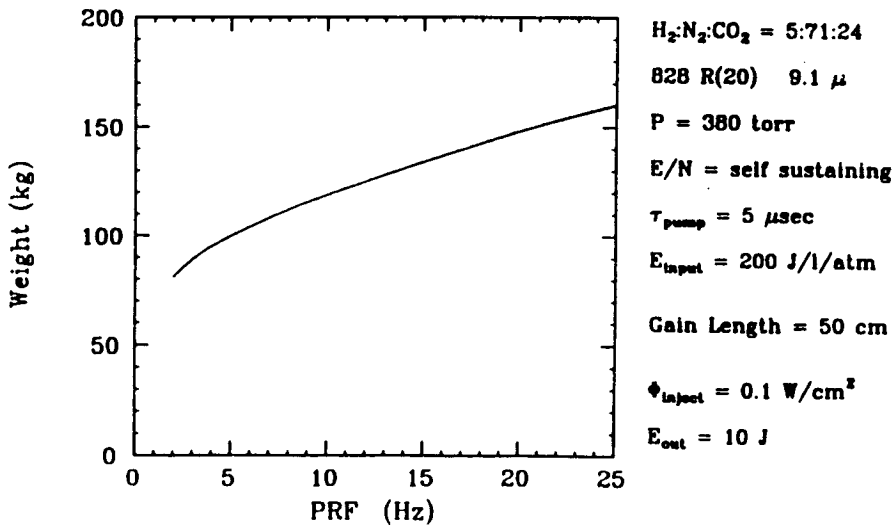

Figure 5-33. Laser Subsystem Weight vs. PRF Trade (Alternate Approach)

5.2.1.4.8 Laser Weight Dependence on the Pulse Repetition Frequency

Figure 5-33 shows the impact on laser gain section weight of varying the laser pulse repetition frequency (PRF) requirement. An increase of 30 kg is apparent for a 20-Hz relative to a 10-Hz device. This is due to increased weights of the pulse power and flow-loop assemblies.

5.2.1.5 *Assessment of Frequency Chirp*

We have found, during previous investigations, that pulse chirp behavior can be explained to first order using a scaling relationship combining pertinent laser parameters. The scaling relationship is derivable from the physics of the late thermal chirp that occurs within the pulse due to gas heating caused by relaxation of the excess vibrational energy and yields a parabolic chirp coefficient that is given by:

$$\text{Chirp Coefficient} = (\gamma-1)\nu K I E/(2L\sigma^2) \quad \text{MHz}/\mu\text{s}^2$$

γ	=	ratio of specific heats of gas mixture
ν	=	laser frequency
K	=	Gladstone and Dale constant for gas mixture
I	=	length of laser gain section
E	=	laser pulse energy/unit volume of discharge region
L	=	resonator length
σ	=	effective beam radius (half of the electrode separation)

This assumes line-center operation of the laser (such that the chirp due to anomalous dispersion is negligible) and negligible electron density gradients across the pulse. We have found by simulation that the latter is a good approximation, if the pumping rate during the pulse is uniform.

Some very significant deductions relative to low-chirp laser design can be drawn from this equation. The ratio of the gain length to resonator length (I/L) should be as small as possible. Results of kinetics studies indicate that 50 cm is at the lower limit of what should be considered for the gain length and is baselined in our configuration. The 3-m resonator length was determined by overall laser envelope considerations and yields a gain-to-resonator length ratio of 0.16. It is advantageous to minimize the laser pulse energy/ unit discharge volume (E), and this occurs at lower cavity pressures since the discharge volume required for a given pulse energy is greater. The inverse squared dependence on the effective beam radius ($1/\sigma^2$) is a very strong contributor to low chirp and occurs at lower pressures because this requires a greater discharge volume and, hence, a wider discharge gap. Thus the incentive to go to lower pressures is very strong and is the reason we are baselining a 0.5-atm. laser. The negative aspect of a lower pressure laser is that it requires the girth of the laser to be larger, and this dependence is fully reflected in the weight trades presented earlier and in the final predicted weight for the laser subsystem.

During Phase II, the chirp for the laser configuration will be evaluated using a fully three-dimensional, time-dependent and coupled gain kinetics, fluid dynamics, and cavity electric field computer model for pulsed CO_2 lasers using an unstable resonator. Such a detailed model is necessary for accurately predicting laser waveform pulse energy, and intrapulse frequency shifts, due to transverse mode-hopping, multi-transverse mode oscillation, or changes in the refractive index (chirp). In this model, the cavity electric field is expanded in terms of the stationary (Fox and Li) eigenmodes of the bare (gain-free) cavity, with time-varying coefficients. Spatially-varying gain and/or index changes serve to couple the bare-cavity modes, and to effectively scatter

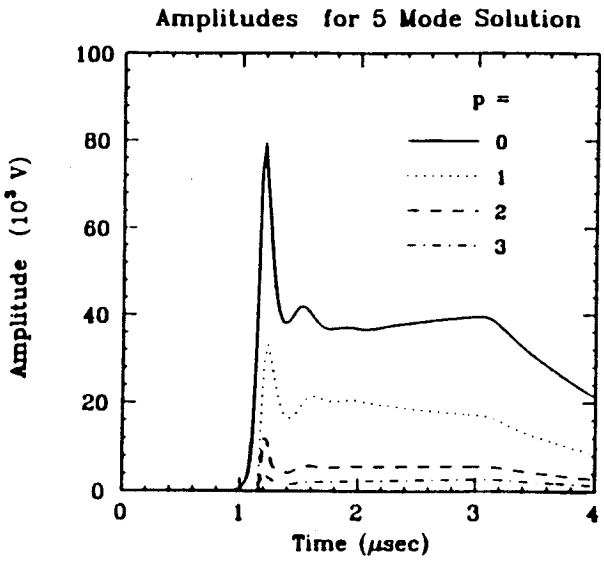

Figure 5-34a. Time Dependence of Modal Amplitudes

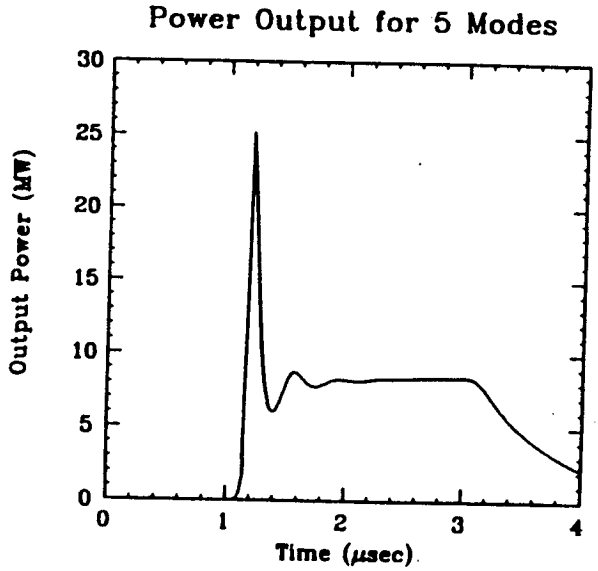

Figure 5-34b. DCM Method with Realistic Time-Dependent CO_2 Kinetics

power from mode to mode. The output from this computer model provides a detailed description of the spatial and temporal output beam characteristics of a CO_2 oscillator. An example output from this code is shown in Figure 5-34. It shows the temporal evolution of the transverse modes (upper curve) and the resultant waveform (lower curve).

5.2.1.6 *Laser Subsystem Baseline Configuration*

Our recommended baseline laser subsystem configuration is described in what follows. The major performance parameters, architecture and assembly characteristics of this configuration are summarized in Figure 5-35. As a result of the foregoing analyses, some major laser parameter selections are summarized in Figure 5-36.

Figure 5-35. Laser Subsystem Baseline Configuration

Performance Parameters:		
Pulse Energy	-	10 J
Pulse Length	-	3 μs
Pulse Repetition Rate	-	≤20 Hz (13 Hz average capability)
Architecture:		
Injection-seeded oscillator transmitter		
Fixed frequency local oscillator		
Assembly Technology:		
Self-sustained discharge		
uv-preionized (corona)		
Graded-reflectivity unstable resonator		
cw RF waveguide local oscillator		

Figure 5-36. Laser Parameter Selections

Gain section length	-	50 cm
Gain section cross-section	-	4.7x4.7 cm.
Resonator length	-	3 m
Cavity pressure	-	0.5 atm
Discharge loading	-	<200 J/(l-atm)
Pump pulse duration	-	5 μs
Gas mix	-	3/2/1($He/N_2/CO_2$)
Injection intensity	-	0.1 W/cm^2

5.2.1.6.1 LAWS Laser Schematic

An optical schematic of the LAWS laser is shown in Figure 5-37. Radiation from a low-power cw waveguide laser is line center locked and its output provided to the receiver as the local oscillator beam and also injected into the transmitter laser through the zeroth order of a Littrow grating. The cw beam, which, exits the transmitter cavity

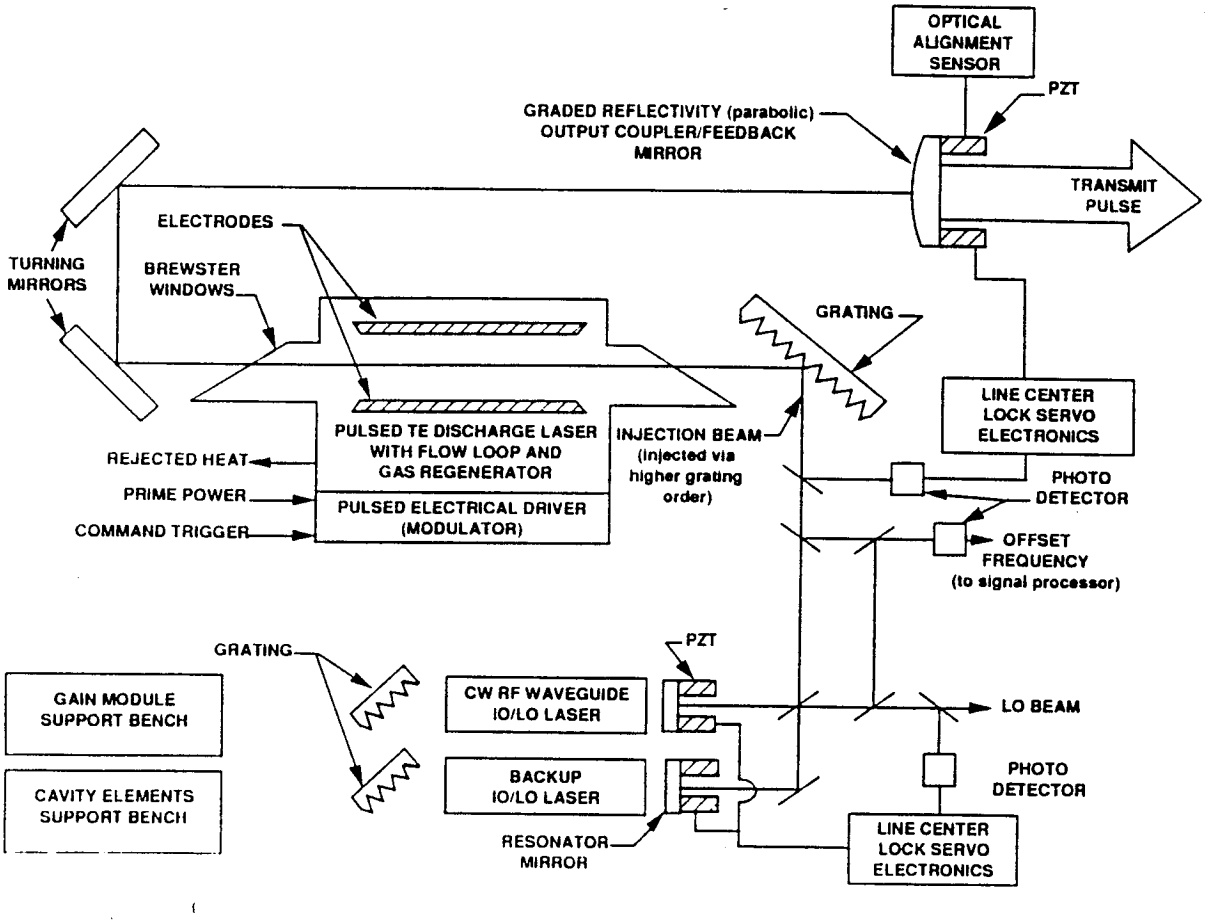

Figure 5-37. Optical Schematic Diagram of LAWS Laser Subsystem Configuration

via this path, is used to tune the transmitter laser cavity to the injection frequency via an active control circuit, while the pulsed output is processed to provide a correction for the offset between the transmitted and injection frequencies that is provided to the signal processor. In the event that the injection geometry provides insufficient isolation between the TE laser and the IO/LO lasers we will investigate the inclusion of a Bragg cell, or other isolation method, in Phase B. The lifetime of the CW waveguide laser is a possible issue and for this reason we have included a redundant CW laser. There are, however, many DoD programs which include waveguide lasers and we will continue to track developments in this area through Phase II. (Note also some recent work (Hochuli et al, 1986) which demonstrated waveguide lasers operating continuously for 30,000 hours (3-4 years).

The cavity incorporates a graded reflectivity feedback/output coupler, which we have chosen because of its superior mode properties, in particular, its mode separation margin and excellent far-field pattern properties. Optical alignment is achieved by an auxiliary alignment sensor. The gain section incorporates the TE laser head, flow-loop, gas regenerator and pulsed power. Prime power is derived from the spacecraft and

thermal control is achieved by a coolant loop connected to the spacecraft thermal control system. Command and control information is derived from the lidar system controller. The gain section is mechanically isolated from the lidar optical bench.

5.2.1.6.2 Integrated Laser Subsystem Detail

Shown in Figure 5-38 is our baseline configuration for the LAWS laser subsystem in orthographic projection and in Figure 5-39 in isometric projection. It incorporates all the elements of the schematic shown in Figure 5-37. All the gain section components, incorporating the discharge, flow loop and pulse power assemblies are enclosed in the cylinder, which is mechanically supported by six vibration isolation mounts that are attached to the sensor/platform. All the optics, injection/local oscillator lasers and control/diagnostic photodetectors are mounted on optical benches at either end of the gain section and supported by an athermal and rigid truss. The truss is in turn supported by four vibration isolation mounts that are attached to the sensor/platform. This approach decouples the optical train from the vibrations of the gain section.

5.2.1.6.3 Gain Module Cross Section

Figure 5-40 shows an isometric view of the gain module. Specific components are called out in the cross-sectional view of Figure 5-41 which shows gain module detail. The lower half of the circular cross section houses the discharge region, flow loop and fan, and half of the pulse power system. Integrated into the flow loop are the heat exchanger and Pt on SnO_2 catalyst bed. The other half of the pulse-power assembly is contained in the upper half of the cross-section.

5.2.1.6.4 Optics Assembly Detail

The arrangement of the laser subsystem optical components is shown in this end view of one of the optical benches - Figure 5-42. It conforms with the optical schematic shown in Figure 5-37. The local oscillator beam is deflected downward to the receiver by the mirror located at the lower left of the truss. The transmit pulse is directed downward toward the telescope by the mirror located at the top of the truss structure. On the opposite optical bench are the two intra-cavity mirrors that direct the beam from the discharge cavity lower level and back along the upper tube to complete the cavity.

5.2.1.6.5 Laser Pulsed Power system

The pulsed power system is required to deliver electrical energy to the laser medium in the form of an electrical discharge between two electrodes. The pulsed power system must deliver a voltage peak on the order of 60 kV to properly initiate the discharge. Once the discharge is developed, the pulsed power system must efficiently deliver approximately 120 J of energy in a 5-μsec pulse (a 5-μsec electrical pulse produces a 3-μsec optical pulse). The voltage at which it will deliver this energy will be on the order of 30 kV. The required current is about 500 amps. The required pulse repetition rate is a maximum of 20 Hz with an average rate of 13 Hz. The required lifetime is greater than one billion shots. These requirements must be satisfied within a pulsed power system package that has minimal weight and volume impact to the laser assembly.

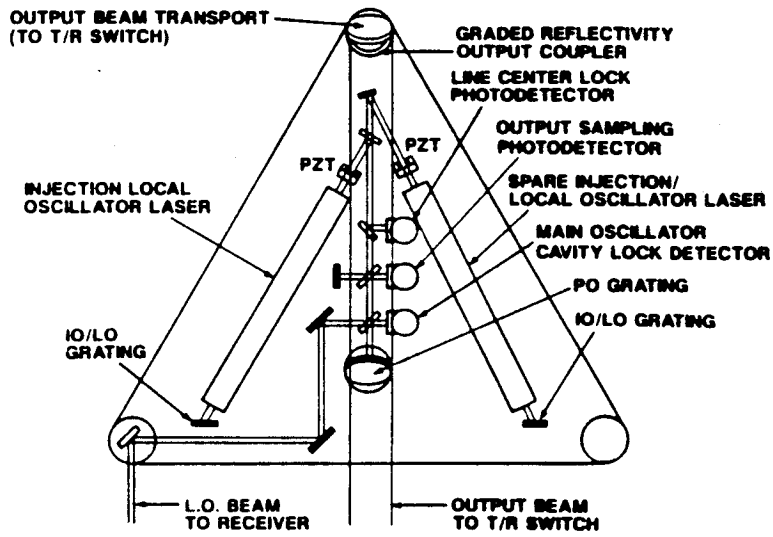

Figure 5-42. Optical Bench Detail

5.2.1.6.6 Laser Subsystem Weight Estimate

The weight trades shown hitherto were limited to that of the gain module. In addition these are to be considered as weight trends rather than absolute values. In Figure 5-43 are shown weight estimates for the total laser subsystem and major assemblies for a 20-Hz maximum pulse repetition rate based on an initial weight assessment of our baseline configuration.

	lb	*kg*
Transmitter Gain Module		
Discharge Region	25	11.4
Flow Loop	15	6.8
Pulsed Power	102	46.0
Mechanical	40	18.2
Thermal Control and Power Interfaces	10	4.5
Optical Module		
Truss	50	22.7
Local/Reference Oscillator	5	2.3
Miscellaneous Optics	10	4.5
Control and Diagnostics Module		
Servo-Loop Electronics	5	2.3
Auxiliary Electronics	5	2.3
TOTAL WEIGHT	267	121

Figure 5-43. Laser Subsystem Weight Estimate

It is assumed that low-voltage power is provided by the sensor/platform, that the fluid loop circulating pump and reservoir are provided by the system, and that the waste heat is dissipated by the sensor/platform radiator. The weights for these assemblies are not included.

5.2.1.6.7 Laser Subsystem Efficiency Estimate

Figure 5-45 summarizes the power flow-down for the laser subsystem. The estimated total for 13-Hz average operation is 2086 W of which 1986 W is taken up by the transmitter gain-module pulse-power system. The power for the fan to circulate the gas within the laser flow-loop is estimated at 17 W. Power required for the injection oscillator (assuming the back-up laser is unpowered until required) is 50 W. The controls and diagnostics hardware power requirement is estimated at 100 W. This translates to a net efficiency for the 130-W optical power output of 6%. This estimate does not include the power consumed by the thermal radiator coolant circulator. The net efficiency is given approximately by the intrinsic efficiency of the discharge (typically 15%) and normalized by the circle-to-square area ratio ($\pi/4$), accommodation for a guard-band (1-2 mm) and the pulse power efficiency (73%). The estimated stand-by power is 30 W for thermal control of the electronics and coolant.

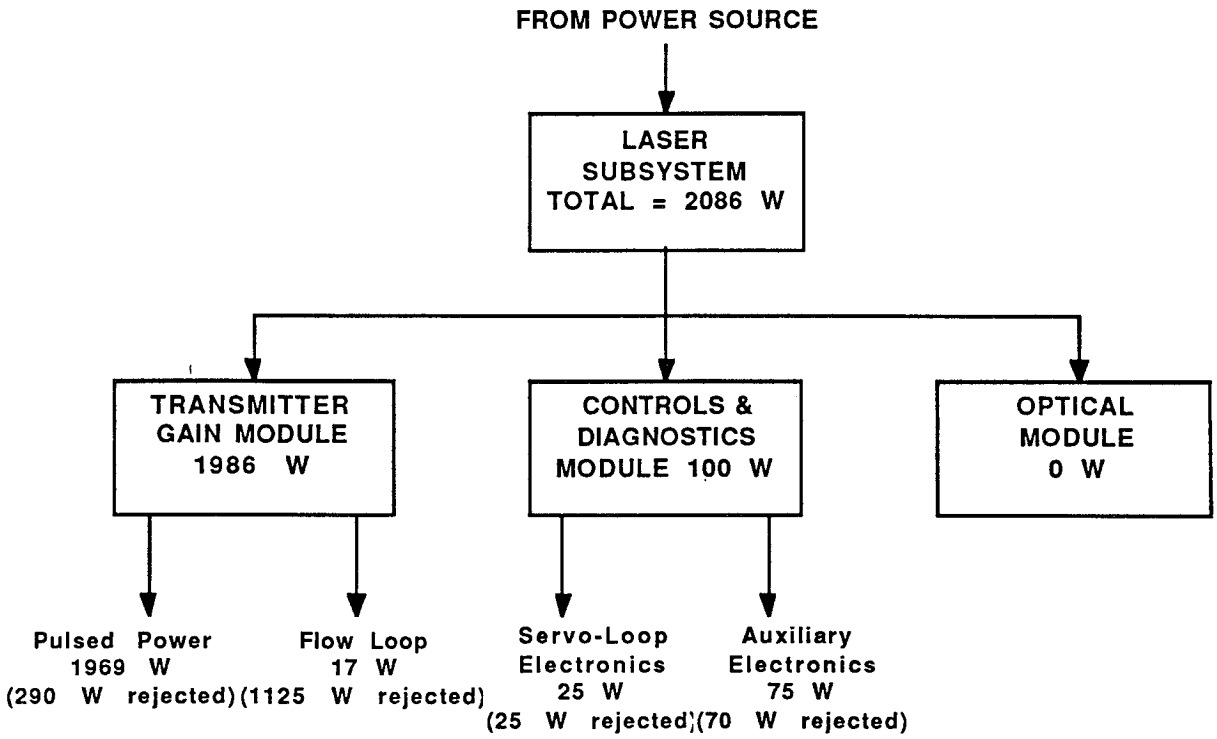

Figure 5-44. Laser Subsystem Efficiency Estimate

5.2.1.7 *Laser Subsystem Technical Issues*

The issues associated with the laser subsystem which have been identified during the Phase I Study fall into three categories. They are 1) those issues associated with using $^{12}C^{18}O_2$ in the discharge, 2) issues associated with component reliability, and 3) the verification of LAWS-scale performance and lifetime. $^{12}C^{18}O_2$ issues have been largely resolved by the MSFC/AFGL Study (Final Report "Kinetic and Extraction Measurements on $^{12}C^{18}O_2$", Spectra Technology Inc., 31 Oct. 1989, GL-TR-89-0292); catalysts for $^{12}C^{18}O_2$ continue to be investigated by NASA LaRC and others. Component reliability studies are being addressed by a number of DoD and internally funded programs, and the NASA Laser Breadboard Program will address LAWS-Scale verification.

5.2.2 *Optical Subsystem Configuration Analysis*

This section develops the configuration for the optical subsystem. A new optical design, based on confocal parabolas, is chosen and shown to be superior to the former WINDSAT design.

5.2.2.1 *Optical Subsystem Requirements Development*

The requirements shown in Figure 5-45 are the system-derived parameters that the Optical Subsystem must meet to fulfill the LAWS concept objectives. In all cases, our baseline configuration is able to meet the minimum requirements, and to approach the goals listed here.

While the fixed 45° conical scan angle is the nominal requirement, there have been discussions of varying this by ~±10°. As the trade studies clearly show, the variable cone angle could be accommodated if required, albeit at the cost of some additional weight and complexity.

The requirement for the transmit/receive function to be asynchronous rules out the previous transmit/receive concept consisting of a spinning fold mirror with a hole for the out-going laser pulse that was studied during the Windsat program. As we show later in this section, our optical configuration accomplishes asynchronous operation, and eliminates the T/R switch entirely.

Since our baseline for the configuration selection is a single detector (with surrounding alignment elements) receiver sized to the diffraction image spot size, another requirement placed on the Optical Subsystem is to stabilize the image to within 3 μradians, which, for the 1.5 m aperture operating at 9.11 μm, is 20% of the image diameter, 15 μradians.

The weight allocation for the Optical Subsystem is 350 kg., with a 300 kg. goal. The allocation is for all of the components of the subsystem, including telescope, scan bearing, mixing optics, image motion compensation (IMC) assembly and electronics, and folding optics and structure.

5.2.2.1.1 Derived Requirements

The derived requirements are shown in Figure 5-46. This list of requirements is derived from the Optical Subsystem Specification (Figure 5-45) or from the error budgets that govern the subsystem performance.

The field of view requirement is derived from the lag angle, which is in turn determined by the scan rate, cone angle, and platform altitude, as shown in the analysis presented in Appendix 5-1. For the 824 km nominal altitude, 12 RPM scan rate, and 45° cone angle, the lag angle will be 0.4° (full field). The altitude is expected to vary

by ±3% due to the non-sphericity of the Earth. The instantaneous field of view (i.e. the diffraction image spot size projected back into object space) will be ~15 μradians.

The limit on the backscatter to the laser arises from the need to prevent the pulling of the laser frequency by the presence of an (unintended) external cavity formed by the telescope optics. The 0.01% figure is an empirical number based on Spectra Technology's experience with similar systems.

The Optical Subsystem is required to stabilize the image on the detector in the presence of a number of disturbances. The spacecraft itself will jitter an appreciable fraction of the 3 μradians requirement. The laser beam will jitter in direction from shot to shot by ~1 μradian and there will be image motions caused by errors in the Optical Subsystem itself that must be compensated. The runout of the scan bearing is an example of such an error. The derived requirements chart (Figure 5-46) lists the expected magnitude of the larger disturbances. We do not expect that the image stabilization requirement can be met without active image motion compensation. The error budget (given below) sets the requirements for individual components of the Optical Subsystem and the image motion compensation configuration, described in a later section.

The absolute knowledge of the boresight relative to the velocity vector must be known for each shot in order to remove the spacecraft velocity component from the Doppler-shifted receiver signal. We will meet this requirement through a unique arrangement of sensors configured as shown later in this section.

Finally, the configuration envelope requirement of a 4.6m diameter is set by the Japanese H-II rocket shroud. It means that the total LAWS package must fit within this envelope in the launch configuration.

5.2.2.1.2 Error Budgets

An important aspect of the derived requirements for LAWS are the error budgets that are derived from the quantitative requirements given in these charts. We have prepared preliminary error budgets for the Optical Subsystem governing the boresight errors during the 8 millisecond time of flight, and the wavefront error budget that governs the quality of the optics. These budgets are shown in Figures 5-48 and 5-49. They differ from the error budgets shown previously in section 4.3.2 in that they are for a confocal parabola optical design rather than the WINDSAT design.

In several cases, the same tolerance or error affects both error budgets. In these cases, the more stringent requirement applies. A key point is the allocation for the figure quality of the primary mirror. The relatively benign requirement is the result of the change to the confocal parabola telescope design.

Additional development of these and the other error budgets is planned for Phase II.

5.2.2.1.3 Functional Block Diagram

Figure 5-49 illustrates the optical subsystem functions.

Starting with the "Telescope" block at the upper right, the outgoing laser beam is expanded by the telescope, the expanded beam being denoted by the heavy arrow pointing to the right. The path from the pulsed laser (at the upper left) is shown by the heavy line (note key at lower right on the figure). The backscattered light from the atmosphere is indicated by the arrow on the right, and the medium weight lines.

Proceeding from the pulsed laser, the first function of the Optical Subsystem is to align continuously the laser beam with the defined line of sight of the telescope. Since the direction of the laser beam will vary from shot to shot (by about 25 μrad, 1 sigma), the actual beam direction will be measured by the enhanced single detector in the receiver and an optical arrangement described in detail in the section on "Alignment

and Controls" below. This function may turn out not to be necessary once the pointing error budget is better defined. It is included here for completeness.

The function of the derotator is to stop the rotation of the outgoing and received beams around each other that is caused by the rotating telescope and the stationary laser and receiver. This function was not necessary in the Windsat optical design, but is one of the trade-offs in the afocal, confocal parabola telescope design chosen. The details of this design are described in section 5.2.2.2.

Proceeding to the right on the top line of the chart, we come to the "IMC & Lag Angle Comp". IMC stands for image motion compensation. As described in section 5.1-2 image motion will be caused by various random disturbances to the telescope line of sight, such as spacecraft attitude jitter, scan bearing jitter, etc. The function of the IMC is to correct or compensate for these motions. The technique for doing this is described in paragraphs later in this section. The lag angle is the change in direction of the line of sight of the telescope relative to the outgoing shot direction, caused by the telescope scan rotation. This deterministic angle must be compensated in order for the received radiation to fall properly aligned on the receiver.

Telescope Aperture	1.5 meters
Nadir Angle	Fixed at 45°
Rotation Rate	Fixed at 12 rpm
Weight	<350 Kg. (goal 300 Kg)
Polarization	Linear to Detector Signal and LO
T/R Switch and Lag Angle Comp.	Support Asynchronous Laser prf
Laser Feedback (Narcissus)	<0.01%
Boresight Stability During Round Trip	3 μrad (goal 1.5 μrad)
Power	<250 W
Other	No Internal Focal Points

Figure 5-45. Optical Subsystem Baseline Requirements

Telescope		
- Field of View	≤0.4°	Lag Angle
- Magnification	33x	Beam expansion
- Wavefront error	λ/13 rms	Difraction limit
- Backscatter to laser	< 0.01%	Laser stability
Accommodate image motion disturbances		
- Allowable uncompensated errors	< 1.5-3 μ radians	See error budget
- External Disturbances	~180 μ radian	Lag Angle and Pitch Rate + Random Spacecraft Attitude
- Laser beam jitter	~1 μ radian	

Figure 5-46. Optical Subsystem Derived Requirements

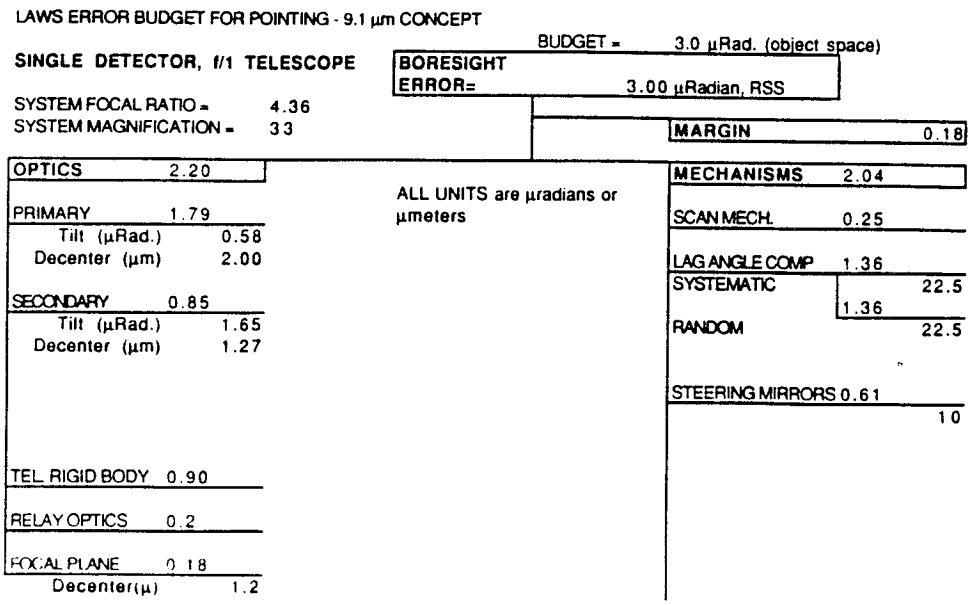

Figure 5-47. Boresight Error Budget

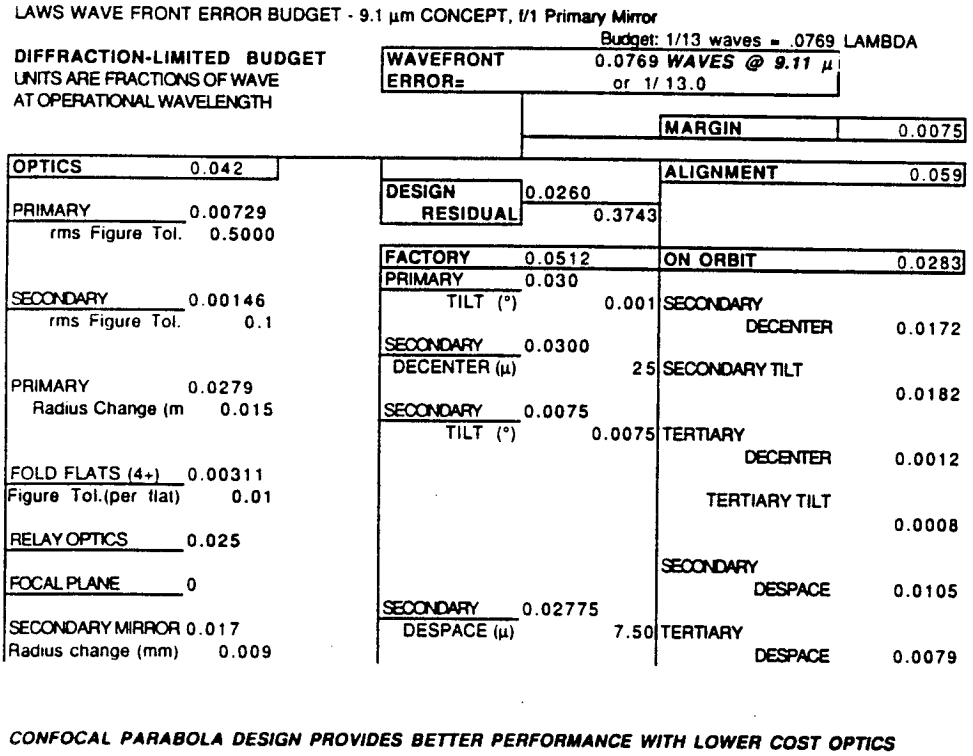

Figure 5-48. Wavefront Error Budget

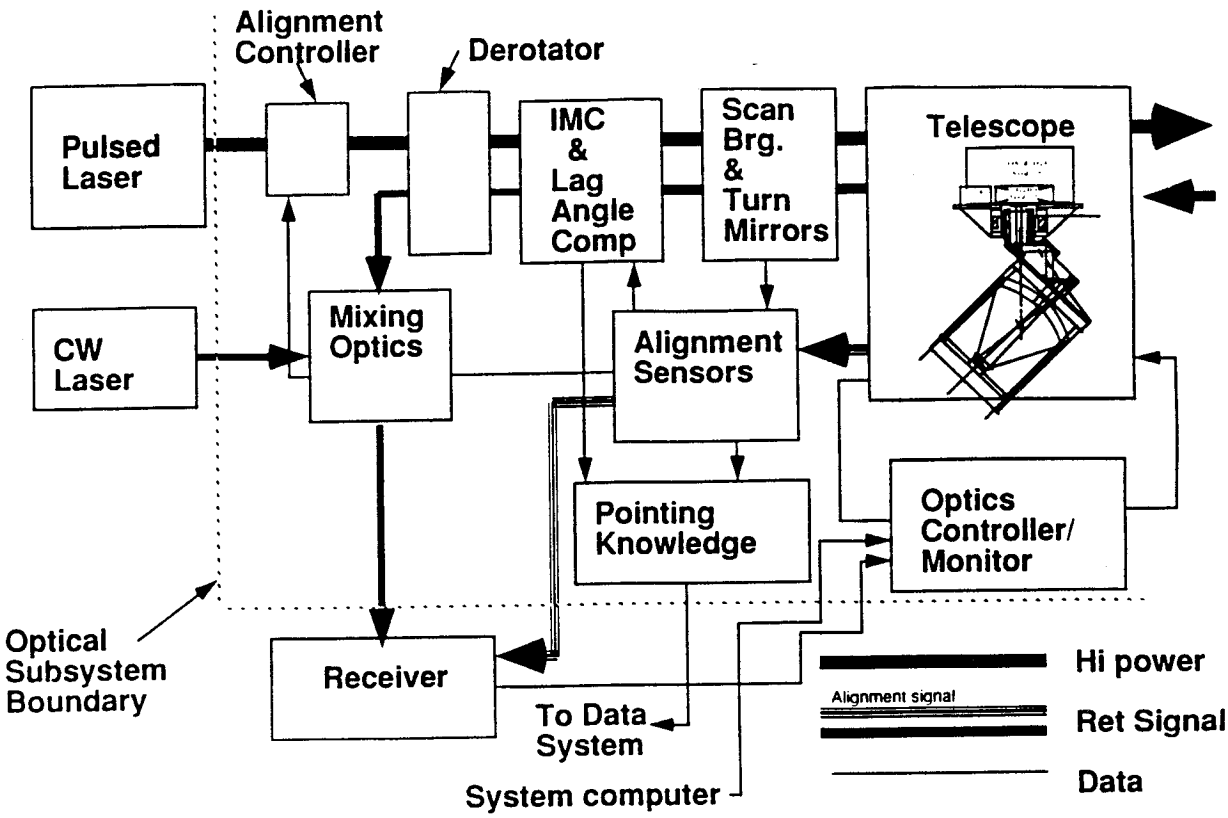

Figure 5-49. Optical Subsystem Functional Block Diagram

The next block to the right in the diagram "Scan Brg. & Turn Mirrors" represents the main azimuth bearing that allows the telescope to perform the conical scan. The scan bearing also contains a drive motor and position encoder. The turn mirrors fold the outgoing and incoming beams so that they will fit through the scan bearing bore, and in our recommended configuration, also correct for the largest component of the lag angle.

The "Mixing Optics" block denotes the heterodyne mixing function. The local oscillator ("CW Laser" in the diagram) is combined with the received beam through a beam splitter, and this block also contains the final focussing lens that forms an image on the receiver.

The "Alignment Sensors" block represents the detectors, mirrors and other references for acquiring and providing the necessary corrective signals for the alignment controller. Again, the details of our configuration are explained in paragraphs below.

Since it is necessary to remove from the signal the Doppler shift caused by the component of spacecraft velocity along the line of sight, a measure of the pointing direction for each shot must be made. That is the function of the block labelled "Pointing Knowledge". Signals from the scan bearing azimuth angle and the IMC will be combined with attitude signals from the spacecraft to give the required pointing knowledge signal for delivery to the system controller.

The final block on the diagram (lower right) is the "Optics Controller/ Monitor". The purpose of this function is to interface with the system controller, enable initial on-orbit optical alignment (focus, secondary mirror decenter and tilt) adjustments, and periodic re-alignment, as required. The error budgets indicate the need for such alignment adjustments, and the state of technology is adequate for achieving the performance goals of LAWS. A configuration for measuring the optical alignment is described later in this section.

5.2.2.2 *Optical Design Configuration*

As stated previously, we determined that an optical design that requires no focal points in the optical train would be highly desirable since the cost of testing the LAWS system in air would be much less than tests in vacuum. Primarily for this reason, we sought alternatives to the Windsat optical design, since it requires two internal focal points.

The primary advantage of the Windsat design is that it does achieve a common optical path through most of the system by compensating for the lag angle at the pupil image formed by the tertiary mirror. This feature may provide some advantages for the maintenance of optical alignment. However, the Transmit/Receive function is performed by a motorized "switch" that consisted of a spinning mirror (spin axis normal to the mirror and at 45° to the beams) with a through hole near the periphery. The mirror spin position and rate was to be synchronized to the out-going laser pulses so that the receive beam would pass through the hole. The spin speed was to be adequate to assure that the hole was out of the way when the laser was fired, so that its beam would always be reflected from the mirror. A disadvantage of this scheme is that it would be very difficult to operate asynchronously, since the spinning mirror would be required to speed up and slow down to match the laser shot commands.

We considered a number of possible optical designs with no internal focal points, (or "afocal" designs). These designs and their relative advantages and disadvantages are listed in Figure 5-50.

Figure 5-50. LAWS Optical Design Choices

Design	Comment
1. Parabolic primary and secondary, coma-compensated secondary for beam steering, pivoted about focus	Too much astigmatism and defocus
2. Any design, pupil on secondary	Too much beam walk on primary
3. Two parabolas, coma compensated secondary pivoted about vertex for beam steering	Too much astigmatism and defocus
4. Two confocal parabolas with two flats for beam steering	Need to correct defocus (move secondary? Detector?)
5. All three mirror systems	Internal focus

The chart shows the superiority of the Confocal Parabola design (which was also selected for the SCALE experiment.). The optical schematic is shown in Figure 5-51.

We evaluated the Windsat and the confocal parabola design by rating each against a number of specific selection criteria. These criteria and the relative evaluation scores

are shown in Figure 5-52. This rating procedure shows quantitatively why the confocal parabola design is selected as the baseline design.

In the confocal parabola design, the lag angle will cause the transmit and receive beams to separate by a large angle for any appreciable scan rate. With a telescope magnification of 33x, the lag angle (typically 0.1° to 0.5°) will cause a beam separation of 3.3° to 16.5°. At the primary mirror, the beams will be separated by more than their diameters: 86mm - 432mm, respectively. This separation permits us to delete the T/R switch and all of its weight, complexity, as well as its inflexibility of operation. The beams are steered by the fold mirrors so that they are parallel and close together for passage through the rotating scan bearing.

The most important advantage of the confocal parabola design is its superior optical performance, being free of all third-order aberrations, except for field curvature. For a single detector, the field curvature can be accommodated by a pre-determined focus shift of the final focussing lens (or shift of the detector itself). With essentially zero optical aberrations, the optical manufacturing error budget can be opened up, alleviating the optical tolerances, decreasing the manufacturing cost and avoiding the tight optical alignment tolerances of the Windsat design.

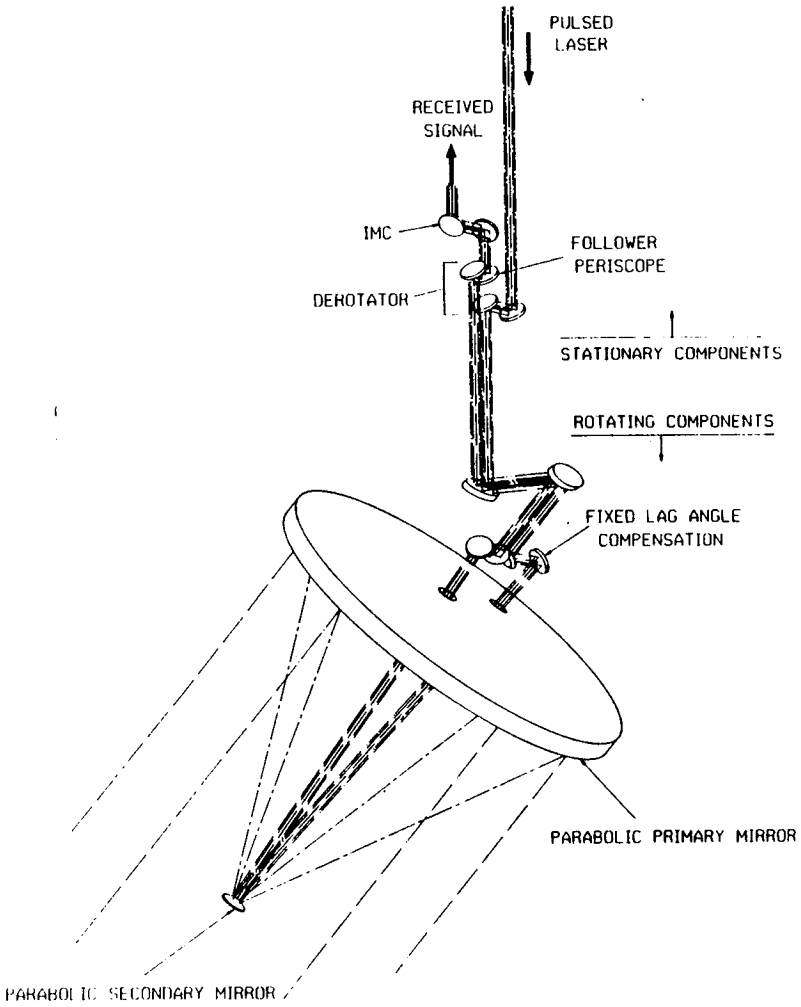

Figure 5-51. Confocal Parabola Optical Schematic

5.2.2.2.1 Polarization Considerations

The current heterodyne detection concept for LAWS is similar to an unequal path interferometer. As such, it will experience degraded performance if polarization-producing phase shifts at mirror reflections are not minimized by the optical coating design, or compensated for by the optical design.

The local oscillator will be linearly polarized, as will be the pulsed laser. LAWS performance will be degraded if the polarization of the back-scattered signal at the detector plane differs from the local oscillator. For example, a linearly polarized light wave can readily be changed to an elliptically-polarized beam by non-normal reflection from a dielectric material or a metal (or a combination of both). This occurs because a relative phase shift will be imparted to the s- and p-components of the light due to a thin film coating or a complex index of refraction. If the accumulated phase shift should reach 90° after passage through the optical system and back again, the return light will be circularly polarized and a reduced signal will be detected.

A design rule for avoiding this potential degradation can be stated as follows[1]: Each beam of an interferometer must experience reflection with the same sequence of direction cosines between the point where the beam is divided and the point where it is combined.

Clearly this rule cannot be applied to LAWS, since the rotating telescope will continuously rotate the fold mirrors in the telescope relative to those in the reference local oscillator beam, which is stationary.

We are left with a requirement to design the reflective coatings with zero or minimal phase shift characteristics, or to compensate for the polarization changes caused by the rotating telescope by intentionally and continuously altering the polarization of the local oscillator.

We have the in-house capability of designing suitable coatings, and we also have the analysis capability[2] for determining the effects of polarization on the performance of the entire LAWS system. This analysis will be performed during Phase II when the optical and mechanical design is sufficiently mature.

5.2.2.2.2 Optical Feedback to Laser

As shown earlier in the requirements, the LAWS optics must reflect less than 0.01 % of the laser energy back into the TEM_{00} mode of the laser. To determine the magnitude of the feedback the laser may be modeled as a spatial filter of diameter $4\lambda/D$. Our results show 1.5×10^{-6} of the laser energy being specularly reflected back into the laser from the vertex of the secondary mirror. This is almost two orders of magnitude below the requirement; hence specular optical feedback from the telescope will not impact the LAWS performance. Scattered radiation from folding flats or beamsplitters in the beam will be investigated during Phase II as another possible source of feedback radiation.

The above result is based upon the assumption that the laser beam incident upon the LAWS telescope secondary mirror is a Gaussian beam of diameter D_L = 45mm as defined by the $1/e^2$ points in the Gaussian distribution (See Figure 5-53).

If the expanded Gaussian beam is truncated by the F/1 telescope primary mirror (D_p = 1.5 meters) at the $1/e^2$ points, the angle θ_m is given by

---

[1] Wesley A. Traub, *Polarization Effects in Stellar Interferometers*, Private communication

[2] Eugene Waluschka, *Polarization Ray Trace,* Optical Engineering, February 1989, Volume 28, Number 2, Pg. 86.

$$\theta_m = \tan^{-1} (D_p/2f) = \tan^{-1} (0.5) = 26.6\ ^\circ \quad (1)$$

The Gaussian intensity distribution reflected from the secondary mirror can thus be written as

$$I(\theta) = \exp[-2(\theta/\theta_m)^2] \quad (2)$$

We are now concerned with the fractional encircled energy contained within the angular radius, θ', that can produce feedback in the laser

$$\theta' = 2\lambda/D_L = (2)\ (9.11 \times 10^{-3}\ \text{mm})/45\ \text{mm} = 0.023^\circ \quad (3)$$

Since the fractional encircled energy of a Gaussian beam is given by one minus that Gaussian evaluated at the radius of concern

$$EE(\theta') = 1 - \exp[-2(\theta'/\theta_m)^2] \quad (4)$$

we obtain the result stated above in the summary that

$$EE(\theta') = 1.5 \times 10^{-6} \quad (5)$$

SELECTION CRITERIA	Weighting	Windsat	Confocal Parabola	Comment
BEAM QUALITY	5	5	45	
INTERNAL FOCUS (in laser path)	5	0	50	
COMPLEXITY	3	9	21	More parts for Windsat
ACCOMMODATION OF:				
• 3% ALTITUDE VARIATION	2	14	6	Larger IMC in confocal
• JITTER	2	12	8	
• VAR. SCAN RATE	1	7	3	
DIFFICULTY OF IMC	3	21	9	
THRUPUT	2	8	32	Smaller obscuration
LASER FEEDBACK	4	4	36	
ASYNCHRONOUS OPERATION	4	8	32	
SCORE		88	222	

CONFOCAL PARABOLA IS SUPERIOR TO WINDSAT DESIGN

Figure 5-52. Optical Design Evaluation Scores

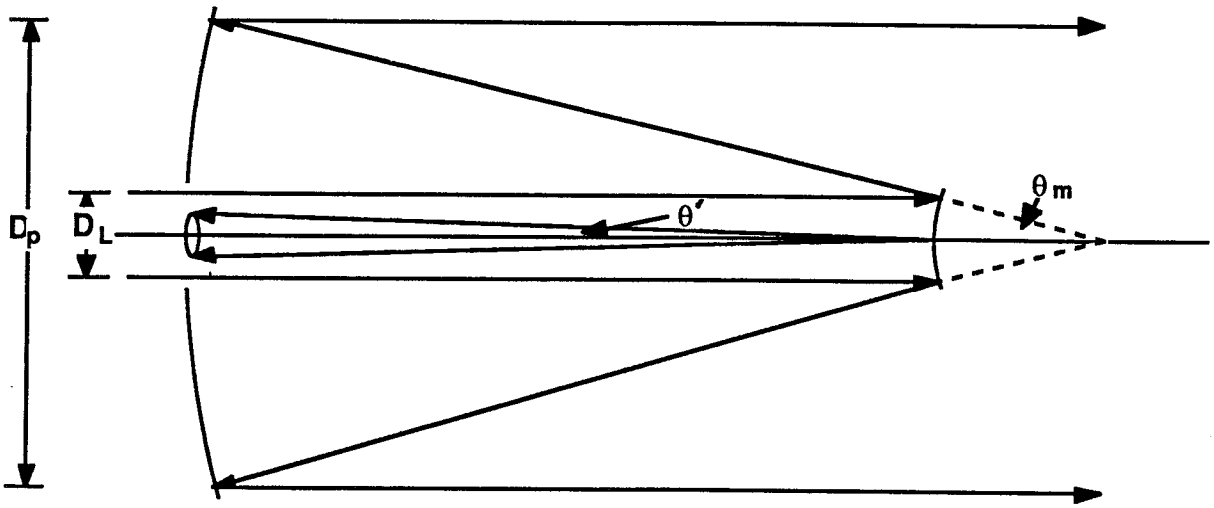

Figure 5-53. Optical Feedback Schematic

5.2.2.3 *Telescope Scan Configurations*

Several mechanical scan configurations, shown in Figure 5-54, have been investigated in order to determine the optimum approach for the design of the Optical Subsystem. In this trade, both functional and nonfunctional requirements were considered for the evaluation criteria. These criteria included such items as weight, compatibility with our baseline optical form, launch vehicle envelope constraints, etc. Figure 5-55 is the evaluation trade matrix for the different scan configurations.

As can be seen by this evaluation, we are recommending the spinning telescope configuration as our baseline design approach. Several important aspects of this configuration vs the other two should be pointed out. With the relatively aggressive weight allocation to the Optical Subsystem, weight is an extremely important criteria. The spinning flat configurations add additional weight to the system because of the need for the scanning flat to be properly sized (on the order of 1.6 m). If this requirement is combined with the fact that the flat has to be fabricated to extremely tight tolerances to avoid large aberrations (i.e., astigmatism), this further discredits these options. Another advantage to the spinning telescope is the ability to implement a thermal control system around the telescope. The other approaches do not readily allow this to be implemented. The disadvantage to the spinning telescope is the large rotating inertia (and therefore momentum) which adds to the disturbance profile. However, with dynamic balancing and the addition of a contrarotating momentum wheel the disturbance torques should be manageable.

5.2.2.3.1 Rotating Telescope Trades

The next step in the selection process was to consider options for the rotating telescope configuration. There are two approaches which we investigated. The first being the Windsat design. The second the "CG" mounted design. Shown in Figure 5-56, these two approaches share a common Telescope Assembly but depart from one another in the method by which the Telescope Assembly is rotated. As was the case for the scan

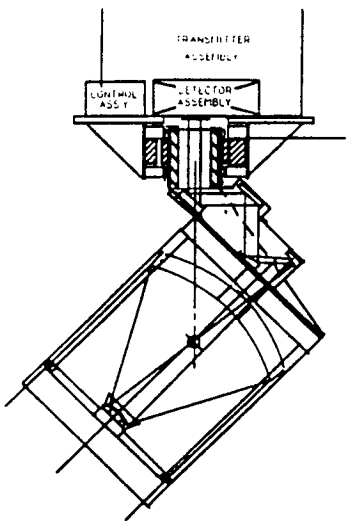

Spinning Telescope

- Minimum weight
- *Large momentum*

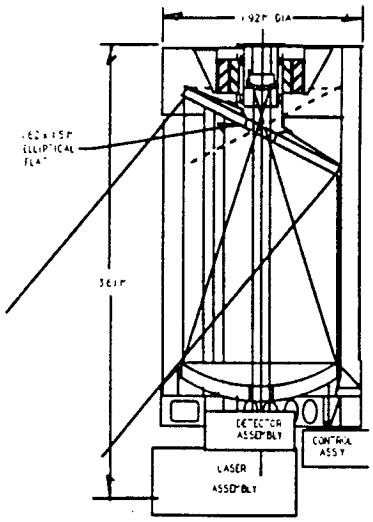

Spinning Flat with Cassegrain

- Minimum momentum
- *No thermal baffle*
- *Laser supported on optical metering structure*

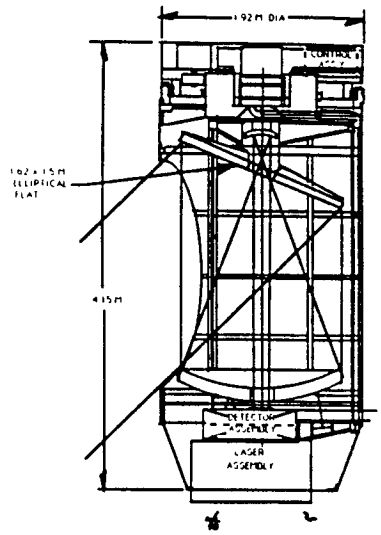

Spinning Telescope with Gregorian

- Adequate thermal baffle
- *High weight*
- *Difficult interface*

Figure 5-54. Mechanical Scan Configurations

configuration trades, the weight criteria plays an extremely important role in this evaluation. This is even more evident as shown in Figure 5-57. This evaluation trade matrix highlights the fact that if we did not consider weight, the CG-mount approach would be the preferred configuration. However the additional 121 kg needed to implement this design far exceeds the weight budget (detailed weight estimates follow). However, If LAWS requires a variable pitch angle (this is currently considered a desirement not a requirement), the recommended approach certainly becomes the CG-mounted design. In order to accommodate the variable pitch capability with the end-mounted design, some type of yoke structure is required. This implies two changes; the first being additional weight and complexity, the second being additional structural compliance which will lower the systems' natural frequency and therefore impact the telescope launch induced environment along with on-orbit, higher frequency performance degradation.

Weighting Factor	Selection Criteria	Candidate Approaches: Spinning Telescope	Spinning Flat w/Cassegrain	Spinning Flat w/Gregorian
5	Weight	5/25	2/10	1/5
4	Optical Form Compatibility	5/20	3/12	1/4
3	Envelope	4/12	4/12	3/9
3	Thermal Control	4/12	2/6	2/6
3	Interface Compatibility	4/12	2/6	3/9
3	Dynamic Response	2/6	4/12	4/12
4	Complexity	3/12	3/12	2/8
5	Risk	3/15	1/5	1/5
	Totals	114	75	58

Figure 5-55. Scan Configuration Trade Matrix

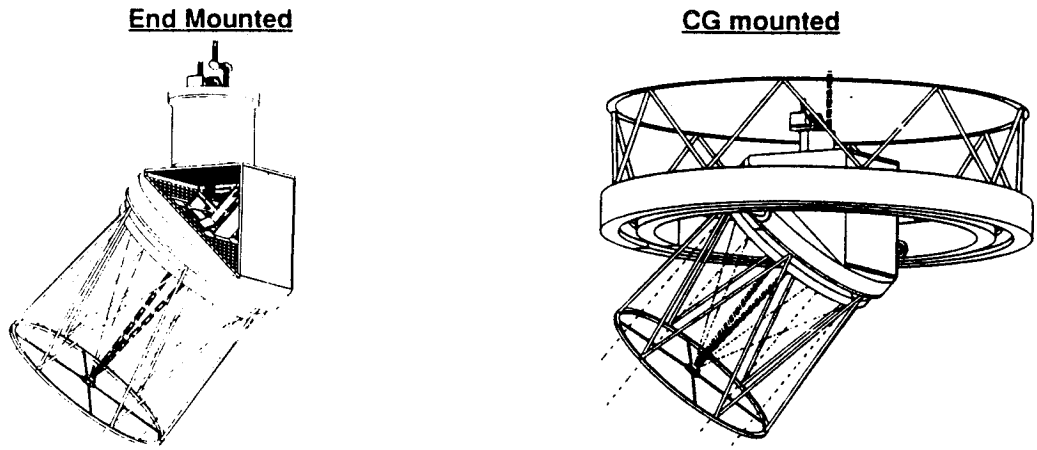

Figure 5-56. Rotating Telescope Candidate Configurations

Weighting Factor	Selection Criteria	Candidate Approaches: End-Mounted Telescope	Candidate Approaches: CG Mounted Telescope
5	Weight	5/25	1/5*
3	Power Req'd	3/9	3/9
3	Envelope	2/6	3/9
2	Wobble (Low Frequency Error)	2/4	3/6
4	Jitter (High Frequency Error)	3/12	2/8
2	Launch Lock (caging) Accommodation	1/2	4/8
3	Cantilever Action	1/3	5/15
2	Stiffness	2/4	3/6
2	Low Scan Rate	1/2	4/8
2	Wear Rate	3/6	2/4
4	Complexity	3/12	2/8
5	Risk	3/15	2/10
4	Pitch Angle Accommodation	(2/8)**	(5/20)**
	Totals	100	96

Notes: * exceeds the top level requirement.
** selection criteria not included in evaluation score.

Figure 5-57. Spinning Telescope Trade Matrix

The leading two alternatives for a variable nadir angle design are shown in Figure 5-58. One is the classic, ground-based astronomy telescope configuration, the end mounted/yoke design. It can use the same scan bearing arrangement as our recommended baseline configuration. However, the weight of the yoke is excessive when compared to the fixed end mount design. In addition, the expected normal modes of deflection of the yoke (i.e. "tuning fork" mode) could be very serious to the optical alignment of the primary mirror. Finally, a caging mechanism for this configuration would be difficult to implement.

The CG mount/Roll ring configuration lends itself to the addition of a limited-range variable nadir angle. It is very stiff dynamically. The design enjoys the heritage of the Apollo Telescope Mount (ATM) design for MSFC's Skylab program, and the same launch lock and caging concept would be applicable.

If the required nadir angle becomes large, the ring diameter must be increased, adding to the weight of the design.

Referring again to the trade matrix, several other salient points should be noted. In general, performance parameters suggest that the CG mount design is the preferred approach while power requirements are a "wash" because one trades bearing loss (end mounted) versus motor efficiency (CG mounted). The complexity and risk tend to favor the end mount. However, as mentioned above, we have successfully flown a similar CG-mount design for the Apollo Telescope Mount (ATM), a part of the MSFC'S Skylab Program.

As might be expected from this discussion, there was not a clear cut winner in this evaluation. However, based on the requirements as we currently understand them, the end-mounted, Windsat design was chosen as the baseline. Both configurations, however, will be carried into the next phase of the program. Additional methods to reduce the weight of the CG mounted approach will be undertaken along with continuing the dialog concerning the need for a variable pitch angle capability. In either case, if this capability does become a requirement, the weight allocation to the Optical Subsystem must be increased to accommodate the inherent structural members, mechanisms, and hardware associated with a variable nadir angle.

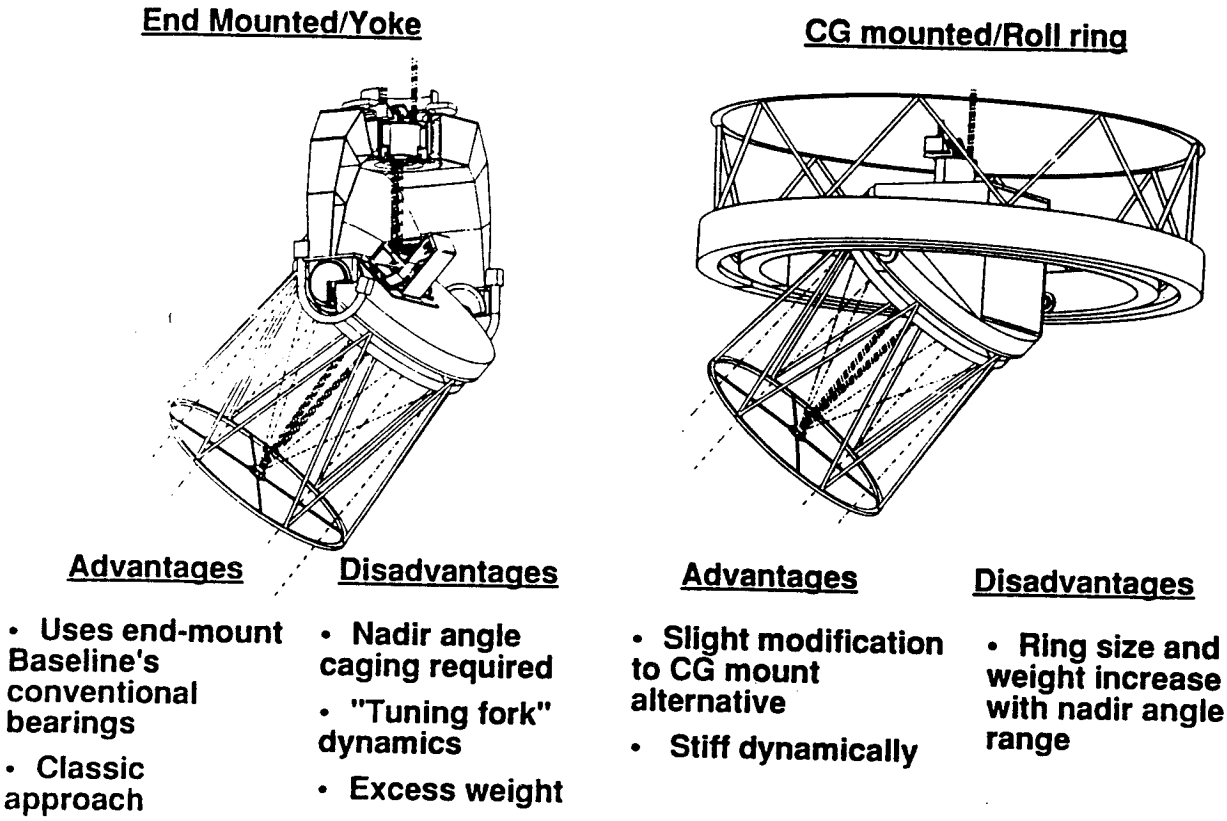

Figure 5-58. Variable Nadir Angle Alternatives

5.2.2.4 *Baseline Configuration*

This section describes in detail the configuration of the optical subsystem concentrating on the telescope optical and mechanical design. The alignnment and controls part of the optical subsystem is covered in section 5.2.2.5.

5.2.2.4.1 Mechanical Description

Our baseline end-mounted Laws Optical Subsystem is shown in Figure 5-59. This isometric layout together with the top level hardware family tree (Figure 5-60), shows the Optical Subsystem composed of essentially five distinct assemblies. These five assemblies when integrated, must meet the derived mechanical requirements as shown in Figure 5-61. Preliminary performance predictions against several of these requirements are also shown in Figure 5-61.

The following is a description of the components and the materials selected for the five major assemblies which comprise the Optical Subsystem.

The Telescope Assembly

Comprised of the Primary Mirror (PM), Secondary Mirror (SM), and Metering Structure Sub-Assemblies, the Telescope Assembly forms the core of the Optical Subsystem. The PM is fabricated from HIPP'ed Beryllium, which represents a low risk, low weight, high stiffness approach to the PM design. Its f/1, 1.5 m clear aperture is consistent with several HIPP'ed beryllium optics which we have recently fabricated for two other in-house programs. Because of the overall weight criticality, beryllium appears to be a natural choice although other lightweight materials will be considered in Phase II.

The PM is kinematically attached to its mount ring via three sets of bipod flexures. These flexures which are attached at three places on the PM, have their lines of action at the PM's center of gravity. This is done in order to minimize any overturning moments which tend to distort the optic. The PM and its flexures are supported by a light weighted, high inertia graphite-epoxy mount ring. This mount ring provides the "back-bone" of the entire Optical Subsystem. Therefore, it must provide enough strength and stiffness to ensure structural integrity during ascent events. Additionally it must remain thermally stable during on-orbit operations. The graphite-epoxy chosen, P75S, is a standard isotropic layup which has many space-borne optical system applications. We have been working closely with its manufacturer, Composite Optics, Inc in San Diego, so that our configurations are compatible with their manufacturing techniques.

The SM and Metering Structure Sub-Assemblies complete the Telescope Assembly. The SM, fabricated from low expansion glass (i.e. ULE, Zerodur, etc) is mounted to its optical bench via six actuators. Currently the 3 degree-of freedom (dof) capability needed can be accommodated by utilizing several SM/actuator designs currently in hand. The six linear actuator configuration provides 2 dof's that are not required for LAWS. However, on several other in-house programs (i.e. Orbiting Solar Laboratory) after much time and effort was expended, it was determined that it is less difficult and costly to use a six actuator design approach. The six actuator approach exploits the cost-effective and proven technology for the LAWS recommended baseline. The Metering Structure is currently baselined as a one-bay "zigzag" truss with closure ring at either end. Fabricated from P75S, it serves as a thermally stable structure between the PM and SM, it supports the SM spider assembly, as well as supporting the thermal enclosure (including multi-layer insulation (MLI)). As seen in Figure 5-62, preliminary analyses have been conducted to investigate optimum truss structures. During the next Phase, we will be continuing this evaluation and include a ring-stiffened tube structure as another viable option for the Metering Structure design.

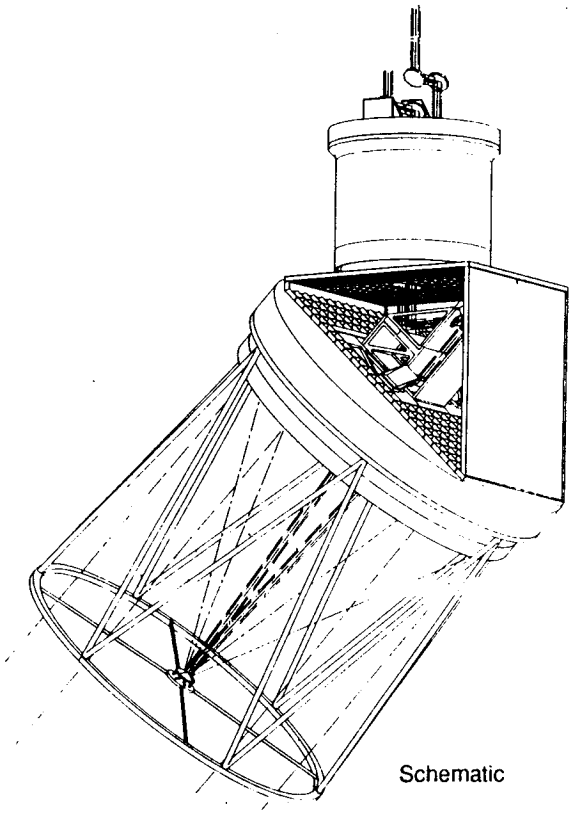

Figure 5-59. Baseline LAWS Optical Subsystem

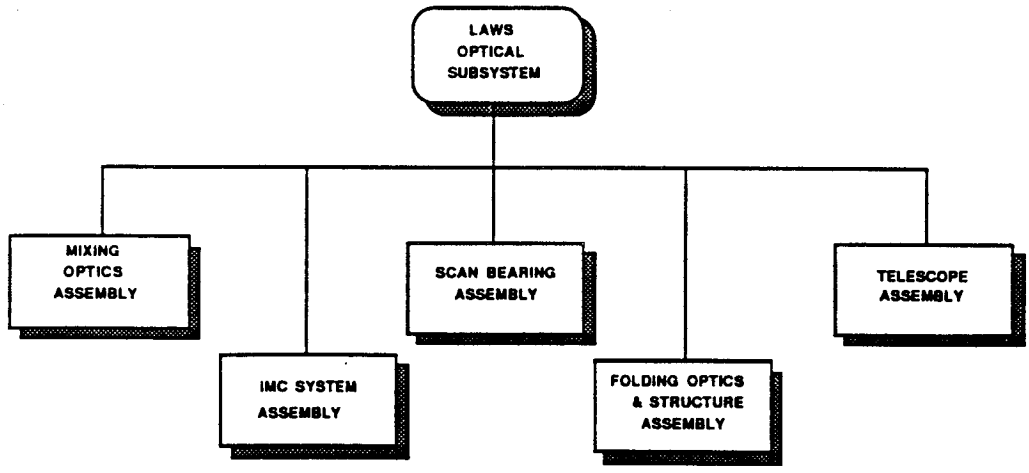

Figure 5-60. LAWS Optical Subsystem Top Level Hardware Family Tree

Item	Requirement	Comments	Performance Prediction
Fundamental Frequency	> 50 Hz	Above L.V. Forcing Func.	75 Hz
Total Power	< 200 watts	Thermal Control, Br'g Motor, Mechanisms	180 watts
Total Weight.	< 350 kg	Includes Contingency	334.4 kg
Bearing Wobble	TBD m-rad	Abs. Know. of Boresight	TBD m-rad

Figure 5-61. Derived Mechanical Requirements

Folding Optics/Structure Assembly (FO/SA).

Located immediately in back of the PM mount ring, the Folding Optics/Structure Assembly serves two purposes. Its first purpose is to house four sets of periscopes which allows the transmit and receive signals to follow the correct path to and from the laser/receiver. This is accomplished by integrally machined optical bench which allows alignment between periscopes to be accomplished off the "mainline" of the telescope assembly integration flow. Once these periscopes are properly aligned, the integrated optical bench assembly is then aligned to the telescope assembly. This is accomplished by using the PM mount ring as the reference surface. If necessary, alignment adjustments (six dof's) can be accomplished by shimming. The second purpose of this assembly is to provide a transition structure between the Telescope and the Scan Bearing Assemblies. This structure, also fabricated from P75S, is a closed box section with cutouts in the mount ring interface plate and in the Scan Bearing interface plate to allow the nominally 4.5 cm beams to pass.

Within the hardware family tree (Figure 5-60), the derotator and its associated electronics are included in FO/SA Assembly. The derotator's purpose is to accommodate the rotation of the spinning telescope while coupled to the stationary laser transmitter and receiver. As shown earlier in the optical design description, our design eliminates the transmit/receive switch by having separate optical paths for the transmit beam and the receive beam. Since these beams are laterally separated at the scan bearing, they will rotate around each other. The derotator renders the two beams stationary on the spacecraft side of the scan bearing.

The selected derotator configuration is based on a simple follower periscope. The transmit beam is folded down the axis of the scan bearing, as shown in Figure. 5-63, rendering it stationary. The receive beam is parallel to the transmit beam and offset by one beam diameter plus enough to accommodate the edge bevels of the fold mirrors. The receive beam rotates around the stationary transmit beam as viewed from the stationary side of the scan bearing. The "follower" periscope views the receive beam through the window shown in the diagram. A window is necessary to support the central fold flat that folds the transmit beam, since the return beam rotates completely around the transmit beam. (A spider could be used to support this fold flat, but would obscure the receive beam at parts of the azimuth. The idea was rejected for this reason.)

The rotating follower periscope aligns the receive beam to the scan bearing spin axis where it is stationary. The follower periscope rotates on its own set of bearings at the same speed as the telescope. The periscope has the property of forgiving small

amounts of rigid-body tilt, which alleviates the bearing tolerances for its bearings and drive.

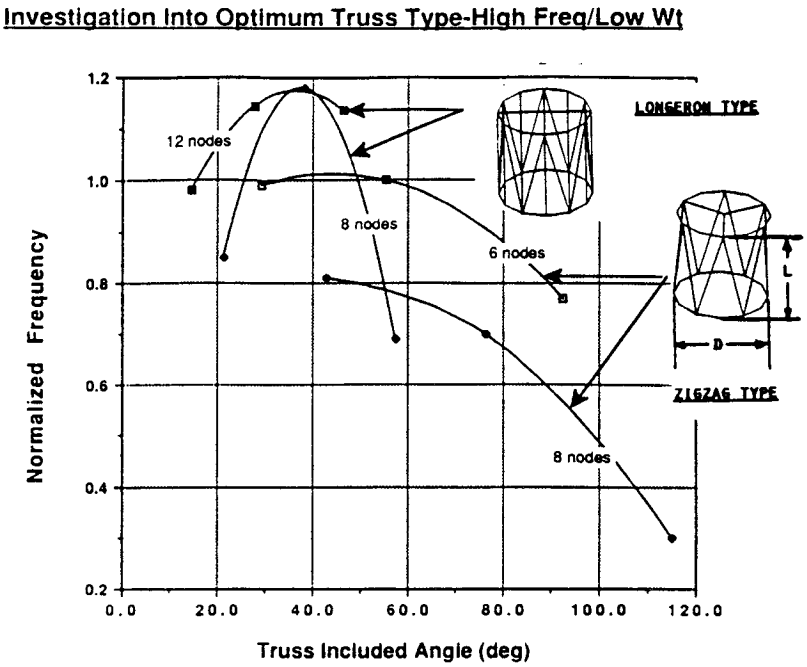

Figure 5-62. Investigation into Optimum Truss Type-High Frequency/Low Weight

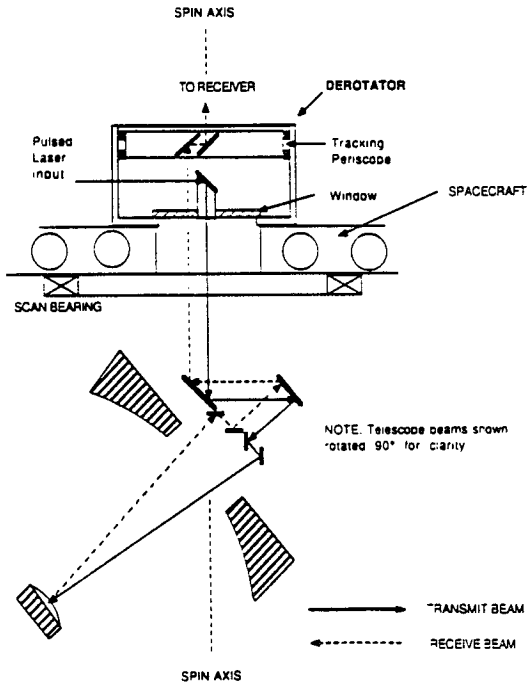

Figure 5-63. Derotator Configuration

ORIGINAL PAGE IS
OF POOR QUALITY

Scan Bearing Assembly (SBA).

The Scan Bearing Assembly drives the rotating telescope at nominally 12 RPM over the 5 year lifetime of the program (approximately 25 million cycles). This assembly can be divided into the stationary, rotating, and position sensor sub-assemblies and is considered the most demanding assembly to design and fabricate because of its relatively tight requirements and large size. Specifically, bearing radial run out and jitter induced noise must be minimized and structural stiffness must be high to maintain fundamental frequency.

Currently, both the stationary and rotating housings are fabricated out of 9.5 mm thick beryllium. The beryllium was baselined in order to minimize weight for the specific diameter which was chosen. Our baseline design uses "typical" ball bearings with steel inner and outer races (i.e., Kaydon Corporation model KF250ARO). The potential concern is alleviated by simply flexure mounting the bearings to the aluminum housings. The bearings (one duplex, one single) will probably be a special order due to our tight boresight error allocation.

A "wrap-around" torquer motor will be used as the driver for the rotating telescope. We have investigated both brush and brushless types of motors for the LAWS application. The brushless type has been baselined for our Optical Subsystem due to its high reliability and good performance characteristics. This motor will also be a "special" but a representative motor is a Magnetic Technology 16000-280 brushless d.c. motor with an inside rotor using a rear earth magnet.

Position Sensing will be accomplished via a rotary Inductosyn transducer located very close to the torquer motor. It is located in this position so that there will be no loss of position between the motor and Inductosyn due to on-orbit disturbances. A trade was made on an optical encoder versus a rotary Inductosyn for position sensing. Because of its large size (i.e., alignment concerns with the optical pattern) and because of the simplicity, high reliability in space application, the Inductosyn was baselined. We have been using Farrand Controls Inductosyns as a basis for our mechanical layouts.

IMC Assembly

The IMC Assembly is composed of the IMC and the Alignment Sensor and Controller. The different alignment schemes which we have investigated have been addressed earlier and therefore only the IMC Sub-Assembly will be addressed here. Basically, this sub-assembly is composed of a 2 dof dynamic mirror driven by voice coil actuators which receives its command from a closed loop, high bandwidth servo system. The mirror is fabricated from glass and is mounted to its mounting bracket in a kinematic fashion. In order to get the receive signal to the receiver a fold flat/mounting bracket is also required.

Mixing Optics Assembly

The purpose of this assembly is two fold. First, it mixes the local oscillator beam with the receive beam (accomplished by a beam combiner and LO lens) and then takes this collimated beam and illuminates the receiver with this signal using a detector lens. The mechanical aspect of this assembly is to provide mounting hardware and bracketry on the receiver side of the physical interface.

5.2.2.4.2 Weight Estimates

Detailed weight estimates have been made for both the end-mounted and CG mounted configurations. Shown in Figures 5-64 and 5-65 respectively, these estimates are based on strength, frequency, material considerations, thermal environment, and ease of assembly. As can by seen by these two figures, the end-mounted approach meets the weight allocation with a margin of approximately 16 kg (35.2 lbs). This includes a "built-in" weight contingency of 18% which we use based on historical data which

investigates contingency factors as a function of program maturity. Center-of-Gravity calculations have been made on the end-mount configuration to ensure that the CG is located on the axis of rotation. Of course as the design matures, the CG will move slightly. However. this configuration allows the rotating portion of the Optical Subsystem to be shifted accordingly. These changes will have minimal impact on the overall design.

Figure 5-65 shows that for the CG mounted configuration, the weight budget allocation of 350 kg is exceeded by 121 kg. But as was mentioned earlier, we are carrying both approaches into the next phase of the program because of performance and variable pitch angle possibilities.

Component		Weight (kg)	
OPTICAL SUBSYSTEM	**334.4**		
Telescope Assembly		105.6	
Primary Mirror Subassembly			83.8
Secondary Mirror Subassembly			8.2
Metering/Thermal Control Subassembly			13.6
Folding Optics and Structure		50.0	
Mixing Optics Assembly		5.4	
IMC Assembly		12.6	
IMC & LAC Subassembly			4.0
Alignment Sensor & Controller Subassy			8.6
Scan Bearing Assembly		155.8	
Bearing Housing Subassembly			97.1
Drive Subassembly			46.8
Position Sensor Subassembly			11.9
Miscellaneous		5.0	

Figure 5-64. Optical Subsystem Weight Estimate-Configuration #1

Component		Weight (kg)	
OPTICAL SUBSYSTEM	**455.3**		
Telescope Assembly		105.6	
Primary Mirror Subassembly			83.8
Secondary Mirror Subassembly			8.2
Metering/Thermal Control Subassembly			13.6
Folding Optics and Structure		39.8	
Mixing Optics Assembly		5.4	
IMC Assembly		13.6	
IMC & LAC Subassembly			5.0
Alignment Sensor & Controller Subassy			8.6
Roller Track Bearing Assembly		285.9	
Rotating Ring Subassembly			85.0
Stationary Ring Subassembly			144.4
Intraface Truss Subassembly			56.5
Miscellaneous		5.0	

Figure 5-65. Optical Subsystem Weight Estimate-Configuration #2

5.2.2.4.3 Power Estimates

A fairly detailed thermal power analysis was conducted in order to bound the power required to thermally control the Optical Subsystem. Shown graphically in Figure 5-66, the ground rules and assumptions of this analysis were:

1) A 1.5m x 1.5m cylinder, in a near polar orbit with an orbit angle 22.5° off the sun vector.
2) LAWS positioned at a constant pitch angle of 45° from nadir.
3) Altitude=824 km.
4) MLI and local heaters are to be utilized.
5) The operating temperature is equal to the assembly temperature (70° F)

Using these guidelines, the estimated thermal power required was calculated for two different emissivity values for the PM. The first, with ε=0.03 corresponds to a beginning-of-life (BOL)-calculated 126 watts average power. If ε was degraded to 0.05 (possibly after 5 years), the power required increased slightly to 132 watts (average). Since this analysis was conducted at a top level, a 25% contingency factor was added to these estimates. This contingency will be substantiated once more specifics on interfaces conductances and radiation, operating temperatures, view factors, local power dissipation, and similar phenomena are baselined and analyzed.

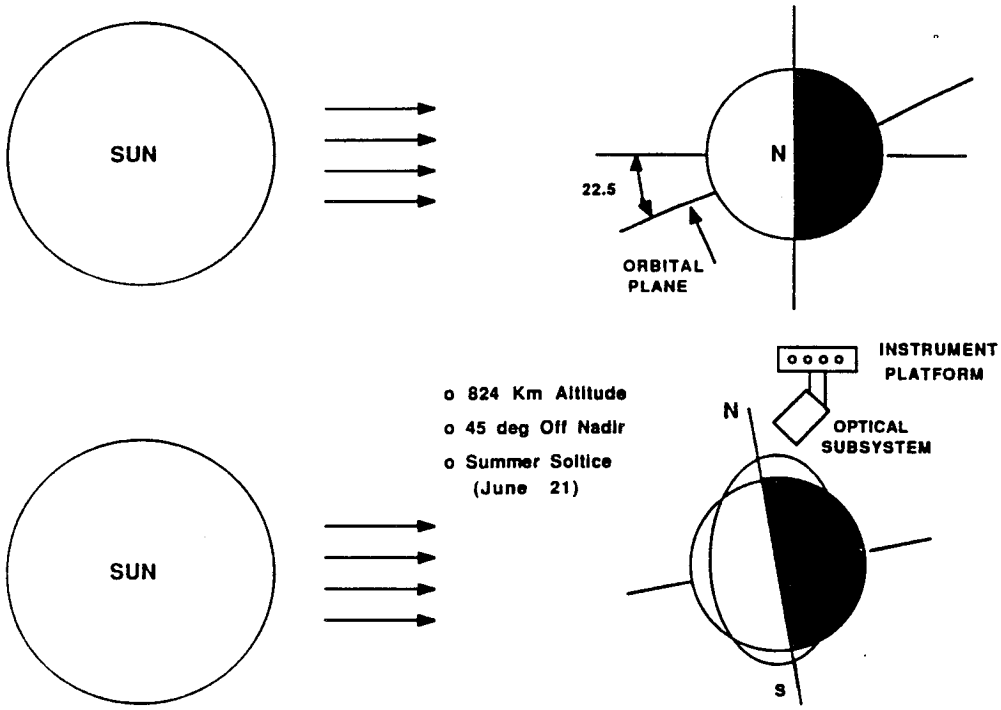

Figure 5-66. Thermal Power Analysis

5.2.2.4.4 Envelope Compliance and Interfaces

As can be seen in Figure 5-67, the Optical Subsystem meets all requirements with respect to envelope constraints and interfaces with the other subsystems. Specifically, the O.S. easily fits into the assumed launch vehicle 4.6 m diameter envelope. The physical interface between the O.S. and the polar platform is straightforward and non-complex. It consists of a series of local flanges which connects the stationary portion of the bearing housing to the platform at a number of "theta" positions to provide torsional stability, and at two "axial" position to provide both axial and rotational restraint. As further work is accomplished, it is anticipated that the packaging and placement of components will be optimized therefore providing even greater envelope margin.

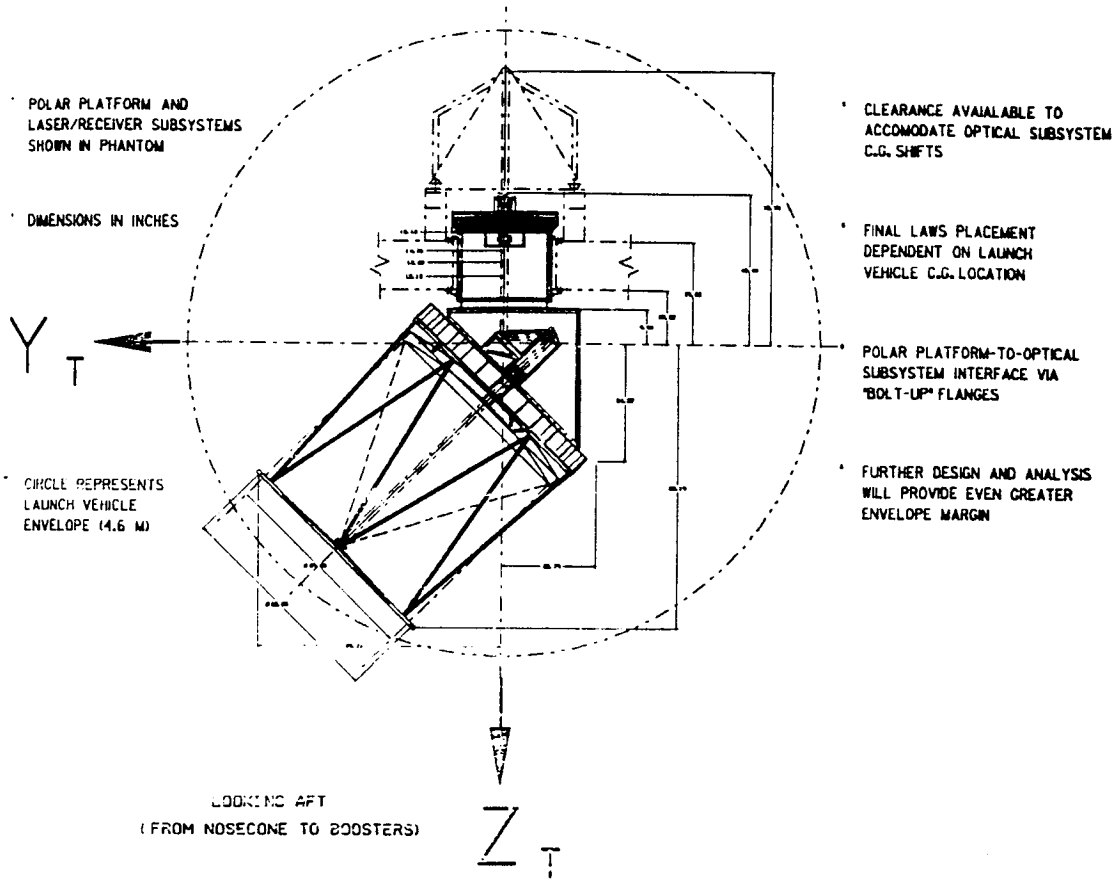

Figure 5-67. Optical Subsystem Isomatic Drawing Including Envelope Constraints

5.2.2.5 *Alignment and Controls Requirements*

The objective of the beam sensing and control subsystem is to maintain accurate pointing and alignment stability of the optical system. In order to accomplish this, necessary sensors and control elements with proper dynamic range, accuracy and bandwidth need to be configured and incorporated into the optical system. For the specified LAWS operational scenario and performance requirements, a baseline beam control concept has been selected based on a trade-off study performed during Phase I of the LAWS program. Shown in Figure 5-68 is the baseline alignment and control system schematic.

This section summarizes the effort associated with the requirement definition, concept development, trade-off analysis, and baseline selection of the beam sensing and control subsystem. In paragraphs below, optical system error sources and their characteristics are identified and described. The sensing requirements to recognize these disturbances and control requirements to compensate for such are discussed. Several viable concepts are evaluated, and the chosen baseline is described.

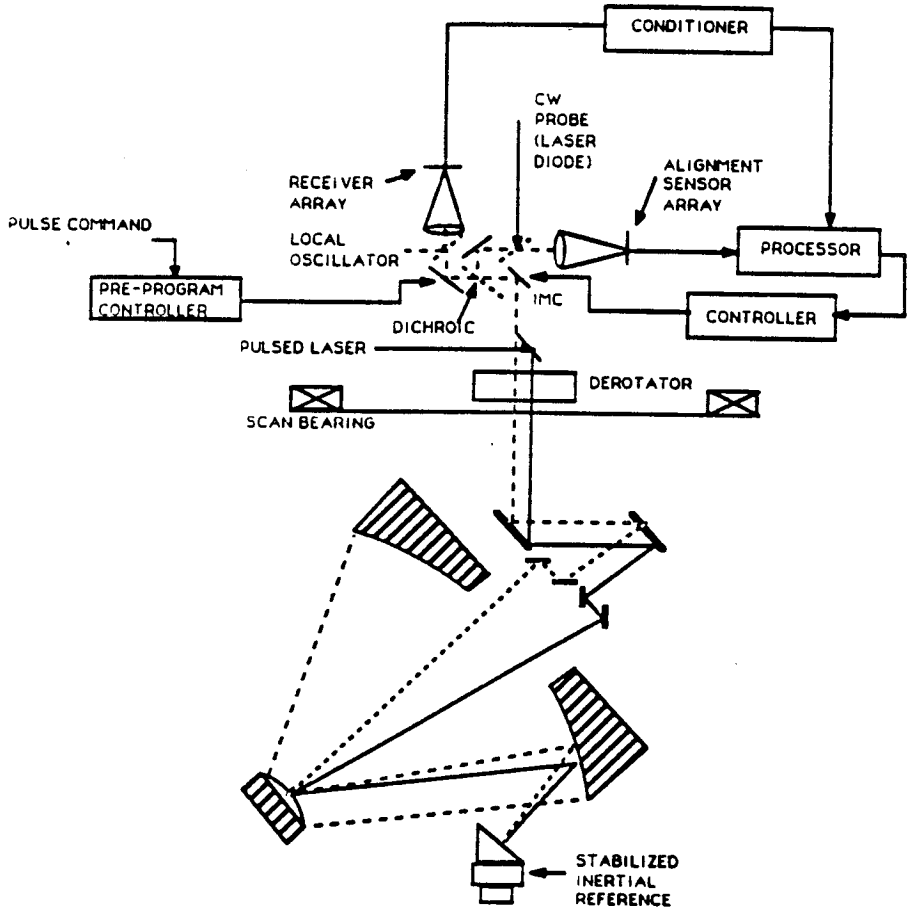

Figure 5-68. Baseline Alignment and Control System Schematic

5.2.2.5.1 Error Sources And Effects

The errors which adversely affect the optical system performance can be categorized into two groups, systematic errors and random errors. The systematic errors include such errors as residual error of the optical system design, and errors associated with the operational lag angle and spacecraft pitch motion. These errors are known in advance, thus can be compensated by calibration, or by providing known amounts of adjustment during operation.

The random errors, on the other hand, are indeterminate. When these types of errors exceed the allowable, they can only be corrected by real-time active sensing and control. Such errors include thermally induced misalignment, laser jitter, gimbal noise error, and structural vibration induced errors.

The various error sources, their characteristics and impact on the optical system design and requirement are summarized in Figure 5-69.

Error Characteristics	Source	Impact on Design Requirement
Systematic Errors		
Static errors	Static lag angle	- Requires WFOV telescope design and separate beam paths
Dynamic errors	Transmit pulse	- Instantaneous return beam cause slight smear
	Return pulse	-Requires large angle compensating beam steering mirror
	Spacecraft pitch	-Requires compensating beam steering mirror
Random Errors		
Low frequency	Thermally induced Low frequency vibration Gimbal rate change Inertia unbalance Derotator mechanism	-Requires low BW closed-loop control
Mid-frequency	Mid-frequency vibration Scan bearing noise Laser jitter	-Requires high BW closed-loop control
High frequency	High frequency vibration	-Requires isolation and/or structural stiffness/damping enhancement

Figure 5-69. Error Sources and Impact

5.2.2.5.2 Systematic Errors

To best describe the systematic errors and their effect, an operational timeline versus LOS error chart was plotted, as shown in Figure 5-70. The plot is for a design scan rate of 12 RPM and the spacecraft orbit of 824 km.

Error corresponding to transmit pulse length

During the 3 microseconds output laser pulse period, the telescope optical axis rotates approximately 2.77 microradians. This LOS change spreads the laser beam and causes the returning beam to have an instantaneous field of a corresponding amount. The net effect is slight smear of the far-field spot at the the detector, as illustrated in Figure 5-71. It is assumed that no beam correction is necessary for such effect because the extent of the smear is only 1/5 of the spot size, although the effect will be included in the detailed performance modeling to be undertaken in phase II.

Error corresponding to lag angle

The laser beam round trip time of ~8 milliseconds corresponds to a LOS change of 6.9 milliradians. To compensate for this magnitude of lag angle, the optical system design needs to provide a wide-field-of-view telescope having separate transmitting and receiving optical paths. The residual wavefront error over the ~7 milliradians FOV

(0.4°), based on the baseline telescope design, is very small at 0.026 waves rms (@ 9.11 μm) after focus. Therefore, there is no further beam control requirement to compensate for this lag angle error.

Error corresponding to return pulse length

As the laser pulse travels through the earth's atmosphere and is reflected at various altitudes, the return beam pulse period is correspondingly lengthened. Assuming the atmosphere has a thickness of 15 km, the return pulse period will be increased to 144 microseconds. Thus, during the receiving period, the telescope optical axis will rotate a total of 181 microradians. This angle change is dynamic and equivalent to about 10 spot diameters. To compensate for this pointing error, a beam steering control element is necessary to maintain the returning beam stable on the detector.

Error due to spacecraft pitch motion

The spacecraft constantly adjusts its pitch angle while orbiting the earth. This spacecraft motion causes the return beam to follow a slightly deviated optical path. The amount of error is 8.14 microradians, large compared to the pointing accuracy requirement of 3 microradians. Therefore, a compensating beam steering control is required.

5.2.2.5.3 Random Errors

Unlike the systematic errors, the random errors are caused by random disturbances on-board the spacecraft. These errors could be induced thermally, mechanically, or optically. Depending on the characteristics of these errors, active or passive means of control need to be implemented.

Low temporal frequency errors can be introduced by thermal gradient, low frequency spacecraft vibration, and pointing telescope inertia unbalance and gimbal rate variation. These errors need to be compensated by employing low bandwidth closed-loop alignment controls.

Thermally induced misalignment

Due to sun illumination, equipment heat dissipation, and other on-board thermal loadings, thermal gradients can exist and cause misalignment of the optical system. Thermally induced misalignments are slow in changing. Active correction during one measurement period of roughly 8 milliseconds is not necessary in general. However, over long periods of operation, the total optical misalignment can become excessive, producing an unacceptable amount of pointing and wavefront errors.

Low frequency spacecraft vibration

Low frequency spacecraft vibration can cause either the optical system mis-register with respect to the inertia reference, or distortion of the beam train. In either case, the optical LOS is disturbed and thus needs to be corrected.

Telescope inertia unbalance and gimbal rate variation

The telescope inertia unbalance can cause the pointing LOS to oscillate at the rotating rate. Also any rotation rate change during operation can cause mis-representation of systematic errors. Active control mechanisms to correct these errors are therefore necessary.

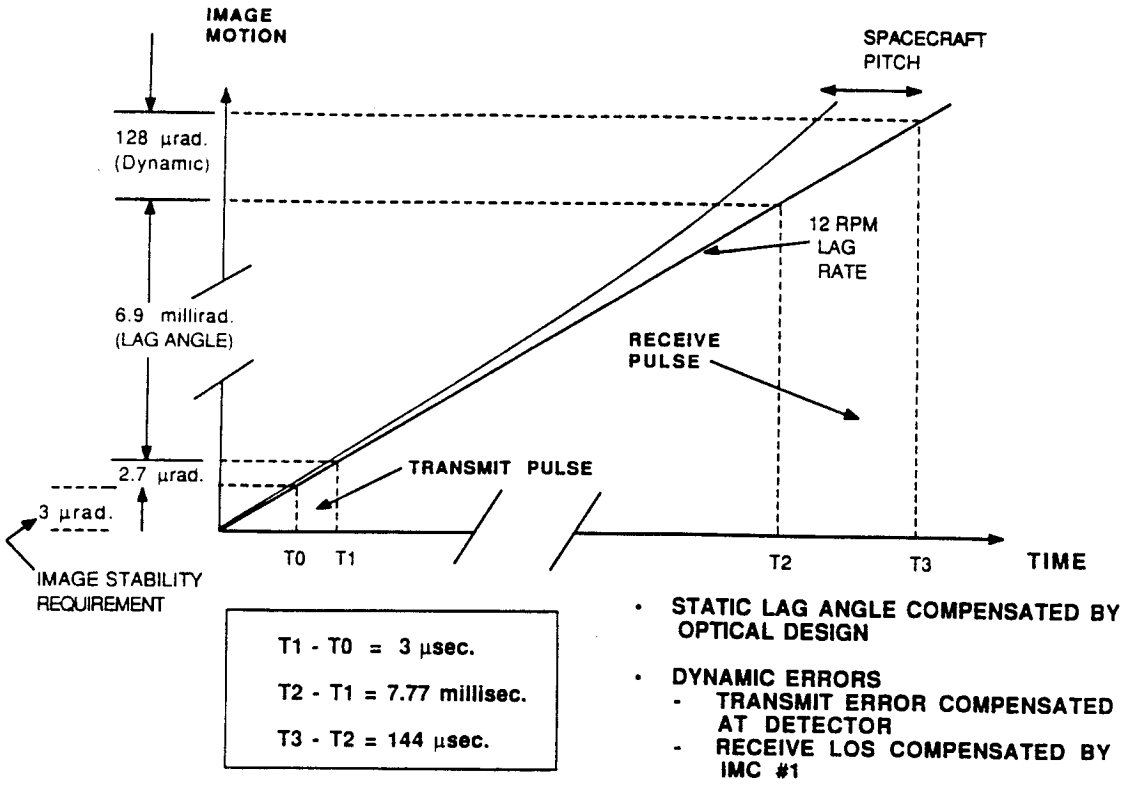

Figure 5-70. Operational Timeline and Deterministic LOS Error

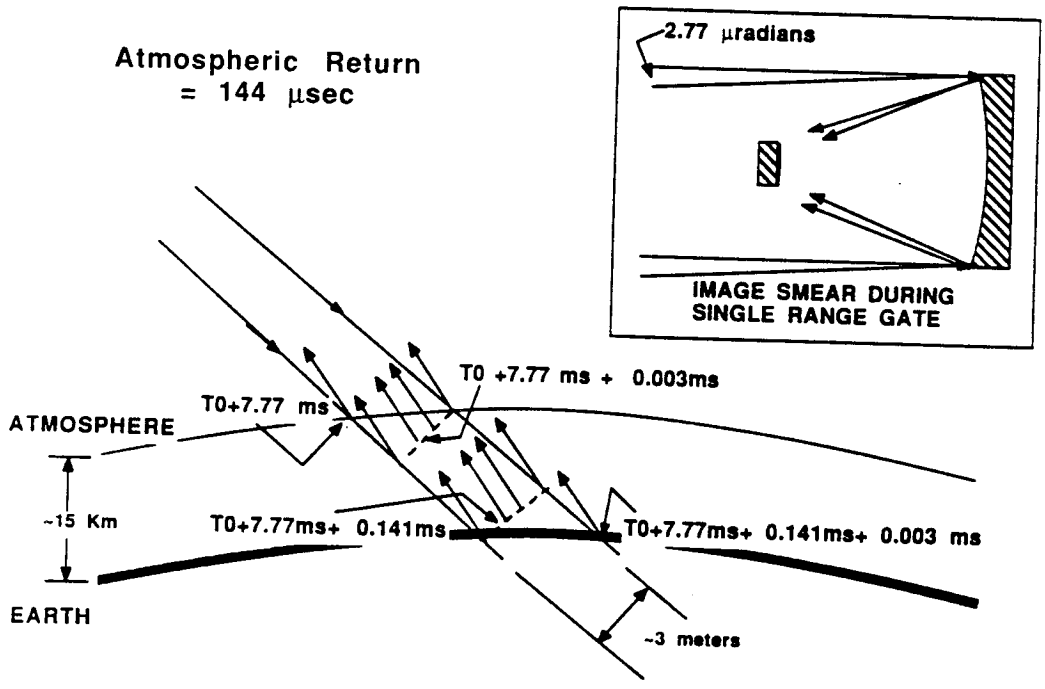

Figure 5-71. Pulse Length Effect on LOS Stability

Derotator positioning

The error in the derotator positioning mechanism can also produce LOS error of the laser beam.

5.2.2.5.4 Mid-temporal Frequency Errors

The origin of the mid-frequency errors can be traced to structural vibrations, gimbal noise and laser beam jitter. This type of error can be corrected by high bandwidth control servo loops. Depending on the control servo design, the mid-frequency error can range from a few Hertz to a few hundred Hertz.

Mid-frequency structural vibration

Because of the specific frequency range of concern, structural vibration may not be properly reduced by isolation or stiffness/damping enhancement. If this is the case, the optical system misalignment caused by the structural vibration at mid-frequency band needs to be sensed and controlled actively.

Scan bearing noise

Scan bearing noise is another source of disturbance that can cause mid-frequency LOS errors. Correction can be made mechanically at the scan bearing interface, or optically by directly compensating the LOS error.

Laser jitter

The laser itself has pointing error from pulse to pulse. The laser pointing error needs to be recognized while it is being transmitted and compensated for during the receiving period. The adjustment has to be accomplished within an 8 milliseconds round trip time of the laser beam.

5.2.2.5.5 High Temporal Frequency Errors

Error at the very high end of the frequency spectrum can be introduced by high frequency structural vibration. Beyond the control loop ability to correct, such error needs to be properly attenuated by isolation or stiffness/damping enhancement of the structural system.

5.2.2.5.6 Sensing Requirements

Based on the operational and performance requirements specified for the LAWS optical system and the expected disturbances and errors discussed above, critical sensing requirements for the beam sensing and control subsystem are shown in Figure 5-72.

Wavefront error sensing

Due to thermal gradients or structural vibration, the primary and secondary mirrors could be out of alignment during operation. Such misalignment can produce LOS error as well as wavefront error. To ensure a satisfactory LAWS beam quality, the amount of wavefront error needs to be identified, and corrected if it becomes excessive.

For the baseline telescope design, only large amounts of misalignment can cause a wavefront error of concern. Since we can only expect large misalignment to be produced by the slow changing thermal gradient, not by the high frequency but low amplitude structural vibration, the wavefront sensing may be performed at a relatively low rate.

Furthermore, since the misalignment of the telescope will produce only low spatial frequency wavefront errors, predominantly tilt, defocus, and coma, the wavefront sensing spatial resolution needs only to identify these low order errors. The accuracy of wavefront sensing needs to be $\lambda/40$(TBR) wave rms or better, to be consistent with the system wavefront error budget.

Transfer optics misalignment

The misalignment of beam transfer optics along the outgoing and returning beam train will cause LOS errors. Such misalignment can be introduced by thermal distortion, structural vibration, or residual errors of mechanisms such as the derotator and beam steering mirrors.

Depending on the alignment system concept, these misalignment errors can be detected by local sensors relating to a common reference, or by an auxiliary alignment beam. The local sensing scheme can be applied most efficiently when only one or two elements are contributing to the misalignment. Without an auxiliary alignment beam, however, correction made based on the local sensing is essentially open loop.

Using an auxiliary alignment beam, all contributions from the various optical elements are sensed simultaneously and can be corrected in a closed-loop fashion.

The sensing rate needs to be high in order to have a high bandwidth beam jitter control loop to correct mid-frequency LOS errors. A sensor accuracy in the order of 0.3 microradians (object space) is required.

Telescope scan bearing assembly pointing error

The telescope scan bearing assembly pointing error exists because of scan bearing rotating rate variation, scan bearing noise, and/or assembly inertia unbalance. The pointing error contribution of telescope tilt differs from that of transfer optics by the telescope magnification factor. The telescope pointing error may need to be measured independently for certain beam control concepts. The sensing accuracy and rate are comparable to those for the transfer optics.

Laser jitter error

The outgoing laser will have pointing error from pulse to pulse. This error has to be identified during the transmitting period so that correction can be made during receiving. The sensing rate should be consistent with the pulse rate with accuracy comparable to that required for telescope tilt measurement.

5.2.2.6 *Alignment and Controls Concepts and Trade-Offs*

The Beam Sensing and Control concepts to be described in this section are based on maximizing heterodyne detection efficiency within the constraints of the LAWS operational environment. The purpose is to maintain coincidence of the local oscillator beam with the returning pulse beam at the detector, over the detection period, and to maintain optical system alignment at the same time in order to control wavefront error.

Heterodyne detection efficiency is reduced by any effect that causes relative phase difference in the signal at the detector, such as wavefront error, obscuration, or inadequate coherence. However, the foremost need in any detection problem is to get the signal onto the detector in the first place. Some kind of alignment system is required. The LAWS operational mode (rotation of the telescope line of sight about a nadir-pointing axis at 12 RPM) imposes special considerations for an alignment system. The next most sensitive effect on heterodyne efficiency is the presence of relative phase difference due to system aberrations. By far the strongest contributor to this error is telescope secondary mirror despace, but tilt and decenter also have an effect. A wavefront measurement and control system is therefore required.

Category	Objective	Requirement
Wavefront sensing	Identify telescope misalignment induced wavefront errors for WF control	-Accuracy < 1/40 waves rms (TBR) -Spatial resolution consistent with tilt, defocus, and coma errors -Low BW
Transfer optics	Identify LOS error contribution from transfer optics for active control	-Accuracy < 0.3 µrad rms (O.Space) -High BW -local or global sensing
Telescope pointing	Identify LOS error contribution from telescope for active control	-Accuracy < 0.3 µrad rms (O.S) -High BW
Laser jitter	Identify outgoing laser jitter error for adjusting receiving path	-Accuracy < 0.3 µrad rms (O.S) -Laser pulse rate

Figure 5-72. Sensing Requirements

5.2.2.6.1 LAWS Recommended Baseline Wavefront Sensing and Control Concept

Wavefront error in an optical system is the result of fabrication errors, environmental disturbance, and misalignment of elements and components. In LAWS, the alignment errors that contribute to wavefront error are secondary mirror despace, resulting in defocus, and secondary mirror decenter and tilt, resulting in coma, astigmatism, and boresight error. These errors can be compensated either by controlling the secondary mirror, or by controlling the spacing and tilts of a simple refractive compensator. Use of a compensator circumvents the need to route electrical power through the rotating telescope assembly to the secondary mirror.

One common wavefront sensing concept is the Hartmann method, which involves spatially sampling a wavefront by placing small apertures in a pupil, measuring the relative locations of the resulting spots of light in the focal plane, and comparing those locations to some appropriate standard. A modern implementation in laser systems is to place Holographic Optical Elements (HOE's) on an optical surface, which serve to redirect a small portion of the incident radiation to some secondary focal plane, where spot position analysis can be done. For LAWS, such a system is proposed. Preliminary indications are that a four-HOE sample will be adequate to discriminate between the three aberrations expected from secondary mirror motion, defocus, coma, and astigmatism. Also, the center of mass of the four spots will provide secondary mirror tilt information, once telescope tilts are factored out. This wavefront control system can operate at a low update frequency if the LAWS structure can be adequately designed, so that alignment of the secondary to the primary can be considered constant during the round trip time of a pulse.

Figure 5-73 shows the basic optical schematic of the LAWS baseline wavefront sensing and control system.

A continuous wave laser probe beam is used to generate wavefront samples from each of four HOE's on the primary mirror. The HOE's act like a diffraction grating, sending a portion of the incident energy back into the beam train. The redirected beams emerge collimated from the telescope.

The beams sent back into the system by the HOE's are directed to a lens which focuses them onto a focal plane. The beams form far-field spots in a roughly square pattern. The relative spot locations are then compared to locations measured previously during a calibration procedure. Figure 5-73 shows the spot patterns for despace (focus error) and tilt/decenter (coma and/or astigmatism).

The error signal is processed and is used to drive the secondary mirror into alignment (or is used to adjust a compensator).

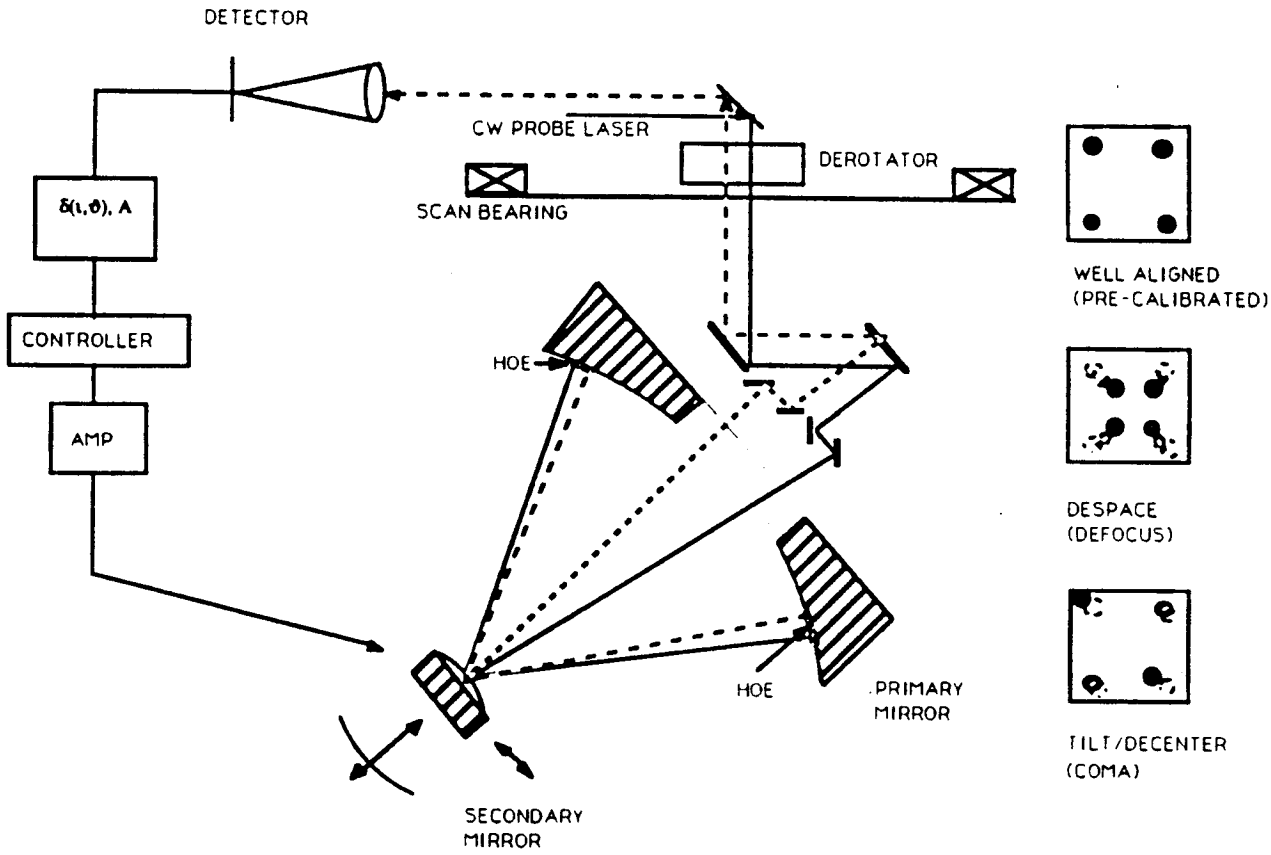

Figure 5-73. Wavefront Sensing and Control System Optical Schematic

5.2.2.6.2 Boresight Alignment Concepts

Boresight alignment of the LAWS optical system is complicated by the fact that different components of the system affect the alignment of the receive channel to the returning pulse in different amounts. (The transmit channel optics which are not common to the receive channel do not require monitoring once the pulse has left.) See Figure 5-74.

Figure 5-74. Alignment Errors and Effects

Alignment Error	*Effect*
Bearing tilt	33.3
Telescope alignment (pri/sec)	1.0
Derotator tilt	2.0
Beam train optics	2.0
Spacecraft attitude	33.3

Three concepts for alignment/boresight of the Local Oscillator (LO) and the main laser pulse to the heterodyne detector are presented. In each case, the state of the optical system is measured at the time the pulse is sent. Misalignment of the pulse to the detector due to beam jitter is measured immediately and IMC correction is applied. The same occurs for the LO, except for the fact that a single mirror can not effect a correction for both beams. Therefore, a separate control is necessary in order to maintain LO alignment. The use of a circularly-symmetric-array signal detector ensures that the heterodyne signal can be used for this purpose. This decouples the alignment problem, and allows use of the LO beam as an alignment monitor probe beam during the pulse travel time for the global alignment concepts. In all concepts to be shown, an Image Motion Compensation (IMC) mirror will be used to compensate for the lag angle accumulated during the traversal of the pulse through the atmosphere.

Local Sensing and Control

In this alignment concept (illustrated in Figure 5-75), all sources of send/receive pointing error are monitored and controlled or accommodated separately. The error signals generated are modified in a control processor according to the effect of each on the alignment of the LO and returning laser pulse to the detector. A control signal is sent to a high-bandwidth steering mirror. See Figure 5-76 for a listing of error sources and sensors.

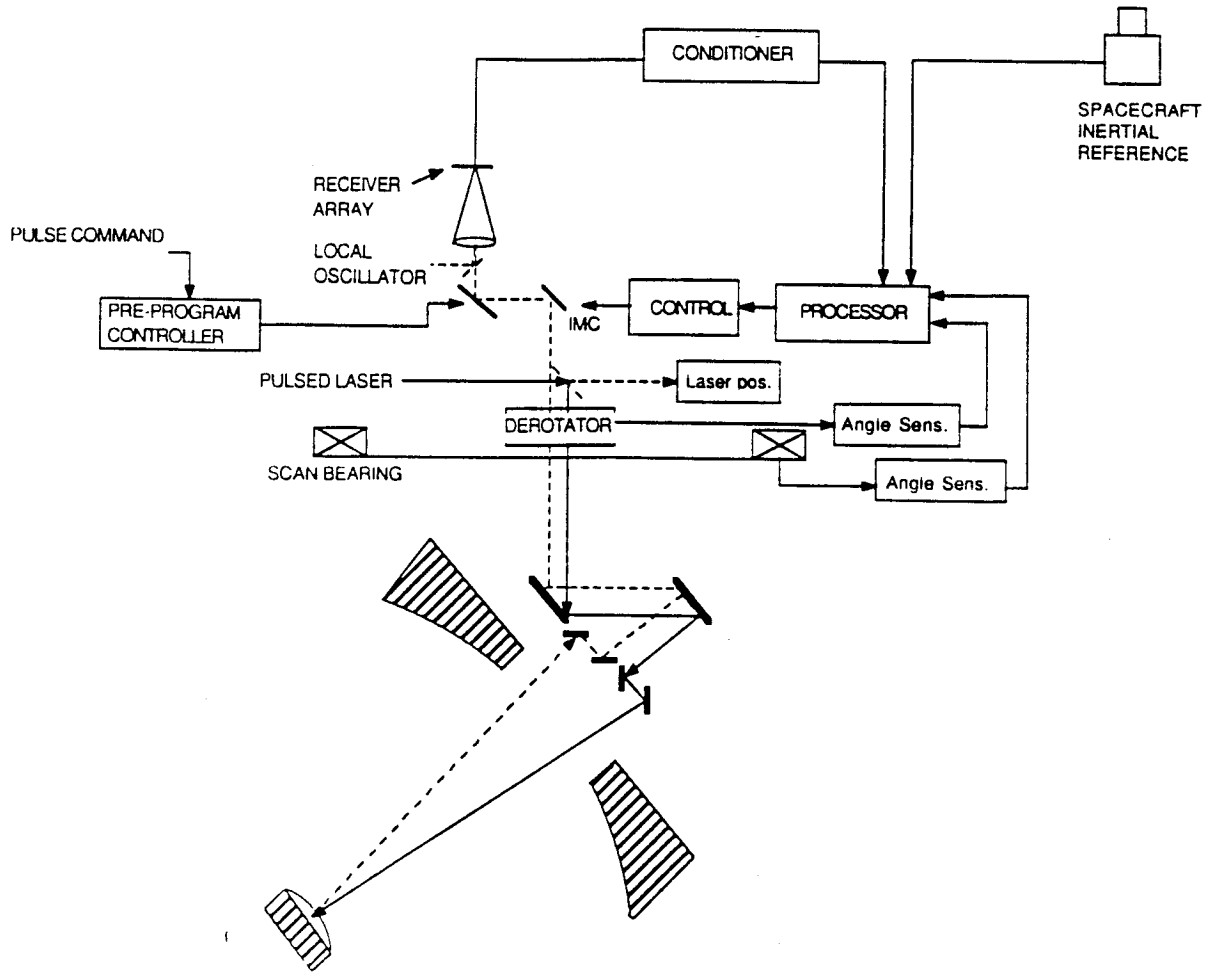

Figure 5-75. Optical Subsystem Local Sensing and Control

In operation the state of the optical system would be measured at the time the pulse is sent. Misalignment of the pulse to the detector due to beam jitter is measured immediately and IMC correction is applied. The heterodyne detector signal is used for alignment of the LO. This signal is processed and sent as a control signal to a separate steering mirror which maintains LO alignment. Each alignment error listed in Figure 5-76 is monitored by its respective sensor during the pulse travel period. The signals are sent to a central processor which scales each according to its effect on the alignment of the pulse receive optical train. A control signal is sent to the IMC electronics, which amplifies and sends the final control signal to the steering mirror. The final state of the system at the moment of return of the pulse is such that the image of the heterodyne detector and the apparent LO source projected into the far-field falls onto the pulse track through the atmosphere.

Error Source	Sensor
Bearing tilt	Spacecraft-mounted capacitive gap sensor
Telescope LOS	Wavefront sensor (Hartmann)
Derotator	Spacecraft-mounted capacitive gap sensor
Beam train optics	Retro-probe alignment beam
Spacecraft attitude	Stable Inertial Reference (SIR), laser gyro

Figure 5-76. Error Sources and Sensors

Global Sensing and Control: Beam LOS Sensing and Control, Dual Probe Beam System.

Global sensing of the LAWS optical system is possible by use of two CW probe beams, one of which samples the LOS of the entire optical train, the other of which samples just the beam train optics out to the last element before the telescope. The concept is illustrated in Figure 5-77. HOE's are used to return beam samples. Two probe beams are needed because the telescope LOS errors affect the returning pulse direction by a factor of the magnification, whereas the other optics affect it by a factor of two. Therefore, the telescope LOS disturbance is derived by subtraction of the two signals. Each is then appropriately scaled in a control processor which finally sends a corrective signal to the IMC. In addition, any correction in the telescope LOS due to misalignment of the telescope secondary to the primary is made before the pulse is sent. It is possible to arrange a nulling control. Figure 5-78 shows the disturbances and the effect on the pulse of each.

The operation is as follows: The state of the system at the moment the pulse is sent is sampled. The IMC makes corrections for the pulse pointing error, and the LO steering mirror is engaged to trim the LO pointing. The LO beam is then used as a probe beam for global pointing control. Part of the probe beam is returned via a HOE etched into the last beam train optical element to the beam train jitter sensor, which sends its scaled signal to the IMC controller. Part of the LO laser beam continues on to HOE's on the primary mirror, which send a signal back to the system jitter sensor. The system wavefront sensor delivers information about the telescope LOS disturbance due to secondary mirror tilts and decenter. Enough information is then in hand to determine the steering mirror control signal.

Global Sensing and Control: Beam LOS Sensing and Control, Single Probe Beam System.

Global sensing of the LAWS optical system is possible by use of a single CW probe beam, by incorporating a stabilized inertial reference mirror in the output space of the LAWS telescope. The reference mirror must rotate at the telescope rotation rate such that its normal represents the telescope LOS. This condition is monitored by means of accurate encoding relative to the output of a laser gyro. Any deviation of the retro mirror is input open loop to the steering mirror after proper scaling. The CW laser beam may provide a probe beam for pointing trim during pulse travel. Since the reference mirror represents outgoing space, the entire optical system is sampled by the probe beam, thereby simplifying control of the LAWS pointing operation.This concept was illustrated earlier in Figure 5-68.

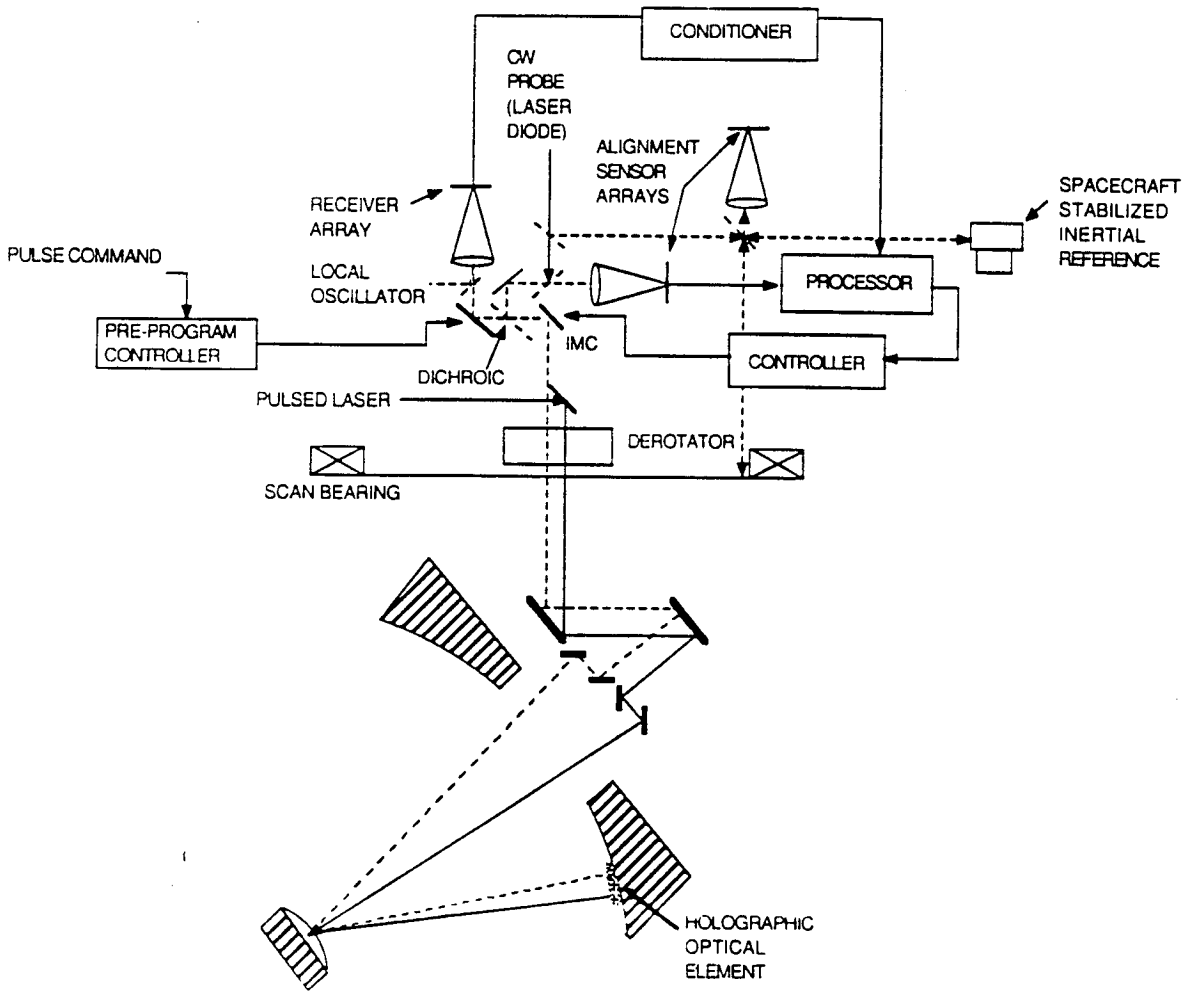

Figure 5-77. Global Sensing Optical Schematic

The state of the system is sampled at the moment the pulse is sent. The pulse outgoing pointing error and the telescope pointing error are corrected by the IMC mirror as shown in Figure 5-68. The CW probe laser beam reflected back into the system from the output space reference mirror (stabilized inertial reference (SIR) in the figure) forms a spot on a nulling detector. The reference mirror is overlaid with a binary optics grating acting as a wedge. The wedge angle is equal to the lag angle. A small part of the outgoing pulse is diffracted to the receive path. A spot position signal from the array of detectors around the heterodyne receiver at the moment the outgoing pulse is sent becomes the reference for the closed loop nulling correction. Any jitter or drift from any part of the LAWS system during the pulse transit time will result in spot motion, which, when nulled out by the steering mirror, will restore the LOS of the receive optics to alignment with the returning pulse.

5.2.2.6.3 LAWS Alignment Baseline

The preliminary Laws alignment baseline is the concept discussed in section 5.2.2.5, and is based on global sensing using a gyroscopically stabilized reference mirror located in the telescope output space (see Figure 5-68). This type of system is the simplest to implement, requiring only one probe beam, and can be arranged as a nulling control system. Figure 5-79 lists several characteristics for the sensors shown.

Figure 5-78. Error Sources and Sensitivities

Error Source	Sensitivity (Q_{pulse}/Q_{error})
Beam train jitter	2
Telescope LOS	
bearing jitter	33.3
primary/secondary misalignments	0.5
Spacecraft attitude	33.3

Figure 5-79. Baseline Alignment System Characteristics

Characteristic	Type
LO alignment	heterodyne detector (circularly symmetric array)
Pulse LOS	quadrant detector
Beam train	quadrant detector
SIR	laser gyro
Output space reference	5 DOF controllable optical flat,12 RPM (to match LAWS telescope)

5.2.2.6.4 Initial On-Orbit Alignment

Initial on-orbit alignment of the LAWS telescope consists of two parts: alignment to obtain adequate wavefront quality, and boresight alignment to align the received image with the receiver. Each of these operations will be extensively studied during Phase II to establish the likely launch-induced misalignments, establish safe margins, and set the requirement for the range of measurement and adjustment of both the Wavefront Sensing and the End-to-end Boresight Alignment Controls.

The alignment control for the telescope to achieve the wavefront quality is based on the classical Hartmann test, which has an intrinsically higher dfynamic range than

competing interferometric alignment techniques. Our initial evaluation indicates that the alignment sensor is capable of operation over a range of about 45 μm radians equivalent in object space. The full capabilities of the concept will be determined for the LAWS parameters during Phase II.

Initial boresight alignment of LAWS is expected to be similar to the "bootstrap" alignment procedure being used for the Hubble Space Telescope. For LAWS, an iterative procedure involving the Wavefront Alignment Control (internal alignment), the End-t-end Alignment system probe beams, and finally, calibration of the Stabilized Inertial Reference using ground returns and the auxiliary detectors in the receiver will be used to align the system once on orbit. Our design will provide margin over expected launch-induced misalignments.

5.2.2.7 *Optical Subsystem Technical Issues*

The issues associated with the optical subsystem which have been identified during the Phase I Study are associated with the tight pointing requirement over the round trip time, the establishment and maintenance of the transmit/receive axis alignment and weight. Pointing and alignment issues have been addressed by previously funded programs and continue to be the focus of on-going work at Hughes Danbury.

In order to reduce the weight of the optical subsystem extensive use will be made of a lightweight materials (e.g. Be, SiC) and composites.

5.2.3 *Receiver Subsystem Configuration Analysis*

The receiver subsystem consists of a detector element, a detector pre-amplifier, a cooler assembly, intermediate frequency, or IF, electronics, a Doppler processor, a receiver controller and a receiver power supply. The total subsystem requirements are that this receiver consume no more than 300 watts, weigh less than 40 kilograms and have a lifetime exceeding 3 years in a space environment. In addition, the receiver must operate in a heterodyne mode with a carrier wavelength of 9.11 microns and a bandwidth of up to 1.5 GHz. This receiver should also operate with a quantum efficiency exceeding 40% at the maximum bandwidth. From the receiver subsystem requirements a set of derived requirements can be determined which will ensure that the top-level requirements will be met. These derived requirements can be specified for each of the receiver subsystem assemblies, such as the detector or cooler.

The basic derived requirement for the detector is that the detector operate at 80 K in order to maximize the quantum efficiency. In addition, it was determined through analysis of the detector mixing efficiency for several detector configurations that the optimum detector is made up of a circular element with a ~65 micron diameter surrounded by a ring of four elements which pick up the energy in the first ring of the Airy pattern. This specific array geometry will be presented in more detail in a later section. The detector pre-amplifier must have a low noise figure which in turn requires that the pre-amp operate at a temperature around 120 K.

Given the above cooling requirements, and the baseline heat loads as presented later, the receiver must include a long-life cooler with the capability to dissipate 1-2 watts at 80 K from the detector array and 3 to 5 watts at 120 K from the pre-amplifiers. In addition, the cooler must be designed to introduce a minimum amount of vibration into the detector array.

The receiver must include IF circuitry with the capability to remove the spacecraft and earth Doppler which varies between -1.2 and 1.2 GHz (for the 45° nadir angle). This gross Doppler shift must be removed while maintaining the desired wind signal which has a Doppler velocity of plus or minus 16 MHz. The IF amplifier must also have a means of generating the "I" and "Q" phase quadrature channels in order to maximize the Doppler estimator performance as well as minimize the A/D conversion

rate. After A/D conversion the signal processing should be able to estimate the line-of-sight wind velocity given the output from the 5 element detector.

The receiver subsystem should also provide some method of controlling and monitoring the entire subsystem and may include a power conditioner to condition the raw system power to that required by the various elements of the receiver subsystem. Figure 5-80 is a functional block diagram showing the interrelationships between the various receiver subsystem elements.

5.2.3.1 *Detector Baseline and Trades*

The baseline detector array involves a single, optimum-sized single detector element surrounded by four alignment elements. This configuration has the optimum performance provided by a single detector as well as additional capabilities for detecting alignment errors. Strong signals (from cloud or ground returns) can be used to determine the location of the center of the Airy pattern and thus determine any systematic alignment errors. Additionally, the fact that the receiver is a heterodyne detector also allows one to measure the relative phase between the various detector elements and potentially determine optical system aberrations.

This specific geometry was arrived at by comparing the performance for a variety of detector geometries, including a single element, a quad, a square array, the FIREPOND detector geometry and the baseline geometry. Each of these geometries was evaluated quantitatively in terms of its heterodyne mixing efficiency for various amounts of misalignment as well as qualitatively in terms of redundancy and robustness.

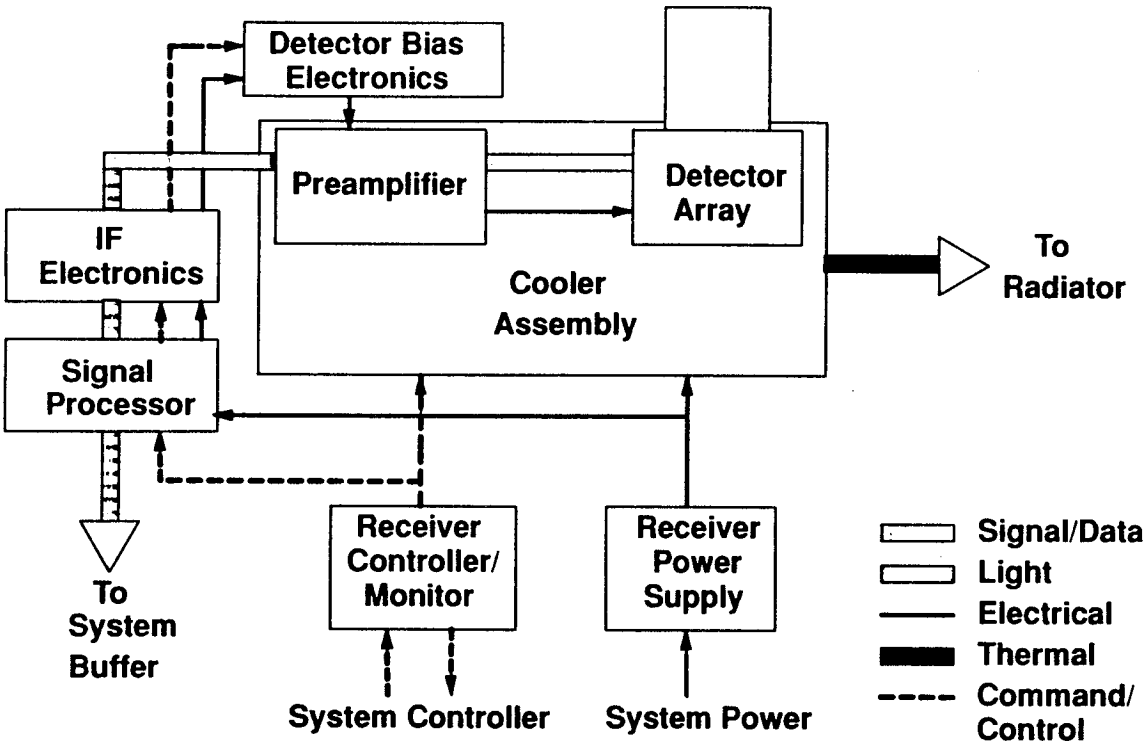

Figure 5-80. Receiver Subsystem Functional Block Diagram

Figure 5-81 compares these various detector geometries both quantitatively and qualitatively. The performance numbers are all relative to the nominal single detector element performance. It can be seen that the ring detector provides enhanced performance for the nominal case due to the fact that the energy in the first bright ring (which is out of phase with the central lobe) is being added to the signal in the central lobe. All of the other array geometries suffer some loss under nominal conditions due to the presence of dead-streets which block some of the incident energy. All of the detector geometries, with the exception of the square array, suffer a loss in signal as the spot is moved from the center of the array, however, the ring geometry has the most graceful degradation in this respect. Another consideration is the desire to have the ability to measure the systematic, long-term pointing error. Only the multi-element detectors have this capability without performing some type of search scan. Finally, the multi-element arrays have a built-in redundancy which provides for the continuation of the mission, albeit at reduced performance, if the primary detector element fails. Another consideration in the detector trades is the required cooling for the various elements as well as the detector pre-amplifiers. The pre-amps perform best when operated at a reduced temperature, around 120 K, which greatly increases the cooling heat load. Since each detector element has its own pre-amp, this heat load is directly proportional to the number of detector elements.

All of the performance numbers for the multi-element detectors assume that the various signals from each element can be coherently combined, that is, the phases of each signal can be determined and corrected so that the signals all combine constructively. The phase map for the entire array can be measured on-orbit using a strong signal moved across the detector array. This phase map will then be used to adjust the phase of each element before combining the various signals coherently. The specific ring detector dimensions are shown in relation to the diffraction-limited Airy pattern in Figure 5-82. This Airy pattern is based on a wavelength of 9.11 microns and an F/4 optical system. The central element is about 65 microns, or 70% of the central Airy disk, with a 15 micron dead-street which covers the first dark ring of the Airy pattern. The outer ring of detector elements has a total outside diameter of about 155 microns, which results in the 5 elements having nearly the same active area.

As stated earlier, the detector will be operated at 80 K in order to maximize performance. The diode is operated in a reverse-bias mode with a bias of 0.2 to 1.5 volts and 6 to 9 milliamps. The present detector and cooled preamp require an LO power density of about 10 to 20 watts per square centimeter in order to ensure shot-noise limited operation. The specific operating characteristics as well as a rigoruos evaluation of the various array options will continue into Phase II.

5.2.3.2 *Pre-amplifier Baseline and Trades*

The baseline preamplifier for the LAWS receiver is a GaAs Field Effect Transistor, FET, operating at a temperature of 120 K. This pre-amp will provide a 10 dB gain with a noise figure around 0.5 dB. The lower end cut-off for this device, (3 dB point), is around 100 MHz and will provide sufficiently high gain and low noise out beyond the required 1.2 GHz (for a 45° scan angle). The typical operating conditions for this amplifier are around 12 volts and 60 milliamps.

The preamps will be maintained at the desired 120 K by mounting them on the receiver vacuum shell near the displacers (see the cooler configuration). There will be 5 of these preamps, one for each detector element in the ring array geometry. Each generates roughly 0.7 watts of heat (12 v x 60 ma) which must be dissipated. This is a significant heat load at 120 K and tends to drive the detector design to a minimum number of elements.

5.2.3.3 Cooler Baseline and Trades

As shown earlier, the primary cooling load is 1 to 2 watts at 80 K for the 5 detector elements and the secondary cooling load is 3 to 5 watts at around 120 K for the pre-amps. These loads include the estimated parasitic losses due to the vacuum shell and any required cooling tubes. Additional cooler requirements are that the cooler vibration and microphonics at the primary load must be minimal and the cooler must be space-qualified with a three year life within the next 5 or 6 years. This are very stringent requirements for the state-of-the-art coolers and result in very little choice in cooling options. Figure 5-83 shows various cooler capabilities and projected performance. The only two options that meet the LAWS receiver requirements are the next generation split Stirling cryo-cooler under development and the future pulse tube cryo-cooler. Another option being investigated is the possible use of passive radiators for cooling the detector array and preamplifiers. This option would require that the array be operated at an elevated temperature (above 80 K) and would thus result in sub-optimal performance. This option is being carried in the event that the projected advances in the state-of-the-art for either of the mechanical cooler options do not materialize.

The split Stirling mechanical cooler has been chosen as the baseline for the receiver since there is a large amount of development effort in this area and a similar device is due to be flown on the UARS ISAMS instrument. These present design is slightly smaller than that required here, however, the next generation split Stirling cooler under development would meet the present requirements. These devices are currently being developed by both British Aerospace and NASA and would provide a cooling power of around 50 watts/watt, depending on the load and heat rejection temperature.

The baseline design for the LAWS receiver is to use an opposing pair of split Stirling coolers to provide the required cooling as well as to reduce the vibration and microphonics. Figure 5-84 shows the proposed mechanical cooler configuration. The two expanders are mounted on opposite sides of the vacuum shell and are mechanicaly separated from the two compressors. Most of the vibration is in the compressors which can be mounted at some distance from the vacuum shell and the detector array. Heat rejection will be accomplished by means of copper tubing which will carry the 300 K waste heat to the system radiator.

Type	Nominal Perf. (dB)	3.0 urad Misalign. Perf. (dB)	Align. Sens.	Redun-dancy	Comments
Single[2] 	0	-2.1 (-1.5 1σ)	none	none	Single Point Failure
Quad[1,2] 	-2.4	-3.4	very good	some	2.4 dB Loss in Nominal Situation
'Ring'[1,2,3] 	+0.3	-1.5 (-1.0 1σ)	good	some	Baseline Choice
Array[1] 	-1.1	-1.1	excell	excell	Requires Larger Cooler Design
'FIRE-POND'[1,2,3] 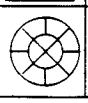	-2.0*	-2.5*	excell	excell	Requires Larger Cooler Design

Notes: 1) 5 um Dead Streets; 2) Optimum Size Central Element, 3) 15 um Dead Ring
* Estimated

Figure 5-81. Comparison of Various Detector Geometries

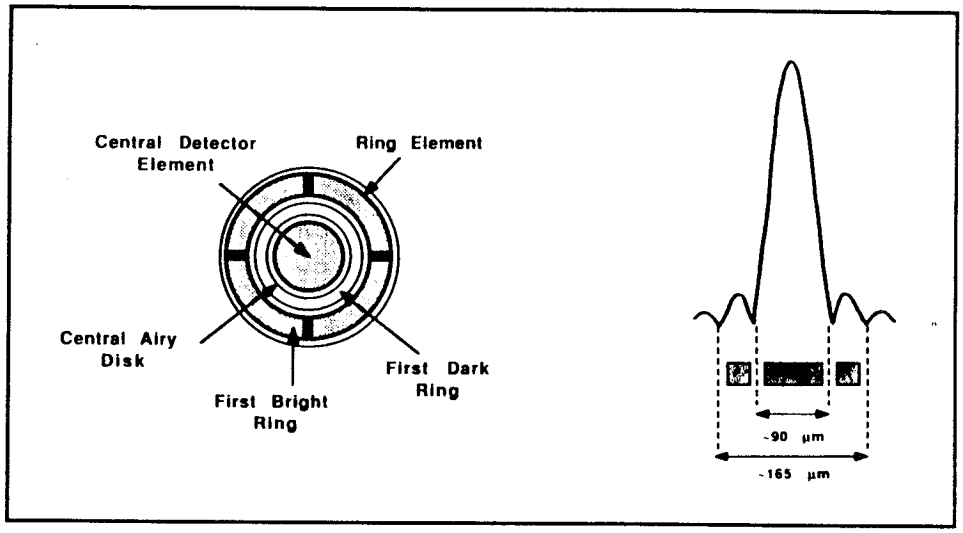

Figure 5-82. Baseline Detector Geometry

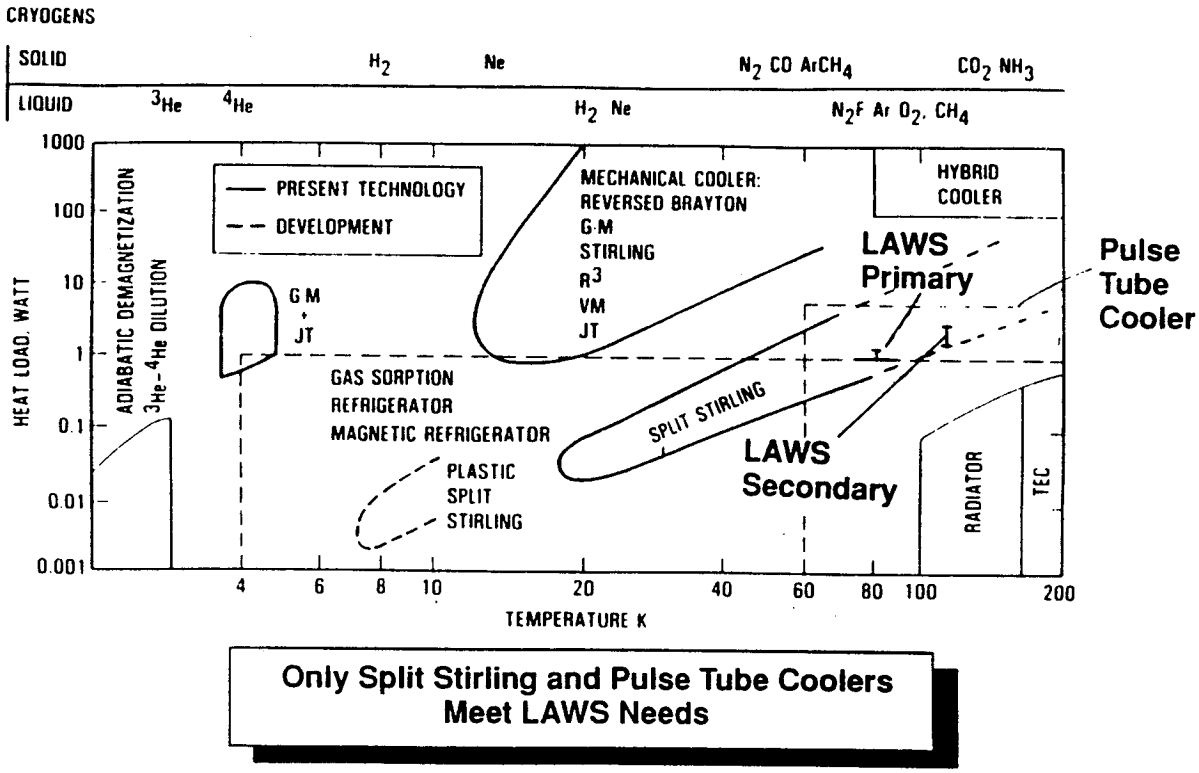

Figure 5-83. Various Cooler Option Capabilities

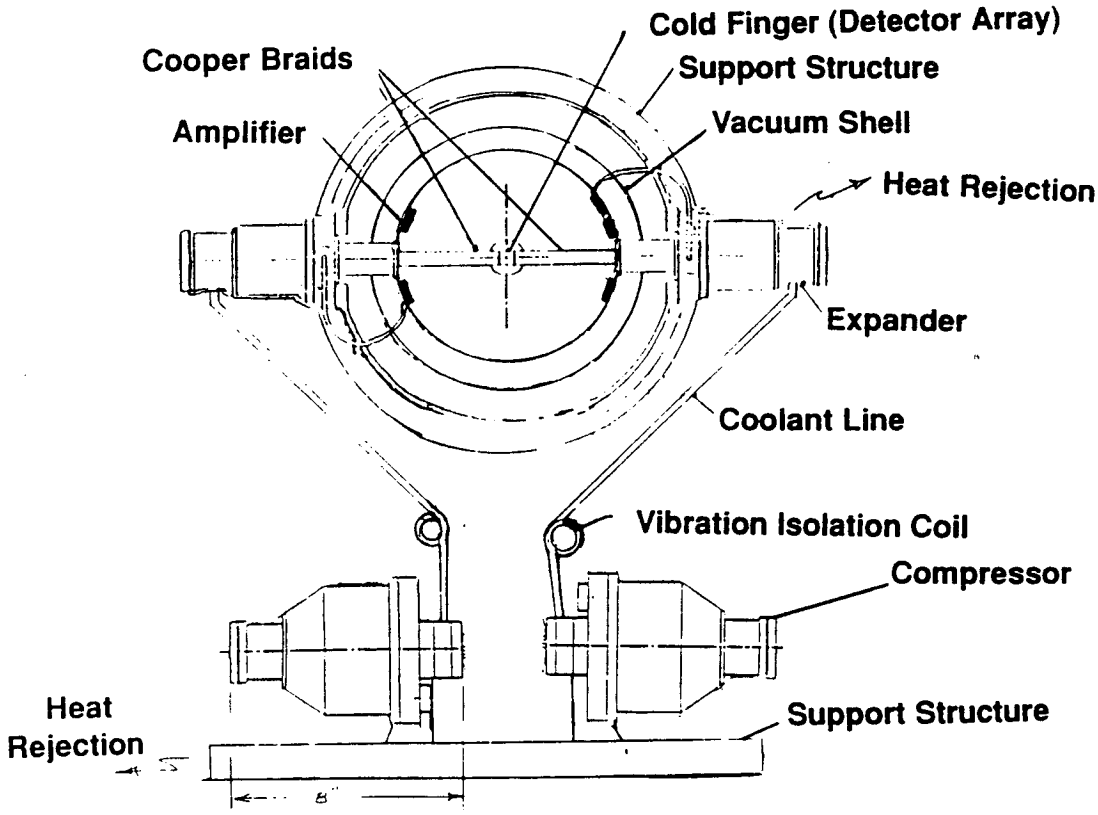

Figure 5-84. Proposed Mechanical Cooler Configuration

5.2.3.4 *Receiver Electronics Baseline and Trades*

Figure 5-85 is a block diagram of the receiver electronics including the IF amplifiers and signal processing. There are 5 IF channels, one for each of the detector elements, and a sixth channel for the transmit laser detector element. This sixth channel is used to monitor the specific frequency transmitted by the laser. The LO and transmit laser have a 40 MHz IF (asuming the use of a Bragg Cell to offset the LO) and this is detected by an element as part of the transmitter subsystem. Each of the six channels in the IF electronics chain are identical with the exception that the transmitter channel does not require the second LO. The second LO is required to remove the known spacecraft and earth Doppler shift from the return signal.

The Baseline IF design for the 5 detector channels is shown in Figure 5-86. Each IF electronics channel has a calibration input which is used to calibrate the IF electronics amplitude and phase characteristics. This is important when the individual signals are coherently combined. The next step is the second LO which removes the known spacecraft and earth Doppler shift. The high bandwidth signal is mixed down to a carrier frequency of around 100 MHz, plus or minus the 16 MHz wind velocity, by the second LO. Following the second LO is a series of switched attenuators used for gain control. Also shown is a LOG IF channel which may be required for very strong signals from cloud or ground returns. The Doppler processor will not be significantly degraded by a saturated signal, however, the use of the strong returns for alignment calibration and phase retrieval would require the LOG IF channel. Several wide-band amplifiers in

a gain stage follow the gain control attenuators. A bandpass filter with a 100 MHz center precedes the complex demodulator, or COHO. This COHO produces the "I" and "Q" phase quadrature signals from the split input. Each of these signals is then low pass filtered prior to A/D conversion. The A/D converters will sample the signal at a 32 MHz, or higher, rate with 8 to 10 bits of precision.

The baseline signal processor is the Adaptive Poly-Pulse-Pair algorithm developed by Lassen Research. There will be an identical processor for each channel which will provide redundancy as well as significant parallel processing capability which could later allow for uplink of new algorithms once the sensor is on-orbit. The processor will also include the capability to precisely determine the location of the center of the Airy disk on the detector array for use in alignment. The processing throughput is estimated to be around 75 MFLOPS total for the 5 channels. Figure 5-87 is a functional diagram of the proposed signal processor design based on two DSP chips per channel. This proposed adaptive poly pulse pair (APPP) algorithm provides a significant improvement in performance over the previously proposed pulse pair algorithm, while still remaining simple enough for on-board implementation. Other algorithms being investigated may provide improved performance over the APPP approach, however they will be limited to ground-based implementation due to their complexity and subsequent computing requirements. Thus, the present performance analysis (see section 6.3) using the APPP algorithm is somewhat conservative and is based on the expected results from the on-board Doppler processor.

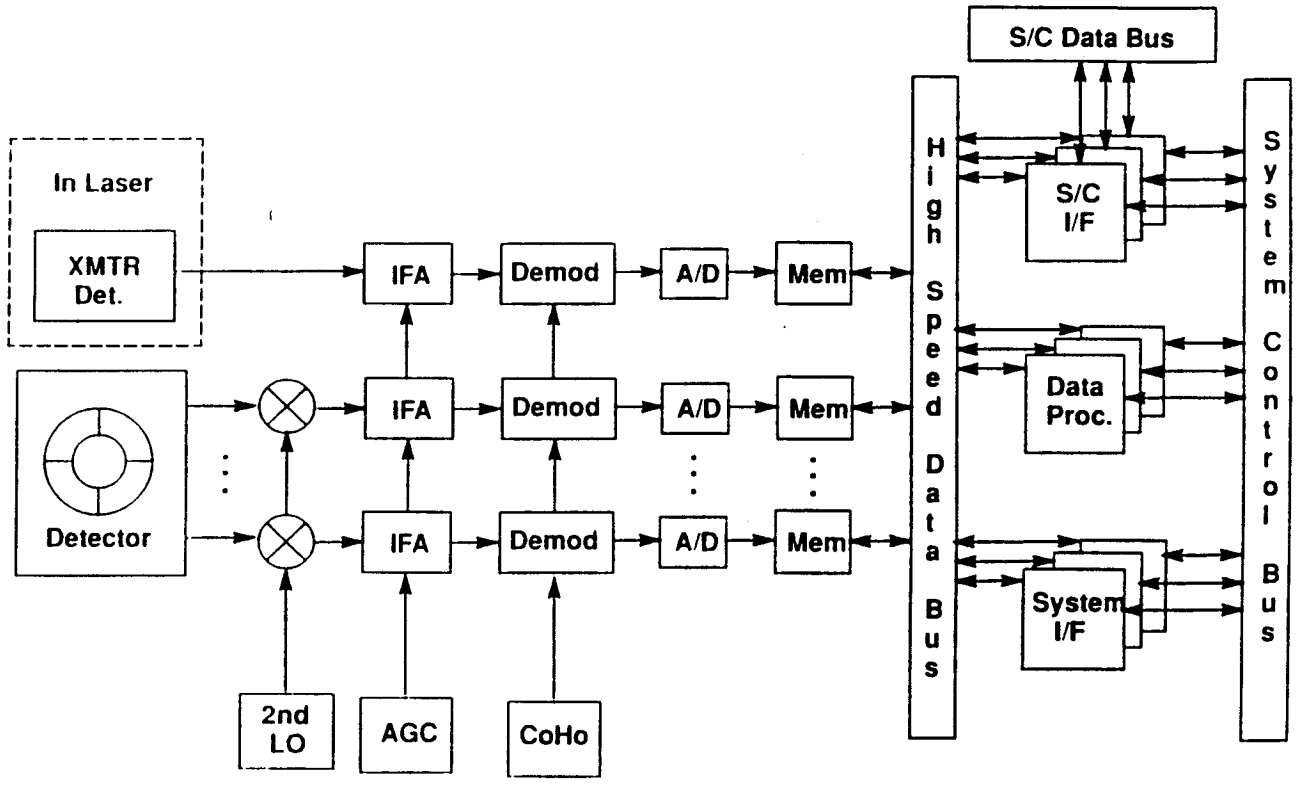

Figure 5-85. Receiver Electronics Block Diagram

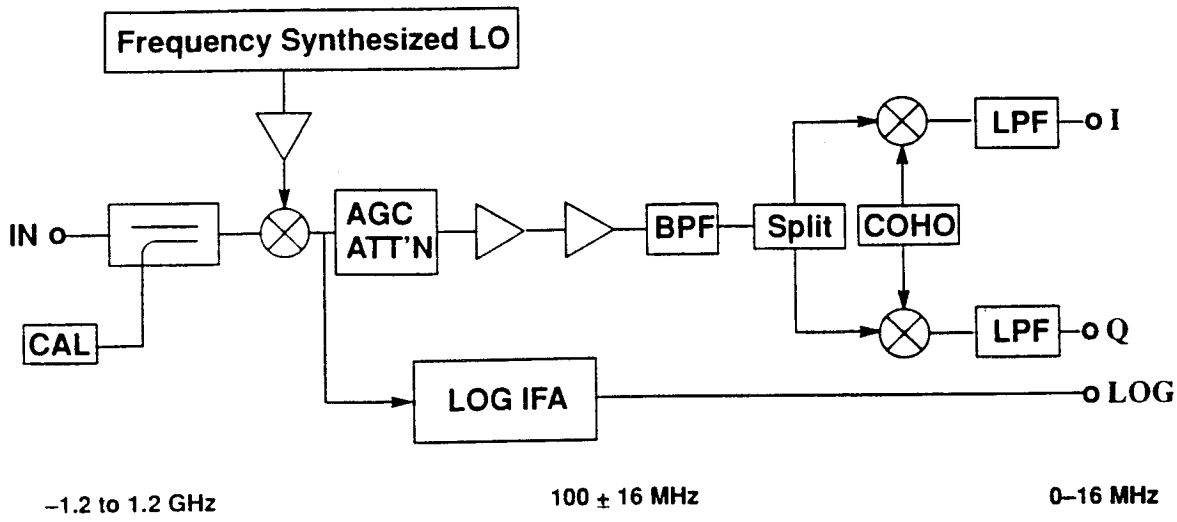

Figure 5-86. Baseline IF Electronics Schematic

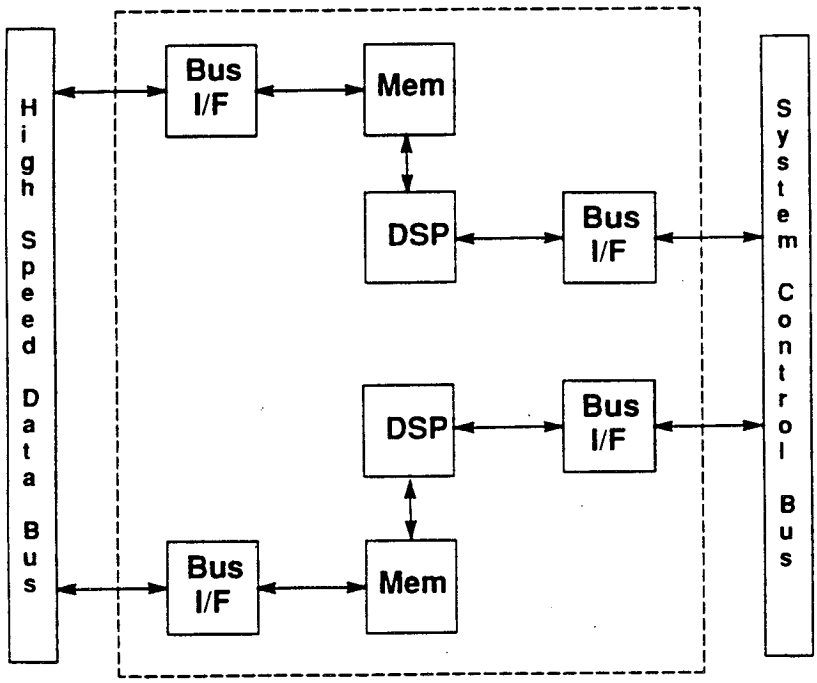

Figure 5-87. Baseline Signal Processor Schematic

5.2.3.5 *Receiver Power Supply*

The final element of the receiver subsystem is the power supply and power conversion hardware. We assume that the spacecraft power supply provides 120 volts DC to the receiver subsystem. The total receiver power requirement is 270 watts at several voltages. The baseline power converter is actually two separate power converters, one for the cooling engines and one for everything else. The cooler requires about 200 watts at 28 volts for running the compressors and displacers. The second converter will supply about 70 watts at around 10 volts for the remaining receiver subsystem elements. In addition to the converters, there will be an isolated detector bias voltage supply which will provide the .2 to 1.5 volt reverse bias for the detector elements.

5.2.3.6 *Design Summary*

A summary of the receiver properties is given in Figure 5-88. The total weight of the receiver is right at the 40 kg requirement and the power requirement of 269 watts is below the 300 watts budget. The receiver configuration consists of the cooler assembly, including the detector and pre-amps, and a separate electronics box containing the IF circuits, processors, power supply and subsystem controller. The cooler assembly is roughly 26 by 24 by 6 inches, not including the heat rejection. The electronics box consists of 12 printed wiring boards inside a chassis measuring about 8 by 10 by 12 inches.

A receiver configuration has been outlined which either meets or is projected to meet the system requirements by the beginning of Phase C/D. The receiver has been configured with the maximum redundancy and robustness possible while still meeting the system level requirements. The five element detector array, the dual split Stirling cooler assembly and the identical IF and processing channels provide significant redundancy as well as an increased performance capability and flexibility at this early stage of design. Significant analysis and development will continue through Phase II to further evaluate and improve the receiver baseline.

Assembly	Size(in)	Weight(kg)	Power (w)
Detector	*	*	4.0
Pre-Amp			
Cooler	26 x 24 x 6	30.0	200.0
IF Circuits	6 PWB	3.0	25.0
Processor	2 PWB	1.0	10.0
Power Supply	2 PWB	3.0	25.0
Controller	2 PWB	1.0	5.0
Chassis	8 x 10 x 12	2.0	- - -
Total	< 3 cu. ft.	40.0	269.0

** Included in Cooler Assembly*
PWB ==> Printed Wiring Board (7" x 11" x 0.5" each)

Figure 5-88. Receiver Size, Weight and Power Estimates

5.2.3.7 *Receiver Subsystem Technical Issues*

The issues associated with the receiver subsystem which have been identified during the Phase I Study are 1) improving the performance of HgCdTe detectors, 2) the cooler requirements for the detector and preamplifiers, and 3) the Doppler estimator performance.

HgCdTe detector improvements are the subject of a number of DoD programs as well as in-house efforts at GE. Split-Sterling coolers with the capability required for LAWS are being developed by British Aerospace and NASA for the Eos program. Finally, improved Doppler estimators are under development by Lassen Research and members of the LAWS Science Team.

5.3 Baseline Configuration Summary

As stated in section 5.0, the configuration selection process is somewhat different from the concept evaluation process in that more of the decisions are made at the subsystem level, once the system requirements are defined. Accordingly, this section largely reiterates and summarizes the information which has already been presented in the relevant subsystem sections, from a system perspective.

In the laser subsystem we have seen that there is a strong preference for selecting a self-sustained discharge laser over an e-beam sustained laser. Accordingly a self sustained laser is chosen as baseline.

The choice of optical resonator is important from the laser subsystem perspective in that, in order to maximize the laser efficiency, we must choose a design capable of extracting as much of the energy stored in the discharge as possible. It is also important from a system perspective, however, because simply generating large amounts of raw energy is no guarantee of high performance. The energy must be generated in a beam of high quality, close to diffraction limited in order to maximize the energy in the central lobe of the far-field beam pattern. As discussed in the laser subsystem section these considerations mandate the choice of a Gaussian reflectivity unstable optical resonator.

The main laser transmitter is an injection seeded device and we have seen that by using a frequency swept local oscillator we can ease the requirements on the heterodyne detector in the receiver subsystem. Such an approach would we believe unnecessarily complicate the laser subsystem, and furthermore in-house research on HgCdTe detectors is yielding encouragingly high quantum efficiencies which lead us to believe that a figure of 40% quantum efficiency at 1.5 GHz is achievable. A fixed frequency LO and injection seed laser is therefore our baseline choice.

In the optical subsystem we have shown that, by adopting a confocal parabola design, we can reduce or eliminate entirely the problems inherent in the historical Windsat design. The new optical design has no focal points, allowing the system to be tested in air, and it has a much reduced figure for the optical feedback. A further benefit of the design is the elimination of the T/R switch. Also by having a fixed offset to accommodate the lag angle we are able to offer true asynchronous laser operation.

For the optical subsystem mechanical configuration we have been offered two choices, an end-mounted design and a CG mounted design, both capable of meeting the top-level performance requirements. The CG mounted design offers some potentially desirable features: the large bearing should have less runout than the smaller bearing in the end-mount design, the mechanical interface is a plane making the CG design easier to support and launch caging should be easier. Furthermore, if a variable nadir angle became a requirement it would be more easily accommodated in the CG configuration. The weight of the design is an issue however, and so we have chosen the end-mounted design as baseline although we are maintaining the CG mounted design as an active option.

Considerations of image motion compensation led us to choose a detector array for the receiver. The configuration chosen is a central circular element approximately equal to 70% of the return-signal Airy disk size for optimum mixing efficiency, with four circularly symmetric detectors around the periphery. These auxiliary detector elements offer the potential of measuring the amplitude and phase of the return signal to facilitate the measurement of any misalignment as well as contributing approximately 0.5 dB to the SNR.

The detector array is operated at 80 K and the preamplifiers are maintained at 120 K. The cooler which has been baselined for the receiver is the next generation split Sterling engine cooler under development by both British Aerospace and NASA. In the event that lifetime issues arise with this cooler we can operate the detector at a higher temperature using a passive radiator (for the sun-synchronous POP) at the expense of some reduction in the SNR.

As detailed above and in the relevant subsystem sections the configuration decisions which have been made are looked upon as conservative and realistic. Section 6.0 illustrates the anticipated performance of our baseline system and shows how the requirements are met with the chosen instrument parameters. Nevertheless, we are proposing to carry forward into Phase II certain active options. These options are summarized in Figure 5-89.

Option #1, the alternate telescope configuration refers to the CG mounted design discussed above. Options #2 and #3 are concerned with possible future enhancements to laser performance. Option #4, a larger detector array, will be kept open so that as our in-house understanding of the potential and pitfalls of HgCdTe arrays matures, we will be able to decide if it is worth reducing the optical subsystem requirements further, at the expense of added complexity in the receiver. Options #5 and #6 refer to possible enhancements in the Science requirements for LAWS. Neither depolarization nor backscatter is a requirement at present but as our design matures we will bear them in mind in the event that they become so in the future.

The next section presents our configurations for the integrated instrument as a payload on a polar orbiting platform and as an attached payload on Space Station.

Option	Mission/Science Benefit	Trades/Issues
1) Alternate telescope configuration	Variable nadir angle (coverage vs SNR)	Weight. Mechanisms required to accommodate different lag angles
2) Higher repetition rate	Local wind accuracy	Peak power, weight
3) Higher pulse energy	Vertical resolution, velocity accuracy	Weight, power
4) Larger detector array	Reduce optical subsystem complexity	Increased cooling, Receiver complexity
5) Depolarization channel	Cloud studies	Increased cooling, Optical complexity
6) Backscatter measurement	Aerosol statistics	Calibration

Figure 5-89. Active Options for Phase II

5.4 Integrated System Description

LAWS is a candidate payload for the Japanese Polar Orbiting Platform (JPOP) and Space Station. The design of JPOP is currently in a very early stage and details as to e.g. mechanical, thermal, electrical instrument accommodation requirements are not available. To develop concepts for mounting LAWS to JPOP we therefore need a surrogate platform which is representative of what can be expected as the JPOP design matures. Since NASA, the Europeans and Japan are all involved in the Earth observing system (Eos) program we have selected a platform concept modeled after Eos-A, for which GE is the systems integrator, as the platform to illustrate our approach to instrument accommodation. Eos-A has been selected for launch on a Titan-IV which has an envelope of 15 ft (4.6 m) identical to the Japanese H-II launch vehicle envelope.

A perspective view of LAWS accommodated on the Eos-type platform is shown in Figure 5-90. The instrument has been divided into two parts for ease of accommodation. Mounted to the front of the platform is the sensor module which consists of the telescope assembly, the laser and the receiver assembly. A support module is mounted on the earth facing panel of the end bay of the platform. The support module takes up two of the payload mounting plate locations on the end bay as shown in the +z facing view of Figure 5-91. One plate supports the laser fluid circulation system, the system controller, power conditioner and momentum wheel. Heat from these components is dissipated through a platform-supplied cold plate. Alongside this plate is the laser heat exchanger and cold plate assembly, which has been sized to dissipate an average of 2 kW. Weights for the two modules are given in Figure 5-92.

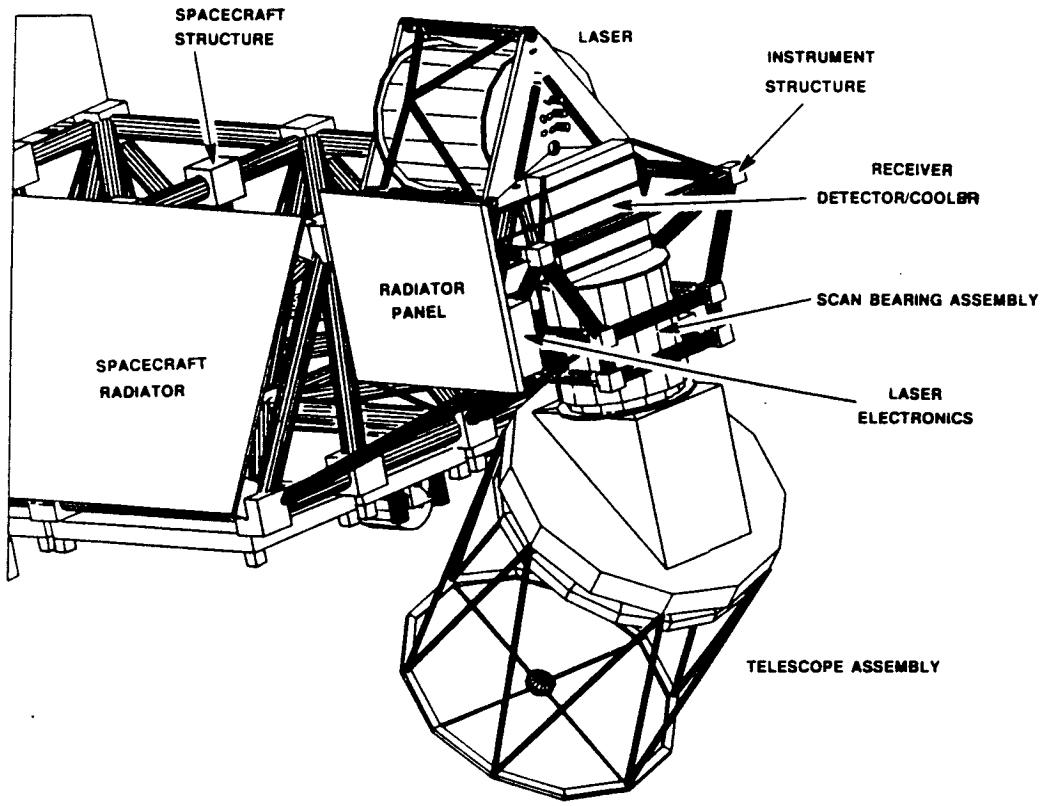

Figure 5-90. Perspective View of LAWS Mounted on Eos-Type Platform

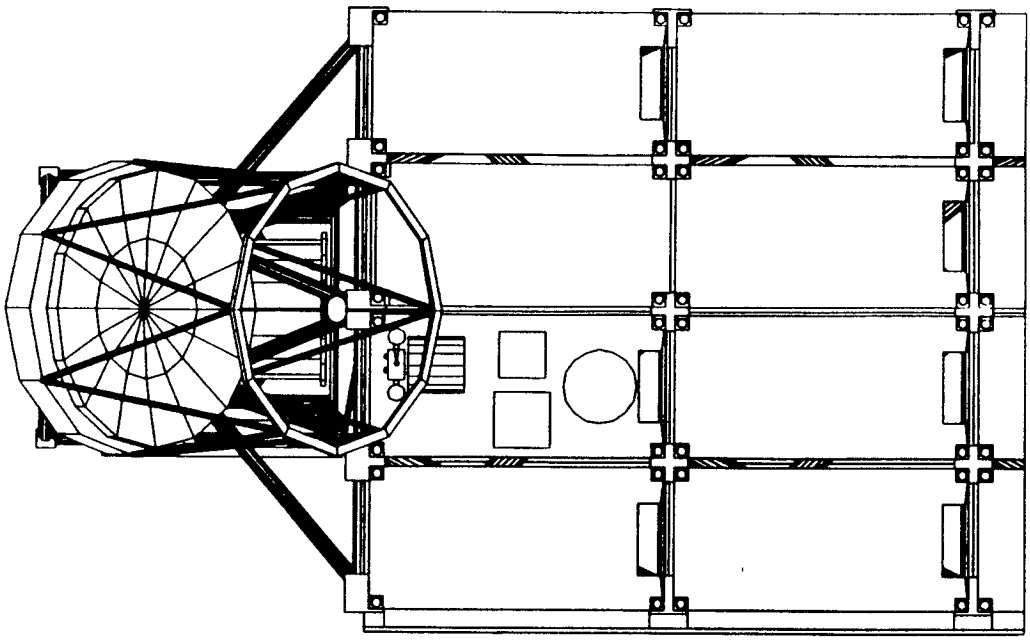

Figure 5-91. Earth Facing Panel View of the LAWS Platform

Component	Weight
Sensor Module	580 kg
Support Module	100 kg
Reserve (15%)	100 kg
Total Allocation	800 kg

Figure 5-92. Weights for the Two LAWS Instrument Modules

The thermal subsystem also comprises two parts. There is the laser heat rejection subsystem which uses a cold plate to dump heat from the laser on to the platform thermal bus. As stated above the laser heat rejection subsystem is sized to reject 2 kW. The design allows the laser burst mode of 20 Hz to be sustained for 1-2 minutes.

The concept of having a central platform thermal control system is currently baselined on Eos-A and we therefore assume one will be available on JPOP. If it is not and LAWS has to carry its own cold plate and radiators to handle the laser heat then the weight will increase about 100 kg.

The second part of the thermal subsystem is a local radiator attached to the sensor module which rejects heat from the receiver cooler assembly and sundry electronics boxes. The radiator faces the anti-sun side and has an area of 15 sq. ft.

To facilitate electrical accommodation studies we have assumed that JPOP will deliver power to the payloads at a nominal 120 V DC, as is the case for Eos-A. LAWS requires power to be supplied to two different types of end-users. There are the various electronics boxes and the receiver which require low voltages and moderate powers and which offer essentially benign loads to the electrical bus, and then there is the laser which operates at high voltages, on the order of 60 kV. The system, therefore, provides a power conditioner to take care of all the power with the exception of the laser. The laser power conditioner is internal to the laser head itself. The laser switches the applied voltage at up to 20 Hz and is designed to minimize radiated EMI and conducted transients. In order to meet the EMI requirement we need to enclose all of the pulsed power components in a conductive shell, in this case the laser gain module, and isolate the input electrical bus by using filters and other standard techniques.

Our analysis of the electrical power required from the platform to operate LAWS has assumed a 20 Hz maximum repetition rate laser operating at an average rate of 13 Hz. The laser efficiency has been assumed to be 6%. In order to calculate the orbit average power we have assumed a 90% duty factor per orbit, i.e., the laser would be turned off (e.g. over the Poles) for 10% of the orbit. This is a conservative assumption; shot management scenarios presented at the LAWS Science Team Meeting in January 1990 (G. D. Emmitt, R. Brown, T. Miller, J. Paegle *Shot Management for LAWS*) indicated potential shot suppression factors of 16% (705 km orbit) and 22% (824 km orbit). Under these assumptions, the orbit average power requirement is 2735 W (2935 W with a 7% reserve).

In practice over the lifetime of the instrument we will have an average rate of 10 Hz, which gives a power consumption of about 2470 W (2840 W with 15% reserve). For the 1/cos algorithm, a 10 Hz maximum repetition rate laser and a 90% duty factor per orbit the average power requirement becomes 1835 W (2110 W with a 15% reserve).

The peak power requirement is 4500 W and assumes the laser operating in its burst mode of 20 Hz (for a maximum of 1-2 minutes) and a worst case thermal environment for the telescope assembly. The telescope is maintained at its assembly temperature of 21°C by heaters which have a peak power requirement of 612 W.

The standby power required is 534 W (614W with 15% reserve). In the standby mode we assume that the telescope is rotating (and also the compensating momentum wheel), the detector is cooled to its cryogenic temperature, and that the laser fluid loop is operating. The power requirements are summarized in Figure 5-93.

A breakdown of the LAWS system configuration parameters for the JPOP platform with LAWS operating at 10 Hz peak, 13 Hz average and 90% duty factor is shown in Figure 5-94. The chart shows all of the major subsystems which make up the LAWS instrument including both the end-mounted configuration (#1) and the CG mounted configuration (#2) for the optical subsystem. The bottom line totals are shown for both configurations.

Baseline Power Requirement	Assumptions
2735 W Average (2935 with 7% Reserve)	13 Hz Average Rate Laser Operation, 90% Duty Factor
4500 W Peak	20 Hz Burst Mode (Laser), Worst Case Thermal (Telescope)
534 W Standby	Telescope Rotating, Detector Cooler Operating, Fluid Loop On

Optional Power Requirement	Mode of Operation
2470 W Average (2840 W with 15% Reserve)	10 Hz Average Rate Laser Operation
1835 W Average (2110 W with 15% Reserve)	10 Hz + Shot Management (6.5 Hz Avge), 90% Duty Factor

Figure 5-93. Electrical Power Requirements for LAWS

Component Description	Weight lbs	Weight kg	Peak Power (W)	Avge Power (W)	Standby Power (W)	Heat Reject. (W)
Optical Subsystem						
Configuration #1	737.23	334.40	699.50	212.50	81.00	0.00
Configuration #2	988.33	448.30	699.50	212.50	81.00	0.00
Laser Subsystem	267.20	121.20	3170.00	1889.10	30.00	1749.00
Receiver Subsystem	88.18	40.00	280.00	280.00	200.00	280.00
Support Subsystems	94.78	42.99	153.00	153.00	23.00	153.00
Thermal Subsystem	120.50	54.66	200.00	200.00	200.00	200.00
Mechanical Support Structure	146.75	66.56	0.00	0.00	0.00	0.00
Total with Configuration #1	1454.64	659.81	4502.50	2734.60	534.00	2382.00
Reserve	218.20	98.97	675.38	200.00	80.10	357.30
Total with Configuration #2	1705.74	773.71	4502.50	2734.60	534.00	2382.00
Reserve	255.86	116.06	675.38	200.00	80.10	357.30
Total + Reserve Configuration #1	1672.83	758.78	5177.88	2934.60	614.10	2739.30
Total + Reserve Configuration #2	1961.60	889.77	5177.88	2934.60	614.10	2739.30

Figure 5-94. LAWS System Configuration Parameters

The sensor module support structure is shown in Figure 5-95. It uses a graphite epoxy truss structure with titanium fittings. This approach provides a very stiff structure with a high degree of thermal alignment stability. The design has been based on the UARS structure technology which is also being used on the US Polar Platform designs being developed by GE.

Figure 5-96 shows the LAWS telescope in its as-launched configuration. The primary mirror assembly is held at its periphery by launch locks as shown.

Figure 5-97 shows a side view of the platform in its launch configuration inside the Titan IV shroud. Note that the platform is four bays long to accommodate the laser heat rejection radiator.

Figure 5-98 shows the LAWS instrument reconfigured as an attached payload for the manned Space Station. The telescope, laser and receiver are now mounted on the same side of a deck carrier and the telescope has been raised about 6" to accommodate the input and output beams. The ADS required to provide the pointing knowledge is the large box shown alongside the telescope, opposite the laser. The deck carrier mounts to a station interface adaptor (SIA) which mounts to the space station via the SIA leg assembly. The deck carrier, SIA and SIA leg assembly are all parts of the standard attached payload accommodation equipment (APAE). The assumption has been made that the instrument heat rejection would be handled by a Space Station thermal control subsystem. The provision of such a system is, however, currently under review. LAWS requires a radiator area of about 180 sq.ft. and if the instrument had to carry its own radiators a place for them would have to found. A very preliminary analysis has shown that there is room for two 6ft. x 15 ft. radiators which could be deployed and steered to offer the most favorable thermal rejection.

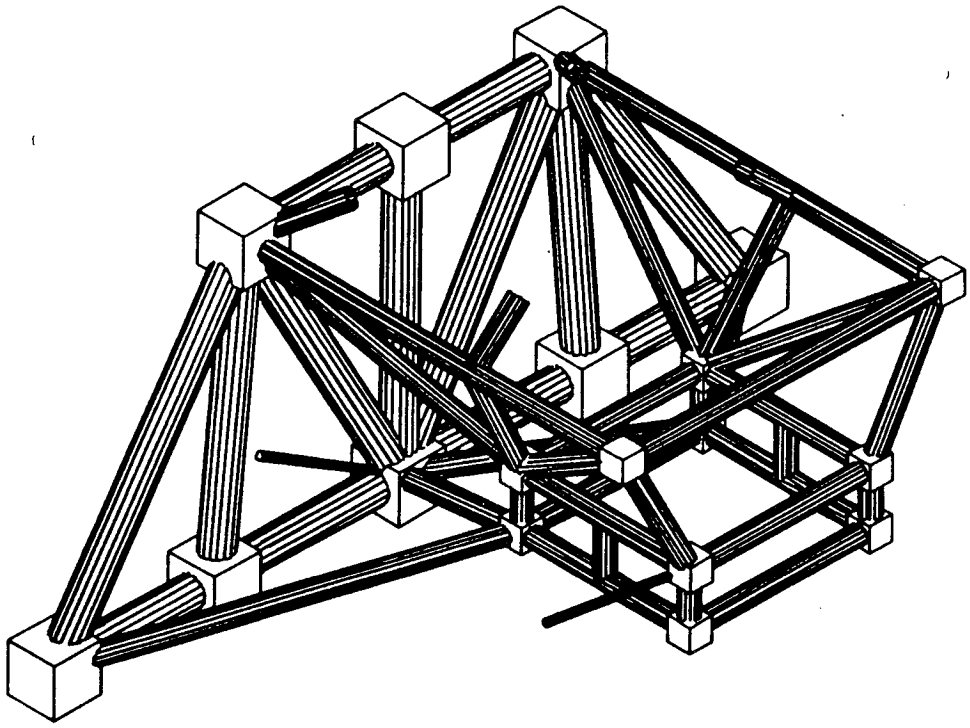

Figure 5-95. LAWS Sensor Module Support Structure

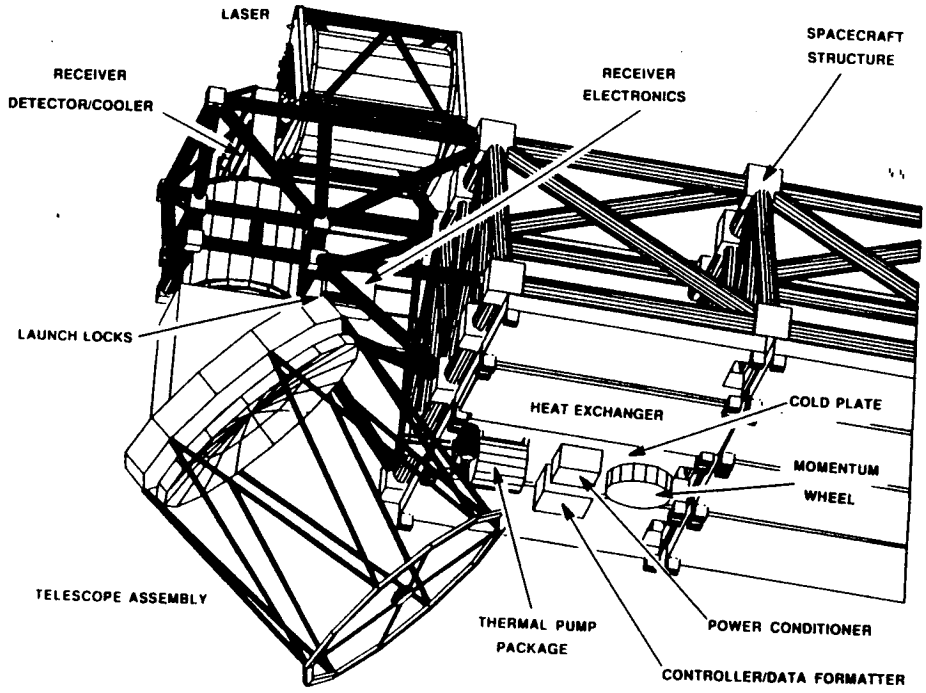

Figure 5-96. LAWS Telescope Launch Configuration

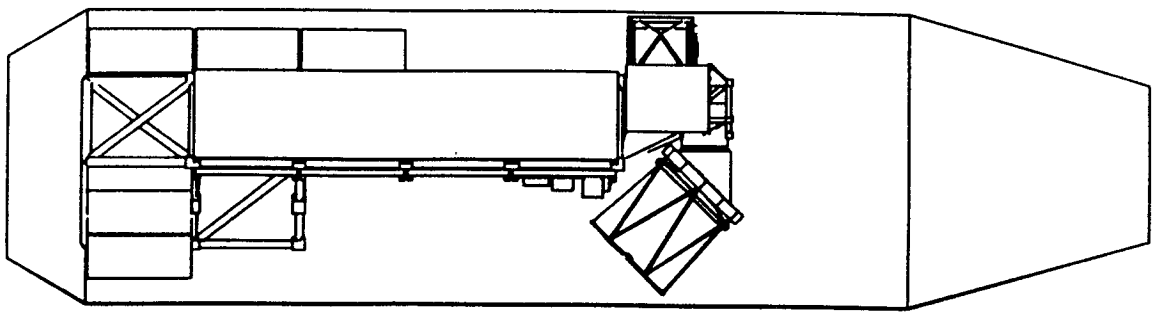

Figure 5-97. LAWS Platform Inside the Titan Shroud

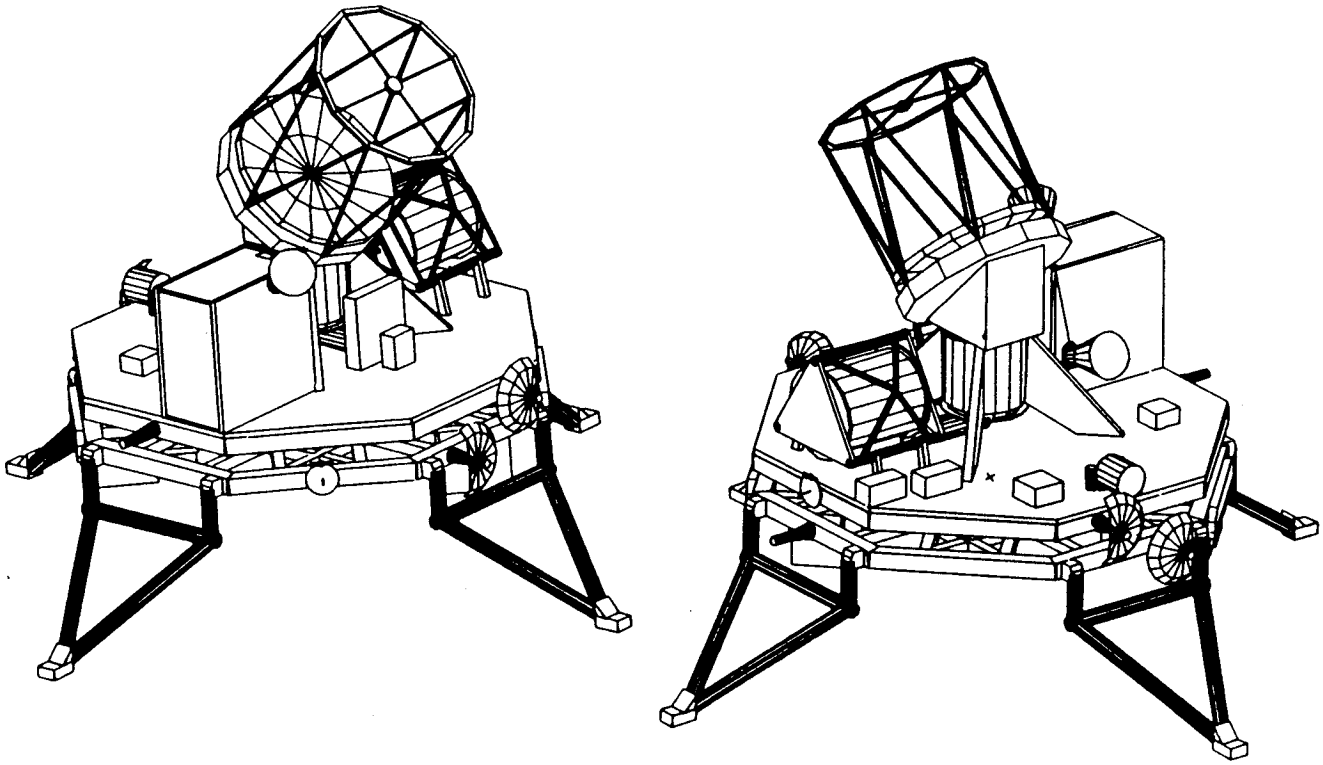

Figure 5-98. LAWS Configured as an Attached Payload for Space Station

6.0 LAWS CONFIGURATION PERFORMANCE

Given the chosen system configuration, the preliminary LAWS performance can be estimated. This performance will be presented in terms of coverage, SNR, line-of-sight velocity error and horizontal inversion performance. This performance analysis is based on the Lidar equation as presented in, for example, NOAA Tech Memo ERL-WPL-37.

6.1 Coverage

An orbital analysis program was used to calculate the 12 and 24 hour coverage for several sensor altitudes. All of the orbits are circular polar orbits and the configuration scan angle of 45 degrees was used. Figure 6-1 is a plot of the percent coverage for the 824 km altitude orbit which is used for all further performance calculations. Figure 6-2 shows the actual ground coverage on the earth surface for 12 and 24 hours, assuming the 824 km orbit. The 24 hour plot shows there are some uncovered areas between 20 and 30 degrees latitude. This corresponds to the 70 to 80% coverage at these latitudes shown in Figure 6-1. Figure 6-3 is a plot of the percent coverage assuming a 705 km altitude orbit. The 12 and 24 hour coverage here is somewhat less than the 824 km orbit, however, the lower altitude results in an increase in SNR of roughly 1.4 dB due to the shorter range. Figure 6-4 shows the field of view coverage on the earth's surface for the 705 km orbit. Finally, Figures 6-5 and 6-6 show the results of the coverage analysis for the alternate low altitude polar orbit of 540 km.

6.2 SNR Estimates

All of the subsystem parameters can be used to calculate the sensor signal-to-noise ratio using the Lidar equation:

$$SNR = \pi\eta E\beta c D^2 \exp(-2kR)/(8h\nu BR^2)$$

where:

η is the overall system efficiency including the heterodyne quantum efficiency,
E is the transmitted pulse energy,
β is the atmospheric backscattering coefficent,
c is the speed of light,
k is the atmospheric extinction coefficient,
R is the range,
D is the diameter of the transmitter/receiver telescope,
$h\nu$ is the photon energy,
B is the electronic bandwidth.

One of the parameters in the Lidar equation is the system efficiency. This term is actually made up of the optical efficiency, the heterodyne performance efficiency, the receiver quantum efficiency and the transmitter Gaussian beam truncation loss. The optical efficiency is a combination of the optics throughput, including any obscuration losses. The configuration optical design has 7 surfaces in the transmitter and 18 surfaces in the receiver (a mirror is one surface and a lens 2 surfaces). Each of these surfaces is either anti-reflection coated (for lenses) or high-reflection coated (for mirrors) with a design coating efficiency of around 99.5% at 9.11 microns. A conservative assumption for the actual on-orbit throughput would be 98.5% per surface. This assumption results in a transmitter optical efficiency of .90 and a receiver optics efficiency of .76. The other factor in the optics eficiency is the loss due

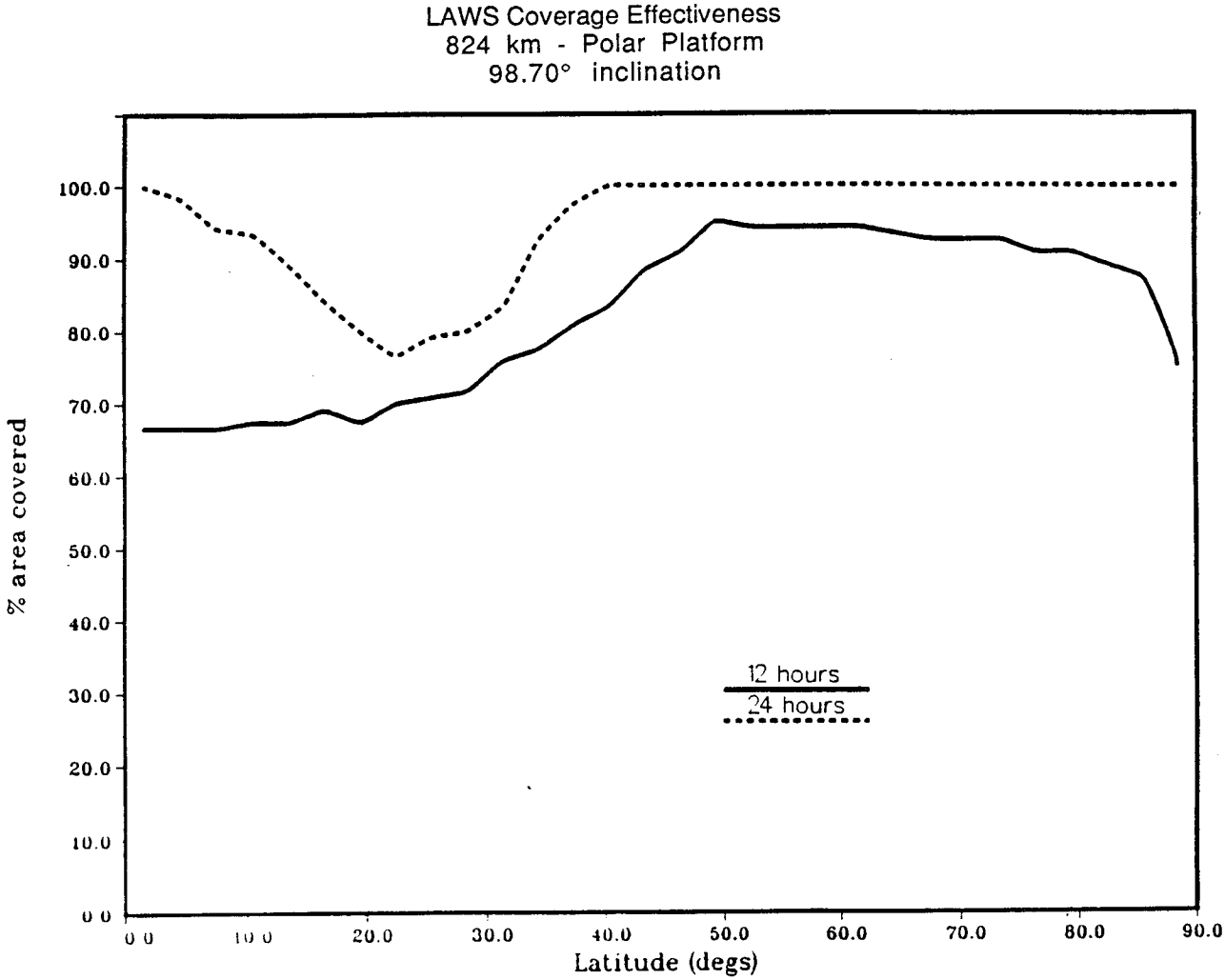

Figure 6-1. Percent Coverage for 824 km Orbit

to obscuration by the secondary mirror. The configuration optical design has a clear aperture of 99.73%, much higher than the previous Windsat design. Thus, the entire optical system efficiency is .68 (.90 x .76 x .9973).

The next terms in the system efficiency are the heterodyne performance efficiency and the detector AC quantum efficiency. The performance term is a product of the encircled energy, or the amount of light passing through the receiver which falls on the detector element, and the heterodyne mixing efficiency. All of the SNR estimates presented will be based on the use of a single detector, potential improvements due to the use of a multi-element detector are presented in the receiver section. If the optical system is diffraction limited, 84% of the energy incident on the aperture will fall in the central lobe of the Airy pattern (ignoring the throughput covered in the optics efficiency term). Previous analysis using the GE developed HETEVAL (HETerodyne EVALuation) program suggests that the optimum size for a single circular detector is roughly 70% of the Airy disk diameter. This results in a diffraction limited encircled energy of 79%. The theoretical maximum heterodyne mixing efficiency for this diameter detector is .90 if a plane wave local oscillator, LO, is used. This mixing efficiency is a measure of the match between the LO and signal amplitude and phase maps. Combining the theoretical mixing efficiency and the diffraction limited encircled energy results in a maximum heterodyne performance efficiency of .71 (.90 x .79). A more conservative number of .60 (about -.75 dB) has been used in this analysis for the heterodyne performance efficiency. This loss from the theoretical accounts for the fact that the optics will not be completely diffraction limited and there will be some misalignment between the Airy pattern and the detector.

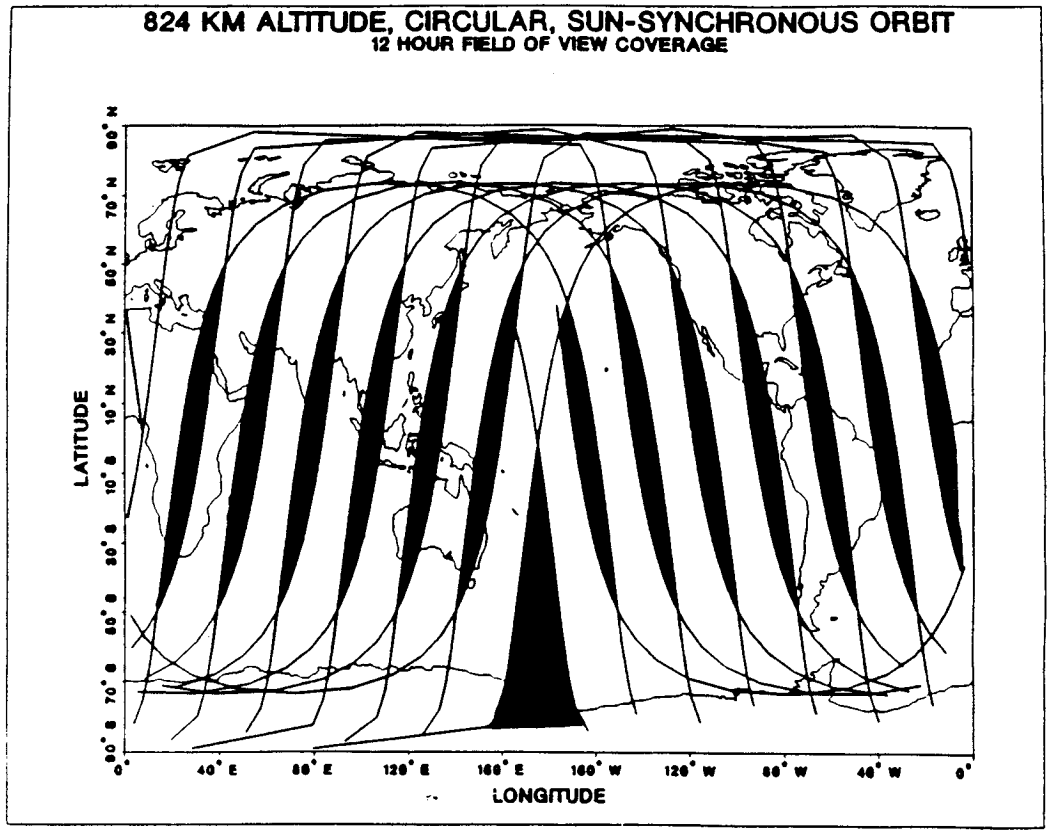

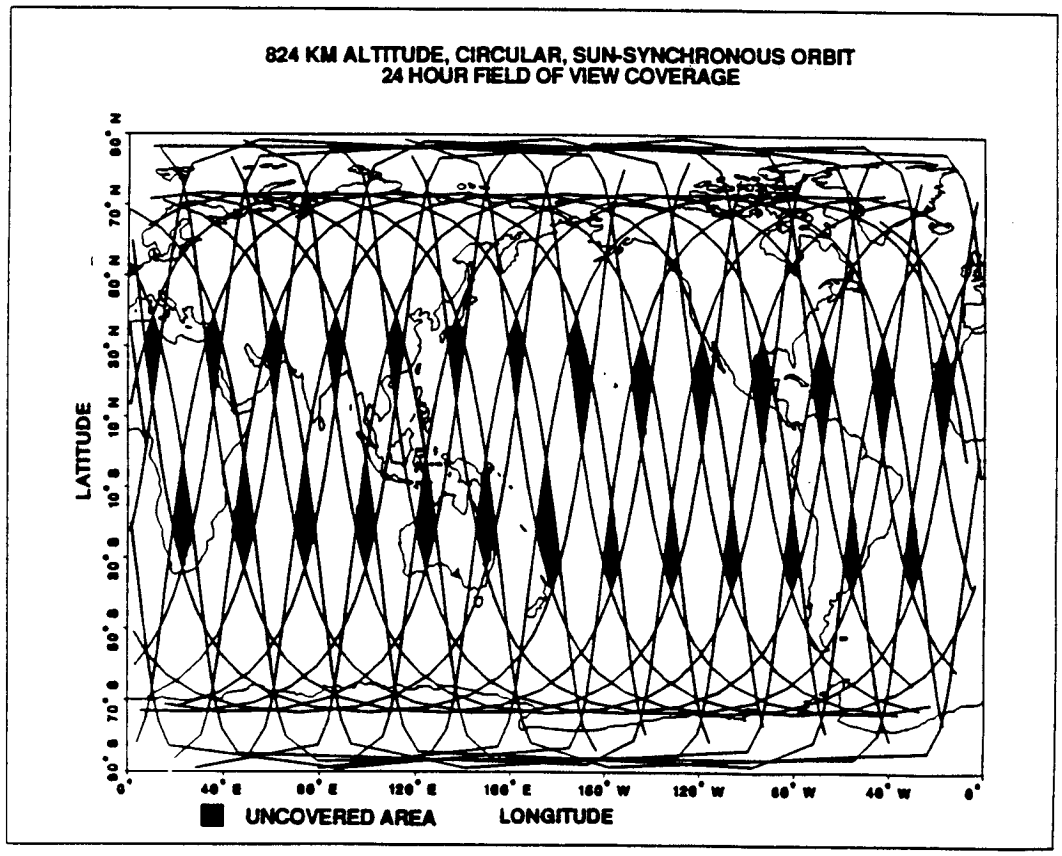

Figure 6-2. 12 and 24 Hour Coverage for 824 km Orbit

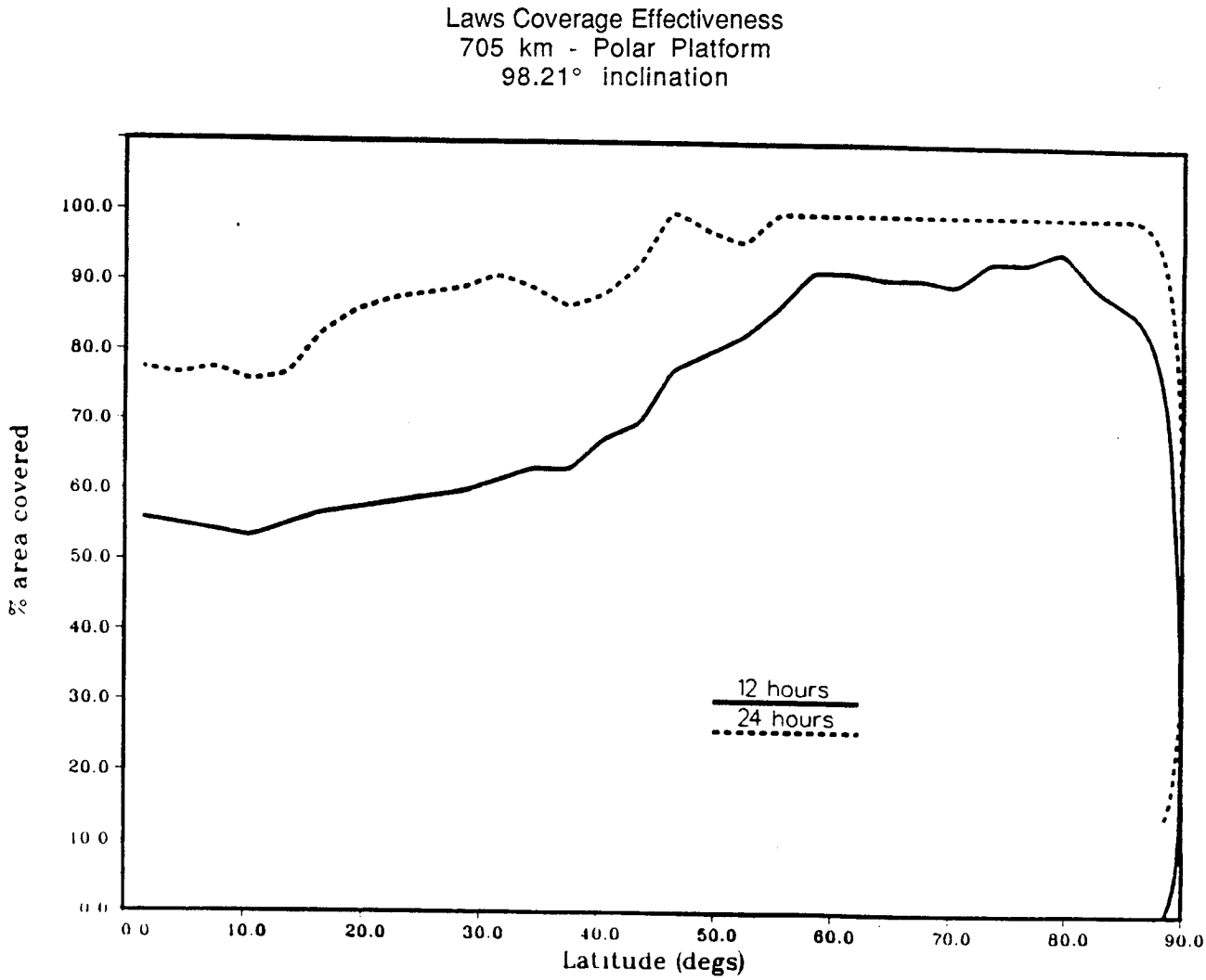

Figure 6-3. Percent Coverage for 705 km Orbit

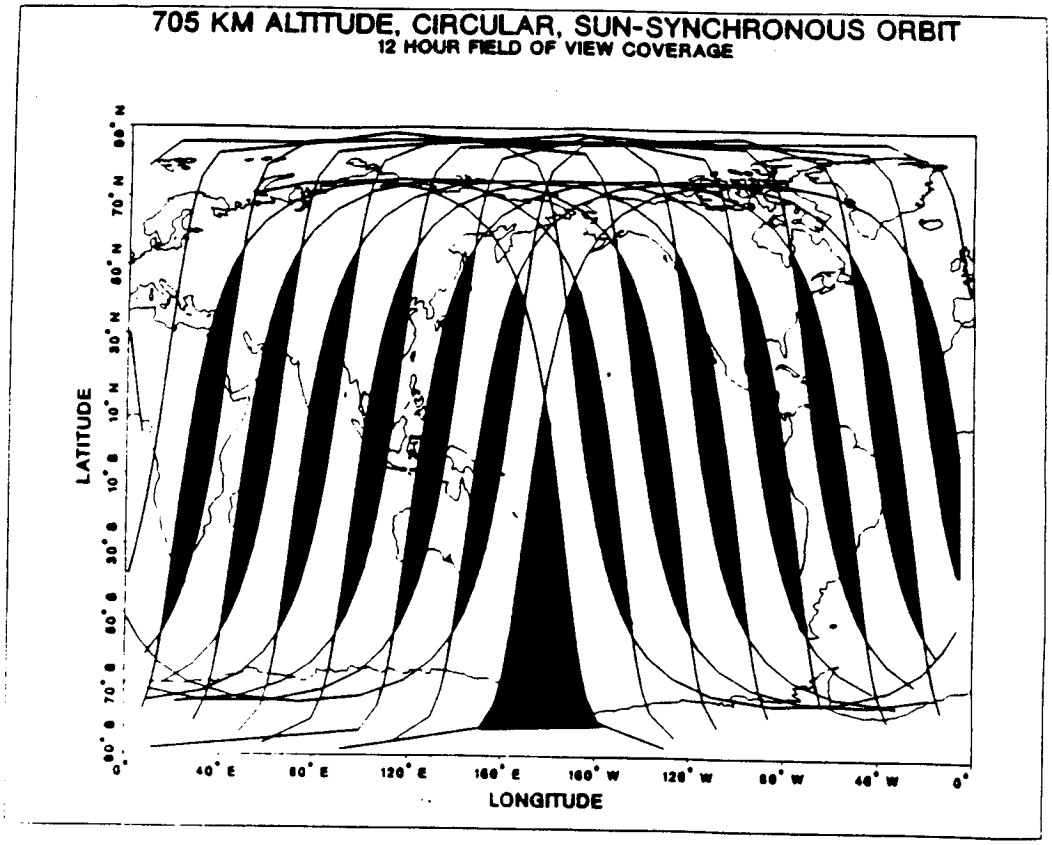

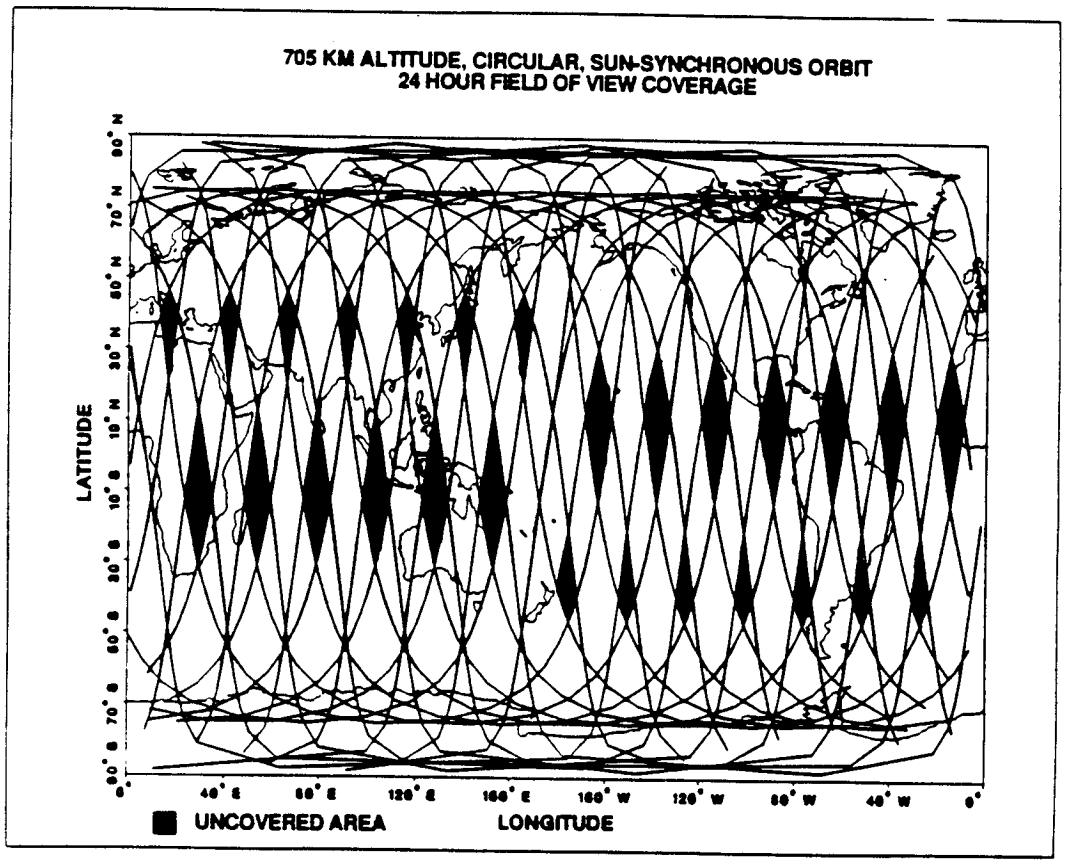

Figure 6-4. 12 and 24 Hour Coverage for 705 km Orbit

LAWS Coverage Effectiveness
540 km - Polar Platform
97.55° inclination

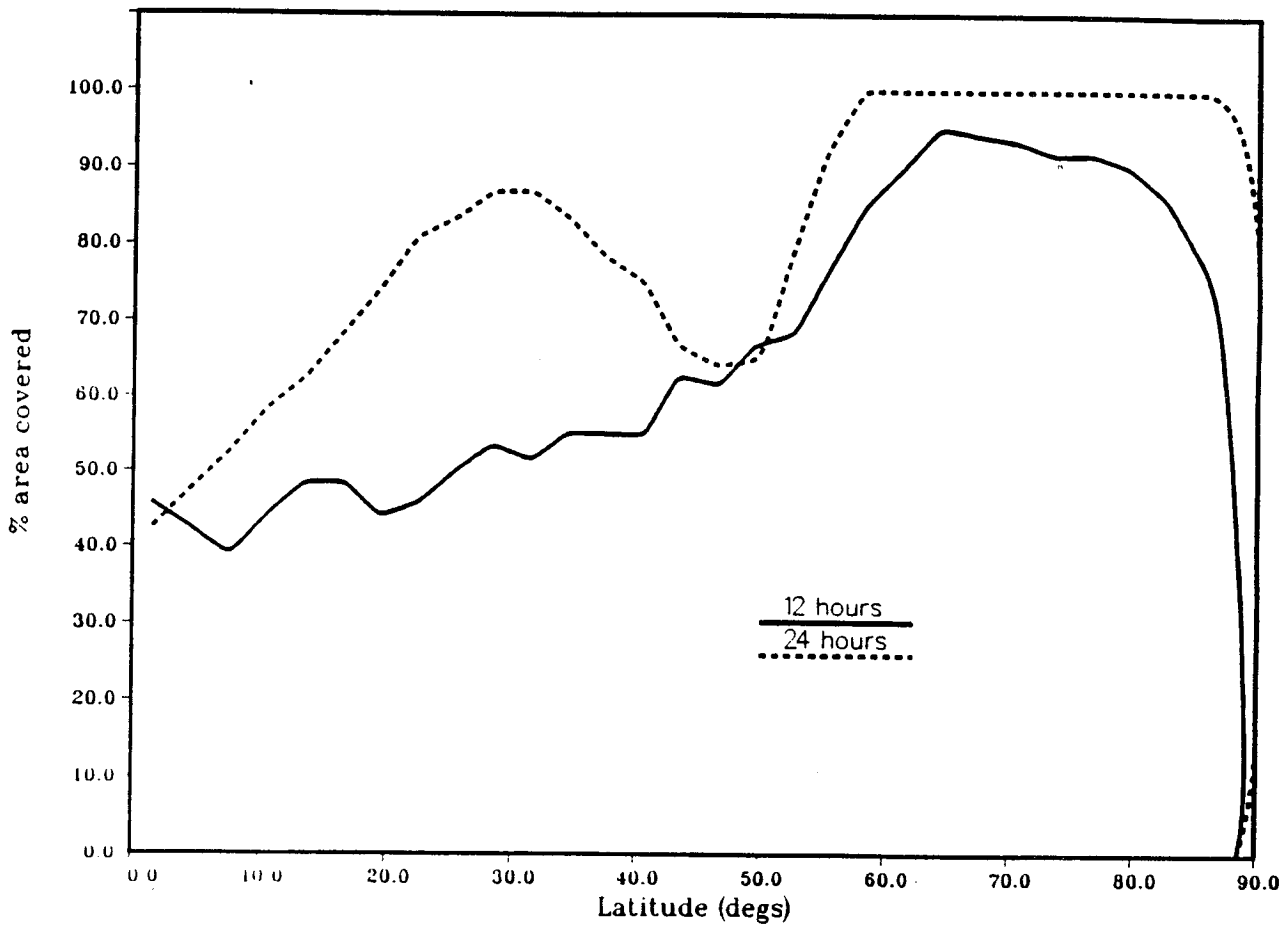

Figure 6-5. Percent Coverage for 540 km Orbit

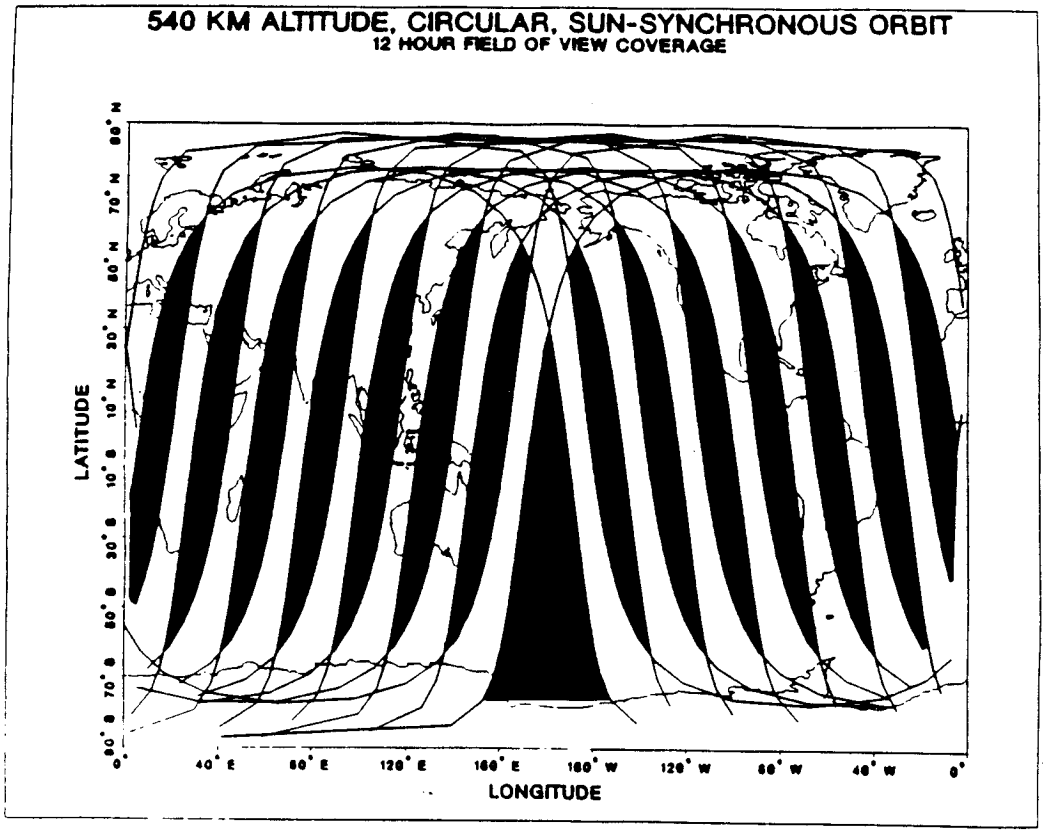

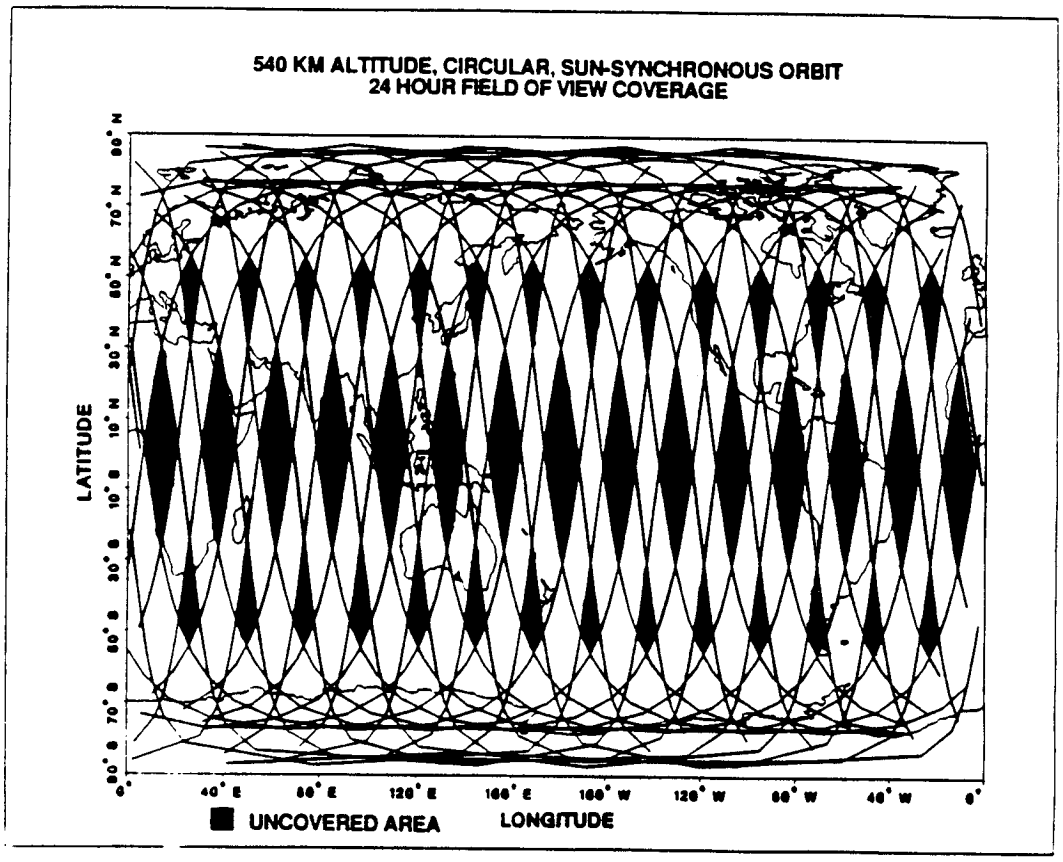

Figure 6-6. 12 and 24 Hour Coverage for 540 km Orbit

The detector itself also has a heterodyne, or AC, quantum efficiency which is not unity but it is estimated that the heterodyne quantum efficiency will reach 40% by the time LAWS has reached the hardware stage. Therefore, 40% has been used in this analysis for the heterodyne quantum efficiency. It must also be remembered that this value is for the worst case Doppler frequency of 1.15 GHz; the Doppler shift due to the spacecraft motion will be less than this value for a large portion of the scan.

The final factor in the efficiency term is the Gaussian beam truncation loss. Assuming a Gaussian beam from the laser truncated at the exp(-2) points results in a 3 to 5 dB loss in the energy falling in the central maximum in the far field. A factor of 0.46 has been used in this analysis for the Gaussian beam truncation loss, however, continuing analysis of the graded reflectivity mirrors used in the transmit laser may significantly improve this factor.

The total system efficiency, combining the optics, heterodyne, detector and Gaussian beam terms, is 7.5%. As stated, this efficiency term will continue to be investigated, especially the Gaussian beam truncation loss and the heterodyne efficiency for both single and array detectors.

The atmospheric backscatter profile that has been used for the performance evaluation is the baseline LAWS model provided by NASA MSFC. Figure 6-7 shows the median value of this backscatter profile, both with and without the high altitude cirrus contribution. The SNR will be presented for this median backscatter value and then the statistical nature of this profile will be addressed. Using these median backscatter profiles, along with the system and subsystem parameters presented earlier, results in the narrow band SNR shown in Figure 6-8. In the upper altitudes, a median backscatter, without cirrus, of $2x10^{-11}$ results in an SNR of -6.7 dB. This curve can then be used to determine a first-order relationship between backscatter and SNR. That is, a backscatter of about $3x10^{-11}$ corresponds to -5 dB, $1x10^{-10}$ corresponds to about 0 dB, and so on. This first-order relationship ignores the altitude dependence of the SNR, including the atmospheric transmission and turbulence effects, however, it is still very useful in order to get a simple picture of the system performance.

Using the SNR and backscatter realtionships presented in Figures 6-7 and 6-8, the effect of the statistical nature of the backscatter on performance can be evaluated. Figure 6-9 is a plot of the probability of achieving a given SNR based on the backscatter distribution and the first-order backscatter/SNR relationships. For the case without cirrus, the SNR can be expected to be greater than -5 dB 50% of the time in the upper troposphere. The distribution for 0 and +5 dB are also presented both with and without cirrus.

6.3 Line-of-Sight Velocity Error

Several Doppler velocity algorithms are available for estimation of the line-of-sight velocity. Lassen Research has developed an Adaptive Poly-Pulse Pair, APPP, algorithm under GE IR&D funding. Figure 6-10 compares the APPP median performance (designated "Lee" in the Figure) with the Cramer-Rao one sigma lower bound error estimate for the baseline LAWS SNR. These curves were generated based on a 23 m/s velocity search window. The curve on the far left of Figure 6-10(a) represents the Cramer-Rao lower bound estimate for velocity error assuming a 1 km vertical resolution. The baseline range gate is about 500 m (3 micro-second pulse) along the line-of-sight which corresponds to 3 independent measurements within a single vertical resolution of 1 km. Therefore, these velocity error estimates assume that 3 independent measurements will be used for a single, 1 km, line-of-sight velocity. The right-most curve represents the median error for the APPP algorithm with the same assumptions. Clearly, one method of improving the velocity estimate is to average more

LAWS Baseline Backscatter Profiles
Median Value, With and Without Cirrus

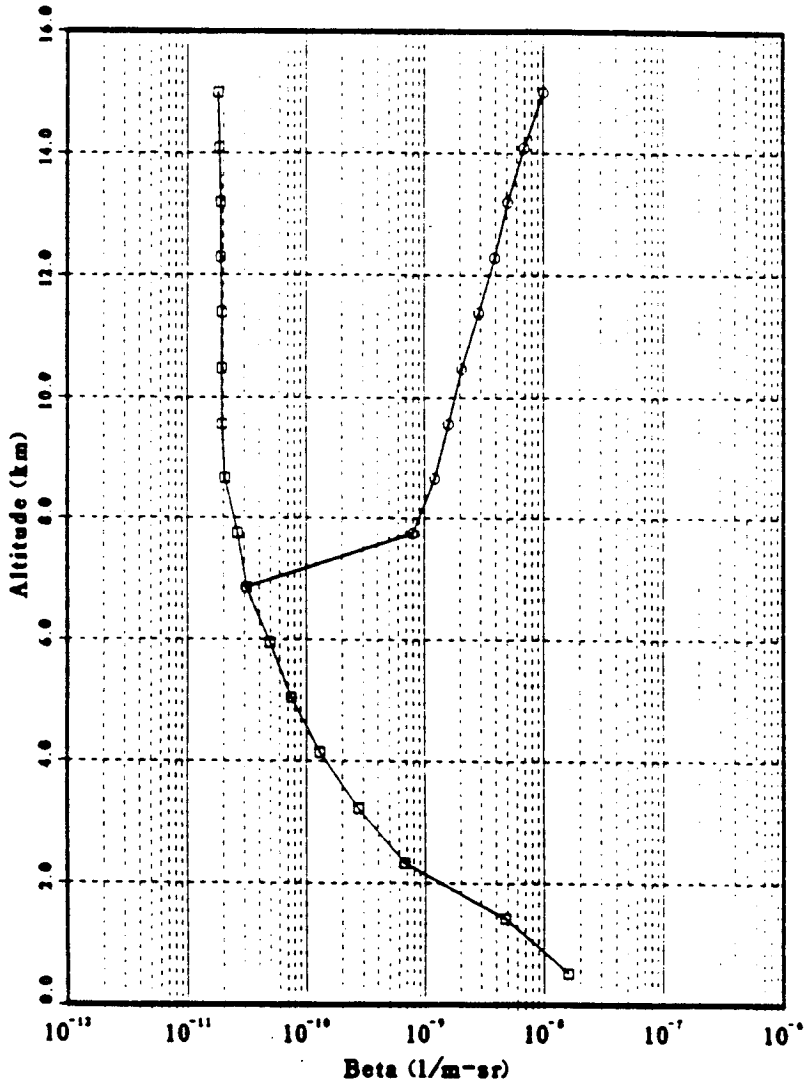

Figure 6-7. Median Backscatter Values

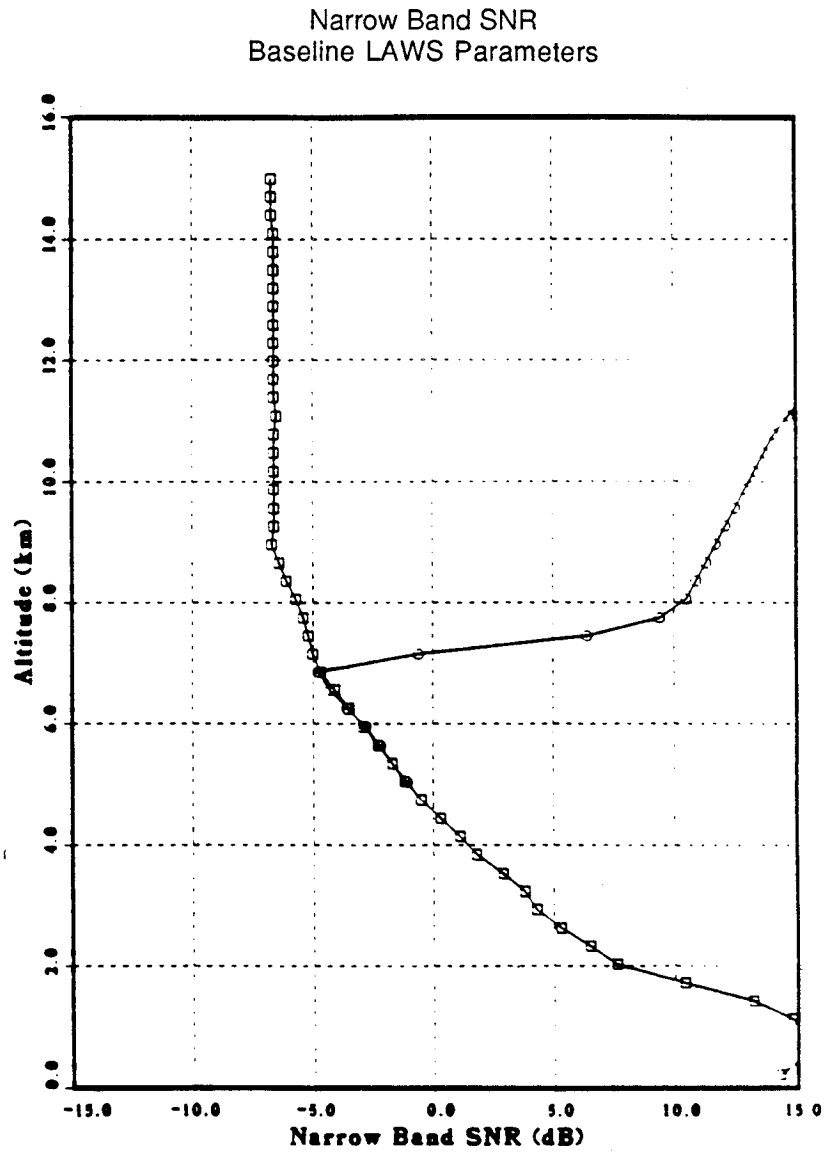

Figure 6-8. Narrow Band SNR for Median Backscatter

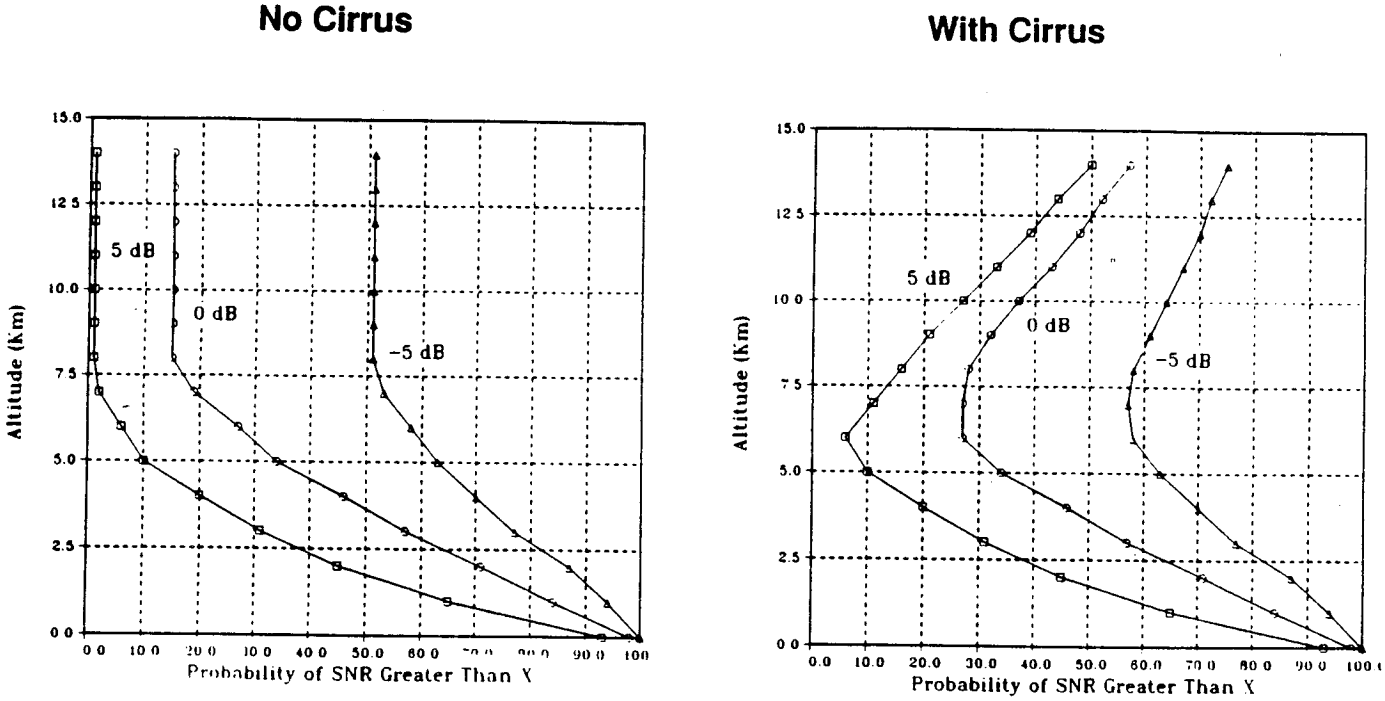

Figure 6-9. Probability of Achieving SNR Values of -5, 0 and 5 dB

measurements, assuming they are truly independent and the true velocity is the same for each. The middle curve in Figure 6-10(a) uses a 2 km resolution above 6 km altitude to improve the median error for the APPP algorithm to about 5 m/s. In the presence of cirrus (Figure 6-10(b)) the LOS velocity estimate is about 0.4 m/s.

As mentioned in the receiver configuration section (5.2.3) the choice of the APPP algorithm provides significant performance improvement over the previously proposed FFT and pulse pair algorithms while still maintaining the simplicity required for on-orbit implementation. Ground-based velocity estimation algorithms (see for example, Anderson and Hardesty, LAWS Science Team Meeting Minutes, Jan 15-17, 1990), will provide somewhat enhanced performance over the results presented here.

6.4 Horizontal Inversion Results

A set of line-of-sight velocity estimates within a chosen resolution volume can be used, together with the scan direction cosines, to perform the horizontal inversion. The LAWS simulation presented here uses a least squares algorithm which equally weights all of the realizations in the chosen volume.

The input wind field is a homogeneous wind field, that is, it is constant throughout the atmosphere. There is, however, a random distribution of winds with a mean value of 10 m/s and a one sigma value of 1 m/s. This distribution is in the horizontal component of the wind and will be somewhat less in the line-of-sight velocity.

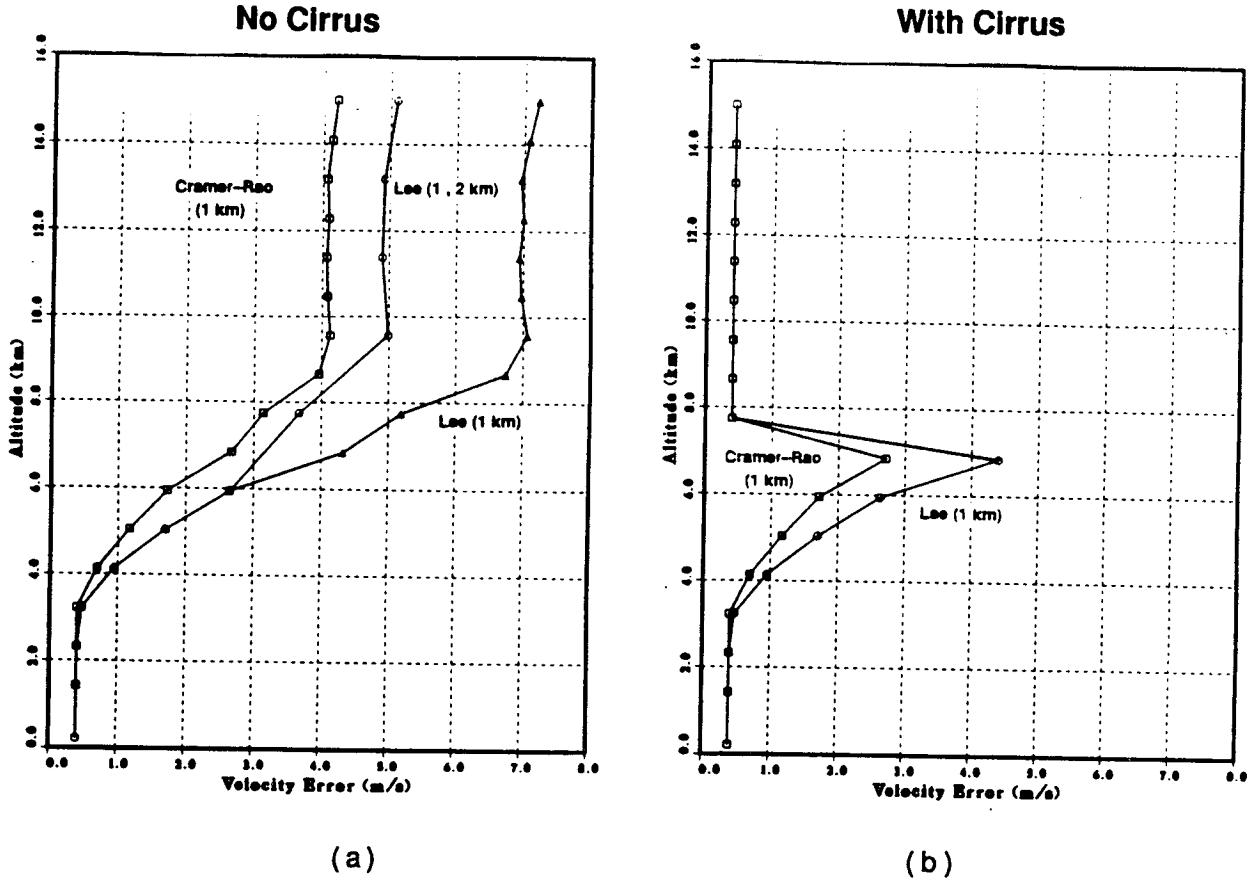

Figure 6-10. Line-of-Sight Velocity Error Estimates

In order to perform a horizontal inversion, we first specify a resolution volume. The simulation then runs through the scan and saves any measurements that intersect the chosen volume, each of which has a median line-of-sight velocity determined by the APPP algorithm. These realizations are then input to the least squares horizontal inversion, resulting in an estimated horizontal wind velocity and direction. The inversion has been performed for a 20 Hz maximum repetiiton rate laser operating in an asynchronous mode with a firing algorithm based on 1/cos of the azimuthal angle. This results in a scan average repetition rate of 13 Hz.

Figure 6-11 is a plot of the result of this inversion assuming a 100 by 100 by 1 km resolution volume centered at 4.5 km altitude which corresponds to an SNR of about 0 dB. The cell numbers along the x-axis represent the distance from the satellite ground track. Therefore, cell 1 is along the ground track and cell 9 is at the cross-track portion of the scan. Figure 6-11 clearly shows the inversion accuracy is very poor in the volumes both directly under the spacecraft and at the extreme cross-track position. The other horizontal velocity measurements fall generally within the 1 m/s band about zero. The dashed curve and the right hand scale are for the wind direction error. There is no single requirement for the wind direction error since it is a function of both the actual wind velocity and the wind velocity error. It can be seen, however, that for a 10 m/s true wind and a velocity uncertainty around 1 m/s, the wind direction estimate is within roughly 10 degrees of the true value in most instances.

The inversion at this resolution, 100 by 100 by 1 km, and the scan parameters of 20 Hz asynchronous rep rate and 12 RPM scan rate, result in 30 or so measurements per resolution volume. At higher altitudes the vertical resolution must be increased from one to two km in order to meet the required horizontal wind accuracy of 5 m/s. Figure 6-12 shows the inversion performance for the same homogeneous wind field at 12 km. In this case the SNR is about -6.5 dB and roughly 60 measurements fall within the 100 by 100 by 2 km resolution volume. The wind velocity error is generally within plus or minus 5 m/s and the direction within 20 degrees.

Note that the inversion results shown above in Figure 6-11 and 6-12 are single realizations of a statistical phenomenon and should be used only as examples of possible performance. A more detailed analysis would involve running many realizations and then computing the average performance.

6.5 Summary

The system performance requirements have been met for the chosen configuration. The median line-of-sight velocity errors for a 1 km vertical resolution are less than 1 m/s below an altitude of 4 km, less than 5 m/s between 4 and 7 km, and are a maximum of 7 m/s in the upper troposphere. Increasing the vertical resolution to 2 km in the upper troposphere results in a median LOS error of less than 5 m/s. These line-of-sight velocities are sufficient to meet the horizontal velocity accuracy requirements based on the analysis using the least squares algorithm and a homogeneous wind field input. These horizontal requirements are met based on a resolution of 100 by 100 by 1 km in the lower atmosphere and 100 by 100 by 2 km in the upper troposphere. All of the present analysis assumes a clear, cloud-free atmosphere. High cirrus will improve the performance while lower altitude clouds will significantly reduce the number of measurements.

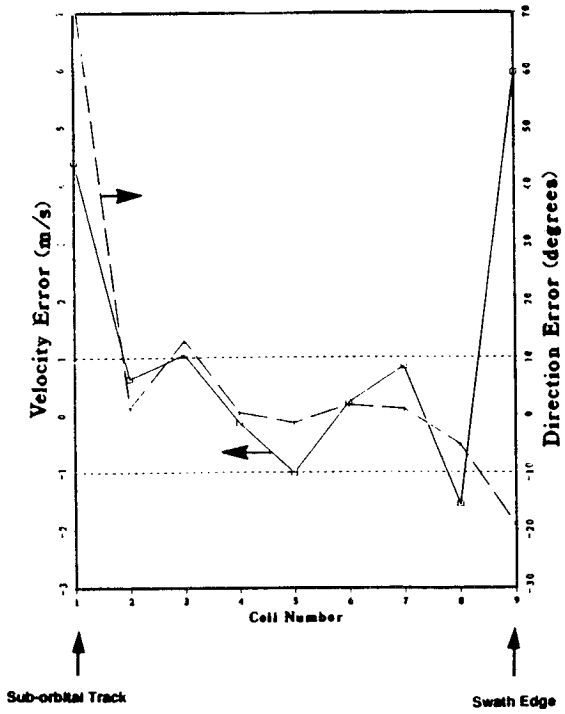

Figure 6-11. Horizontal Inversion for 4.5 km Altitude

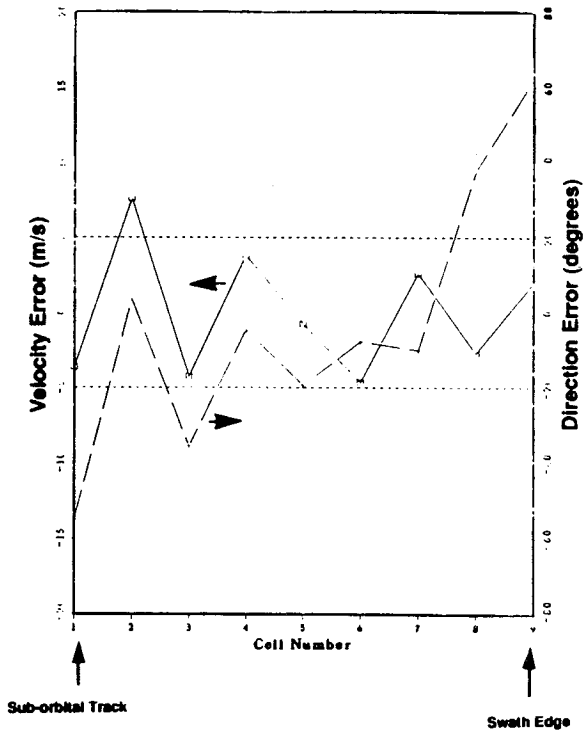

Figure 6-12. Horizontal Inversion for 12 km Altitude

C-3

7.0 LAWS BIBLIOGRAPHY

1972

Benedetti-Michelangeli, G., F. Congeduti and G. Fiocco (1972) " Measurements of Aerosol Motion and Wind Velocity in the Lower Troposphere by Optical Radar" J. Atmos. Sci., v29, pp 906-910.

1975

Eloranta, E.W., J.M. King, and J.A Weinman, "The Determination of Wind Speeds in the Boundary Layer by Monostatic Lidar, " Jo. Appl. Meteor., 14,1485, 1975.

1976

Huffaker, R.M., Beran, D.W., and Little, C.G., "Pulsed Coherent Lidar Systems for Airborne and Satellite Based Wind Field Measurements," 7th Conference on Aerospace and Aeronautical Meteorological and Symposium on Remote Sensing from Satellites, FL, Nov. 1976.

Holzapfel, W., "Laser Equipment and Optoelectronic Systems in Flight Guidance and Satellite Technology," NTIS 77N19433, 1979.

1978

Mandics, P.A., Huffaker, R.M., Lawrence, T.R., Hall, F.F., Jr., "Satellite-borne, Pulsed Coherent Infrared Lidar System for Global Wind Measurement," 21st Plenary Meeting, COSPAR, Innsbruck, Austria, May-Jun. 1978.

Huffaker, R.M., ed., "Feasibility Study of satellite-borne Lidar Global Wind Monitoring System," NOAA Tech. Memo, ERL WPL-37, Sep. 1978.

1979

Abreu, Vincent J., "Wind Measurements from an Orbital Platform Using a Lidar system with Incoherent Detection: An Analysis," Appl. Opt. 18, 2992,1979.

Huffaker, R. M., Lawrence, T.R., Mandics, P.A., Hall, F.F., Jr., "Global Wind Monitoring by Satellite-borne Coherent Lidar," SPIE Electro-Optical tech. Symp. & Workshop, Huntsville, AL., May 1979.

Post, Madison J., "Efects of the Earth's atmosphere on a Spaceborne IR Doppler Wind Sensing System," Appl. Opt. 18, 2645, Aug 1979.

Hinkley, E.D., "Global Wind Summary Report," JPL pub. 715-15, Nov. 1979.

M. Kh. Ashurov, Yu. K. Voron'ko, E.V. Zharikov, A.A. Kaminskii, V.V. Osiko, A.A. Sobol, M.I. Timoshechkin, V.A. Fedorov, and A.A. Shabaltai, Inorg. Mater., vol. 15, pp. 979-983, 1979.

1980

Bilbro, James W., "Atmospheric Laser Doppler Velocimetry: an Overview," Opt. Eng., Vol. 19, no. 4, 533-542, Jul./Aug. 1980.

Gardner, Philip J., "WINDSAT Laser Transmitter Design," Tech. Digest of the OSA Meeting on Coherent Laser Radar for Atmospheric Sensing, Aspen, CO, TuC7-1, Jul. 15-17 1980.

Huffaker, R.M., "Feasibility of a Global Wind Measuring Satellite System (WINDSAT)," ibid, WC5-1- WC5-6 .

Kidd, A.M., Altman, W.P., Hutter, E.C., "Wind Sensing Lidar System Testing on Free-Flying Satellites," ibid, TuC2-1-TuC2-3.

Kunkel, K.E., E.W. Eloranta and J.A. Weinman (1980) " Remote Determination of Turbulence Spectra and Energy Dissipation Rates from Lidar Measurements" J. Atmos. Sci., v37, pp 978-985.

Osmundson, J.S., Tuffo, A.G., Parks, J.K., Forsyth, J.B. and Morgan, L.L., "Shuttle-Borne Coherent Lidar Feasibility,", ibid, TuC3-1-TuC3-4.

Parks, J.S., Dobrov, W.I. and Osmundson, J.S., "WINDSAT Signal Processing," ibid, TuC6-1-TuC6-3.

Pepin, Theodore, J., "Aerosols in the Global Atmosphere," ibid, Wb7-1-Wb7-2.

Huffaker, R.M., Lawrence, T.R., Keeler, R.J., Post, M.J., Priestley, J.T., Korrell, J.A., "Feasibility Study of Satellite-Borne Lidar Global Wind Monitoring System Part II," NOAA Tech. Memo. ERL WPL-63, Boulder, CO, Aug 1980.

Sroga, J.T., E.W. Eloranta and T.L. Barber (1980) " Lidar Measurements of Wind Velocity Profiles in the Planetary Boundary Layer: J. Appl. Meteor., v19, pp598-605.

1981

Atlas,D. and C.L. Korb (1981) " Weather and Climate needs for Lidar Observations from Space and Concepts for their Realization" Bull. Am. Met. Soc., v62, pp 1270-1285.

Hinkley, E.D., "Advanced Instrumentation for Remote Sensing," Future Space Applications Paper, Jo. Astronautical Sciences, 29, 97, 1981.

McGuirk, Michael, "Wind Satellite (WINDSAT) Coherent Lidar Pointing System," Proc. SPIE, 265, Shuttle Pointing of Electro-Optical Experiments, pp 395-398, 1981.

Osmundson, John S., "Wind Satellite (WINDSAT) Experiment," ibid, pp 395-398.

"Global Wind Measuring Satellite System," Final Report NOAA Contract, NA79RAC00127, Boulder, CO, Apr. 1981.

"Accommodations Assessment: Spaceborne Doppler Lidar Wind Measuring system," NASA Tech. Memo. TM82435, Marshall Space Flight Center, Huntsville, AL, Aug 1981.

Hays, P.B., T.L. Killeen and B.C. Kennedy (1981) "The Fabry-Perot Interferometer on Dynamics Explorer" Space Sci. Instrum., v5 pp 395-416.

1982

Hinkley, E.D., "Advanced Sensors for Spaceborne Measurements of the Earth's Atmosphere," Proc. 32nd International Astronautical Federation Congress, 1981, Pergamon Press, UK, p235,1982.

Lawrence, T.R., Huffaker, R.M., Keeler, R.J., Post, M.J., Richter, R.A., Hall, F.F., Jr., "Feasibility and Design Considerations of a Global Wind Sensing Coherent Infrared Radar (WINDSAT)," Proc. SPIE, Physics and Technology of Coherent Infrared Radar, 300, pp 34-43, 1982.

"Feasibility Assessment: Satellite Doppler Lidar Wind Measuring System," Prepared by Marshall Space Flight Center, Huntsville, AL, Apr. 1982.

Emmitt, G.D., "Conical Scanning from LEO- The Effects of Meso Beta and Convective Scale Atmospheric Phenomena," Tech Digest of the 11th International Laser Radar Conference, Madison, WI, June 21-25, 1982, NASA CP-2228, pp 187-190, 1982.

Osmundson, John s., Huffaker, R.M., and McGuirk, Michael, "WINDSAT/Atmospheric Multi-User Lidar Compatibility," ibid, pp 183-186.

Deepak, A., Kent, G.S., and Yue, G.K., "Atmospheric Backscatter Model Development for CO2 Wavelengths," NASA Final Report 3638, 1982.

Sansano, Y., H. Hirohana, T. Yanasaki, H. Shimizu, N. Takeuchi and T. Kawamra (1982) " Horizontal Wind Vector Determination from the Displacement of Aerosol Distribution Patterns Observed by a Scanning Lidar" J. Appl. Meteor., v21, pp1516-1523.

1983

"Feasibility Study of a WINDSAT Free-Flyer," Final Report NOAA Contract NA82RAC00141, Boulder, CO, Jul 21, 1983.

Altman, W.P., Gurk, H.M., and Kaskiewicz, P.F., "Feasibility of a WINDSAT Free-Flyer Using an Advanced TIROS-N Satellite," Tech. Digest of the OSA 2nd Topical Meeting on Coherent Laser Radar: Technology and Applications, Aspen, CO, Aug. 1-4, p TuC3, 1983.

Byron, S.R., Moody, S.E., and Znotins, T.A., "Definition Study of the WINDSAT Laser Subsystem" ibid, p TuC4.

Emmitt, G.D., "Influence of Coherent Mesoscale Structure on Satellite Based Doppler Lidar Wind Measurements," ibid, p TuC2.

Huffaker, R.M., "Global Wind Measuring Satellite System (WINDSAT) Feasibility Studies," ibid, p TuC1.

McHugh, T.J., and Hancock, K.C., "WINDSAT Free-Flyer Telescope Concept Using Ultra-Lightweight Beryllium Technology," ibid, p TuC5.

1984

Bilbro, James, W., and Emmitt, George, D., "Airborne Simulation of a Satellite Based Doppler Lidar," Proc. SPIE, 493, National Symposium and Workshop on Optical Platforms, pp 321-325, 1984.

Gurk, Herbert M., Kaskiewicz, Paul F., and Altman, Wolf P., "WINDSAT Free-Flyer Using the Advanced Tiros-N Satellite," Appl. Opt. 23, 2537-2544, 1984.

Huffaker, R.M., Lawrence, T.R., Post, M.J., Priestley, B.T., Hall, F.F., Jr., Richter, R.A., Keeler, R.J., "Feasibility Study for a Global Wind measuring Satellite System (WINDSAT): Analysis of Simulated Performance," ibid, pp 2523-2536.

Hays, P.B., V.J. Abreu, J. Sroga and A. Rosenberg (1984) "Analysis of a 0.5 micron Spaceborne Wind Sensor" in Preprints of the Conference on Satellite/Remote Sensing and Applications, Clearwater Beach Fla.,June 25-29,1984, pp 266-271.

Killeen,T.L. and P.B. Hays (1984) " Doppler Line Profile Analysis of a Multichannel Fabry-Perot Interferometer", Appl. Opt., v23, pp612-620.

1985

Curran, Robert J., "State of the Art in Global Doppler Lidar Wind Profiler Development," Third NASA/NOAA Infrared Backscatter Workshop, Incline Village, NV, pp iv-v, Jan 14, 1985.

Bowdle David, A., "An Airmass-Based Global Model for Aerosol Backscatter," ibid, pp 106-118.

Fitzjarrald, Daniel, E., "Status of Global Doppler Lidar Wind Profiler System Study," ibid, pp 28-32.

McCormick, M. Patrick, "Stratospheric Aerosols: A Global Climatology," ibid, pp 43-76.

Hinkley, E.D., Lesh, J.R., and Menzies, R.T., "Lasers in Space," Laser Focus/Electro-Optics, pp 78-, Feb. 1985.

Hess, R.V., Brockman, P., Schreyer, D.R., Miller, I.M., Bair, C.H., Sidney, B.D., Wood, G.M., Upchurch, B.T., and Brown, K.G., "Technology Assessment of High pulse Energy CO2 Lasers for Remote Sensing from Satellites," NASA Tech. Memo., TM-86415, Apr. 1985.

Arnold, C., "Results of an Observing System Simulation Experiment Based on the Proposed WINDSAT Instrument," Tech. Digest of the 3rd Topical Meeting on Coherent Laser Radar: Technology and Applications, Great malvern, UK, p 190, July 7-11, p 176, 1985.

Curran, R., and Tilford, S., "NASA Activities in Space Lidar," ibid, pp 92-93.

Huffaker, R.M., "Global Wind Profiling System Technology," ibid, pp 1-4.

de Villiers, N., "How Space Based Laser Instruments Might Contribute to ESA's Future Earth Observation Space Plans," ibid, pp 185-189.

Arnold, Charles P., Jr., Dey, Clifford H., and Bostleman, William J., "Results of an Observing System Simulation Experiment Based on the Proposed WINDSAT Instrument," Proc. NASA Symposium on Global Wind Measurements, Columbia, MD, Jul 29-Aug 1, pp 81-88, 1985.

Bowdle, David A., "Aerosol Measurement Program Strategy for Global Aerosol Backscatter Model Development," ibid, pp239-242.

Chang, Ho-Pen, Worley, Gary G., and Frost, Walter, "Develop a Plan for Establishing Global Aerosol Backscatter Coefficient Data Base," ibid, pp 243-246.

Dey, Clifford H., Bostleman, William J., and Arnold, Charles P., Jr., "Design of a WINDSAT Observing System Simulation Experiment," ibid, pp 73-80.

Fitzjarrald, D., Beranek, R., Bilbro, J., Mabry, J., "Preliminary Plan for a Shuttle Coherent Atmospheric Lidar Experiment (SCALE)," ibid, pp 207-214.

Gurk, Herbert M., Kaskiewicz, Paul F., and Altman, Wolf P., "WINDSAT Free-Flyer Using the Advanced TIROS-N Satellite," ibid, pp 201-206.

Huffaker, R.M., "The WINDSAT Concept for Measuring the Global Wind Field," ibid, pp 215-222.

Menzies, Robert T., "A Comparison of Doppler Lidar Wind Sensors for Earth-Orbit Global Measurement Applications," ibid, pp 189-194.

Osmundson, John S., and Martin, Stephen C., "Lockheed Design of a Wind Satellite (WINDSAT) Experiment," ibid, pp 195-201.

Fitzjarrald, D., Bilbro, J., Beranek, R., and Mabry, J., "Doppler Lidar Measurement on Eos," AIAA NASA Earth Observing System Conference, Virginia Beach, VA, Oct 8-10, 1985.

"Shuttle Coherent Atmospheric Lidar Experiment (SCALE)," Prepared by George C. Marshall Space Flight Center, Oct. 1985.

Baker, Wayman E., and Curran, Robert J., editors "Proc. NASA Symposium on Global Wind Measurements," A. Deepak Publishing, Dec 15, 1985.

Baker, Wayman E., and Curran, Robert J., editors "Report of the NASA Workshop on Global Wind Measurements," A. Deepak Publishing, STC-2081, Dec 15, 1985.

Lawrence, T.R., "Effects of Wavelength on Coherent Doppler Lidar Performance," ibid, pp 183-187, 1985.

Eloranta, E.W. (1985) " Aerosol Pattern Correlation Technique of Wind Measurement" in Proceeding of the NASA Symposium on Global Wind Measurements, W.E. Baker and R.J. Curran, eds., A. Deepak Publishing, Hampton, VA., pp 163-165.

McDermid, I.S., J.B. Laudenslager and D. Rees (1985) " Ultraviolet-Excimer Laser-Based Incoherent Doppler Lidar System" in Proceedings of the NASA Symposium on Global Wind Measurements, W.E. Baker and R.J. Curran eds., A. Deepak Publishing, Hampton, VA, pp 149-155.

1986

Curran, R.J., "Lidar Remote Sensing from Space: NASA's Plans in the Earth Sciences," Tech. Digest of the 13th International Laser Radar Conference, Toronto, Ont., Aug 11-15, NASA CP 2431, p 2, 1986.

Huffaker, R.M., "Coherent Lidar Technology for Global Wind Profiling," ibid, p 4-5.

Hochuli, U.E. and P.R. Haldemann, "Life Problems of dc and rf Excited Low-power CW CO_2 Waveguide Lasers," Rev. Sci. Instr. 57, 2238, 1986.

Kavaya, Michael J., and Huffaker, R. Milton, "Wavelength Dependence of Coherent and Incoherent Satellite-Based Lidar Measurements of Wind Velocity and Aerosol backscatter," ibid, pp 269-272.

Hooper, W.P. and E.W. Eloranta (1986) " Lidar Measurements of Wind in the Planetary Boundary Layer: The Method, Accuracy and Results from Joint Measurement with Radiosonde and Kytoon" J. Climate and Appl. Meteor, v25, pp990-1001.

Menzies, R.T. (1986) " Doppler Lidar Atmospheric Wind Sensors: A Comparative Performance Evaluation for Global Measurement Application from Earth Orbit" Appl. Opt., v25, pp 2546-2553.

1987

"Feasibility Study of a Carbon Dioxide Doppler Lidar on an Earth Orbiting Platform," RCA Astro-Electronics Final Report, JPL Contract Number 957746, 1987.

LAWS Instrument Panel Report, NASA Earth Observing System Report Vol. IIg, 1987.

Sroga, J., and Rosenberg, A., "0.53 μm Incoherent Doppler Lidar: Current Status,", Optical Society of America Topical Meeting on Laser and Optical Remote Sensing: Instrumentation and Techniques, Cape Cod, Sept. 28- Oct. 1, 1987.

T.Y.Fan, G. Huber, R.L. Byer, and P. Mitzscherlich, IEEE J. Quantum Electron., vol. 24, pp. 924-933.

G.J. Kintz, R. Allen, and L. Esterowitz, Postdeadline Papers, Conf. Lasers Electro-Opt., Opt. Soc. Amer., Washington, DC, 1987, paper ThU4.

1988

Ancellet, G.M., R.T. Menzies, D.M. Tratt, "Atmospheric Backscatter Vertical Profiles at 9.2 and 10.6 μm: a Comparative Study," App. Opt. 27, 4907, 1988.

Krishnamurti, T.N., et al, LAWS as a Space Station Attached Payload," Proposal to NASA in response to OSSA Earth Observing System A.O. number OSSA-1-88, 1988.

Kolev, I., O. Parvanov and B Kaprielov (1988) " Lidar Determination of Winds by Aerosol Inhomogeneities: Motion Velocity in the Planetary Boundary Layer" Appl. Opt. 27, 2524, 1988.

1989

Petheram, J.C., Frohbeiter, G. and Rosenberg, A, "Carbon Dioxide Doppler Lidar Wind Sensor on a Space Station polar Platform," Appl. Opt. 28, 834, 1989.

Petheram, J.C., Shanley, J.F., Sroga, J.T., Vitz, R.C., Wissinger,A.B., and Lawrence, T.R., "The Laser Atmospheric Wind Sounder (LAWS)-Preliminary Design", SPIE O-E LASE, Paper 1062-41, January 1989.

Beranek, R.G., Bilbro, J.W., Fitzjarrald, D.E., Jones, W.D., Keller, V.W., and Perrine, B.S., "Laser Atmospheric Wind Sounder (LAWS)", SPIE O-E LASE, Paper 1062-36, January 1989.

Hamilton, C.E., Pidroh, A.L., Lawrence, T.R., and Fisher, C.H., "Small signal Gain and Vibrational relaxation for Rare Isotope $^{12}C^{18}O_2$, 5th Conference on Coherent Laser Radar, Munich June 5-9, 1989.

G. Kintz, I.D. Abella, and L. Esterowitz, "Upconversion Coefficient Measurement in Tm3+, Ho3+:YAG at Room Temperature," source of reference unknown.

APPENDIX 5-1

LAWS LAG ANGLES AND INTERNAL BEAM GEOMETRY

The objective of this memo is to document the relationships between the LAWS operational parameters (altitude, scan rate, cone angle) and the resulting lag angle and beam geometry inside the telescope.

LAG ANGLE DERIVATION

First, let's tackle the lag angle relationships. Lag angle is defined as the angle through which the LAWS line of sight turns during the time required for a laser shot to travel to the atmosphere and return. We'll refer to this time as the "echo time", or T_e.

The first step in solving the problem is to determine the echo time from the path length from the telescope to the ground and return. The LAWS geometry is shown below (with the simplifying assumption that the Earth is flat).

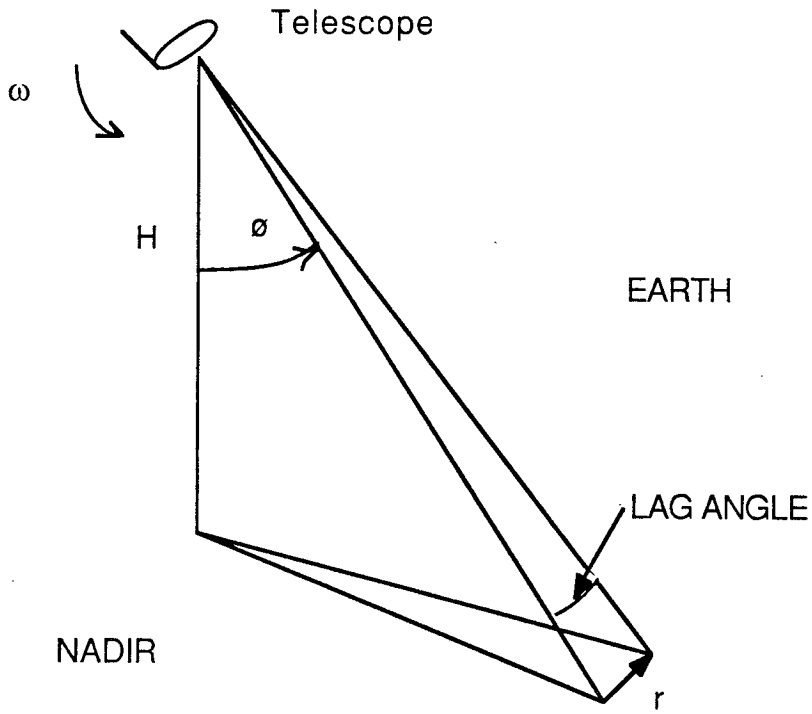

The length of the path followed by the laser pulse is given by

$$2\,H/\cos ø$$

where the factor of two is for the round trip. The time for light to cover this distance is obtained by dividing by the speed of light, c (= 3E8 meters per second).

The current nominal altitude for the LAWS mission is 824 Km, and if flown on the space station, the altitude will vary between 500 Km and 300 Km. For ø = 45°, we can obtain the echo time, T_e :

H	T_e
824Km	7.77E-3
500	4.71E-3
300	2.83E-3

So we see that the echo time will nominally be slightly less than 8 milliseconds, and could be a little less than 3 milliseconds for the Space Station at its lowest altitude.

Now let's determine the lag angle for these conditions. Referring again to the figure, the lag angle is given by

$$r/(H/\cos ø),$$

which is simply the the angle subtended by the distance travelled on the ground by the intercept of the LOS. r is given by the angular velocity times the echo time T_e times the radius from the rotational axis to the ground intercept. The radius is H tan ø and defining the angular velocity as ω, we have

$$\text{Lag Angle} = \frac{\omega (H \tan ø)}{H/\cos ø} T_e$$

Since $T_e = 2 \frac{H}{\cos ø} \frac{1}{c}$, the expression simplifies to

$$\text{Lag Angle} = \frac{2 \omega (H \tan ø)}{c}$$

For a scan rate of 12 RPM, ω = 1.257 radians per second (72° per second). Evaluating for the same altitudes as used above,

H	Lag Angle		
824 Km	6.905E-3 radians	(0.4°)	(Baseline mission)
500	4.190E-3	(0.24°)	
300	2.514E-3	(0.144°)	

Note that these angles are the total change in the line of sight, not semi field angles

This derivation should be repeated for a round Earth.

PULSE GEOMETRY

The outgoing laser pulse duration is 3 μseconds. The scanning is continuous, which means that the transmitted laser pulse will be somewhat skewed. In addition, the backscattered pulse returning from the atmosphere will be considerably stretched in time, and the scan rotation will require continuous correction in order to maintain the image stationary on the detector. Let's determine the magnitude of these effects.

In 3 μseconds, light travels 3E-6 x 3 E 8 = 900 meters. The scan direction during the 3 μsecond transmit time will change by 3E-6 x 1.257 = 3.77 μradians. Since the beam spread[3] for the 1.5m aperture is ~ 15 μradians, the beam skew is an appreciable fraction of the beam spread (or projected image diameter) and cannot be ignored.

The lag angle effect during reception of the backscattered pulse is even more pronounced. This is because the return pulse is stretched as it reflects from all the different altitudes in the atmosphere that have sufficient scatterers to produce a signal. If the highest altitude for sensible backscattering is 15 Km, then the pulse length would be (15 Km/900) x 3E-6 x 2, where the factor of two is to account for the pulse stretching that occurs as the distance to each successive atmospheric layer increases. For a 45° cone angle, the return pulse time will be (15 Km/900) x 3E-6 x 2/cos 45° = 141 μseconds plus the length of the original pulse, or 144μseconds.

During the 144 μseconds the backscattered pulse is being received, the telescope will rotate 144E-6 x 1.257 = 181 μradians. Since this is larger than the image, it is clear that the telescope rotation rate must be compensated by a counter-rotating mirror in the beam.

There is also an angular change in LOS direction due to the pitch velocity required to maintain scan axis alignment with the Nadir. For a nominal 100 minute orbit, this pitch velocity amounts to $2\pi/100*60$ radians per second. The change in line of sight direction during the 7.77 millisecond echo time is $7.77E\text{-}3*2\pi/6000$ = 8.137 μradians. Since this is half the image diameter, it must also be compensated. Note that this error vector will appear to rotate relative to the lag angle discussed above.

Since, in the current design concept, the IMC mirror is not at a pupil, it will be larger than the beam. The next section deals with the size of the IMC mirror.

---

[3] Assuming a uniform intensity distribution for the projected laser beam yielding an Airy pattern. A Gaussian beam will have a different beam spread. The LAWS beam profile will be somewhat irregular.

BEAM GEOMETRY INSIDE TELESCOPE

The magnification of the confocal parabola telescope is 33.33333x, and the separation between the primary and secondary mirrors is nominally 1455 mm. Thus, the separation of the outgoing and incoming beams on the primary mirror will be 33.33333 x 1455 times the lag angle in radians. For the baseline mission case (12 RPM and 824Km altitude; lag angle = 6.905 milliradians), the center of the two beams will be separated by 334.9 mm. Since the beams are 45 mm in diameter, the beams themselves will be separated by 290 mm (11.4in.).

The minimum scan rate that could be accommodated will be limited by the case in which the beams just touch. The beam centers would be separated by 45 mm, and the angular subtense in object space would be (45/1455)/33.333... = 927.8 μradians. Solving for the rotation rate in the lag angle equation, we get ω = 0.169 radians per second (or 1.6 RPM).

The beams must be folded so that they are parallel and close together for passage through the center of the scan bearing. If we choose to split the lag angle between the outgoing and incoming beams, each beam will be inclined at an angle of 33.33333 x 6.905/2 = 115.1 milliradians (6.6°) relative to the optical axis of the telescope. If we use a pair of pre-set folding mirrors at nominally 45° as shown in the optical diagram, the angle between the two mirrors will differ by half of this, or 57.6 milliradians. The image motion compensation (IMC) mirror will be located on the stationary side of the scan bearing as shown in the optical schematic. The path length to the IMC may be as much as 5 meters.

How much beam motion would result from the lag angle during reception of the return pulse?

For each microradian of beam motion in object space, there will be 33.333333 x 5 μmeters (=166.67 μm) of motion on the IMC mirror. For the largest uncompensated error (the lag angle during receive) discussed above, the beam motion will be 166.67 x 177.2 μradians = 29533.33 μm or 29.5 mm. This is an appreciable fraction of the diameter of the beam and may require an excessively large IMC mirror. Placement of the IMC mirror closer to the exit pupil of the telescope would help. Note that the IMC mirror cannot be closer to the exit pupil than the primary mirror is (i.e. ~1.5m). If the IMC were at the primary mirror, the beam displacement would be ~8.85 mm. Of course, we will need to accommodate more beam motion than just this, because other motions (e.g. spacecraft jitter) are to be accommodated by the IMC. We also need to determine the sensitivity of wave front errors to this magnitude of beam motion.